

Review

Plasma assisted combustion: Dynamics and chemistry

Yiguang Ju^{a,*}, Wenting Sun^b^a Department of Mechanical and Aerospace Engineering, Princeton University, NJ 08544, USA^b School of Aerospace Engineering, Georgia Institute of Technology, GA 30332, USA

ARTICLE INFO

Article history:

Received 14 July 2014

Accepted 4 December 2014

Available online

Keywords:

Plasma assisted combustion

Combustion enhancement

Chemistry

Dynamics

Diagnostics

Non-equilibrium plasma

Kinetic model

ABSTRACT

Plasma assisted combustion is a promising technology to improve engine performance, increase lean burn flame stability, reduce emissions, and enhance low temperature fuel oxidation and processing. Over the last decade, significant progress has been made towards the applications of plasma in engines and the understanding of the fundamental chemistry and dynamic processes in plasma assisted combustion via the synergetic efforts in advanced diagnostics, combustion chemistry, flame theory, and kinetic modeling. New observations of plasma assisted ignition enhancement, ultra-lean combustion, cool flames, flameless combustion, and controllability of plasma discharge have been reported. Advances are made in the understanding of non-thermal and thermal enhancement effects, kinetic pathways of atomic O production, diagnostics of electronically and vibrationally excited species, plasma assisted combustion kinetics of sub-explosion limit ignition, plasma assisted low temperature combustion, flame regime transition of the classical ignition S-curve, dynamics of the minimum ignition energy, and the transport effect by non-equilibrium plasma discharge. These findings and advances have provided new opportunities in the development of efficient plasma discharges for practical applications and predictive, validated kinetic models and modeling tools for plasma assisted combustion at low temperature and high pressure conditions. This article is to provide a comprehensive overview of the progress and the gap in the knowledge of plasma assisted combustion in applications, chemistry, ignition and flame dynamics, experimental methods, diagnostics, kinetic modeling, and discharge control.

© 2014 Elsevier Ltd. All rights reserved.

Contents

1. Introduction	1
1.1. Needs of combustion and emission control in extreme conditions	1
1.2. Plasma assisted combustion: a new way to control combustion, emissions, and fuel reforming	2
1.3. Non-equilibrium plasma and the impact of plasma on combustion	3
1.4. Progress and challenges in fundamental studies of plasma assisted combustion	4
1.5. Focus of this review	7
2. Plasma assisted combustion: applications and technological development	7
2.1. Plasma assisted combustion for supersonic propulsion and scramjet engines	7
2.2. Ignition enhancement by plasma in internal combustion engines	10
2.3. Plasma assisted combustion for pulse detonation engines	14
2.4. Plasma assisted combustion for flame stabilization in gas turbine engines	14
2.5. Emission control and fuel reforming by plasma	17
3. Flame dynamics and chemistry in plasma assisted combustion	18
3.1. Dynamics and chemistry of plasma assisted ignition	18
3.2. Dynamics, chemistry, and transport of plasma assisted flame propagation	20
3.3. Dynamics, chemistry, and transport of flame initiation and minimum ignition energy and the role of plasma discharge	22
3.4. Plasma assisted ignition by creating a large discharge volume	23

* Corresponding author. Tel.: +1 609 258 5644; fax: +1 609 258 6233.

E-mail address: yju@princeton.edu (Y. Ju).

4.	Kinetic studies of plasma assisted combustion using idealized experiments	24
4.1.	Kinetic process in plasma discharge	25
4.2.	Effects of plasma on ignition	26
4.3.	The thermal and kinetic effects of plasma on flame extinction	28
4.4.	Effects of plasma on flames: the role of O_3 and $O_2(a^1\Delta_g)$	30
5.	Advanced diagnostics for plasma assisted combustion	32
5.1.	Measurements of plasma properties	32
5.1.1.	Thomson scattering for electron density and electron temperature measurement	32
5.1.2.	Electric field measurement	33
5.2.	Measurements of plasma generated excited species	33
5.2.1.	Measurement of ozone	33
5.2.2.	Measurement of singlet delta oxygen, $O_2(a^1\Delta_g)$	33
5.2.3.	Measurement of electronically and vibrationally excited nitrogen	34
5.3.	Measurements of active radicals by laser induced fluorescence method	34
5.3.1.	OH measurement by OH PLIF method	34
5.3.2.	Atomic O and H measurement by TALIF method	35
5.4.	Temperature measurements	35
5.4.1.	Planar Rayleigh scattering thermometry	35
5.4.2.	Coherent anti-Stokes Raman scattering (CARS) thermometry	36
5.4.3.	NO laser induced fluorescence (LIF) thermometry	36
5.5.	Measurement of intermediate species	36
5.5.1.	CH_2O measurement by CH_2O PLIF method	36
5.5.2.	Measurement of H_2O , CH_4 , CH_2O and C_2H_2 by mid-IR absorption method	37
5.5.3.	Faraday rotation spectroscopy for HO_2 measurement	37
6.	Development of kinetic mechanisms and methods for plasma combustion modeling	37
6.1.	Coupling plasma mechanisms with combustion mechanisms	38
6.2.	Recent developments of plasma mechanisms	38
6.3.	Plasma assisted combustion modeling	39
7.	Technical challenges and future research	39
8.	Conclusion	40
	Acknowledgment	41
	References	41

1. Introduction

1.1. Needs of combustion and emission control in extreme conditions

More than 80% of world energy today is converted by combustion. In air transportation, combustion has been playing a dominant role because of the high energy density of liquid fuels and the advantage in fast refueling. However, the energy conversion efficiency of existing combustion engines is still low, and the combustion of fossil fuels has become a major concern due to its influence on climate change and air pollution [1].

For ground transportation, various new combustion engine technologies such as the Homogeneous Charge Compression Ignition (HCCI) engines [2–4], Partially Premixed Compression Ignition (PPCI) [5], and the Reactivity Controlled Compression Ignition (RCCI) engines [6] have been developed. These engines use a higher compression ratio and lower combustion temperature to increase engine efficiency and reduce emissions and heat losses. However, at a high compression ratio and engine load, control of ignition timing at low and intermediate temperature conditions near the negative temperature coefficient (NTC) [7] region becomes extremely difficult. Failure to accurately control ignition timing and heat release rate may lead to either excessive unburned hydrocarbon emissions or engine knock. Although fuel stratification and dual fuel combustion technologies have been demonstrated to be able to control ignition, the use of multiple fuel pumping systems and multi-pulse fuel injectors increases the complexity of ignition control over a broad engine loads. Therefore, there is a great need to develop an alternative method with rapid control of engine ignition.

For air transportation, in order to increase the fuel efficiency and meet the stringent emission standards of the Committee on Aviation Environmental Protection (CAEP-6) and NASA (N+3), new lean burn aircraft combustor concepts such as the twin annular pre-mixing swirled (TAPS) lean-burn burners [8,9], lean direct injection (LDI) burners [10], trapped vortex combustion (TVC) lean burners [11], and pressure gain combustors [12] have been developed. One of the biggest challenges in the development of lean burn engines is flame instability. Therefore, it is important to develop a novel flame stabilization method to achieve stable ultra-lean combustion. On the other hand, the recent interest in supersonic propulsion, such as for the X-51, has highlighted the increased challenge of ignition control and flame stabilization under these conditions [13–15]. For example, near flight Mach number 5, the flow residence time is so short that the ignition and flame Damköhler numbers (respectively, the ratio of flow residence time to ignition delay time and fuel consumption time) are less than unity. As a result, there is not enough time for the fuel to auto-ignite and to be oxidized completely. Therefore, it is also necessary to develop new technologies to enhance ignition, stabilize flame, and to complete combustion for scramjet engines.

For ground power generation and industrial burners, CO_2 capture and NO_x emission reduction are the primary drivers to the development of ultra-lean high hydrogen content (HHC) gas turbines [16,17], flameless combustion [18,19], and oxyfuel combustion [20]. In the development of ultra-lean HHC gas turbine combustion, combustion instability and flame flashback are among the greatest challenges. Another challenge is the broad distribution of syngas energy density (5–80 MJ/kg) [21] that further increases the problem of flame instability. For conventional flameless

combustion, the oxidizer temperature needs to be preheated to 1300–1400 K to achieve auto-ignition. As a result, the flameless combustion technique is difficult to use in high pressure combustors such as gas turbines due to material failure. The question is whether we can develop a new ignition enhancement technique so that the temperature of flameless combustion can be significantly reduced. In oxyfuel combustion, excessive exhaust gas recirculation (EGR) of CO_2 is used to reduce NO_x emissions from trace nitrogen. Therefore, a reliable lean burn technology is needed for oxyfuel combustion.

Furthermore, recent development of alternative and bio-derived fuels to address energy sustainability and CO_2 emissions further complicates the combustion and emission control [1,22–24]. In Europe, biogas produced from bio-wastes attracts great attention as a renewable energy source for power generation. The EU Sustainable Bio-Fuel Jet Mandate targets 80% biofuel for aviation by 2050. In the US, about 49 billion liters of corn ethanol and 4.1 billion liters of biodiesel were produced in 2012. At the same time, unconventional shale gas production reached one-third of the total US natural gas production. Oil production from tar sands, high hydrogen syngas production from coal and biomass, synthetic aviation fuel production from natural gas, coal and ethanol, and bio-oils from plant oil and lignocellulosic biomass are also increasing [25–27]. These alternative fuels have completely different molecular structures and ignition properties from traditional transportation fuels [28–32]. Moreover, biogas consists of trace amounts of hazardous materials such as sulfur volatile organic compounds (VOCs), silicone, and sulfur compounds [33]. Therefore, ignition and emission control using biofuels and alternative fuels can be very challenging. Moreover, the existing technology for fuel reforming and hydrogen (H_2) production from large hydrocarbon fuels using steam reforming is very energy intensive and requires expensive noble metal catalysts [34]. As such, an alternative method for fuel reforming and hydrogen production is needed.

These new regulations and requirements have posed unprecedented challenges for combustion researchers to develop new engine and fuel technologies to drastically increase the engine efficiency, reduce emissions, and achieve extended flight envelopes of high speed propulsion at extreme conditions [28,35].

1.2. Plasma assisted combustion: a new way to control combustion, emissions, and fuel reforming

Plasma, which is the fourth state of matter, provides an unprecedented opportunity for combustion and emission control (Fig. 1.1) owing to its unique capability in producing active species and heat and modifying transport processes. New reaction pathways, such as atomic O production from the collisions between high energy electrons/ions and oxygen molecules, can be

introduced into combustion systems to modify the fuel oxidation pathways considerably.

In last the two decades, plasma has been demonstrated as a promising technique to enhance combustion, reduce emissions, and improve fuel reforming [36–43]. In high speed propulsion such as scramjet engines, since the pioneering work of Kimura et al. [44] in 1980s, recent studies using plasma torch [41,45–50], filamentary discharge [42,51], microwave discharge [52], low frequency arc discharge [53], streamer high frequency (HF) discharge [54], surface discharge [55], and nanosecond pulsed discharge (NSD) [56] have showed that plasma can enhance ignition, flame stabilization, and fuel/air mixing via chemical, thermal, and plasma induced aerodynamic effects. Recent studies [57–62] have also demonstrated that plasma discharge in pulsed detonation engines (PDE) can shorten the ignition delay time, and facilitate the transition from deflagration to detonation. In applications for gas turbine engines, pulsed and steady plasma jets [63], gliding arc [64], DC electric field [65], and HF streamer discharge [66,67] have been tested to increase flame stabilization. The results have showed that plasma discharge can extend lower lean blowout limit and lean flammability limit. For internal combustion engines, successful demonstrations of plasma assisted ignition and combustion have been achieved by using microwave discharge [68–71], single and multi-spark discharges [72], radio frequency discharge [73], laser ignition [74–78], and corona and nanosecond pulsed discharge [79–81].

In addition to combustion enhancement, plasma has also been used in emission control [82]. By using a plasma jet [83], gliding arcs [82], pulsed corona discharge [84–86], and dielectric barrier discharge [87,88], extensive studies have shown that NO_x emission can be effectively reduced. Recent studies have extended plasma emission control to remove SO_x [82,89,90] and unburned hydrocarbons (e.g., toluene and naphthalene) [91,92] in flue gas as well as soot formation in the exhausted gas of diesel engines [93–96].

High hydrogen syngas, acetylene (C_2H_2), and formaldehyde (CH_2O) can also be produced from methane (CH_4), large hydrocarbons, and biofuels by low temperature plasma to accelerate the non-equilibrium kinetic process for maximizing chemical yield. Compared to conventional catalysts and steam reformers, plasma reformers have the advantages of fuel flexibility, lower cost, high energy efficiency, and being fast and compact [97]. Successful demonstrations of plasma assisted hydrogen production from hydrocarbons have been conducted by using a thermal plasma [98], gliding arcs [99–102], dielectric barrier discharge (DBD) [103,104], microwave discharge [105], and nanosecond pulsed discharge [106]. Recently, by using DBD and nanosecond pulsed discharge, low temperature cool flames have been successfully stabilized to reform large hydrocarbon fuels such as n-heptane (nC_7H_{16}) and dimethyl ether (DME, CH_3OCH_3) to C_2H_4 , CH_2O , H_2 and CO [107,108] without carbon deposit.

Although the above studies have successfully demonstrated the effectiveness of plasma in combustion and emission control as well as fuel reforming, it remains unclear what kind of plasma is the best option for combustion enhancement in a given environment. Moreover, detailed plasma-combustion chemistry is not well understood. Quantitative kinetic modeling remains difficult even in one-dimension. In addition, due to the large variation of plasma properties and complicated interactions between plasma, combustion chemistry, and transport processes and aerodynamics, it is even more difficult to know whether the observed enhancement is simply due to the thermal effect or favorably by the kinetic effect. For example, there has been a debate on whether a non-equilibrium plasma discharge can kinetically enhance flame speed and flammability limit or can only promote ignition. Many controversial results have been reported. It is not clear what the

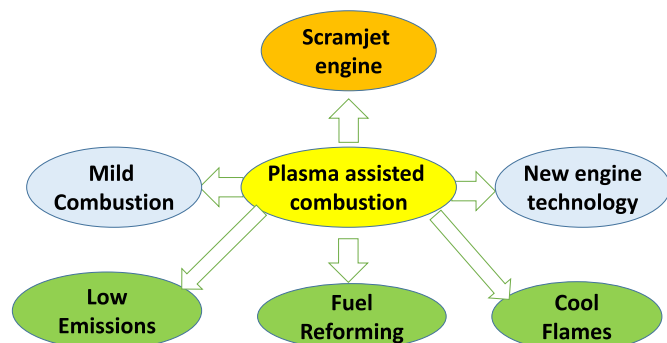


Fig. 1.1. Schematic of plasma assisted combustion and applications.

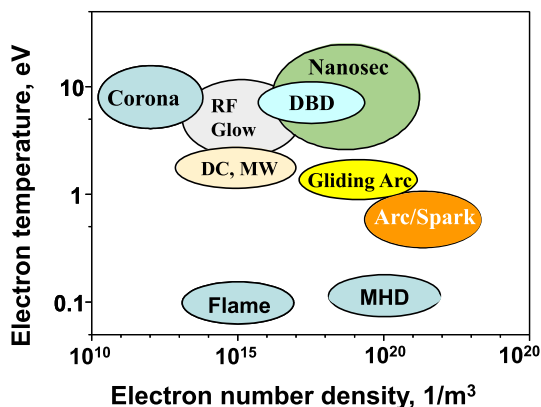


Fig. 1.2. Schematic of electron temperature and number density for different discharges, Corona, direct current (DC) discharge, microwave (MW) discharge; dielectric barrier discharge (DBD), radio-frequency discharge (RF), glow discharge, gliding arc, nanosecond pulsed discharge (NSD), arc, magneto-hydrodynamic discharge (MHD), and flame.

important kinetic pathways, radicals, and excited intermediate species are in plasma assisted combustion. There are many unanswered fundamental questions behind the plasma “magic”. For example, how is the kinetic pathway of plasma assisted combustion dependent on plasma properties, temperature, and fuels? What is the role of plasma if a fuel has low temperature chemistry? How does plasma chemistry affect combustion chemistry and properties and so on? As such, fundamental understanding of plasma properties and plasma assisted combustion chemistry in well-defined physical and chemical conditions is necessary to answer these questions.

1.3. Non-equilibrium plasma and the impact of plasma on combustion

Plasma is a collection of neutral and charged particles which are electrically neutral on average and exhibit collective effects. There are two types of plasmas, one is the equilibrium plasma in which the electron temperature, rotational and vibrational temperatures of particles are in equilibrium and the neutral gas temperature and electron number density are very high. The above mentioned plasma torch and spark plugs belong to this category. The other is the non-equilibrium plasma in which the electronic, vibrational, and rotational temperatures are very different and the neutral gas temperature and electron number density are relatively low. Plasmas such as microwave discharge, DBD, gliding arc, streamer discharge, and glow discharge belong to this category. Compared to equilibrium plasma, non-equilibrium plasma has higher electron temperature (1–100 eV) and is more kinetically active due to the rapid production of active radicals and excited species via electron impact dissociation, excitation, and subsequent energy relaxation

[109,110]. Many of these electron impact processes are strongly electron energy dependent. Therefore, the extent of combustion enhancement by non-equilibrium plasma strongly depends on plasma properties, i.e., the electron temperature and electron number density.

The electron temperature and number density of plasma are governed by the reduced electric field (E/N , the electric field strength divided by the molecular number density). A schematic diagram of the averaged electron temperature and electron number density is shown in Fig. 1.2 for different types of plasmas. More detailed plasma characteristics are summarized in Table 1.

Among different types of plasmas, spark and arc discharges are close to equilibrium plasmas. Spark discharge is an unsteady process and occurs at a voltage above the breakdown level at pressures generally above the atmospheric pressure. A fully developed spark channel is a good conductor and has a large electrical current. If the large current is sustained, a spark discharge transforms into an arc. Therefore, spark and arc have a high neutral gas temperature and electron number density, but a low electron temperature. It consumes a large amount of energy and has less kinetic enhancement effect in combustion compared to non-equilibrium plasmas. On the other hand, non-equilibrium plasma such as corona, DC, glow, RF, DBD, NSD, gliding arc, and MW all have higher electron temperature [37]. Among them, NSD can produce a very strong reduced electric field and allow energy transfer mainly for electronic excitation and dissociation [37]. As such, a nanosecond discharge is a highly non-equilibrium process and has a high electron temperature to enable fast electron impact dissociation in a large volume. For this reason, nanosecond plasma has attracted increasing interest in plasma assisted combustion. Corona is also a weakly ionized discharge appearing in the neighborhood of an electrode, where the electric field is locally enhanced and highly non-uniform. Ionization takes place only locally and produces glow. As shown in Table 1, the electron number density of corona is significantly low compared to streamer and spark (arc) discharges. On the other hand, gliding arc which has relatively lower electron temperature but reasonably higher electron number density and neutral gas temperature [38,111] also has wide applications in fuel reforming [82,89] and flame stabilization [38], where large and continuous energy deposition is needed. In non-equilibrium plasma, the energy distribution is highly non-Boltzmann. Due to the different degrees of non-equilibrium in different plasmas, the energy transfer rate between different energy excitation states in different plasmas are also different. For example, the rotational-translational energy transfer is very fast, and equilibrium between these two energy modes usually can be reached with a few collisions. However, vibrational-translational energy transfer is much slower, and usually takes 10^3 – 10^8 collisions [36]. Therefore, the time scale for combustion control has to be consistent with the timescale of energy transfer. For example, in supersonic combustion, an increase in rotational energy in plasma is necessary to accelerate the

Table 1
Summary of typical characteristics of different types of plasmas.

	Arc	NSD	RF	DBD	Corona	Streamer	Spark, arc	MW
Pressure (atm)	Up to 10–20	Up to 2	10^{-3} –1	10^{-3} –1	0.1–10	0.1–1	Up to 10–20	0.1–1
Current (A)	1 – 10^5	50–200	10^{-4} –2	10^{-4} – 10^{-3}	0.01–50	10^{-4} – 10^{-3}	1 – 10^5	0.1–1
Voltage (kV)	0.01–0.2	1–100	0.5–2	1–10	0.1–50	10–100	10–100	0.1–100
E/N (Td)	0.5–2	100–1000	10–100	10–100	50–200	10–100	10–100	10–50
T_g (K)	3000–10,000	300–600	300–1000	300–500	500–1000	300–500	500–20,000	300–6000
T_e (eV)	0.5–2	5–30	1–5	1–5	1–5	1–3	1–5	1–5
n_e (m^{-3})	10^{21} – 10^{22}	10^{17} – 10^{19}	10^{17} – 10^{19}	10^{17} – 10^{19}	10^{12} – 10^{15}	10^{17} – 10^{18}	10^{17} – 10^{23}	10^{15} – 10^{23}
Refs.	[110]	[37,112]	[113]	[37]	[110,114,115]	[110]	[110]	[37]

energy transfer to enhance ignition. Therefore, plasma assisted combustion is also application dependent. To optimize plasma assisted combustion, it is necessary to understand which elementary process or what properties of plasma can generate the greatest merits for combustion enhancement in each practical application.

Due to a large difference in plasma properties, different plasmas interact with combustion in different ways. Fig. 1.3 shows a schematic of three major enhancement pathways of plasma interaction with combustion. Since plasma produces heat, electrons, long-lifetime intermediate species, radicals, ions, excited molecules, fuel fragments, ionic wind, a large density gradient, and Coulomb and Lorentz force, it affects combustion mainly via three different pathways: thermal, kinetic, and transport (including aerodynamic). In the thermal enhancement pathway, plasma increases temperature and accelerates chemical reactions and fuel oxidation according to the Arrhenius law. In the kinetic enhancement pathway, plasma produced high energy electrons and ions will further produce active radicals (e.g., O, OH, and H) via direct electron impact dissociation, ion impact and recombination dissociation (e.g., O_2^+ and N_2^+), and collisional dissociations of reactants with electronically excited (e.g., N_2^* , $O_2(^1\Delta_g)$) and vibrationally excited (e.g., $N_2(v)$) molecules. In addition, plasma can produce long-lifetime reactive (e.g., ozone (O_3)) and catalytic intermediate species (e.g., NO) which can accelerate low temperature fuel oxidation. Despite many efforts in plasma assisted combustion research, quantitative or even qualitative understanding of the kinetic enhancement pathways has not been well-accomplished. In the transport enhancement pathway, plasma can breakdown the large fuel molecules to small fuel fragments changing the fuel diffusivity and thus modifying the combustion process [116]. Alternatively, the ionic wind and the hydrodynamic and Rayleigh instabilities produced by plasma change the local flow velocity and increase the flow turbulization and mixing. More importantly, the three different enhancement pathways often couple together and render it difficult to understand the main mechanism of the plasma assisted combustion. For example, the kinetic enhancement produces heat from the accelerated fuel oxidation to enhance the thermal effect, and vice versa the thermal effect also accelerates the kinetic processes. Similarly, the kinetic effect and thermal effect are also both affected by the molecular and convective transport induced or modified by the plasma discharge. Therefore, design of well-defined experimental platforms with isolated enhancement pathways and advanced diagnostics is extremely important to understand the enhancement process of plasma assisted combustion.

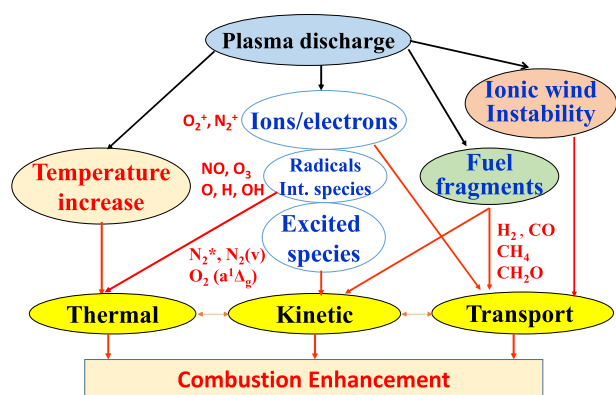


Fig. 1.3. The schematic of major enhancement pathways of plasma assisted combustion.

1.4. Progress and challenges in fundamental studies of plasma assisted combustion

The earliest observation of electric field (plasma) interaction with flames by applying an electric field to various flames goes back to the work of Brande [117] in 1814. They found that flames were attached to one of the electrodes due to the existence of charges in the flames. Earlier observation of plasma assisted ignition was reported by Haselfoot and Kirkby [118] in 1904. They found that an electric discharge was able to ignite the mixture at low pressure when otherwise it would not burn. In a later work, Kirkby [119] applied an electric discharge to a low pressure H_2/O_2 mixture. The chemical effect of H_2O and atomic O formation was identified. He also suggested that O collided with H_2 to form H_2O directly. In 1924, Southgate [118] applied an arc discharge to a flame front to enhance the flame. More detailed work about the application of arc discharges and plasma jets to flames was conducted in 1960s [120,121]. Since then, arc discharge has been used widely in combustion enhancement [44–46,48,50]. As shown in Fig. 1.2, since arc discharge is equilibrium plasma and the temperature of a plasma torch is as high as 10,000 K, the observed combustion enhancement is dominated by the thermal effect (Fig. 1.3) and the energy consumption of arc discharge is very high. Therefore, thermal enhancement by arc discharge is not an efficient way for combustion enhancement because of the poor chemistry selectivity and excessive thermal heating [118].

To find an energy efficient plasma to control combustion, following the work of Brande [117], extensive attention was paid to study the effect of electric field on flame dynamics and flame chemionization. Earlier work by Lewis [122], Calcote [123] and Wortberg [124] made significant progress in measuring the electron density in flame fronts ($\sim 10^{17} \text{ m}^{-3}$) by using Langmuir probes and in understanding the formation mechanism of negative and positive ions (e.g., H_3O^+) in flames. It was found that a strong electric field increased flame speeds and improved stabilization due to collisional energy transfer (heating) between electrons and neutral molecules. At the same time, a strong electric field also induced flow motion due to the collisions between positive ions and neutral molecules [125]. The former effect was thermal and the latter effect was termed “ionic wind.” By using a DC electric field, quantitative measurements of the increases in flame speed and flame extinction limits [125–127] as well as electron temperature [128] via electric field flame interaction were conducted. It was concluded that the increase in electron temperature and the ion chemistry affected the combustion properties. When a strong electric field was applied, it was found that the strong ionic wind induced by an electric field increased the flame instability and reduced the soot formation. Unfortunately, in these experiments, the coupling between ionic wind and electron heating and ion chemistry effects made it difficult to quantify the contributions of individual enhancement pathways. In order to understand the mechanism of the effect of an electric field on flame speed enhancement and to suppress the effect of ionic wind, many experiments since the 1970's have used high frequency electric field such as HF (5–6 MHz) [129] and microwave discharges [130–133] to study the interaction between electric field and flames. Unfortunately, the earlier results in the 1970s were not conclusive as to whether an electric field increased flame speed. Some studies reported flame speed increase by 20% but others failed. The methane–air microwave flame experiments (200–500 W) by Ogawa et al. [133] showed that although electron temperature linearly increased with microwave field, increased burned gas temperature was observed. A recent experiment and numerical simulation [134–137] on microwave assisted combustion using high power (2–4 kW) in a high Q microwave resonator demonstrated that the

flame speed of lean methane–air mixture increased by approximately 20%. Both the numerical modeling [134] and laser diagnostics [137] showed that microwave absorption by the electrons in the flame zone led to a flame temperature rise of about 200 K and thus accelerated flame propagation. Unfortunately, to avoid microwave–flame front interaction, the intensity of the electric field used had to be lower than the breakdown voltage. Therefore, both the energy and density of electrons in microwave discharge were low and a large portion of the microwave energy was absorbed in the burned gas, leading to a very inefficient energy coupling between the flames and the electric field.

To increase the electric field and the electron number density for the effectiveness of plasma assisted flame stabilization, gliding arcs were tested in a counterflow diffusion flame to study extinction and ignition of plasma assisted flame [38,138–140] by isolating the complexity of flow field from plasma–combustion chemistry. The results from this idealized platform showed that a gliding arc with a moderate discharge power extended the flame extinction limit by a factor of three. However, by quantitatively measuring the temperature and OH distributions, it was found that almost all the enhancement was contributed by the thermal effect (Fig. 1.3). This result raised a question of whether and at what conditions plasma can have a kinetic effect on combustion enhancement. The authors then extended their studies by comparing the ignition temperature of hydrogen and methane with and without plasma [138,139]. It was found that gliding arc discharge in air reduced hydrogen and methane ignition temperature kinetically by more than 100 K via the catalytic NO_x reaction pathways.

Subsequent quantitative measurements of radicals formation of nanosecond plasma discharge in counterflow diffusion flames demonstrated that [43,106], although far less than the effect on ignition, plasma still extended slightly the extinction limit via kinetic effect. These results prompted many questions on the mechanism of plasma assisted combustion. First, why did gliding arc have only primarily thermal effect for flames but have a large kinetic effect on ignition? Does plasma really increase the flame speed and flammability limit non-thermally (via kinetic pathway)? If yes, what is the main mechanism? In addition, as shown in Fig. 1.4, if plasma has a greater kinetic effect on ignition than on the flame speed, can plasma accelerate ignition so fast that the ignition S-curve will be changed into a monotonic curve and no flame extinction limit will exist between ignition and flame (red dashed line)? If this is true, different from the classical ignition S-curve (blue line) [141–144], a new flame regime with a stretched ignition

S-curve and continuous transition from ignition to flame (Fig. 1.4) should be observed in plasma assisted combustion.

To prove the concept of the stretched S-curve transition by plasma, an *in situ* nanosecond pulsed discharge (NSD) experiment was conducted for a methane/air mixture in counterflow diffusion flames. The experiments successfully demonstrated the plasma assisted transition from the classical ignition S-curve to the monotonic stretched S-curve [144]. The S-curve transition in Fig. 1.4 due to plasma assisted ignition enhancement is equivalent to a decrease of the activation energy of the global fuel oxidation reaction at low temperature because plasma can provide new reaction pathways to produce radicals faster than the fuel oxidation chemistry alone. More recently, the S-curve transition and plasma activated low temperature combustion were observed for dimethyl ether (DME) flames [107]. This experimental finding clearly demonstrated that although plasma can enhance both ignition and flame extinction (flame speed) kinetically, the kinetic enhancement to flame extinction (flame speed) is much less than that to ignition. More importantly, ignition can be significantly enhanced kinetically by plasma creating a new ignition to flame transition regime without an extinction limit (Fig. 1.4). It is therefore necessary to ask: what are the kinetic pathways of plasma to enhance ignition? How does plasma enhance ignition if a fuel has low temperature chemistry?

To understand the plasma assisted ignition chemistry, it is necessary to produce a homogeneous plasma discharge and to remove the non-uniform discharge effect. Significant progress was made by the research group at the Moscow Institute of Physics and Technology (MIPT) who introduced a discharge known as “Fast Ionization Wave (FIW)” or NSD (nanosecond pulsed discharge) [146] to combustion. NSD is generated by repetitive nanosecond high voltage pulses and has a high reduced electric field (E/N) (up to 1000 Td). It provides uniform pre-ionization and efficient electron impact dissociation at relatively higher pressure. NSD provided a new research opportunity to understand the chemistry of plasma assisted combustion. Shock tube NSD experiments were conducted to measure the ignition delays of different fuels ranging from H_2 to C_5 alkanes up to 2 atm [112]. Significant shortening of ignition delay time by NSD discharge was observed. Different kinetic mechanisms were also developed to model the plasma assisted ignition enhancement. Despite the earnest efforts of this group, the experimental results measured through optical emission spectroscopy did not agree well with the simulated results. In addition, most of the experiments have been focused on high temperature ignition. The kinetic mechanism of plasma ignition enhancement at low temperature was not well understood. Therefore, in order to understand the kinetic enhancement effects, time-resolved and *in situ* experimental measurements of plasma generated radicals and intermediates at low temperature are greatly needed.

To address these challenges, *in situ* temperature and OH measurements by NSD discharge in a rectangular quartz reactor were conducted at different initial temperatures and reduced pressures [39,147–149]. It was found that ignition temperature decreased by about 200 K due to the accumulation of H atoms from H_2 collisions with electrons or excited N_2 . The studies suggested that plasma discharge can have different kinetic effects for different fuels and diluents. *In situ* NSD discharge in $\text{CH}_4/\text{He}/\text{O}_2$ [144] and $\text{DME}/\text{He}/\text{O}_2$ [107] diffusion flames also showed that O atom production via electron and helium ion (He^+) impact dissociation of O_2 played a dominant role in ignition enhancement which led to the transition to the stretched S-curve without an extinction limit (Fig. 1.4).

More recently, focus of research in plasma assisted combustion has been placed on low temperature ignition. This is an entirely new research area of plasma assisted combustion. Using a counterflow flame with NSD discharge, Sun et al. [107] demonstrated

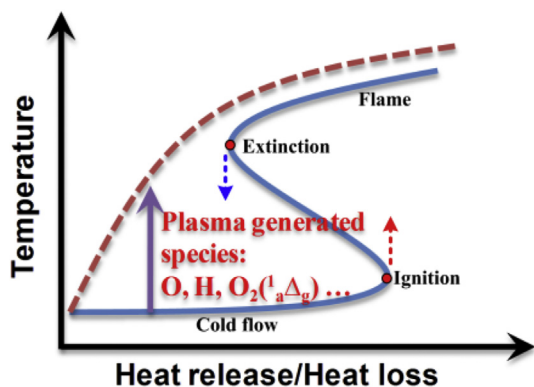


Fig. 1.4. Schematic of the plasma assisted transition from the classical ignition and extinction S-curve (solid blue line) to the monotonic stretched S-curve (red dashed line) [145]. (For interpretation of the references to color in this figure legend, the reader is referred to the web version of this article.)

that plasma can activate low temperature multi-stage ignition even at reduced pressure. Starikovskiy et al. [150] conducted NSD discharge in a Rapid Compression Machine (RCM) to study the ignition kinetics at elevated pressures up to 40 bar and low temperature regions (600 K–800 K). Two-orders of magnitude of ignition delay reduction was reported due to the streamer development. Similar work of ignition enhancement by nano-second pulsed surface dielectric barrier discharge in RCM was conducted by Stepanyan et al. [151]. Significant decrease of ignition delays for methane and n-butane mixtures in the pressure range of 7.5–15 atm was observed. A transient streamer plasma discharge in methane and ethylene (C_2H_4) [152] ignition was also conducted. Ignition enhancement was reported. Unfortunately, in the above experiments, due to spatial non-uniformity of discharge, the kinetic pathways of ignition enhancement were not well understood. As such, quantitative studies of the kinetic effect on combustion enhancement by plasma generated radicals and intermediate species on combustion in well-defined experimental platforms are needed.

As shown in Fig. 1.3, plasma generated intermediate species, radicals, and excited molecules can kinetically enhance combustion. Singlet delta oxygen ($O_2(a^1\Delta_g)$) is a long-lifetime electronically excited molecule. Its reaction with H atom ($H + O_2(a^1\Delta_g) = OH + O$) is much faster than the most important $H + O_2 = OH + O$ chain branching reaction. Unfortunately, despite many numerical simulations of combustion enhancement by $O_2(a^1\Delta_g)$ [153,154], few experimental studies on $O_2(a^1\Delta_g)$ combustion enhancement have been carried out. Smirnov et al. [155] performed experiments aimed at isolating the effect of $O_2(a^1\Delta_g)$ on the ignition of H_2/O_2 mixtures at very low pressures (1–3 kPa). The results showed decreased induction time, but $O_2(a^1\Delta_g)$ concentration was only qualitatively estimated from the plasma emission. Due to the lack of quantitative diagnostics and the co-existence of ozone (O_3), atomic O and other radicals, it was not certain whether $O_2(a^1\Delta_g)$ was the only species causing the enhancement. The isolated effect of $O_2(a^1\Delta_g)$ on the propagation of C_2H_4 lifted flames was studied quantitatively for the first time by Ombrello et al. [156] by isolating the effect of O_3 and atomic O via NO quenching. The results showed that $O_2(a^1\Delta_g)$ only slightly increased the flame speed. Using the same method, the kinetic enhancement effect of O_3 on flame speed was reported [157]. The O_3 enhancement of flame speed was also observed in a flux burner [158,159]. More recently, it has been discovered that O_3 can enable stabilization of a self-sustained cool flame for n-heptane (C_7H_{16}) [108]. These experimental results, contrary to the previous results, have clearly indicated that O_3 can kinetically activate cool flame chemistry by releasing atomic O at a low temperature. However, large discrepancies between the model prediction and experiments have been found.

Since atomic O formation in plasma has a significant impact on combustion, another major achievement in the fundamental study of plasma assisted combustion has been the success of quantitative diagnostics of atomic O. Uddi et al. measured the absolute atomic O concentration in NSD discharges using the Two Photon Laser Induced Fluorescence (TALIF) technique [160]. They found that O was formed primarily from $N_2(A)$ collision with O_2 and that atomic O decayed much faster in fuel/air mixtures than that in pure air. This indicated that atomic O production and its consumption by hydrocarbon fuels and radicals are one of the primary pathways for plasma assisted combustion. To further understand the formation pathways of atomic O production by excited N_2^* (e.g., $N_2(A)$, $N_2(B)$ and $N_2(C)$) at a higher pressure, the absolute number densities of $N_2(A, B, C)$ were measured by Cavity Ring Down Spectroscopy (CRDS) and Optical Emission Spectroscopy in a NSD discharge at atmospheric pressure in air [161]. Slightly different from the low pressure results of [160], the results showed that O_2 collisions with

$N_2(B)$ and $N_2(C)$ were the major reaction pathways to product atomic O (probably due to the difference in pressure). These quantitative measurements significantly advanced the understanding of plasma assisted combustion. Measurements of atomic O production and consumption of NSD in a helium (He) diluted oxidizer stream of counterflow diffusion flames was also measured by Sun et al. [106] using TALIF. It was also found that NSD discharge produced significant amount of atomic O via electron and helium ion impact dissociation of oxygen. These findings support the observation of improved flame stabilization of NSD discharge in a turbulent flow [40,67,162,163].

Recently, diagnostics has been further advanced to use femto-second TALIF for H radicals [164], picosecond CARS [165] for vibrational states of nitrogen, mid-IR Faraday rotational spectroscopy (FRS) [166,167] for HO_2 and OH, and laser absorption for time dependent measurements of C_2H_2 , CH_4 , and H_2O [168] in plasma assisted combustion. As shown in Fig. 1.5, the above research has provided a much better understanding of the electron impact dissociation and radical production in the initial 100 ns plasma discharge process and the kinetic coupling process for high temperature ignition. However, the energy transfer and kinetic interaction between the plasma generated radicals and excited molecules and the reactants at intermediate timescale and low temperature region (100 ns–1 ms and 300–900 K), at which low temperature fuel oxidation pathways dominate, remains unclear. The plasma interaction with cool flames is also poorly understood [107,108]. The current plasma-combustion kinetic model cannot predict key intermediate species at low temperature and high pressure conditions. Many reaction pathways and rate constants are still missing. Furthermore, producing uniform discharge at a high pressure is still challenging. The transport of thermal energy [169] and radicals/intermediates [170] produced from the local plasma discharge needs to be investigated to understand the mechanism of ignition and flame-holding at high pressure and low temperature conditions. More fundamental studies of plasma assisted combustion focusing on the kinetics at low temperature and high pressure with *in situ* laser diagnostics and high level quantum chemistry computations are needed.

1.5. Focus of this review

Three review articles respectively on the physics of plasma discharge [37], the plasma kinetics and applications [36], and ignition and development of plasma assisted combustion kinetic mechanism [171] were published previously by the members of

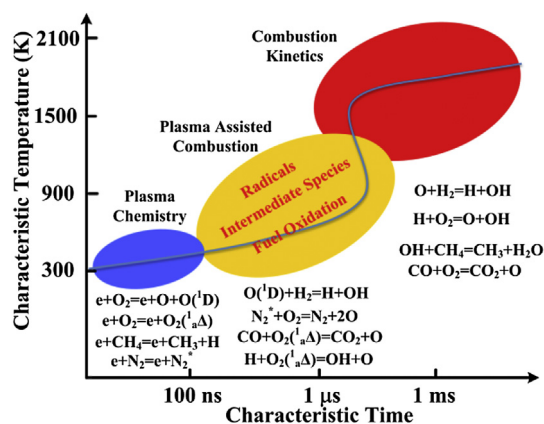


Fig. 1.5. Schematic of timescales and key kinetic pathways at different stages of plasma assisted ignition and combustion.

former MIPT group. The first review emphasized on experimental and theoretical analyses of various non-equilibrium plasmas and their applications on ignition and combustion. The second review paper expanded the first review by including applications in low and high speed propulsion as well as discharge kinetics. The third review covered the results obtained from 2006 to 2014 with a focus on ignition study and developing a particular kinetic mechanism for plasma assisted combustion. Although all reviews provided excellent overviews of plasma assisted combustion from the view point of plasma physics and kinetics, the underlying physics of combustion dynamics and chemistry as well as advanced diagnostics were not emphasized. For example, questions such as how and whether plasma can extend lean burn limit and change minimum ignition energy were not answered. Moreover, the question of how different the kinetic pathways and combustion chemistry are for low and high temperature fuel oxidation in plasma assisted combustion was not addressed. Furthermore, significant progress in advanced laser diagnostics and combustion kinetic mechanism development has been made. As such, this review intends to discuss and summarize the progress and challenges of plasma assisted combustion using the most recent experimental results from combustion theory, flame dynamics, chemistry, and advanced diagnostics. The goals of this review are to: 1) discuss different enhancement pathways of plasma assisted combustion and bridge the gap between combustion dynamics and chemistry in plasma assisted combustion, especially for ignition, flame initiation, propagation and flammability limit; 2) present the important kinetic pathways in low, intermediate, and high temperature combustion and use them to explain the physics and chemistry for plasma combustion enhancement in practical applications and laboratory experiments; 3) provide a broad overview of fundamental phenomena and kinetic processes in plasma assisted combustion experiments with well-defined boundary and discharge conditions; 4) present the recent progress and findings made by advanced laser diagnostic techniques and combustion theory; and 5) discuss the recent findings of plasma assisted low temperature combustion and cool flames; and finally 6) discuss the challenges and needs of future research in plasma assisted combustion.

2. Plasma assisted combustion: applications and technological development

In the last two decades, many different plasmas including plasma torch, dielectric barrier discharge (DBD), gliding arc, corona, nanosecond pulsed plasma discharge, microwave, and lasers have been widely tested and applied in high speed propulsion systems, internal combustion engines, industrial burners, and reactors to control ignition, flame holding, flame stability, lean burn, emissions, and fuel reforming. Table 2 below lists the types of plasma and combustors, merits of combustion enhancement, technical difficulties and challenges, references, and the names of institutions. In the sections below, the details of major research efforts, results and progress, challenges, and future directions will be reviewed and discussed for high speed propulsion, internal combustion engines, emission control, and fuel reforming.

2.1. Plasma assisted combustion for supersonic propulsion and scramjet engines

The major challenges in supersonic ramjet engines for hypersonic propulsion are fuel/air mixing, ignition, flame stabilization, and cooling [13,190]. At a high Mach number, the flow residence time in the engine ($\tau_{\text{flow}} \sim 0.5$ ms) is even shorter than the typical auto-ignition time of jet fuels ($\tau_{\text{ig}} \sim 1\text{--}2$ ms) at 900 K [191]. Moreover, even when the fuel is ignited, the flow residence time may still

be shorter than the time for the fuel to be completely combusted (τ_c). Therefore, both the ignition and combustion Damköhler numbers are less than unity.

$$Da_{\text{ig}} = \frac{\tau_{\text{flow}}}{\tau_{\text{ig}}} < 1 \quad \text{and} \quad Da_c = \frac{\tau_{\text{flow}}}{\tau_c} < 1 \quad (2.1)$$

In addition, if the combustion heat release is too fast, the rapid heat release rate may cause thermal choking of the flow and lead to an engine unstart. Therefore, it is necessary to control both ignition and combustion heat release rate. Plasma torch or plasma jet has been extensively studied as an effective method to ignite and stabilize flame at supersonic conditions [36,41,44–51]. Plasma torch is an equilibrium arc discharge and is considered to enhance ignition due to the thermal effect and abundant active radicals. The extremely high temperature (up to 10,000 K) of the plasma torch makes the thermal effect overwhelm the kinetic effect.

The earliest attempt to use plasma torch to enhance ignition in a supersonic flow was conducted by Kimura et al. [44]. Since then, a large number of experimental studies have been carried out to control ignition in a supersonic flow by using different plasma torches and feedstocks [41,45–50,192]. For example, Takita and co-workers [41] developed a plasma igniter consisting of one and two plasma torches with different plasma feedstocks (e.g., $\text{H}_2/\text{N}_2/\text{O}_2$) and fuels (e.g., H_2 , CH_4 , and C_2H_4). The experiment was conducted using an intermittent suction-type wind tunnel. The plasma torch was tested in a supersonic flow of Mach number (M) 2.3. Fig. 2.1 [192,193] shows the successful H_2 ignition by a plasma torch in a Mach 2.3 supersonic flow and the effect of total heat addition (the sum of electrical energy of plasma and the injected H_2 enthalpy flux) on pre-combustion shock wave (PSW). It can be seen that with the increase of H_2 mole fraction and plasma power (Fig. 2.1(a) and (b)), combustion became stronger and resulted in an increased strength of PSW (an increased possibility of engine unstart). By using twin plasma torches together with upstream and downstream fuel injections, both H_2 and CH_4 flame stabilization were achieved. Moreover, to understand the kinetic enhancement by plasma generated radicals and NO_x , the effect of different plasma feedstocks using $\text{H}_2/\text{N}_2/\text{O}_2$ for the twin plasma torches was also studied [47]. Numerical analysis showed that the addition of a small amount of NO_x by plasma drastically reduced ignition delay time of H_2 and hydrocarbon fuels at a relatively low initial temperature. In particular, it was shown that plasma produced NO_x was more effective than atomic O radicals for ignition enhancement of CH_4 . Ignition tests by a N_2/O_2 plasma torch at Mach 1.7 showed that the ignitability of the N_2/O_2 plasma torch was affected by the composition of the feedstock and that pure O_2 was not the optimum feedstock for ignition with downstream fuel injection.

Recently, Matsubara et al. [181] extended the plasma torch ignition by combining it with a Dielectric Barrier Discharge (DBD) in a supersonic flow. As shown in Fig. 2.2, H_2 was injected upstream of a back-step flame holder. The non-equilibrium DBD discharge produces radicals through the kinetic pathways (Fig. 1.3) at the back-step recirculation zone. The thermal N_2 arc plasma jet was issued from a flat wall at the downstream of the back-step flame-holder to stabilize the flame. Fig. 2.2 shows that non-equilibrium DBD plasma was successfully generated in a supersonic flow at $M = 2.0$ with maximum power consumption of about 8 W. It was found that the minimum peak-to-peak amplitude of the applied sinusoidal voltage of DBD, V_{pp} , to initiate DBD decreased with the increase in the flow Mach number (M) due to the decreased static pressure (about 55, 13, and 6 kPa in $M = 1.0$, 2.0, and 2.5, respectively).

Fig. 2.3 shows the dependence of the minimum V_{pp} on the flow Mach number and the comparison with the results of the same DBD

Table 2
Summary of research objective and applications of plasma assisted combustion technologies.

Plasma	Engine, burner	Objective	Merits	Problems	Institution, company	Refs.
MW + spark	Gasoline engine	Ignition	Stable leaner combustion & improved stability	Not reported	Imagineering, Inc., Princeton University	[172,69]
Radio-frequency plasma	Small IC engine	Ignition	Stable leaner combustion, improved stability, lower emissions	Increased NO _x emission	Michigan State University	[173]
MW + spark	Constant volume combustion chamber	Ignition and flame propagation	Extended lean and rich ignition limits	No effect on flame propagation	Imagineering, Inc., UC Berkeley	[70]
Transient plasma igniter	Gasoline engine	Ignition	Shorter ignition delays, stable leaner combustion	Not reported	University of Southern California, Nissan Motor Co., Ltd.	[79,81]
Transient plasma igniter	Constant volume combustion chamber, counterflow burners	Ignition	Low temperature ignition	Electrode geometry dependence of results	University of Southern California	[174]
Transient plasma igniter	Constant volume combustion chamber	Ignition and flame propagation	Shorter ignition delays, increased flame speeds due to flame wrinkling	Not reported	University of Southern California	[175]
Laser igniter	Constant volume combustion chamber, IC engine	Ignition	Effective ignition, remote ignition	misalignment problems, optics contaminations, high cost	King Saud University	[77]
Nanosecond pulsed discharge	Swirl-stabilized gas turbine burner	Flame stabilization, lean blowout limits	Improved stability, leaner combustion	Plasma can also cause instability	Technical University of Berlin, CNRS and Ecole Central Paris	[163,176,177]
Transient plasma igniter	Pulsed detonation engine	Ignition	Effective ignition, shortened ignition delays	Not reported	University of Southern California, Naval Postgraduate School, Stanford University, U.S. Air Force Research Laboratory	[178]
Nanosecond pulsed discharge	Pulsed detonation engine	Ignition	Effective ignition, leaner and richer ignition	Not reported	Princeton University, U.S. Air Force Research Laboratory	[62]
Ozone from DBD	Diesel engine	Ignition	Decreased ignition timing	Not reported	University of Orléans, CNRS	[179]
Plasma torch	Scramjet	Ignition	Successful ignition	Huge power consumption	Tohoku University	[180]
DBD + plasma torch	Scramjet	Ignition	Successful ignition with lower power consumption	Not reported	Tohoku University	[181]
Nanosecond pulsed discharge	Scramjet	Ignition and flame holding	Shorter ignition delays, effective ignition and flame holding	Not reported	Stanford University	[56,182]
Quasi DC multi-electrode discharge	Scramjet	Ignition and flame holding	Effective ignition and flame holding	Not reported	Russian Academy of Science, U.S. Air Force Research Laboratory	[183–185]
MW	Scramjet	Ignition and flame holding	Effective ignition and flame holding	Not reported	Moscow Radiotechnical Institute RAS, Central Institute of Aviation Motors, John Hopkins University	[186]
Laser induced plasma	Scramjet	Ignition	Effective OH production	Not reported	University of Queensland, University of New South Wales	[187]
DBD	Coflow burner	Soot formation	Effective soot reduction	Not reported	Seoul National University	[96]
DBD	Diesel engine exhaust	Emissions	Simultaneous soot, unburned HC, NO _x , and PAHs reduction	High E/N may cause NO _x formation from the plasma	Tianjin University	[188]
Gliding arc	Industrial burner	NO _x	Reduction NO _x production rate	Increased CO production rate with increased excess air ratio	Korea Institute of Machinery and Materials, Sookkook Corporation	[189]

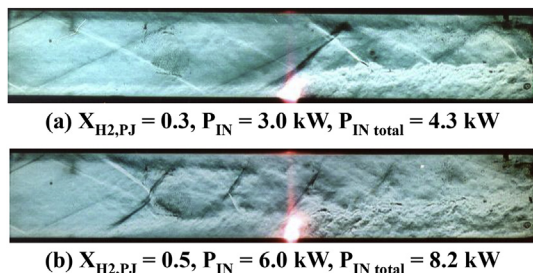


Fig. 2.1. H_2 ignition by plasma torch in a $M = 2.3$ flow and the effect of total heat addition on pre-combustion shock wave, X_{H_2} is hydrogen mole fraction in H_2/N_2 plasma torch; P_{in} : plasma torch electric power, $P_{in\ total}$: total heat addition ($P_{in} + H_2$ enthalpy flux) [192].

discharge in a low pressure desiccators without a flow. Ignition tests were conducted in an $M = 2.0$ supersonic flow. It was confirmed that ignition did occur by only operating the DBD discharge. On the other hand, the wall pressure measurements showed that with a high plasma torch power at $P_{in} = 4.05$ kW, strong combustion occurred, but no combustion enhancement was observed by adding the DBD. However, for relatively weak and unstable combustion at a lower plasma torch power, significant enhancement was obtained when the fuel was injected upstream of the DBD device. It was shown that the wall pressure distribution of plasma torch at $P_{in} = 2.4$ kW with DBD operation was almost equivalent to that at $P_{in} = 3.8$ kW without DBD operation, indicating a significant drop of total electrical energy consumption with combined plasma discharge. This experiment suggests that thermal effect is needed to stabilize a flame in a high speed flow and non-equilibrium plasma can kinetically enhance flame stabilization near its stabilization (or extinction) limit when there is sufficient thermal effect from the plasma torch. The authors explained this observation through O_3 effect from the DBD device. However, the verification of the existence of O_3 was not conducted.

Do et al. [182] integrated a nanosecond pulsed discharge with a wall cavity and investigated the ignition of H_2 and C_2H_4 jet flames in a supersonic crossflow. An expansion tube was used to generate conditions comparable to those of the supersonic flow in the combustor of a scramjet engine. The schematic of the experimental design mimicking a supersonic combustor in a scramjet engine is shown in Fig. 2.4. The discharge consists of a rectangular aluminum plate with inject nozzle and electrodes, and a ceramic plate embedded for electrical insulation of the pulsed discharge

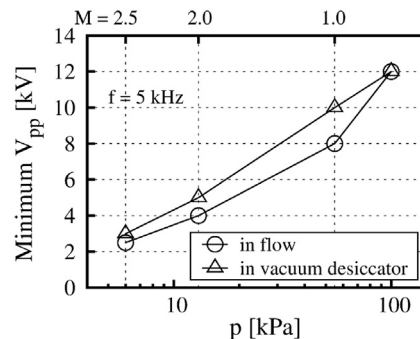


Fig. 2.3. Comparison of the minimum V_{pp} to initiate DBD under different flow conditions [181].

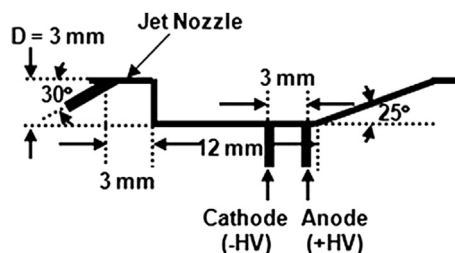


Fig. 2.4. Schematic of the cavity model [182].

electrodes. The electrodes were 2% thoriated tungsten rods with 1 mm diameter. Non-equilibrium plasma was used to generate reactive species at a lower temperature. The discharge was produced by repetitive pulses of 15 kV peak voltage, 20 ns pulse width and 50 kHz repetition rate between the two electrodes. Sonic fuel jets were impinged into the free stream air at Mach number between 1.7 and 3.0. Flame stabilization was found to be improved by the plasma discharge.

Fig. 2.5 provides a comparison of auto-ignition cavity flames and plasma assisted cavity flames at two different flow conditions. The images in the presence of the plasma were taken 1 μs after a discharge pulse and approximately 200 μs after the start of the test time. The plasma was turned on well before the beginning of the test time. Here, J_n (Fig. 2.5) is the cross jet momentum ratio, the ratio of the normal component of the jet momentum flux to the free stream momentum flux: $J_n = (\rho u^2)_{jet} / [2(\rho u^2)]_{\infty}$. The factor of $1/2$

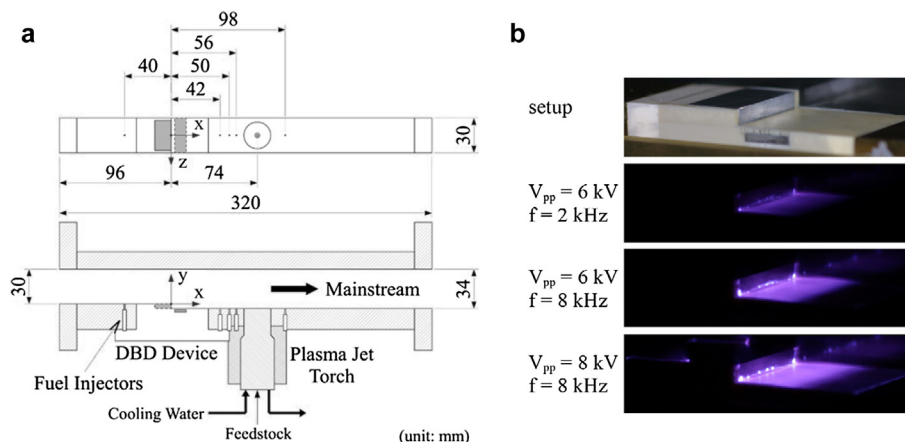


Fig. 2.2. a. Schematic of the test section with DBD and plasma torch [181]. b. Direct photographs of DBD plasma in $M = 2.0$ supersonic flow [181].

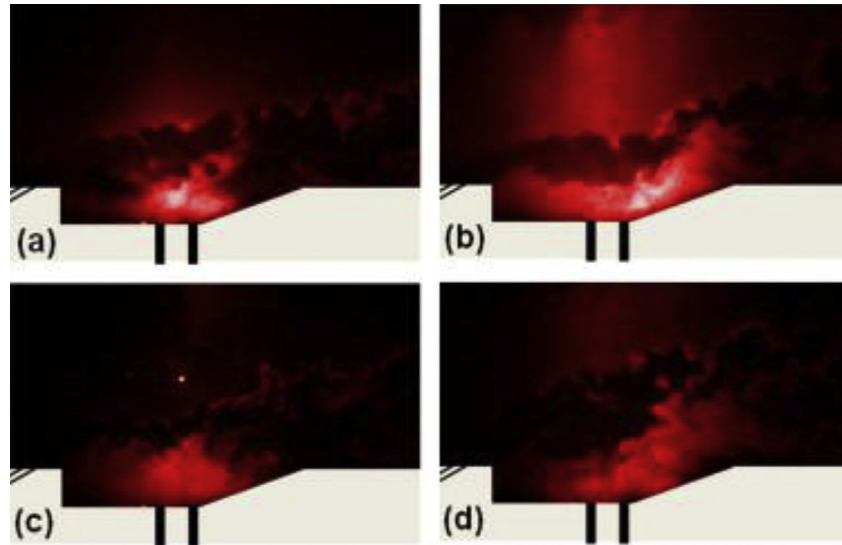


Fig. 2.5. OH PLIF images of a cavity flame in supersonic flows of two different enthalpies: (a) without the plasma and (b) with plasma at $M = 2.9$, $J_n \sim 4$ of H_2 jet, and (c) without plasma and (d) with plasma at $M = 2.6$, $J_n \sim 3.5$ of H_2 jet [182].

comes from the 30° injection relative to the free stream flow direction. The plasma enhanced cavity flames seen in Fig. 2.5(b) and (d) clearly appeared to extend into the free stream flow on the leeward side of the fuel jet. The results showed that the pulsed plasma in the cavity served as a source of both heat and radicals, shortening the ignition delay time of the well mixed flammable mixture. In a marginal case with $M = 2.0$ and stagnation enthalpy ~ 2.0 MJ/kg, H_2 jet auto-ignition was observed within the test time which is about $500 \mu s$ only with plasma enhancement. A simple model was also employed to simulate the experiments. The authors concluded that the reduction of the ignition delays was due to H and atomic O through electron impact dissociation of H_2 and O_2 .

To reduce the pressure loss and eliminate the coupling between cavity and plasma discharge, Do et al. [182] further conducted the flame-holding experiments with plasma discharge in a supersonic crossflow without a cavity. Subsonic (upstream) and sonic (downstream) fuel (H_2 and C_2H_4) jets were injected into a pure oxygen free stream of $M = 1.7$ – 2.4 . The configuration of dual fuel jet injection with plasma in between can couple the plasma energy into the activation of the upstream subsonic fuel/oxidizer mixture that served as a pilot flame that subsequently anchored the ignition of the main supersonic flame downstream. Radical production by this pilot flame can be several orders of magnitude more than that by the discharge alone. The observed flame stabilization enhancement is shown schematically in Fig. 1.3, indicating that both thermal effect (cavity or pilot flame) and kinetic effect are needed for flame holding in a supersonic flow. However, in both experiments it was not discussed at what temperature range and flow residence time this kinetic enhancement is most effective. It was not clear whether the observed enhancement is due to the ignition shortening or due to the flame speed increase.

Leonov et al. [184] developed an experimental platform of plasma assisted supersonic combustion by integrating multi-electrode quasi DC discharge (similar to gliding arc) behind a back-step cavity in H_2 and C_2H_4 with air mixtures (Fig. 2.6). The discharge dynamics in flow behind the back-step and in the cavity was explored. It was found that the discharge effect on the flow structure in the cavity and behind the back-step lied in that an intensive turbulization of gas in the interaction area and simultaneously slight increase of the separation zone volume. The direct

photographs of the multi-electrode discharge and associated combustion are shown in Fig. 2.7. With H_2 injection, the combustion took place in the cavity as well as in the shear layer. For C_2H_4 , combustion was only detected in the cavity. The authors proposed three mechanisms for high-speed combustion control: plasma-induced ignition, plasma-intensified mixing, and flame-holding by plasma generation.

Leonov et al. [183,185] further conducted experiments on plasma-induced H_2 and C_2H_4 ignition and flame holding by means of near-surface electrical discharges in $M = 2$ flow. The modified experimental setup is shown in Fig. 2.8. The fuel injectors were located downstream of the plasma generator on a distance that was less than the plasma filament length. The injectors were arranged at the same position as the electrodes for the most intensive air-plasma interaction with the fuel jet. Fuel injection was started prior to the discharge initiation and was switched off after completion of the discharge. The discharge appeared in the form of oscillating plasma filaments. The individual filaments were blown down due to the main flow at a velocity that was a bit less than the core value. It was found that the flame could only exist in the presence of the plasma. The authors proposed a two zone model of plasma induced ignition to explain the experimental data. In zone 1, the cold combustion took place accompanied by plasma induced fuel conversion and relatively small heat release. In zone 2, combustion was completed or almost completed with high energy release. The plasma launched the cold combustion inside zone 1 owing to the generation of high amounts of active species. The

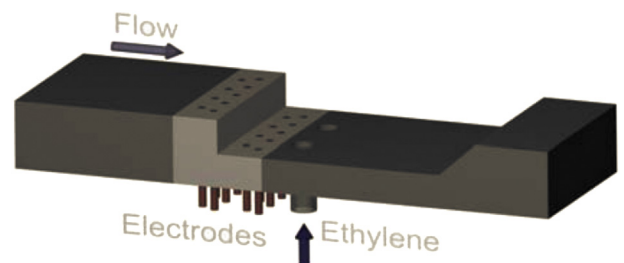


Fig. 2.6. Schematic of experimental setup and electrodes arrangement [184].



Fig. 2.7. Left: discharge without fuel injection. Right: discharge interaction with H_2 injection [184].

lengths of zone 1 in the tests were measured by Schlieren technique in the range from 50 to 150 mm, which corresponded to the induction time range from 0.1 to 0.3 ms. However, the transition mechanism of plasma assisted ignition to strong combustion in zone 2 was not well understood. It might be the classical auto-ignition to flame transition or the stretched ignition to flame transition without extinction limit. More quantitative diagnostics is necessary. The authors are conducting species measurements by using tunable diode-laser absorption (TDLAS). The results may give a clearer picture of the mechanism.

Esakov et al. [186] studied microwave assisted combustion of C_3H_8 /air in a supersonic flow. The experimental setup is shown in Fig. 2.9. The steady state airstream was formed at the outlet of the nozzle with $M = 2$ and a static pressure of 100 Torr, static temperature of 150 K, and stream velocity of 490 m/s. The free stream stagnation conditions were 550 Torr and 300 K. A deeply under critical discharge was created by an incident electromagnetic beam with electric field (E) much smaller than the critical breakdown field. In order to create a local electric field which was larger than the critical breakdown field to initiate the discharge, a passive electrodynamic vibrator was used and the discharge was initiated in the base of the electromagnetic vibrator, which was immersed in cold supersonic airflow. A linearly polarized beam of electro-magnetic radiation with a wavelength of 12.5 cm, power 1.5 kW and a typical transverse size 9 cm was introduced perpendicular to the screen surface. A C_3H_8 or C_3H_8 /air mixture was injected through internal tubes in the pylon and vibrator. The stream velocity on the stream axis was approximately 200 m/s. The experiments demonstrated that the use of a deeply under critical microwave discharge can be used to effectively increase the combustion efficiency of C_3H_8 /air mixture in cold supersonic flow. Stable operation of a hot combustion torch in a supersonic stream in steady state was achieved. However, it was not clear whether the flame stabilization was enhanced by the arc discharge

or by the electron energy absorption of microwave at the flame front.

More recently, Brieschenk et al. [187] has reported experimental investigation on laser induced plasma ignition in a model scramjet engine for the first time. The experiments were conducted in the T-ADFA free piston shock tunnel using a flow condition with a total specific enthalpy of 2.7 MJ/kg and a free stream velocity of 2075 m/s. The scramjet model features a rectangular duct with a 9° compression ramp, followed by a constant-area combustor. H_2 is injected through four 2 mm diameter holes located on the compression ramp of the model, which are distributed across the compression ramp, 120 mm downstream of the leading edge. The laser induced plasma is formed by a Q-switched ruby laser with pulse energies of 750 mJ (only about 54% of the laser energy was absorbed). The location of the plasma is in the shear layers 1.7 mm downstream of the injectors. The temporal evolution of the laser induced plasma ignition region was monitored using OH PLIF technique. Hydroxyl radical (OH) formation was successfully observed. However, the subsequent ignition and flame propagation events were not reported.

In summary, plasma activation can enhance ignition and flame stabilization in a high speed flow through both thermal and kinetic effects. However, due to strong turbulent mixing (heat/radical loss) and short flow residence time (requiring a very short ignition delay time and fast heat release rate), combustion enhancement using non-thermal plasma alone is extremely challenging. A combination of both thermal and non-thermal plasmas such as the gliding arc/microwave and plasma jet/DBD discharge might be more effective for high speed applications. As such, the kinetic mechanism to optimize the combination of thermal and non-thermal plasmas needs to be understood. Furthermore, the introduction of plasma discharge may significantly modify the flow field. The effect of flow perturbation by plasma in affecting ignition and flame stabilization in high speed flow also needs to be addressed.

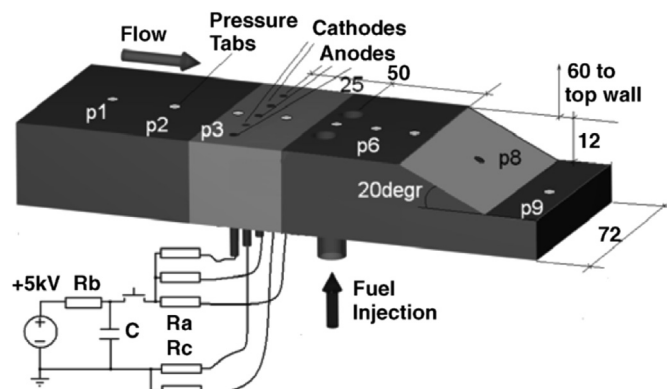


Fig. 2.8. Experimental schematic of the combustor bottom wall and the test arrangement [185].

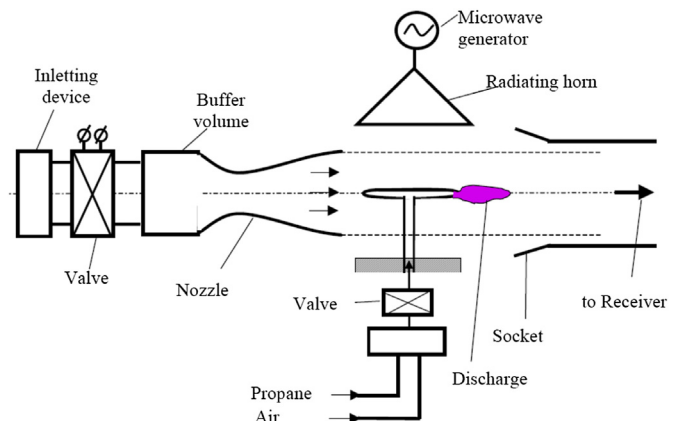


Fig. 2.9. Schematic of experimental setup [186].

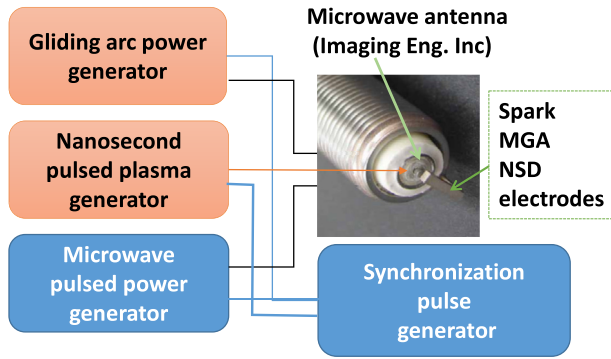


Fig. 2.10. Concept of plasma assisted spark ignition using NSD, gliding arc, and microwave.

2.2. Ignition enhancement by plasma in internal combustion engines

Over the last decade, plasma assisted combustion has attracted increasing attention for applications in internal combustion engines such as gasoline and diesel engines [68–81], gas turbine engines [63,64], pulsed detonation engines [36,37,58–62], and lean burn combustion systems [37,45,51–56,66,67,194,195]. In spark ignition (SI) engines, the development of the initial spark ignition kernel size strongly influences the lean burn limit and emission characteristics. A larger ignition kernel size can extend the lean burn limit for large hydrocarbon fuels [196]. In order to improve the ignition of SI engines, different plasmas such as microwave [68,69],

NSD [81], and gliding arc [197] have been used to replace or integrate with a conventional spark plug. A schematic of the integration of different plasmas with a conventional spark plug and a comparison of spark sizes are shown in Figs. 2.10 and 2.11, respectively. Fig. 2.11 shows that using a gliding arc and microwave discharge at the same pressure of 1 MPa the ignition kernel sizes are much greater than that of the conventional spark plug.

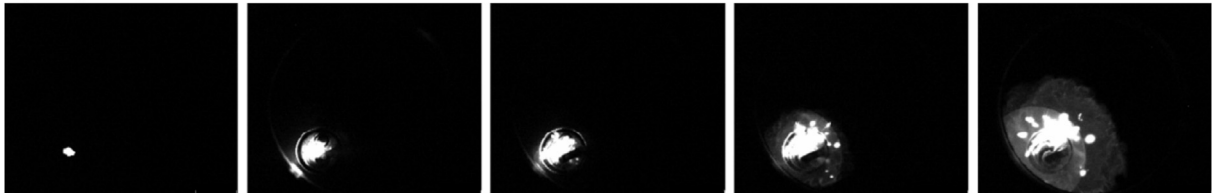
Ikeda and collaborators developed and tested a microwave integrated spark igniter [68,69] that can be applied to existing engine systems without any engine modification. As shown in Fig. 2.10, microwave discharge at a frequency of 2.45 GHz was generated by a commercial magnetron into a non-resistor spark plug which has the same geometry as that of a conventional spark plug. The two electrodes of the spark plug also acted as a microwave antenna. The microwave system operated in burst mode, in which a series of pulses of 2.45 GHz microwave energy were delivered to the spark plug starting before and ending after the standard spark. The microwave energy was then absorbed by the electrons formed by the spark between the two electrodes that raised the electrons to a higher temperature. These electrons collided with the gas molecules and raised the gas temperature and created excited species and active radicals. In an earlier work [198], the rotational temperature and N_2 density were measured by rotational Raman scattering in the region of the microwave discharge. It was shown that at a microwave power less than the ignition energy of a spark plug, the rotational temperature raised to a maximum of 1500 K in a nitrogen/helium mixture by microwave.

Fig. 2.12 shows direct photographs of the flames with spark ignition and microwave plasma ignition with C_3H_8 at the fuel and equivalence ratio of $\Phi = 1$. In the case of using a normal spark plug,

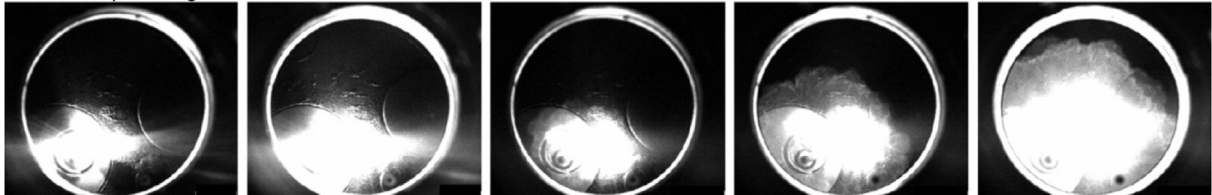


Fig. 2.11. Comparison of ignition using spark plug (left), microwave (middle), gliding arc (right) (Photos were provided by Knite Inc. and Imagineering Inc.) [197].

Spark ignition



Microwave plasma ignition



-14.2 deg. ATDC

-10.6 deg. ATDC

-7.0 deg. ATDC

-3.4 deg. ATDC

0.2 deg. ATDC

Fig. 2.12. Comparison of C_3H_8 flame images in a compression-expansion engine using conventional spark plug and microwave enhanced spark plug, $\Phi = 1$, initial pressure 600 kPa, initial engine speed 600 rpm [172].

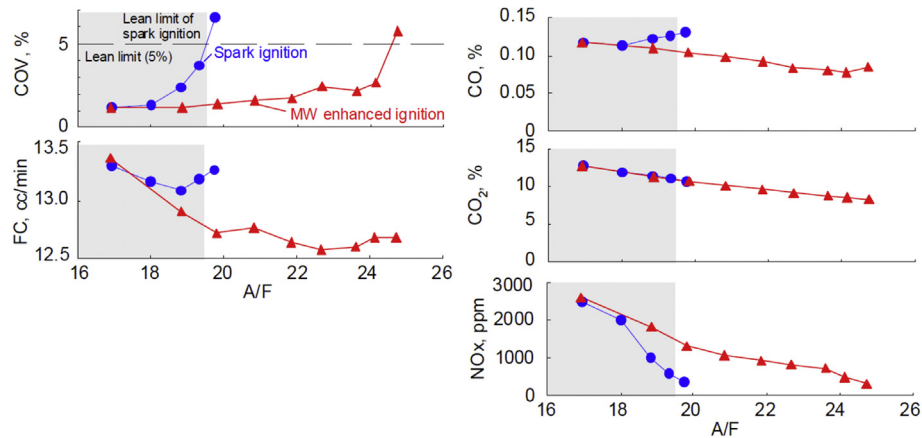


Fig. 2.13. The effect of spark ignition and microwave enhanced spark ignition on COV_{IMEP} , fuel consumption and exhaust emission [172].

spark discharge was observed at -14.2° after top dead center (ATDC). The flame kernel was formed at -7.0° ATDC, and then the flame propagated at -0.2° ATDC. With the microwave enhanced spark plug, intense light from the plasma was observed shortly after spark ignition. Then, a large flame kernel was formed by the microwave energy addition at 0.2° ATDC.

The microwave enhanced spark plug was further tested using a 499.6 cc, four-stroke- single cylinder gasoline research engine at a constant indicated mean effective pressure (IMEP) of 275 kPa and 2000 rpm. The effects of the microwave enhanced spark plug on the lean limit, fuel consumption, and exhaust emissions were evaluated. The results are shown in Fig. 2.13. With a spark plug igniter, at air/fuel mass ratio (A/F) of 17, the cyclic variation coefficient of IMEP (COV_{IMEP}) increased dramatically, indicating close to the lean limit of the engine. In contrast, with the microwave enhanced spark plug, the COV remained essentially constant until $A/F = 22$. Moreover, MW also reduced the fuel consumption (FC) and CO emissions for A/F greater than 18.

Wolk et al. [70] further investigated the performance of the microwave enhanced spark plug in a 1.45 L constant volume combustion chamber at a range of initial pressures and equivalence ratios. The microwave energy input in this study was approximately 225 mJ. The flame development time (FDT, time for 0–10% of total net heat release) and the flame rise time (FRT, time for 10–90% of total net heat release) [70] were used to characterize the

early and the late stage heat release of the combustion. The effectiveness of microwave addition on extending the lean and rich ignition limits was experimentally investigated for initial pressures ranging from 1.08 to 7.22 bar and 300 K for methane/air mixtures. As shown in Fig. 2.14(a), SI + MW (Spark Ignition + Microwave) ignition resulted in lower FDT for all equivalence ratios compared to the SI ignition. Greater enhancement was observed at the leaner conditions than the rich conditions. Fig. 2.14(b) shows that no enhancement of the FRT was observed at any equivalence ratio, indicating that although a more robust ignition event can be achieved with the addition of microwaves, subsequent flame propagation is not influenced due to the small energy addition. Correspondingly, there was no effect on the total heat release with microwave addition as far as ignition can occur.

The pressure dependence of the effectiveness of the microwave addition on extending the lean and rich ignitability limits and FDT was also investigated. Fig. 2.15 compares the ignition limits versus initial pressure with and without microwave addition for initial pressures ranging from 1.08 to 7.22 bar and 300 K. It can be seen that the ignition limits are both extended at the lean and rich limits with microwave use. Note that Fig. 2.15 might leave readers some impression that the enhancement of rich limit is greater than that of the lean limit. In fact, the effect is opposite. This is because of the definition of equivalence ratio. The flame temperature decreases much faster on the lean side than on the rich side. By considering

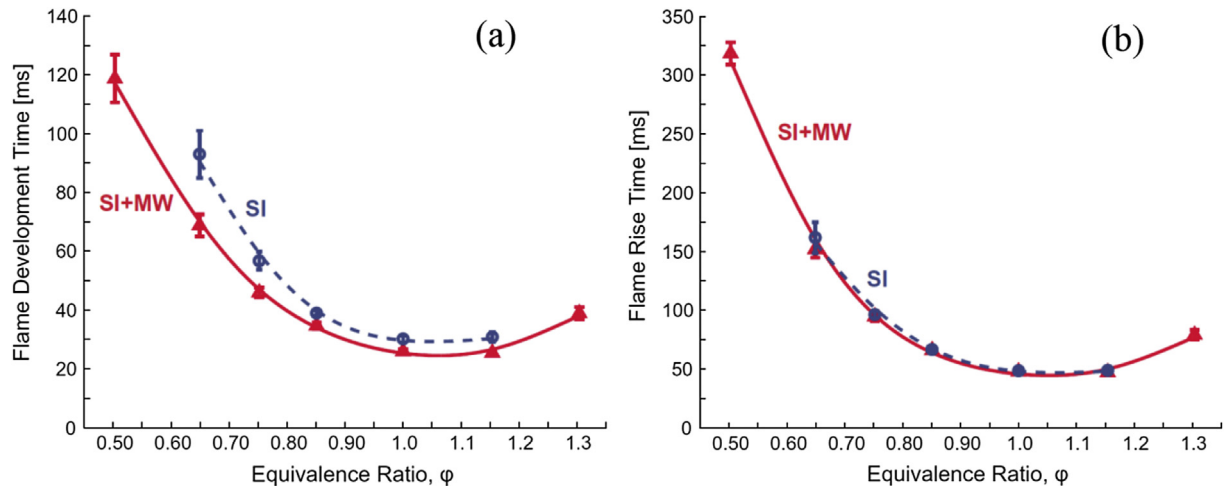


Fig. 2.14. the SI and SI + MW modes as a function of equivalence ratio at an initial pressure of 1.08 bar and 300 K (a) for FDT, (b) for FRT [70].

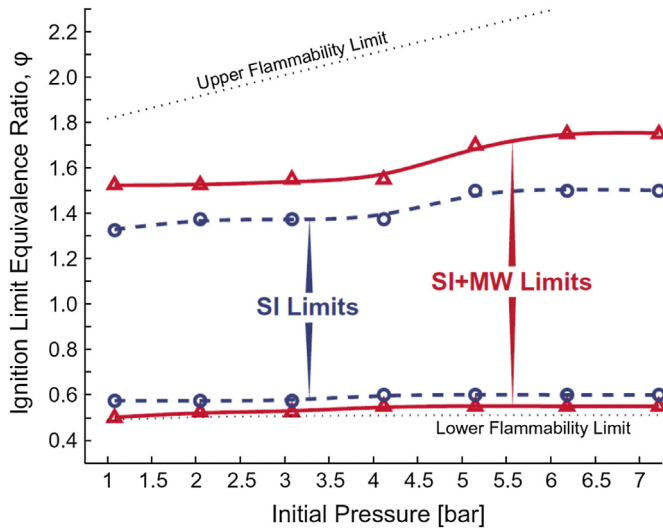


Fig. 2.15. lean and rich ignition limits for SI and SI + MW ignitions for a range of initial pressures at 300 K [70].

the same flame temperature, it can be interpreted from Fig. 2.15 that the enhancement of the lean side is greater than that of the rich side. The experiments also showed that for methane/air mixtures at $\Phi = 0.65, 0.75$ and 1.0 , the reduction of FDT by microwaves decreased with the increase in initial pressure for all equivalence ratios and the enhancement effect became negligible when the initial pressure was greater than 3 bar.

Wolk's experiments raised several important and interesting questions. Why did microwave use have more enhancement effect in oxygen rich conditions than in fuel rich? Why was the extension of the lean limit greater than that of the rich limit with the same flame temperature? Why did plasma enhance ignition kernel development time greatly but only slightly for flame rise time (flame speed)? Why did the enhancement decrease with the increase in pressure? The authors concluded that the observed decreases in flame enhancement were due to the decrease in E/N as the pressure increased. As will be discussed in the next section, E/N is not the major cause of the decreased effect.

The MW assisted ignition system was also tested for small engines which are affected more by the spark ignition energy and radicals losses to the engine wall due to the increased surface/volume ratio. A single cylinder, 34 cc 4-stroke gasoline engine (Fuji Imvac Model BF-34EI) is shown in Fig. 2.16 [69]. It was found that the microwave enhanced spark ignition produced a larger ignition kernel and led to an overall faster ignition and increase of the peak pressure with about 750 mJ MW energy output (1/4 to 1/3 of that energy is reflected back). By comparison, only less than 50 mJ energy was deposited by the standard capacitive spark plug. As shown in Fig. 2.16, the experimental results of COV_{imep} showed that the lean burn limit was extended by 20–30% in terms of the air/fuel ratio. Moreover, for the conventional spark plug the minimum fuel consumption occurred at fuel lean conditions of $A/F = 17–20$, where there was a significant miss fire. The results suggested that the microwave enhanced spark plug is an effective way to improve lean burn for micro and mesoscale engines [199].

Using the same small engine as Lefkowitz et al. [69], Thelen et al. [173], investigated the effect of a radio frequency (RF) plasma ignition system. The RF power generator pulses at 20 kHz and the output pulses are a burst of alternating high (30 kV) and low (0 V) voltage square waves with 25 μ s width. The maximum pulse burst duration was 1.2 ms with the RF system providing maximum amount of energy of 400 mJ to the discharge. The engine was tested at multiple engine speeds and air fuel ratios. The results also demonstrated an improvement in combustion stability at all operating conditions and an extension of the engine lean flammability limit. It was reported that the power output of the small engine was also higher with the RF plasma ignition system for stoichiometric and leaner air fuel ratios and the HC emissions was reduced. However, NO_x emissions increased owing to higher flame temperatures and additional NO_x formation pathways introduced by the plasma.

The USC (University of Southern California) group has developed various transient plasma igniter using corona and nanosecond discharge [79–81] for gasoline engines. The schematic of the nanosecond transient plasma igniter is shown in Fig. 2.17. The transient plasma was generated by applying high voltage short pulses (20–85 ns) that had energy (~ 60 mJ) comparable to that of the conventional spark igniter (~ 2 ms, 80 mJ). The transient plasma igniter can create a large volume of distributed arrays of streamers

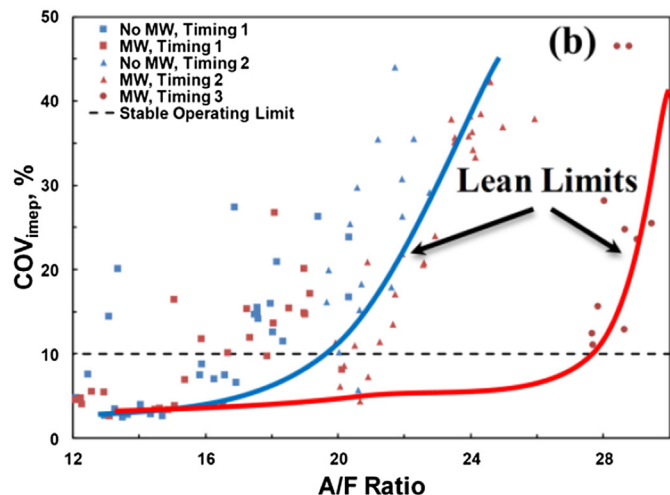
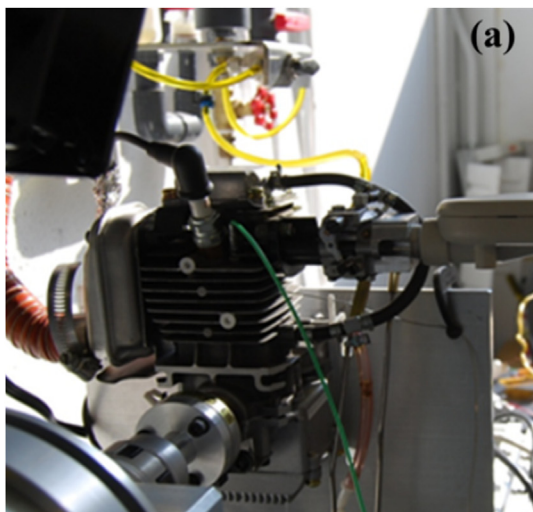


Fig. 2.16. (a) direct photograph of plasma assisted 34 cc Fuji engine test setup and (b) the comparison of limits of stable engine operating conditions with and without microwave (MW) discharge at 2000 rpm [69].

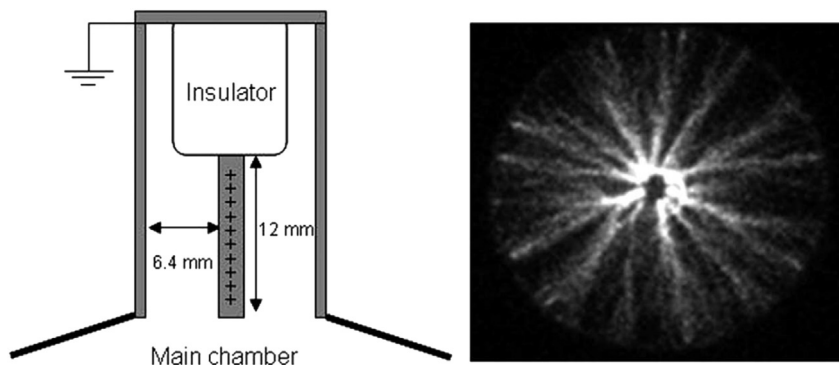


Fig. 2.17. Left: schematic of electrode. The gap is on the order of 6.4 mm, the anode is a 2.2 mm diameter, 12 mm long rod with 0.45 thread/mm thread. Right: transient plasma discharge (85 ns pulse) from the electrode taken with an ICCD of 700 ns gate at 10 atm [79].

(Fig. 2.17 right) which produce reactive species during nanosecond time scales via electron impact fuel and oxygen dissociation.

It was found that by using a transient plasma igniter (TPI), the ignition delay time can be improved. When a 20 ns pulse was used, stable lean combustion was realized at conditions not ignitable by a spark plug. It was also found that the peak pressure relative to spark ignition increased by 20% using a 20 ns pulse transient plasma igniter. High speed imaging illustrated in Fig. 2.18 shows that the transient plasma igniter generated faster flame speeds than the spark ignition. The authors inferred that during the initial phase of ignition, the initiation reaction $RH + O_2 \rightarrow R + HO_2$, where RH is a hydrocarbon fuel molecule, is replaced by fuel and O_2 dissociation reactions, $RH + e \rightarrow R + H + e$ and $O_2 + e \rightarrow 2O + e$. Shiraishi et al. [81] further investigated ignition characteristics in the lean combustion region and the relationship between the pulse width and ignition characteristics. The TPI used in this study operated at 80 ns or 25 ns pulse width with a fixed input energy of 60 mJ. The test fuel was a 90 research octane number (RON) primary reference fuels (PRF, a mixture of 90% iC₈H₁₈ (iso-octane) and 10% nC₇H₁₆ (n-heptane) in volume). Since the decrease of pulse width from 80 ns to 25 ns made the arc transition more difficult, the maximum voltage of the streamer discharge at the same pressure condition was increased, leading to an increase in E/N by roughly 30–40%. The results indicated that a shortened pulse width produced even faster combustion [81]. The USC group also examined the effects of

electrode geometry on the transient plasma induced ignition [79] at atmospheric pressure with a variety of fuels. Amongst all the electrode configurations, the needle-to-semicircle, the authors reported, resulted in the best performance by providing a sheet of transient plasma that was uniformly distributed over the gas volume.

The ignition mechanism of transient plasma ignition was investigated by Cathey et al. [152] in a quiescent, stoichiometric CH₄/air mixture by measuring the OH production in a large cylindrical chamber with the anode rod located in the center. The transient plasma is generated using a 70 ns FWHM, 60 kV, 800 mJ pulse. The total time for avalanche development, avalanche to streamer development and streamer propagation between the electrodes is typically 100–300 ns. Using a short high voltage pulse (<100 ns) in this experiment, energy is effectively coupled into a non-equilibrated plasma without a transition from the streamer to the arc discharge [152]. The number density of OH was measured using Planar Laser Induced Fluorescence (PLIF). It was found that OH was produced throughout the chamber volume after the discharge and decreased below detectability near 100 μ s. Ignition occurs along the surface of the anode around 1 ms and propagates outwardly with a wrinkled cylindrical flame front. The results showed that the production of OH by the streamers in the bulk of the volume was not the cause for ignition because of the low energy release. The authors suggested that a high voltage to produce OH

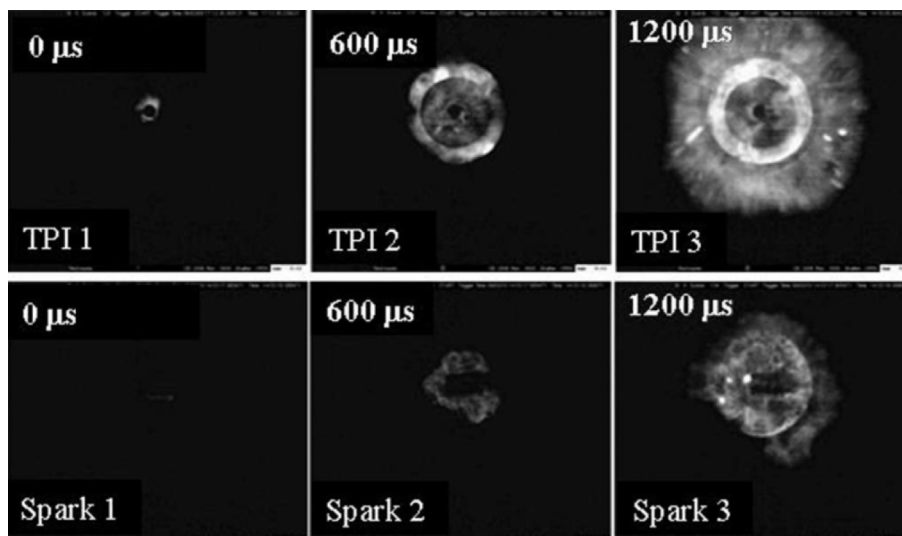


Fig. 2.18. Iso-octane/air combustion at 1200 rpm, 100 mmHg and an advance of 20° before top dead center, each frame is 200 μ s long (TPI: transient plasma ignition) [79].

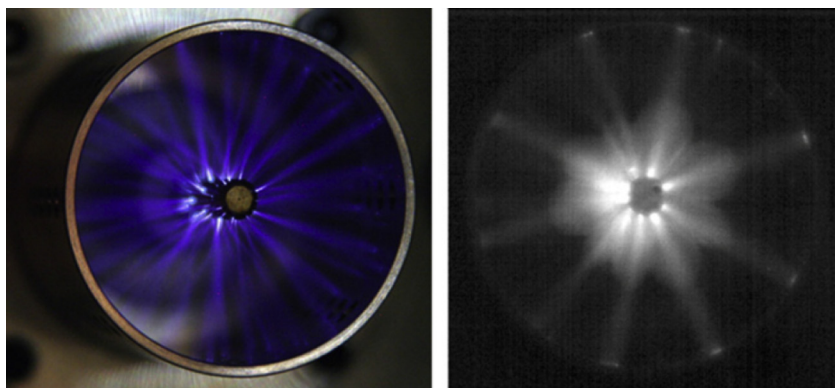


Fig. 2.19. Left: streamers generated by a single 370 mJ, 56 kV, 54 ns pulse (maximum $E/N \sim 400$ Td) in air (10 s gate time); Right: flame propagation from multiple ignition sites at the base of the streamers after a single pulse in $\Phi = 1.1$ C_2H_4 /air mixture (1 ms gate time) [81].

throughout the chamber was not, apparently, critical for ignition. The authors further explained that it was possible due to an electrically enhanced surface catalytic reaction at the anode surface and/or local joule heating of the electrode. Different from the MW experiment, the TPI experiment indicated that the thermal effect played an important role in the enhancement of ignition and that the OH production by streamer affected the flame propagation. Therefore, it is not clear whether kinetic enhancement can enhance ignition or the flame speed.

Singleton et al. [81] recently modified the system and studied the ignition enhancement in C_2H_4 /air mixture using transient plasma at 1 atm initial pressure. The center electrode was shortened and the discharge was produced between parallel electrodes rather than between the center electrode and chamber wall as in the previous experiments. The mixture equivalence ratio was $\Phi = 1.1$. As shown in Fig. 2.19, at atmospheric pressure using a coaxial electrode configuration with constant gas distance, multiple flame kernels were formed along the anode as the bases of the streamer channels after the transient plasma discharge. The plasma-ignition process had two distinct phases. First, an initial non-equilibrium phase where energetic electrons transfer energy into electronically excited species. This phase accelerates fuel molecule dissociation. Second, a spatially distributed thermal phase that produces exothermic fuel oxidation. The heat release from fuel oxidation results in ignition approximately 1 ms after the discharge. Temperature measurement using rotational profile of the N_2 ($C^3\Pi_u, v' = 0$) \rightarrow N_2 ($B^3\Pi_g, v'' = 2$) transition at 380 nm showed that up to 100 ns after the discharge, the temperature in

the streamer channel was close to room temperature. This indicates that the initial plasma process was non-thermal. However, the radical pools generated in the high E/N transient plasma discharge accelerated the initial chain branching reactions to ignition. Unfortunately, the detailed processes were not clear. Fig. 2.20 shows the comparison of flame propagation between spark ignition and TPI. In TPI, the initial flame kernels passed through the holes on the wall of the concentric cathode forming a clover-shaped flame front, in contrast to the hemispherical smooth flame front in the spark-ignited case. An average flame propagation speed of TPI was 15% more than that of spark ignition. However, it was not clear whether the increase of flame speed was solely due to flame wrinkling or there was any enhancement effect on flame speed.

Laser as another high temperature ignition source for internal combustion engine has been tried for gasoline and natural gas engines for a number of years by Toyota, Ford, Caterpillar, and Cummins engines [74–78]. It has been reported that laser ignition was able to ignite leaner mixtures with NO_x reduction. The fundamental mechanisms for laser ignition can be summarized as (1) Thermal ignition in which molecules absorb photon energy and increase temperature; (2) photochemical ignition in which molecules dissociate or are ionized after absorbing multiple photon energy; (3) resonant breakdown in which dissociation and ionization of target molecules or atoms by the resonant multi-photon ionization process; and (4) non-resonant thermal breakdown occurs when the focus laser power is sufficiently high to influence the gas molecules and initiate the electrical breakdown of the gas. By far, non-resonant breakdown has been the most frequently adopted ignition mode to

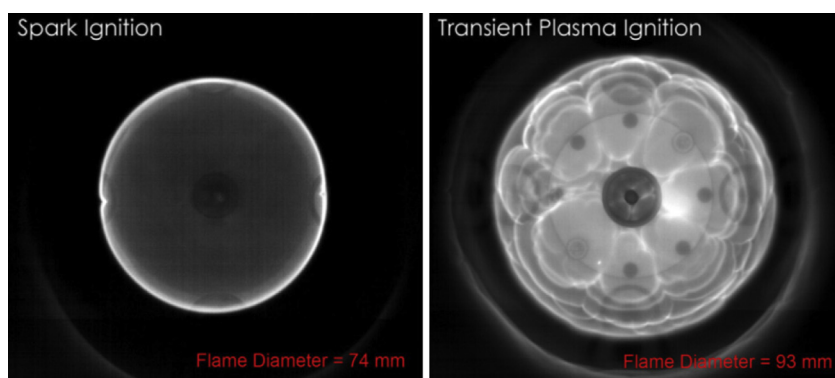


Fig. 2.20. Images of flame development in $\Phi = 1.1$ C_2H_4 /air mixture, 6 ms after ignition. A 300 μ s gate time was used with equal sensitivity for both images and 996×990 resolution. Left: spark ignition using a standard 105 mJ, 10 μ s, 15 kV spark ignition system and a spark plug with a 1 mm gap. Right: transient plasma ignition using a 70 mJ, 12 ns, 54 kV pulse with a 6 mm gap [81].



Fig. 2.21. Direct photograph of a prototype laser igniter showing breakdown in air at multiple points [200].

initiate combustion primarily because of its freedom in selecting the laser wavelength and power. The advantage of laser ignition is that it provides remote and multipoint ignition and avoids heat loss to the electrode. Fig. 2.21 shows a compact prototype laser igniter which is a passively Q-switched Nd:YAG/Cr⁴⁺:YAG giant pulse emitting micro-laser with three beam output. Pavel et al. [200] reported that at a 5 Hz repetition rate, each line delivered laser pulses with approximately 2.4 mJ energy and 2.8 MW peak power within the pulse duration. Recently, Princeton Optronics developed Vertical Cavity Surface Emitting Laser (VCSEL) and increased the efficiency (up to 63.4%) and energy output to 7 mJ per pulse with a repetition rate of 20 Hz at pulse duration of 100 μ s [201]. Although many engine tests have demonstrated the ability of laser ignition to ignite ultra-lean fuel-air mixtures and mixtures with high EGR, the laser stability at a high temperature (e.g., 200–400 $^{\circ}$ C), vibration, and soot formation are still challenging problems [201].

Ozone (O₃), which can be efficiently produced by plasma and can have a strong low temperature kinetic enhancement effect [108] and can modify flame speed [157,202], has also been used for engine combustion control. The effect of O₃ on the combustion of n-heptane (nC₇H₁₆) in a HCCI engine was studied by Foucher et al. [179]. Experiments were performed in a single cylinder diesel engine fueled with n-heptane at constant equivalence ratio of 0.3, intake temperature of 300 K, and engine speed of 1500 rpm. The

intake manifold was seeded by ozone produced by a dielectric barrier discharge reactor. Experimental results showed that low ozone concentrations (<50 ppm) have an important impact on the phasing of the cool and main flame in the engine. It was found that the low temperature ignition and main flame ignition timing decreased significantly when ozone concentration increased from 0 to 20 ppm. However, it was also reported that the influence of O₃ became less important above 20 ppm although the ignition time monotonically decreased. If the O₃ concentration increased from 0 to 54 ppm at the intake of the HCCI engine, it advanced the main flame phasing by 7 CAD (Crank Angle Degree). Comparatively, a variation of 0–60% of EGR (Exhaust Gas Recirculation) retards the phasing of the main flame by 7 CAD. A variation of 60 K of the intake gases mixture temperature affected 3 CAD and a variation of 49 ppm of NO had an effect of 1.5 CAD in this engine at the same condition. Although numerical modeling identified that the effect of O₃ was majorly through the decomposition of O₃ to release an O atom, the detailed kinetic process was not well understood.

In summary, many engine experiments have shown that non-equilibrium plasma can enhance engine performance. However, due to the combined plasma effect on ignition and flame speed through both thermal and non-thermal effects, some observed large-enhancement in the lean burn limit was not appropriately explained. Therefore, there is clear need to understand how plasma affects ignition, flame propagation, and flammability limit from the point of view of ignition and flame dynamics as well as combustion and plasma chemistry. Moreover, since most of the practical engines work at high pressure, there is a great need to understand the kinetic properties of plasma and to develop a large volume plasma discharge at high pressure to enhance combustion at engine conditions.

2.3. Plasma assisted combustion for pulse detonation engines

Since plasma can enhance ignition, non-equilibrium plasma has also been tested to accelerate deflagration to detonation transition in pulse detonation engines (PDE) [203]. Cathey et al. [178] summarized the collaborative work between USC and Naval Postgraduate School (NPS), Stanford University, and AFRL at Wright–Patterson AFB on TPI to accelerate ignition in pulse detonation engines. It was demonstrated that at high flow rates where spark-initiated flames were normally extinguished, the transient plasma was able to ignite and effectively create a detonation wave in the PDE experiment at NPS. Significant reduction (factor of 4) in ignition delay time was also shown for C₂H₄/air mixtures as in Fig. 2.22 together with a direct photograph of the

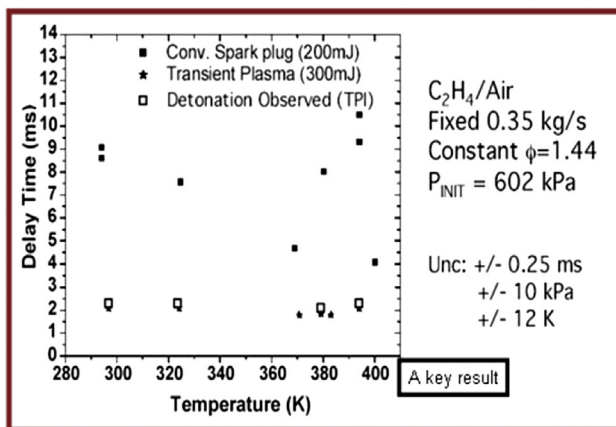
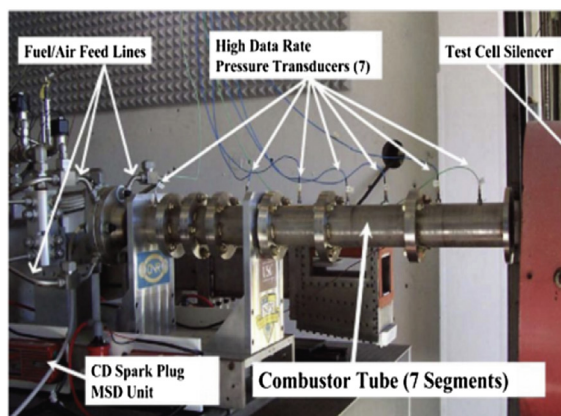


Fig. 2.22. Left: a valveless PDE setup at the Naval Postgraduate School. This type of architecture requires a booster and its anticipated applications are missiles or rockets. Right: comparison of ignition delays for C₂H₄/air mixture using spark plug and transient plasma igniter [178].

PDE setup. Tests were conducted at ARFL with H_2 /air and aviation gasoline/air mixture. A reduction in the ignition delay by factor of 2 was obtained for both H_2 /air and aviation gasoline/air mixture. The transient plasma was able to reliably ignite aviation gasoline/air mixture at equivalence ratios of nearly 0.65, whereas the baseline's lower limit was 0.71. The transient plasma ignition of C_2H_4/O_2 mixture resulted in ignition delay reduction by nearly one order of magnitude (factor 9) in the PDE setup at Stanford University.

Recently, Lefkowitz et al. [62] studied the effect of high-frequency nanosecond pulsed discharges on PDEs as shown in Fig. 2.23(a). By comparing the ignition delay times as well as high-speed imaging of the ignition kernel growth with different igniters (igniter powered by nanosecond pulsed power and conventional multi-spark igniter), they found a significant decrease in the ignition time in the PDE for a variety of fuels and equivalence ratios (Φ). As demonstrated in Fig. 2.23(b), with the same amount of total energy input, higher frequency discharges can initiate flame propagation. Fig. 2.23(c) showed the difference between the nanosecond pulsed plasma igniter and the multiple spark discharge (MSD) igniter. With roughly the same amount of total energy consumption, the MSD ignition kernel eventually extinguishes, while the plasma ignited kernel goes on to become a self-propagating flame. In addition, both the leaner and the richer ignition could be achieved with the help of the nanosecond pulsed igniter. One possible reason of the decrease in the ignition delay is the increase in energy deposition from the nanosecond pulsed power supply. But the plasma–chemical interaction in the discharge is still not clear.

2.4. Plasma assisted combustion for flame stabilization in gas turbine engines

Lean blowout limit, flame stabilization and instability are the key issues of gas turbine engines. Plasma is also used as a new technology to increase the flame stability and achieve ultra-lean combustion. Serbin et al. [204] claimed that a gas turbine combustor with piloted flame stabilization by non-equilibrium plasma can provide better performance, wider turndown ratios, and lower emissions of carbon and nitrogen oxides. However, details were not discussed in the paper.

Moeck et al. [163] studied the effect of nanosecond pulsed discharge on combustion instabilities at 1 atm. The nanosecond pulsed discharges were generated by a solid state pulse generator (FID 300-100MC4K) with 10 ns pulse width at 10–80 kHz pulse

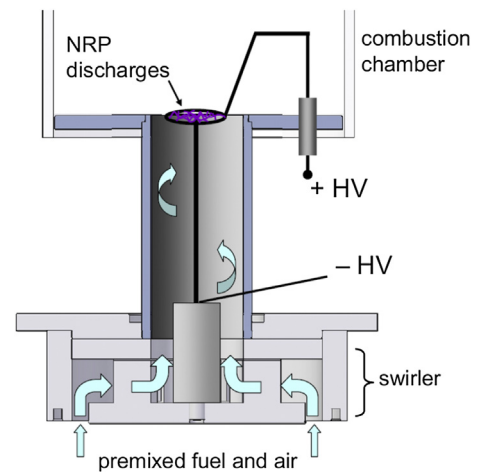


Fig. 2.24. Installation of the electrodes in the Swirl-stabilized burner [163].

repetition frequency (f) and 12 kV amplitude. The discharge was coupled at the nozzle exit of a swirl-stabilized combustor as shown in Fig. 2.24. A central pin electrode was installed at the swirler outlet to the combustion chamber that served as the cathode. With this electrode arrangement, nanosecond pulsed discharge filaments were generated between the central pin electrode and the loop-electrode in a disk-shaped area. The effect of the discharges on the mean flame illustrated on the basis of averaged CH^* chemiluminescence images is shown in Fig. 2.25. The images were taken at an equivalence ratio $\Phi = 0.62$ and a thermal power of 50 kW. The Reynolds number based on the bulk velocity in the burner passage, the diameter thereof, and the viscosity in the unburned gases was 37,000. The mean flame shape without plasma discharges was compared to the case with discharges at pulse repetition frequencies between 5 and 25 kHz, which corresponded to an electrical power of between 30 and 150 W. Without plasma, the flame was lifted off and stabilized in the shear layers associated with the recirculation zone (Fig. 2.25(a)). As the discharges were activated and the pulse repetition frequency was increased, the flame moved successively further upstream and eventually stabilized in the burner passage (Fig. 2.25(b)–(d)).

The effect of steady pulsed discharges on combustion dynamics was further investigated. It was found that the discharges had a strong effect on the pressure pulsations associated with thermoacoustic dynamics. With the consumption of less than one percent of

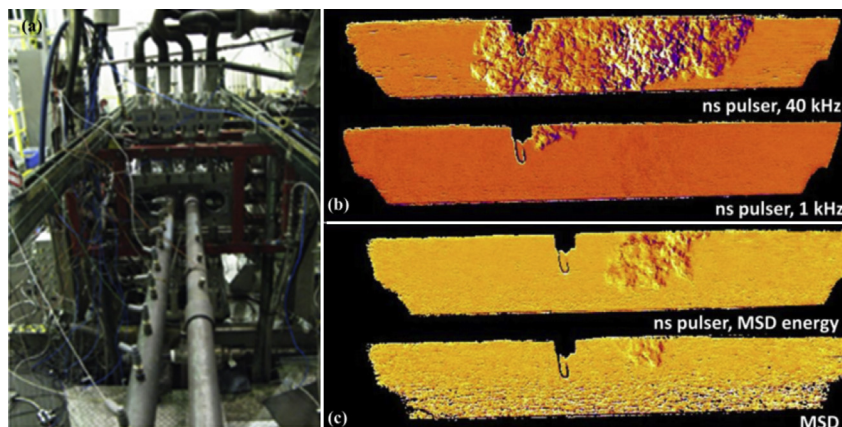


Fig. 2.23. (a) PDE engine facility at the Air Force Research Lab at Wright-Patterson Air Force Base, (b) Schlieren imaging of nanosecond pulsed discharge igniter in CH_4 /air mixture, $\Phi = 1$, (c) Schlieren imaging of nanosecond pulsed discharge igniter in CH_4 /air mixture, $\Phi = 0.8$ [62].

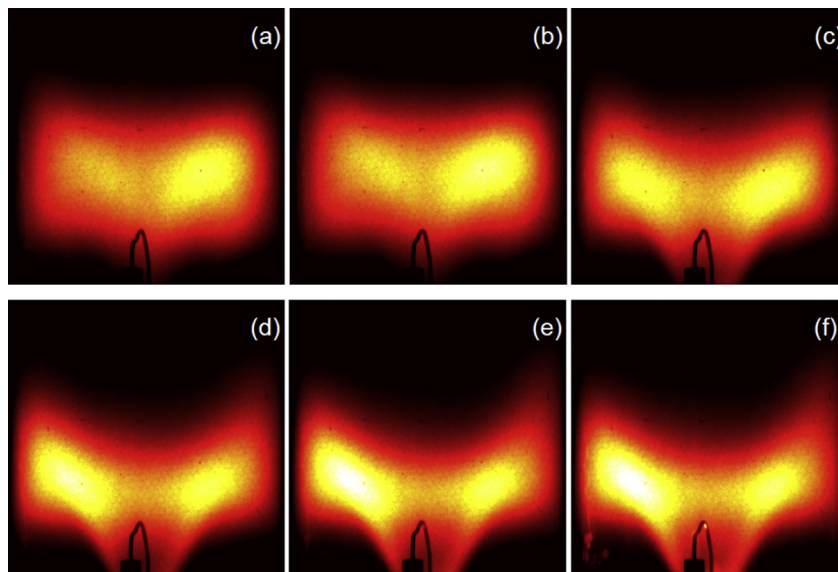


Fig. 2.25. Averaged CH^* chemiluminescence intensity for the case without plasma discharges (a), and with $f = 5, 10, 15, 20$, and 25 kHz (b–f); equivalence ratio $\Phi = 0.62$, thermal power 50 kW [163].

the total power of the flame, the nanosecond discharge can significantly reduce the oscillation amplitude of the acoustic pressure. However, at some conditions, plasma forcing can also destabilize a nominally stable combustion system. Since the discharges affect both the flame shape and the position, they have an influence on the dynamic response of the flame to acoustic perturbations. It may have a stabilizing effect in nominally unstable conditions, but the opposite is also possible. In order to use plasma as an actuator to control the flame dynamics, much more work needs to be done

to reveal the fundamental mechanisms of the plasma/flame interaction.

Recently, Lacoste et al. [176] redesigned the experimental rig and studied the effects of nanosecond pulsed discharges on the dynamics of a swirl-stabilized lean premixed CH_4/air flame at 1 atm with thermal power 4 kW (Fig. 2.26, left). The discharge pulses were 8 kV in amplitude and 10 ns in duration at $f = 30$ kHz, which is equivalent to 40 W electric power. The swirl number was 0.53 . The flame image in Fig. 2.26 (right) was reconstructed for

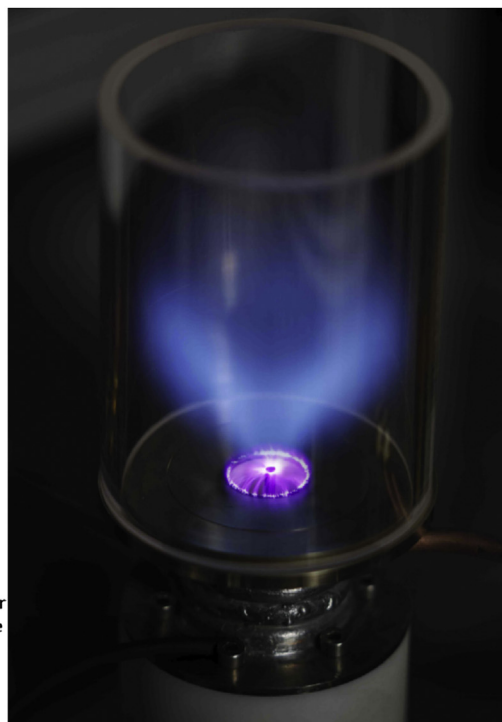
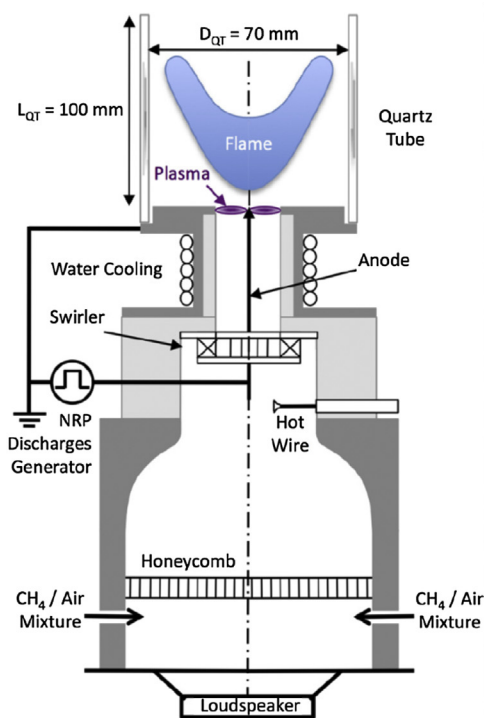


Fig. 2.26. Left: schematic of burner equipped with a loudspeaker and a nanosecond pulsed discharge generator; Right: photographic representation of the burner with a lean premixed CH_4/air swirl-stabilized flame (blue) and discharges (purple) [176]. (For interpretation of the references to color in this figure legend, the reader is referred to the web version of this article.)

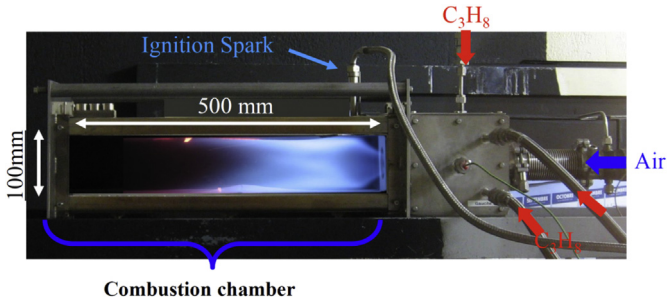


Fig. 2.27. Direct photograph of the combustion chamber during operation [177].

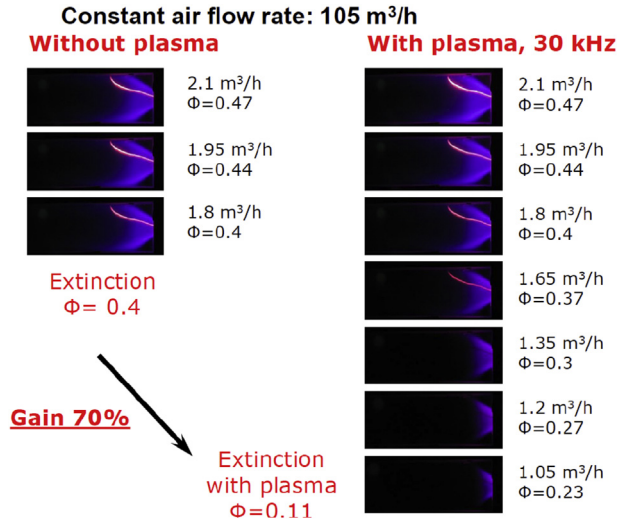


Fig. 2.28. CH^{*} emission images obtained for $Q_{\text{air}} = 105 \text{ m}^3/\text{h}$ and for primary fuel injection rate $Q_{\text{C}_3\text{H}_8} < 2.1 \text{ m}^3/\text{h}$ or $\Phi_g < 0.41$. The repetition rate of the discharge was 30 kHz [177].

demonstration purposes by combining a photo of the flame with plasma contribution with a short exposure time and a photo of the flame without plasma but with a much longer exposure time. The velocity and CH^{*} chemiluminescence signals were used to determine the flame transfer function. The flame response to acoustic perturbations of the incoming flow was investigated in a range of frequencies from 16 to 512 Hz at equivalence ratio $\Phi = 0.7$. It was found that in almost the entire range of excitation frequencies, the discharge affected the gain of the flame transfer function. The phase was also affected by the discharges, but only at high frequencies. In addition, the study showed the flame instability could be effectively mitigated by the application of nanosecond pulsed discharges,

reducing the velocity fluctuation amplitude by an order of magnitude. The authors explained that this phenomenon was mainly caused by the thermal effect of the plasma. The ultra-fast heating of the flow by plasma was followed by expansion of gas and generation of shock waves. This aerodynamical impact on transport affects flow velocity and alters vortex structure, and therefore changes the flame transfer function.

Barbosa et al. [177] further studied the effects of a nanosecond pulsed discharge plasma on the flame stability domain of a lean C₃H₈/air premixed of a swirling burner. A two-stage swirled injector was connected to a rectangular combustion chamber with optical access ports. Both stages were supplied with C₃H₈ and air. Both the swirlers were oriented in the same direction to ensure a strong co-rotating swirling motion. The primary and the secondary stage C₃H₈/air mixtures mixed together upon entering the combustion chamber. The peak power of the combustor was 52 kW with exit velocity 40 m/s. The combustion chamber had a square cross-section of $100 \times 100 \text{ mm}^2$ and a length of 500 mm. The sidewalls of the chamber were made of two silica windows to enable optical diagnostics in the flame, and the top and the bottom walls of the chamber were made of concrete. All studies were performed at ambient pressure and ambient temperature. A direct photograph of the experimental setup and flame stabilization is shown in Fig. 2.27. The discharge was produced using a pulse generator (FID FPG 30-100MS) with 10 ns pulse width. The voltage amplitude was 30 kV at a repetitive frequency $f = 30 \text{ kHz}$ which corresponded to approximately 350 W power.

The operating regimes of the burner were determined as a function of the global equivalence ratio, Φ_g using CH^{*} chemiluminescence. Fig. 2.28 shows the evolution of the flames when the fuel flow rate injected through the primary stage was decreased. It is clearly showing that without plasma, the flame extinction was observed when the equivalence ratios reached $\Phi_g = 0.41$, whereas using plasma the flame stabilization limits were reduced to $\Phi_g = 0.11$. Thus, the plasma discharge significantly extended the global flame stabilization limit. By using a small fraction (~1%) of the flame power, extended stability domain of a laboratory scale gas turbine combustor was demonstrated. This experiment also raised the question whether the observed increased flame stabilization was due to the thermal effect or the kinetic effect and whether the kinetic effect can extend local flammability limit instead of the global equivalence ratio. Further fundamental studies with local flame structure diagnostics are needed.

The ionic wind effect caused by a DC electric field was also used to increase the stabilization of the lean propane flames [65]. The results showed that by using a low DC electric field opposing the gas flow direction, not only the flame structure but also the flame stabilization was significantly modified as shown in Fig. 2.29. The results showed that dissociative recombination of major positive

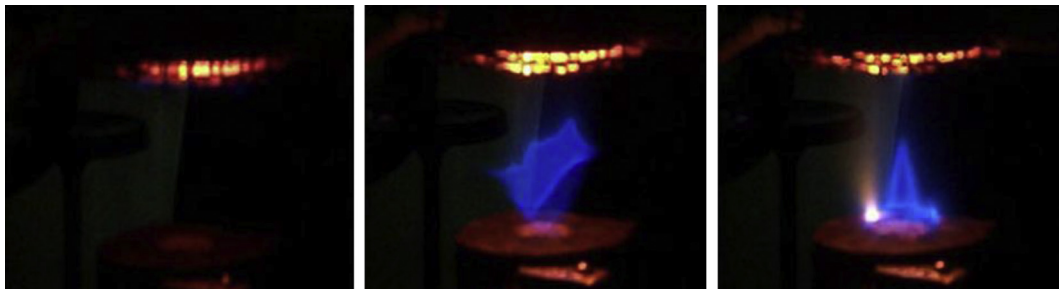


Fig. 2.29. Image sequence of a propane/air flame with an equivalence ratio of 1.2. The applied dc voltage was slowly increased (left to right), leading to the flame blowing off the burner [65].

chemi-ions H_3O^+ and HCO^+ produces 10^{11} cm^{-3} H, O and OH radicals modifying both the combustion kinetics. However, it was not clear why such a low concentration of radicals (below 10 ppb) could have such a big impact on the flame structure and stability. The effect of ion transport induced flow motion and acceleration might produce a more significant effect. Therefore, not only the thermal and kinetic effects but also the transport effect by plasma plays a significant role in modifying combustion. It requires well-defined experiment platforms to isolate these effects so that the fundamental mechanism can be understood.

Recently, Versailles et al. [205] integrated a DBD actuator into the premixer of a combustor to investigate the effect of ionic wind on flashback. Flashback makes combustor design very challenging with the change of fuel properties. A flame flashback will happen when the turbulent flame speed of a high energy fuel is faster than the flow velocity. Due to the wall shear stress, the flow velocity near the wall is very low and the propensity for flashback to occur in the boundary layer is very high. In the study by Versailles et al. [205], a DBD actuator was applied on the wall of the premixer as shown in Fig. 2.30 to create the ionic wind to increase the flow velocity in the boundary layer to prevent flashback. The flow acceleration also helps in strengthening the outer recirculation zone in the combustor to help anchor the flame at the dump plane. As shown in Fig. 2.31, without DBD actuation, the flame stabilized on the rim of the premixer (Fig. 2.31(a)), while with DBD actuation the flame anchoring was provided by the outer recirculation zone (Fig. 2.31(a)). It was reported that with the DBD actuation, the combustor stable operation regime can be stretched as much as 4.6% by shifting the flashback limit to higher equivalence ratios.

In summary, the above experiments have shown that non-equilibrium plasma can enhance flame stabilization and extend the lean burn and flashback limit significantly. However, it is not clear through what kinetic pathways and flame dynamics the flame speed is increased and the flammability is extended because many mechanisms such as the multi-dimensional discharge effect, temperature increase, radical production, fuel reforming, and the ionic wind effect all present at the same time. It is important to understand the reaction pathways of kinetic enhancement and combustion dynamics of plasma assisted combustion based on the fundamental flame theory and using well-defined flame experiments.

2.5. Emission control and fuel reforming by plasma

Plasma has been widely studied for reduction of soot and NO_x emissions as well as fuel reforming [82–108]. Since the focus of this review is on plasma assisted combustion, the applications of plasma on soot/ NO_x /hydrocarbon emissions and fuel reforming are only reviewed briefly here.

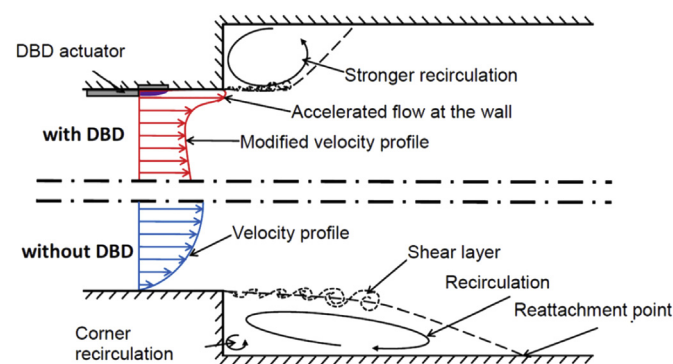


Fig. 2.30. Schematic of tubular flow into a sudden expansion chamber (dump plane) with (top) and without (bottom) DBD actuation [205].

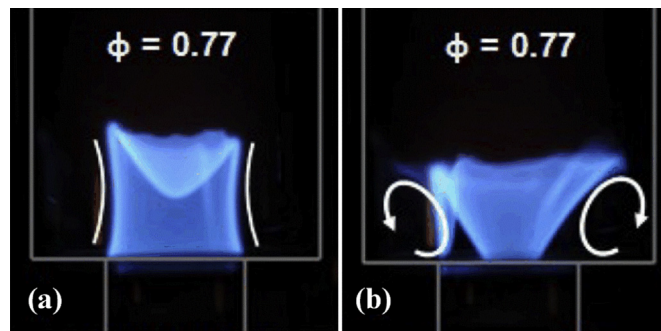


Fig. 2.31. Direct photographs of CH_4 /air flames (a) without and (b) with DBD actuation [205].

For soot emission control, Cha et al. [96] studied a dielectric barrier discharge (DBD) in coflow jet C_3H_8 diffusion flames. The plasma reactor had wire-cylinder type electrodes with AC power supply operated at 400 Hz. The stainless steel wire acted as a central electrode with 1 mm diameter. The cylindrical electrode made from a woven stainless mesh ($1 \times 1 \text{ mm}$) having a width of 10 mm surrounded the outer quartz tube. The effect of the amplitude of applied voltage on flames was studied. It was observed that with the increase of applied voltage, flame length decreased (Fig. 2.32). At the same time, the yellow luminosity indicating soot formation decreased with the decrease in the flame height. Without plasma breakdown, significant soot reduction was reported as demonstrated with low power consumption in the order of 1 W. Further thermocouple and FTIR measurements showed that the change in flame temperature and species concentrations for C_3H_8 , CO_2 and H_2O was negligible. Radical production, such as O, O_3 , OH and H was used to explain the soot reduction phenomenon. The reduction of soot was likely caused by the transport effect of ionic wind on fuel/oxidizer mixing.

As an after-treatment technology for engines, non-equilibrium plasma has also been extensively studied for soot reduction. The challenge for conventional soot reduction methods, such as catalytic coating of the filter, additives or soot oxidation by NO_2 is that they start working at a minimum temperature of 250°C , while the typical exhaust temperatures of engines are in a wider range between 120 and 650°C [206,207]. Plasma is one of the promising after-treatment technologies in this temperature range. Grundmann et al. [206] studied soot treatment by using DBD and ozone. In their study, soot was externally accumulated in the engine exhaust gas pipe of a small emergency generator (Yanmar, 0.4 L, 1 cylinder). The comparison showed that the plasma oxidized soot significantly faster than O_3 . It was possibly due to the radical production by plasma while O_3 decomposed at lower temperature (200°C).

Song et al. [188] characterized the abatement of particulate matter (PM), hydrocarbons (HC), and NO_x from an actual diesel exhaust using DBD technology. A DBD reactor excited by a high frequency AC power supply (sine wave, peak voltage 0–14 kV, frequency: 10–27 kHz) was used to treat the exhaust gases. The abatement capability of PM, HC and NO_x as functions of voltage at fixed frequency are shown in Fig. 2.33. No breakdown occurred when the applied voltage was lower than 6 kV and the removal efficiency of contaminants was very limited. When the increase in the applied voltage had exceeded 6 kV, the abatements of PM and HC increased obviously and saturated at approximately 80%. The trend of NO_x removal efficiency was different from those of PM and HC. In the range of 4–7.5 kV in the peak voltage, a significant increase of NO_x removal efficiency from 0.5% to 67.3% was observed.

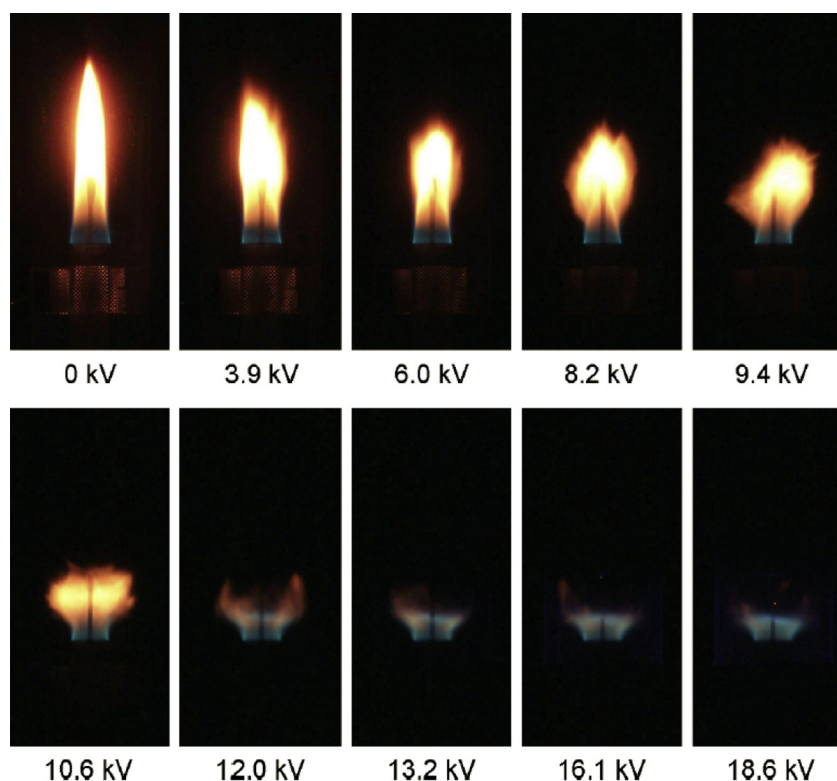


Fig. 2.32. Direct photographs of flame with 0.5 s exposure time by varying applied voltage [96].

However, a further increase in the peak voltage lowered the removal efficiency. A possible reason was the dissociation of N_2 to form NO_x owing to the increase in E/N . The authors also reported the abatements of various alkanes and polycyclic aromatic hydrocarbons (PAHs) including alkanes, alkenes, and aromatics. However, the underlying abatement mechanisms are still missing.

NO_x and hydrocarbon reduction by gliding arc has also been extensively conducted [82,83,91,99,189]. Lee et al. [189] investigated NO_x reduction in industrial burners using gliding arc. A first stage combustor integrated with gliding arc plasma was embedded with the head of the commercial reference burner. The schematic of the burner is shown in Fig. 2.34. The gliding arc was convected

downward with the fluid-dynamic rotation of reactant flow. Liquid nature gas (LNG) was supplied through the bottom hole of the reactor, where it was rapidly mixed with air and allowed to enter into the arc region. The plasma used AC power with a frequency of 10 kHz corresponding to powers 50–150 W which were a value less than 0.1% of the fuel heating value. The comparison of NO_x production rate in the reference and modified burners is shown in Fig. 2.35 as a function of the excess air ratio. The direct photographs of the flame from the two burners were also embedded. Significant NO_x reduction was observed. The first stage combustor operated as a reformer that could host a partial oxidation process, producing hydrogen rich (10% in volume) syngas flow that ignited and stabilized the combustion flame apart from the burner rim. Ultimately, the enhanced mixing and removal of hot flame zone with a broadened flame area acted as the main mechanisms of NO_x reduction.

Plasma has been widely used in fuel reforming, in addition to emission reduction [98–106]. Recently, two different types of fuel reformers, the nanosecond spark discharge and the nanosecond DBD have been developed for propane-air reforming. For the nanosecond spark discharge, 70% fuel conversion was obtained [208]. For the pulsed nanosecond DBD reformer, the effect of temperature on reforming between 900 and 1300 K was studied. A significant influence on mixture conversion efficiency, especially at $T = 900$ K, was obtained (Fig. 2.36). It was found that the energy cost of hydrogen for DBD reformer is higher compared to that for nanosecond spark reformer.

3. Flame dynamics and chemistry in plasma assisted combustion

The experimental results of plasma assisted engine combustion and turbulent flame stabilization in Section 2 sometimes showed

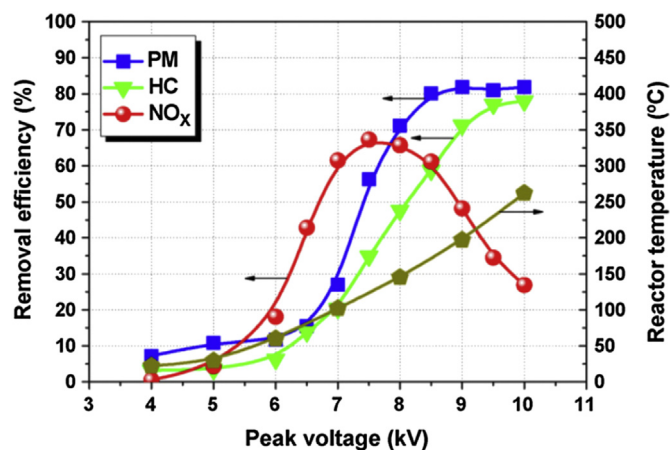


Fig. 2.33. PM, HC and NO_x removal efficiencies as a function of peak voltage (frequency = 15.5 kHz, engine load = 50%, initial PM concentration = 73.67 $\mu\text{g/L}$, initial HC concentration = 107.6 ppm, initial NO_x concentration = 476.3 ppm) [188].

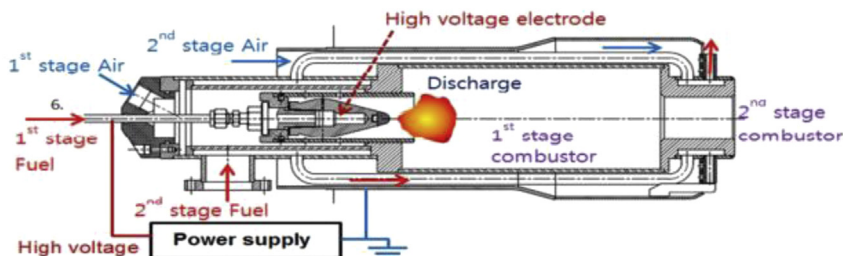


Fig. 2.34. Conceptual design of the proposed plasma-embedded staged burner with modification procedure [189].

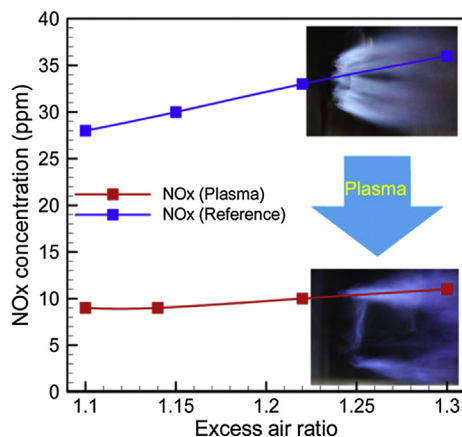


Fig. 2.35. Comparison of NO_x production in the reference and modified burners as a function of the excess air ratio [189].

conflicting results. Some experiments reported that plasma enhanced both the ignition and the lean burn limit. Others showed that plasma had little impact on flame propagation speeds. Some experiments showed that the plasma enhancement was due to thermal effect, while others demonstrated enhancement effects via kinetics and transport (e.g., ionic wind). The experimental results of Wolk et al. [70] clearly showed that the use of microwave had a greater enhancement effect in oxygen rich conditions than that in fuel rich condition and that plasma enhanced ignition kernel development but not for flame speeds. Moreover, the results showed that the enhancement decreased with an increase in pressure. How do we explain these observations from flame dynamics, chemistry, and transport?

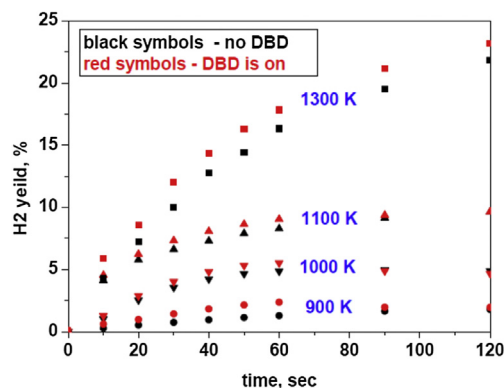


Fig. 2.36. Comparison of hydrogen yield with and without DBD for propane/air mixture at 1 atm and different temperatures [208].

In this section, firstly, we will present an overview of the basic chemistry and dynamics of ignition, flame initiation, propagation speed, and extinction limit as well as their dependence on temperature, chemistry, and transport. By using the physical and chemical properties of plasma, we will discuss the mechanisms and kinetic pathways in which plasma can enhance ignition, flame propagation, and extinction and lean burn limits.

3.1. Dynamics and chemistry of plasma assisted ignition

Ignition is an exothermic, chain-branching reaction process which results in an exponential increase in heat release and fuel oxidation. Therefore, ignition requires two key processes: one is that the temperature needs to reach a threshold of an exothermic chain-branching process and the other is that the radical production chain-branching process is faster than the chain-termination process. As shown in Fig. 1.4, as the heat release of a reaction system increases (or decreases), the temperature of the reaction system increases. At a critical temperature of the chain-branching limit, ignition occurs and both the concentration of radicals and the temperature of the reaction system increase exponentially. In a diffusion controlled system, once ignition occurs, a flame with higher temperature will be formed. If the fuel concentration decreases or the heat loss of the reaction system increases in a flame, the flame temperature decreases. As the flame temperature decreases to a critical temperature, the chain-termination process becomes faster than the chain-branching process and the flame extinguishes. This is the so-called ignition to extinction S-curve (Fig. 1.4) [141–143].

For a given mixture with given initial temperature and pressure, ignition occurs with a time delay. Fig. 3.1 shows an example of a lean n-heptane ignition process at 20 atm and different temperatures. It is seen that for an initial temperature of 1000 K, it takes about 5 ms for ignition (exponential increase in temperature) to occur. This delay time (τ_{ig}) is called the ignition delay time. The ignition delay time is not only affected by temperature and

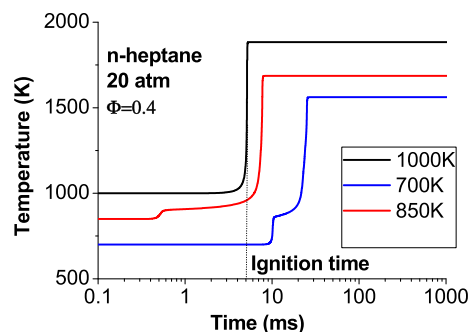


Fig. 3.1. Ignition processes of n-heptane at 20 atm and high (1000 K) and low (700 and 850 K) temperatures.

Table 3Key reactions in plasma assisted $\text{H}_2/\text{O}_2/\text{N}_2$ reaction system.

<i>Chain-initiation</i>	
$\text{H}_2 + \text{O}_2 = \text{HO}_2 + \text{H}$	(R1)
<i>Chain-branching/propagation</i>	
$\text{H} + \text{O}_2 = \text{OH} + \text{O}$	(R2)
$\text{O} + \text{H}_2 = \text{OH} + \text{H}$	(R3)
$\text{OH} + \text{H}_2 = \text{H}_2\text{O} + \text{H}$	(R4)
$\text{HO}_2 + \text{H} = \text{OH} + \text{OH}$	(R5)
$\text{H}_2\text{O}_2 = \text{OH} + \text{OH}$	(R6)
<i>Chain-termination</i>	
$\text{H} + \text{O}_2(+\text{M}) = \text{HO}_2(+\text{M})$	(R7)
$\text{HO}_2 + \text{H} = \text{H}_2 + \text{O}_2$	(R1)
<i>Electron and $\text{N}_2(^*)$ impact dissociation</i>	
$\text{e} + \text{O}_2 = \text{O} + \text{O}(^1\text{D})$	(R8a)
$\text{e} + \text{O}_2^+ = \text{O} + \text{O}$	(R8b)
$\text{N}_2(\text{A,B,C}) + \text{O}_2 = \text{O} + \text{O} + \text{N}_2$	(R9a)
$\text{N}^+ + \text{O}_2 = \text{O}^+ + \text{NO}$	(R9b)
<i>Plasma activated reactions</i>	
$\text{H} + \text{O}_2(^1\Delta_g) = \text{O} + \text{OH}$	(R10)
$\text{O}_3 + \text{O}_2 = \text{O} + \text{O}_2 + \text{O}_2$	(R11)
$\text{O}(^1\text{D}) + \text{H}_2 = \text{OH} + \text{H}$	(R12)
<i>NO catalytic branching</i>	
$\text{NO} + \text{HO}_2 = \text{NO}_2 + \text{HO}$	(R13)
$\text{H} + \text{NO}_2 = \text{NO} + \text{OH}$	(R14)

pressure, but also significantly by the fuel chemistry and the initial level of radicals.

Since hydrogen is the simplest combustion system, we first use hydrogen as an example to understand how the chain-initiation, branching, and termination processes govern the ignition time and explosion limit at different pressure and temperature ranges and to explain how radical production can enhance ignition. Table 3 shows the important chain-initiation, branching, propagation, and termination reactions as well as important plasma generated radical production and NO_x catalytic reactions of H_2/O_2 system. Without plasma, the radicals (e.g., H and HO_2) are initially produced by a slow reaction (R1). After that, one H radical will generate two radicals (OH and O) via the branching reaction (R2). Note that the reaction (R2) has a high activation energy and requires a high temperature (~ 1100 K at 1 atm) to accelerate. Therefore, the produced OH and O radicals quickly generate three H radicals via the chain-propagation reactions (R3) and (R4) (Fig. 3.2, left), leading to an exponential increase in radical concentration for ignition. Therefore, at high temperature, one H radical produces three H radicals via (R1)–(R4) and the ignition delay time is largely controlled by two slower reactions: (R1) and (R2). As such, a small

radical production by plasma significantly shortens the ignition delay time by bypassing the chain initiation reaction (R1).

Fig. 3.2 (right) shows that radical addition into stoichiometric H_2/O_2 mixture at 1000 K reduces ignition delay time. It is seen that only 10 ppm radical addition of H by plasma shortens ignition time by a factor of five because radical addition by plasma bypasses the slowest chain-initiation reaction (R1) and provides the initial radicals directly for branching reaction (R2). In addition, it is interesting to note that atomic O radical addition is more effective than H and OH in a H_2/O_2 system. As seen in Fig. 3.2 (left), this is because adding one OH radical immediately produces one H radical via reaction (R4) since the reaction rate of chain-propagation reaction (R4) is much faster than that of (R2). So OH and H additions are equivalent. However, for one atomic O radical addition, as the reaction (R3) is also faster than (R2), 2H radicals are immediately produced from reactions (R3) and (R4). This is why adding atomic O in a H_2/O_2 system is more effective than adding H and OH for ignition enhancement. Fortunately, non-equilibrium plasma is an effective tool to produce atomic O via electron and excited nitrogen impact dissociation reactions (e.g., (R8a)–(R8c)) [43,148,161].

At lower temperature and high pressure, radical production via branching reaction (R2) is suppressed quickly by the termination reaction (R7) and the reverse reaction of (R1), leading to the occurrence of the second explosion limit [209,210] and a negative burning rate dependence [211] on pressure due to the competition between (R2) and (R7);

$$\frac{k_{-1} + k_5}{2k_{-1}} \frac{2k_2}{k_7[M]} = 1 \quad (3.1)$$

where k is the reaction rate constant and M is the third-body concentration. If pressure further increases, the HO_2 concentration formed by (R7) becomes so high that the reactions (R5) and (R6) become the main branching reaction pathways to produce OH radicals from HO_2 and H_2O_2 . These three different chain-branching pathways at low, intermediate and high pressures lead to the three different explosion limits of the H_2/O_2 system [141–143]. Fig. 3.3 shows that the three different H_2/O_2 explosion limits [212] (red dots (in the web version)) and the successful ignition conditions by plasma [213]. It is seen that without plasma, as discussed above, there are three pressure-dependent explosion limits, low pressure limit, the second explosion limit, and the high pressure limit, controlled by reaction (R2), the competition between reactions (R2) and (R7), and the HO_2 and H_2O_2 branching via (R5) and (R6). It is interesting to note that with a plasma discharge, ignition can occur at a temperature below that of the explosion limit. This is because the radical production by plasma via reactions

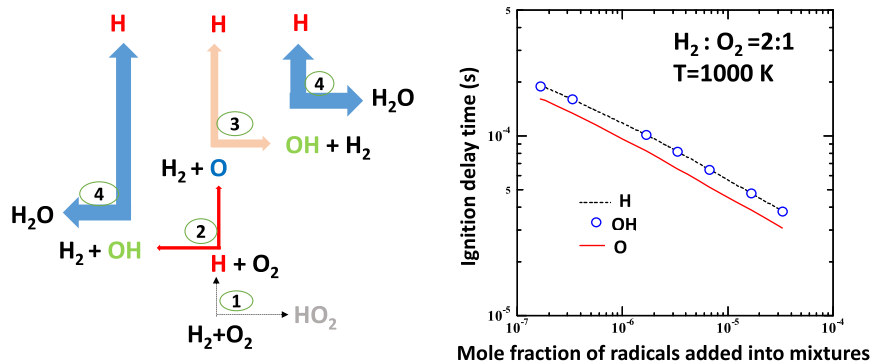


Fig. 3.2. Left: Schematic of the production process of three H radicals from one H radical in the H_2/O_2 chain branching system. The line width here indicates the magnitude of the reaction rate. Right: Ignition delay time decreases with the additions of different initial radicals (H, OH, O) in stoichiometric H_2/O_2 system at 1000 K and 1 atm.

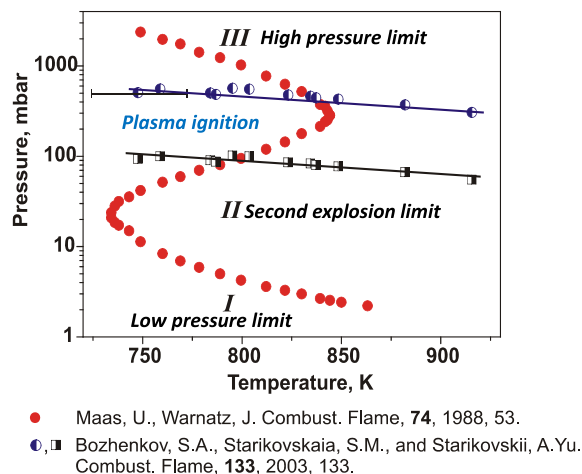
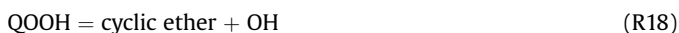
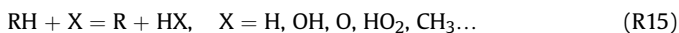


Fig. 3.3. The explosion limits of hydrogen and the ignition conditions by plasma [212,213].

such as (R8) and (R9) in Table 3 breakdown the balance of the chain-branching and termination reactions and thus enhance the chain-branching process.

Moreover, in addition to the radicals at ground states, excited intermediate species and long lifetime species such as $O_2(^1\Delta_g)$, $O(^1D)$ (electronically excited atomic O), O_3 and NO are also produced by plasma, which add new reaction pathways to produce radicals via reactions (R10)–(R14) at much lower temperature than that in (R2). For example, at room temperature, the reaction rate constant of (R10) is about 100 times larger than that of (R2). Therefore, these plasma generated new reaction pathways lead to plasma assisted kinetic enhancement of ignition, especially at low temperature. In addition, if plasma produces NO and NO_2 , the low temperature NO_x catalytic reactions ((R13) and (R14)) can convert inactive radicals such as HO_2 to two OH radicals and thus promote chain-branching reactions and extend ignition limit [138,139]. Details of plasma kinetic enhancement of ignition will be discussed in Section 4.

For large molecule hydrocarbon fuels, the ignition and ignition chemistry become more complicated than for hydrogen. As seen in Fig. 3.1, for n-heptane at 20 atm and initial temperatures of 850 K and 700 K, there are two ignition delay times, a low temperature ignition ($\tau_{ig,LTI}$) and a high temperature ignition ($\tau_{ig,HTI}$). The low temperature chain-branching for radical production (OH) and ignition is mainly caused by the reactions such as [7,24,214,215],



Note that at a low temperature condition, the H abstraction reaction (R15) is very slow because of the extremely low concentration of radicals (X) (e.g., less than 100 ppb). Therefore, (R15) is a limiting step to produce initial hydrocarbon radicals (R). Reactions (R17) and (R19) are the other two limiting reactions to form QOOH and O_2QOOH for radical production. Since (R18) only produces one

OH radical but (R20) produces two OH (branching), the branching ratio of (R18) and (R19) affects the low temperature reactivity significantly. Moreover, the unimolecular decomposition reactions of (R16)–(R20) are all pressure dependent. Therefore, the low temperature ignition has strong pressure dependence.

After low temperature ignition, at an intermediate temperature (800–950 K as seen in Fig. 3.1), the chain branching process via (R6) accelerates in the products of low temperature ignition (via (R15)–(R20)) and leads to the transition to high temperature ignition (HTI). This process is dominated by the temperature dependent reaction (R6), and thus is very sensitive to the concentrations of HO_2 and active radicals (X) as well as the heat release rate. Any external radicals and heat addition will accelerate the transition to high temperature ignition via the key reactions at intermediate temperature ((R21)–(R24), and (R6)),



Due to the distinctive fuel oxidation pathways in low, intermediate, and high temperatures, a typical ignition delay time dependence of a stoichiometric n-heptane/air mixture on temperature and pressure of n-heptane is shown in Fig. 3.4 [216]. It is seen that at the negative temperature coefficient (NTC) region, where the ignition delay time decreases first and then increase with the increase in temperature, the ignition time at low temperature can be much shorter than that of high temperature ignition. In addition, the increase in pressure reduces the ignition delay time.

In the fuel rich condition, in addition to the reaction pathways of R8–R14, the following direct impact dissociation by electron, excited molecules, and ions [217] with fuel molecules in plasma discharge,

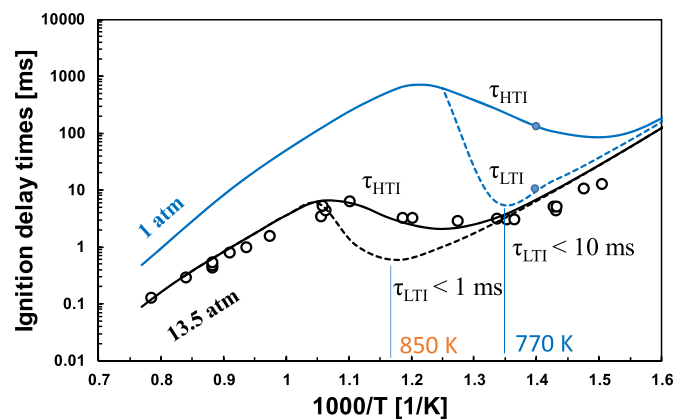
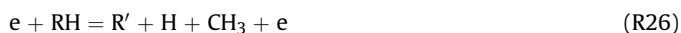
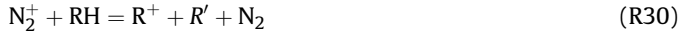


Fig. 3.4. Dependence of low and high temperature ignition time of a stoichiometric n-heptane–air mixture on temperature at 1 atm and high pressure, solid line: 2nd stage ignition, dashed line: 1st stage ignition [216].



also produce additional small and large hydrocarbon radicals to further accelerate reactions of (R15) to (R20), and (R21)–(R23) at low and intermediate temperature ranges.

Note that the plasma reaction pathways are strongly electron temperature or reduced electric field (E/N) dependent. Fig. 3.5 shows an example of the variation of rate constant and reaction flux as a function of the reduced electric field for reaction (R8a) in comparison with the rate constants and reaction fluxes of important chain-branching and propagation reactions ((R1)–(R3) and (R6)). It can be seen that the rate constant of the electron impact reaction is much larger than that of the important radical chain-branching and initiation reactions as shown in Fig. 3.5(a). However, the combustion process is determined by the reaction flux of different reactions [218], not the rate constant. The reaction fluxes of the same reactions are shown in Fig. 3.5(b). In the calculation of reaction flux, the pressure is assumed to be 1 atm. The electron number density is fixed at $5 \times 10^{11} \text{ cm}^{-3}$. In order to mimic a typical flame environment of hydrocarbon fuel, both atomic O and H are fixed at $4.9 \times 10^{15} \text{ cm}^{-3}$ (approximately 200 ppm at 300 K, 1 atm), O_2 concentration is 19%, H_2 concentration is 0.5%, and H_2O_2 concentration is 500 ppm. During the calculation, regardless of the increase of temperature, the number density of e , atomic O and H are held constant. It can be seen from Fig. 3.5(b) that at low temperature conditions ($T < 1000 \text{ K}$), the electron impact reaction (R8a) is much faster than (R2) and (R6) to produce radicals. Especially, a larger difference in fluxes in (R8a) and (R6) than that of in (R8a) and (R2) suggests that the plasma assisted combustion will have more impact in the intermediate and low temperature branching process. Note that when temperature is higher than 1000 K, the conventional chain branching reaction (R2) starts to dominate the radical production process. Therefore, the plasma effect at temperature above 1000 K is more thermal or bypassing the chain-initiation reaction (R1) than kinetic enhancement.

As discussed above, plasma can kinetically shorten the ignition delay time at low, intermediate, and high temperature, in different

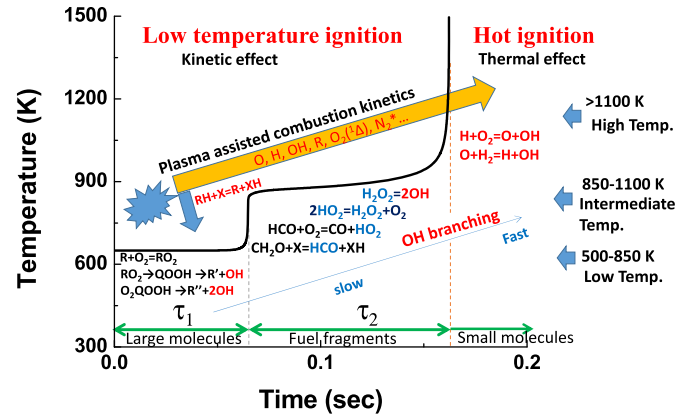


Fig. 3.6. Schematic of kinetic and thermal enhancement pathways of plasma assisted combustion for liquid fuels at high, intermediate, and low temperature, respectively.

ways. At low temperature, a plasma discharge will produce new pathways (R8)–(R14) to form active radicals to accelerate reaction (R15) for the radical branching reaction of (R20). At intermediate temperature, the production of radicals and heat will dramatically enhance the transition from low temperature ignition to high temperature ignition via reaction (R6). As seen in Fig. 3.5(b), at temperature above 1100 K, the plasma assisted combustion enhancement becomes more like thermal effect. Moreover, Fig. 3.5 suggests that the plasma kinetic enhancement effect is much greater at low temperature than that at higher temperature.

To summarize the kinetic effect of plasma discharge on low, intermediate, and high temperature ignition for large hydrocarbons, Fig. 3.6 shows schematically the major reaction pathways of plasma assisted ignition and combustion at different temperature ranges. It is important to bear in mind that (at high temperature) when the temperature is above the critical temperature of the branching reactions ((R2) and Eq. (3.1)), the major role of plasma is thermal enhancement because the branching rate of (R2) is very high. The kinetic effect of plasma chemistry on ignition is much greater at low and intermediate temperatures to promote branching reactions (R6) and (R20). In fact, in recent experiments of plasma assisted combustion by using nanosecond discharge and ozone addition, plasma activated low temperature ignition and cool flames [107,108] were observed even at 1 atm at 550 K with flow residence time less than 10 ms, which is impossible without plasma discharge.

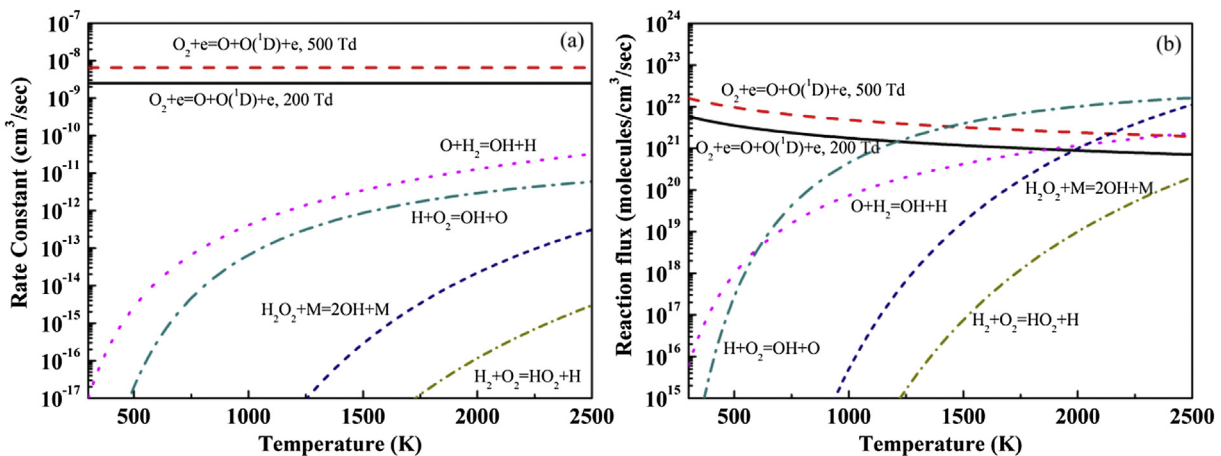


Fig. 3.5. Rate constants (a) and reaction flux (b) for reactions for dissociation by electron impact at electric field values equal to 200 Td and 500 Td and chain branching reactions.

3.2. Dynamics, chemistry, and transport of plasma assisted flame propagation

A flame is an exothermic self-propagating, thermal diffusion driven auto-ignition front. The burning velocity of a premixed flame is a function of fuel oxidation chemistry, transport properties, adiabatic flame temperature, and heat and mass losses. On one hand, a radical or heat loss from the flame decreases the flame speed or can even quench the flame. On the other hand, if external energy and/or radicals are added by plasma to the flame, the flame speed increases and its propagation limit broadens. In order to understand how the plasma produced thermal, kinetic, and transport effects affect flame speed and the lean burn limit, it is necessary to understand how flame speed and lean burn limit depend on these processes.

The lean burn limit or flammability limit is defined as the lowest equivalence ratio at which a one-dimensional, stretch free planar flame can propagate. The theoretical and experimental determination of the limits have been conducted for several decades [141–143,219,220]. It has been concluded that the radiation heat loss from the flame is the cause of the flammability limit [221–223]. The flame speed with radiation heat loss normalized by the adiabatic flame speed as a function of heat loss (H) normalized by the total chemical heat release rate of the fuel mixture (proportional to fuel concentration) is given as [224],

$$U^2 \ln U^2 = -\beta H \quad (3.2)$$

where β is the activation energy (E_a) normalized by the ratio of the temperature difference between the adiabatic flame temperature (T_{ad}) and the unburned gas temperature (T_u) to the product of universal gas constant R_0 and the square of T_{ad} ,

$$\beta = \frac{E_a(T_{ad} - T_u)}{R_0 T_{ad}^2} \quad (3.3)$$

As shown in Fig. 3.7, with the increase in normalized heat loss (H) (or the decrease in fuel concentration), the flame speed decreases. At $\beta H = e^{-1}$, the normalized flame speed reaches a critical value ($e^{-1/2}$), beyond which a leaner mixture (larger H) is not flammable (no flame speed exists). This critical limit (fuel lean concentration) is the so-called flammability limit. From the definition of βH in Eqs. (3.2) and (3.3), for a given heat loss rate, both the activation energy and the heat release from the fuel affect the flammability limit. Note that a flame heat release rate is governed by high temperature chain-branching process such as reaction R2, which is exponentially dependent on temperature. The global activation energy in Eq. (3.3) is largely determined by the activation energy of reaction (R2). Therefore, for flame propagation speed and

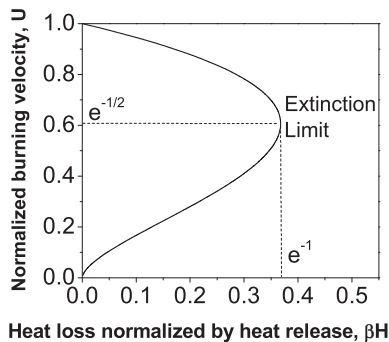


Fig. 3.7. The dependence of the normalized burning velocity on the normalized radiative heat loss of a one-dimensional planar flame [199].

flammability limit, the thermal effect of plasma is greater than the non-equilibrium kinetic effect. This is why as shown in Figs. 2.15 and 2.16, at the same temperature non-equilibrium plasma can barely change the flame propagating speed and the lean burn limit kinetically. This means that we should not expect the plasma kinetic effect alone without the increase of temperature to significantly enhance flame speed and flammability limit of a high temperature flame because the radical production rate by plasma at flame temperature is slower than that by the chain-branching reaction (R2) at the same temperature (Fig. 3.5(b)).

Nevertheless, flame propagation speed and flammability limit can be changed significantly by the transport process which modifies the peak flame temperature and the reaction rate of (R2). For example, a methane/air mixture has a flammability limit near $\Phi = 0.5$. However, the microgravity experiments and computations [223,225] showed that the flammability limit of methane is much lower than $\Phi = 0.5$ if there is a flow velocity gradient (the stretch rate). Fig. 3.8 shows the computed G-curve [223] indicating the extinction limits and flammability limit of premixed counterflow methane/air flames. It is seen that without flow stretch (velocity gradient), the flammability limit of methane is $\Phi = 0.50$ (point E). However, with a stretch rate around 10 s^{-1} , the lean flammability limit becomes $\Phi = 0.42$, which is much lower than the flammability limit of flame without a velocity gradient. This extension is caused by the thermal effect of preferential diffusion or the Lewis number effect, that is, a lighter fuel molecule such as methane can diffuse faster into the reaction zone than the heat lost by the thermal diffusion from the flame. In this case, if the total stretch rate of the flame (flow velocity gradient) is not large, the normalized flame speed of Eq. (3.2) can be given as [226],

$$U^2 \ln U^2 = -\beta H - \beta (Le - 1) Ka \quad (3.4)$$

where Le is the Lewis number and Ka is the Karlovitz number (the flame stretch rate normalized by the thermal diffusion timescale). Therefore, if Le is less than unity and the stretch rate is positive, Eq. (3.4) shows that the flame speed will increase with flame stretch until there is not enough time for combustion to occur. This is why the flammability limit shown in Fig. 3.8 is extended for methane/air mixture if there is a flow stretch ($Ka > 0$). For hydrogen whose Lewis number is even smaller, the extension of flammability limit by flow

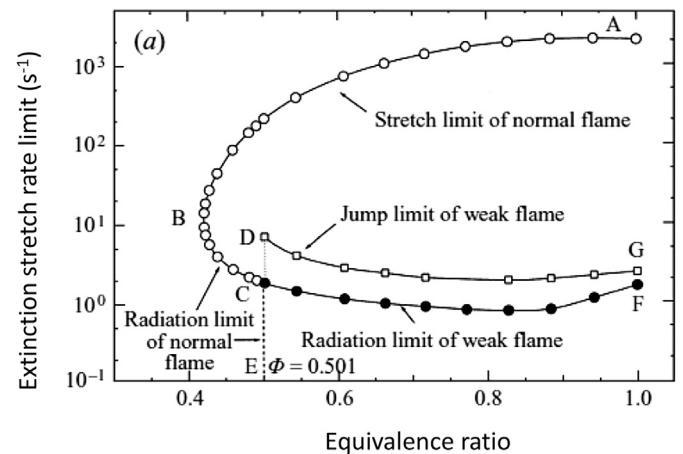


Fig. 3.8. The G-shaped flammability diagram showing the flammable region of unstretched and stretched premixed methane–air flames. E: the flammability limit of an unstretched flame; B: the flammability limit of stretched flames; AB: the stretch extinction limit; BC: the radiation extinction limit. CE: the extinction limit of weakly stretched flames [223].

stretch is significant [227]. Therefore, as shown in Fig. 1.4, if plasma can reduce the fuel Lewis number, it will be able to reduce the flammability limit.

How does plasma discharge affect flame speed and the flammability limit? The flame speed dependence on plasma effects (parameters with superscript of $*$) can be given as following,

$$U^2 \ln U^2 = -\beta^* H + \beta^* Q^* - \beta^* (Le^* - 1) Ka^* \quad (3.5)$$

Firstly, plasma will reduce the global activation energy from β to β^* by creating radicals and new reaction pathways (e.g., reactions (R8)–(R14) and (R24)–(R28)) at high temperature to increase the flame speed. Note that this increase will only be modest because the plasma radical production rate at flame temperature is much slower than that of (R2). Secondly, plasma discharge like microwave can deposit additional heat (Q^*) to the flame and accelerate the flame speed. This thermal effect is very important because the chain branching rate of (R2) is strongly temperature dependent. Thirdly, plasma can lower the effective fuel Lewis number from Le to Le^* in Eq. (3.5) by dissociating or reforming the large fuel molecules to lighter ones such as H_2 , CH_4 , CH_2O , and C_2H_4 so that the flame speed increases. This effect is also large because it increases the flame temperature directly via the transport effect. Finally, plasma will also be able to change the local flow field of the flame and modify the flame stretch to Ka^* . This effect can be twofold depending on the effective Lewis number (Le^*) and whether the flow stretch is positive or negative. In addition, the plasma modified local flow field can increase the mixing between the burned product and unburned mixture and thus enhance the flame speed thermally (like heat recirculation). The above four effects can explain most of the flame speed enhancement by plasma. However, keep in mind that for flames the kinetic enhancement on flame speed and flammability limit is much less effective than the thermal effect and that on ignition.

To summarize the discussions of kinetic, thermal, and transport enhancement effects by plasma on ignition and flame propagation, Fig. 3.9 shows a schematic of plasma activated low temperature ignition as well as flame regime transition for a liquid fuel with low temperature chemistry. Without plasma, the conventional ignition to extinction curve (I) shows three different combustion regimes: the high temperature combustion (HTC), intermediate temperature combustion (ITC), and low temperature combustion (LTC). The low temperature ignition limit ($\tau_{ig,LTC}$), intermediate temperature ignition limit ($\tau_{ig,ITC}$), and the extinction limit separate these three different flame regimes. Note that due to the difference in the rates of chain-branching reactions in LTC (R20), ITC (R6), and HTC (R2),

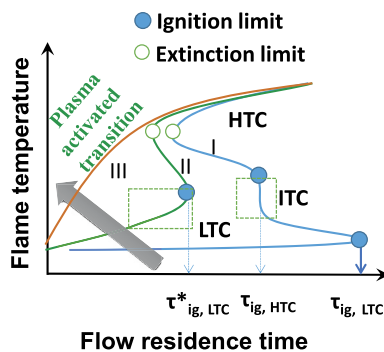


Fig. 3.9. Plasma activated low temperature ignition and flame regime transition from the conventional S-curve (I: no plasma) with separated ignition and extinction limits to a smooth ignition to flame transition curve without extinction limit (III: strong plasma kinetic effect). HTC: high temperature combustion, ITC: intermediate temperature combustion, LTC: low temperature combustion.

the kinetic enhancement effect of plasma discharge is different for different combustion regimes in the order of:

$$\text{Kinetic effect of LTC} > \text{Kinetic effect of ITC} > \text{Kinetic effect of HTC} \quad (3.6)$$

As a result, with a non-equilibrium plasma discharge, the flame curve II in Fig. 3.9 shows that the low temperature ignition, $\tau_{ig,LTC}$, is enhanced much greater than that of the intermediate temperature combustion (ITC) and leads to a new broadened plasma activated LTC branch. Note that the timescale of $\tau_{ig,LTC}^*$ with plasma activation is much shorter than $\tau_{ig,LTC}$ without plasma, allowing us to observe plasma activated cool flames in our recent experiments [107,108]. If plasma discharge increases its intensity further by producing more radicals, the low temperature ignition time of $\tau_{ig,LTC}^*$ on curve II further decreases so that it is shorter than the characteristic time of flame extinction. As a result, the classical S-curve with separated ignition and extinction limits becomes a monotonic curve. This monotonic dependence is the so called stretched S-curve without an ignition limit. The transition from the classical ignition S-curve to the monotonic transition curve without extinction limit has been experimentally demonstrated by Sun et al. with nanosecond plasma discharge [107,144]. As seen in Fig. 3.9, non-equilibrium plasma has a much lesser enhancement effect on the flame extinction limit and flame speed than that on the ignition limit. In order to significantly enhance flame stabilization and lean burn limit, a combination of thermal effect with kinetic effect is necessary. The above conclusions and the experimental evidence are important to design energy efficient plasma assisted combustion engines.

3.3. Dynamics, chemistry, and transport of flame initiation and minimum ignition energy and the role of plasma discharge

In Sections 3.2 and 3.3, we discussed the dynamics and chemistry of plasma assisted ignition and flame propagation, respectively. In many unsteady combustion process such as the internal combustion engines and PDE engines, a plasma initiated ignition process involving unsteady transition from spark ignition to propagating flame is required. In these processes, one of the main questions is: 1) When will ignition be successful? 2) What is the minimum ignition energy? and 3) How can we accelerate the transition process? This process is neither an auto-ignition process nor a flame propagation speed process. Rather it is an unsteady flame initiation process. In order to understand how plasma can enhance flame initiation, we need to understand what physical and chemical processes govern a successful flame initiation.

The measurements of the minimum ignition energy by a spark plug goes back to earlier work of Lewis and Von Elbe [219,228,229]. It was shown that the minimum ignition energy (MIE) increased at both lean and rich sides and had the minimum near the stoichiometric condition. Moreover, the fuel molecule size and diluents also affected the MIE. However, it was not until recently that the mechanism of the MIE has been understood theoretically and experimentally [116,196,230,231]. These studies have showed that a successful flame initiation is governed by a critical flame initiation radius, that is, only the spark which can drive the flame kernel to a size greater than this critical flame initiation radius, can cause successful ignition.

Fig. 3.10 shows the predicted trajectories of the normalized flame speed U (normalized by the adiabatic planar flame speed) of a spherical flame kernel propagating outwardly with different energy depositions (Q , the normalized ignition power given by $\bar{Q}/[4\pi\bar{\lambda}\bar{\rho}_f^0(\bar{T}_{ad} - \bar{T}_\infty)]$ where \bar{Q} is the ignition power, $\bar{\lambda}$ is the thermal

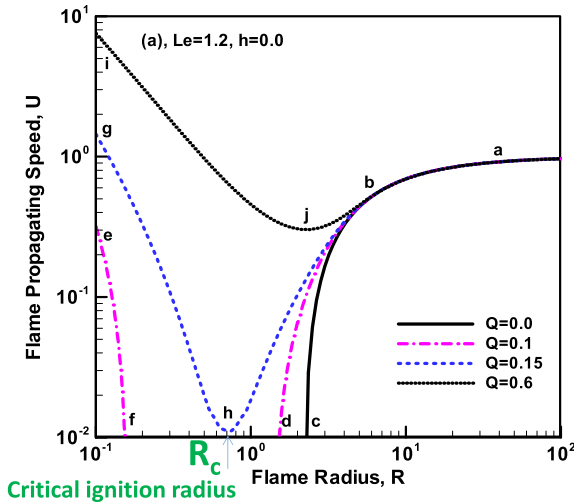


Fig. 3.10. Theoretical prediction of the trajectories of normalized flame speed of a spherical flame kernel initiated by different external energy (Q) as a function of the normalized flame radius by flame thickness for $Le = 1.2$ [116].

conductivity, δ_f^0 is the flame thickness, \tilde{T}_{ad} is the adiabatic flame temperature, \tilde{T}_∞ is the temperature of unburned mixture) in the center of a quiescent mixture of a spherical chamber. It is seen that if there is no energy deposition ($Q = 0$), flame cannot exist at a normalized radius (R , the normalized flame radius by the flame thickness) below $R = 2.5$ (point c) due to the stretch by flame curvature. When a small normalized energy ($Q = 0.1$) is added, a flame kernel is initiated from the center and its flame speed decreases so quickly that the flame kernel extinguishes at location f before it can reach the self-propagating flame branch starting at d . As a result, the flame initiation fails. When the ignition energy is increased to $Q = 0.15$, it is seen that the inner flame kernel trajectory (gh) and the outside propagating flame trajectory (hb) merges at location h where the flame kernel flame is the minimum. As the flame kernel propagates further outwardly, the flame speed increases as the flame radius approaches to infinity. Therefore, a successful ignition initiation is achieved. For any larger energy deposition (e.g., $Q = 0.6$), successful ignition is always achieved. Therefore, the minimum ignition energy of this mixture is $Q = 0.15$ and the critical flame initiation radius is $R = R_c$ (radius at point h). In other words, the minimum ignition energy is the energy required

for a spark to drive the initial flame kernel to reach the critical flame initiation radius (R_c). Note that here R_c is normalized by the flame thickness, which is function of pressure. Therefore, the critical flame initiation radius depends on pressure as,

$$R_c \sim P^{-n/2} \quad (3.7)$$

Therefore, the higher the pressure, the smaller the dimensional critical flame radius and the lower the minimum ignition energy. Eq. (3.7) has a special implication to plasma assisted ignition, that is, a good plasma igniter needs to create an ignition size larger than R_c to not deposit more energy. This result supports the observation of ignition enhancement by microwave, gliding arc, and corona discharge in internal combustion engines and PDE engines because they all produce a larger ignition kernel than a spark at the same energy deposition. In addition, when the fuel mixture becomes leaner, the flame thickness increases due to the decrease in flame speed. As shown in Fig. 3.10, the critical flame radius for a leaner mixture increases and thus a larger minimum ignition energy is required to create a larger ignition kernel size than R_c .

Recently, the critical flame initiation radius was measured for hydrogen and other hydrocarbon fuels [230,231]. Fig. 3.11 shows the results of the flame propagation speed relative to the burned gas as a function of time (flame radius) for a lean n-decane/air mixture. It is seen that similar to the theoretical results in Fig. 3.10, the flame kernel speed decreases first then reaches a minimum, and finally increases back to the adiabatic flame speed as it propagates outside. The measured critical flame radius at 1 atm is as large as 1.4 cm for n-heptane. That means to ignite a lean n-heptane mixture at 1 atm we need a plasma igniter which can generate a flame kernel with radius as big as 1.4 cm. Fortunately, at fuel rich conditions, the critical radius decreases significantly due to the decrease in the mixture Lewis number for large hydrocarbon fuels. In addition, the critical radius decreases with the increase in pressure. These conclusions explain why the ignition enhancement decreases both in fuel rich condition as in Fig. 2.15 and at higher pressure as in Fig. 2.16.

Fig. 3.12 shows the dependence of the minimum ignition power (Q) on R_c^3 for different mixture Lewis numbers. It is seen that the minimum ignition power is linear to R_c^3 . That means R_c is an appropriate measure of the minimum ignition energy. In addition, it is seen that the minimum ignition energy depends monotonically on the mixture Lewis number. The larger the Lewis number, the larger the minimum ignition energy. This is why ignition is always

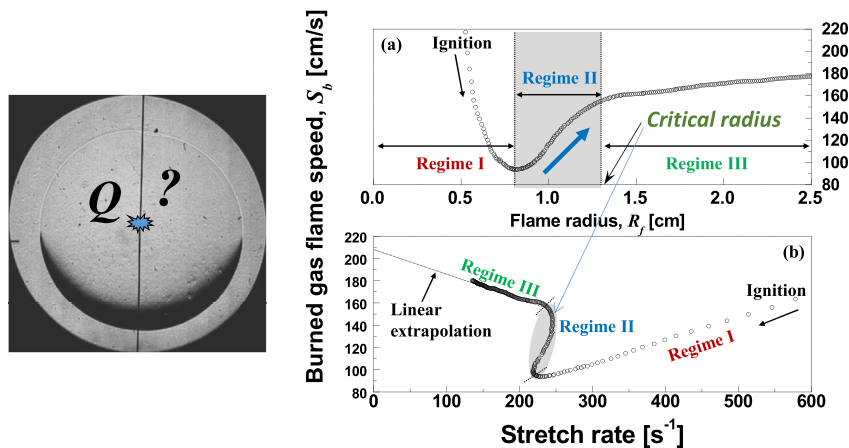


Fig. 3.11. The dependence of flame speed relative to the burned gas as a function of flame radius and stretch rate of n-decane/air ($\Phi = 0.7$) at 1 atm ignited at the center of a spherical bomb [231]. The critical radius is defined at the location of the minimum flame speed.

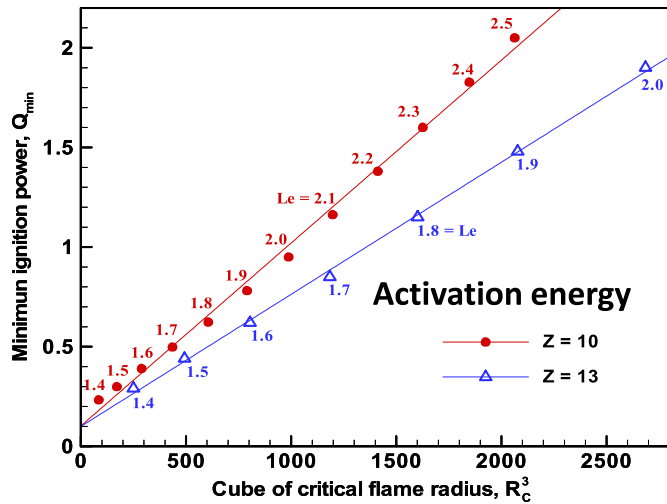


Fig. 3.12. Dependence of the minimum ignition power on critical flame initiation radius (R_c^3) for different mixture Lewis numbers (Le) and activation energies (Z) [116].

more difficult in IC engines when the mixture is lean (large Le) but is easier at fuel rich conditions (small Le). Fig. 3.12 also shows that the activation energy (Z) affects the minimum ignition energy as well, implying that plasma can change the chemistry and reduce the MIE kinetically.

What is the implication of Figs. 3.10–3.12 to plasma assisted ignition in engines? In summary, plasma can help engine ignition in the following ways: 1) Non-equilibrium plasma can be used to generate a larger discharge volume than the critical radius (R_c) to enhance ignition. 2) Plasma can dissociate or reform the large fuel molecules to smaller ones so that the mixture Lewis number becomes smaller and the critical radius is smaller; 3) Plasma can reduce the activation energy of fuel oxidation to reduce the flame thickness and the critical radius; and 4) plasma can increase the temperature so that the flame thickness decreases, leading to a smaller dimensional critical flame initiation radius. In fact, recent theoretical studies by Chen and coworkers confirmed these conclusions [232].

3.4. Plasma assisted ignition by creating a large discharge volume

In order to create a large ignition kernel, different discharges and their combinations have been used to enhance ignition and ignition to flame propagation. Recently, Wang et al. have developed a microwave ignition system in a constant volume cylinder chamber with high speed imaging [71] (Fig. 3.13). The results showed that compared to a spark igniter, pulsed microwave energy deposition (50 mJ) in 2 ms is able to achieve successful ignition of

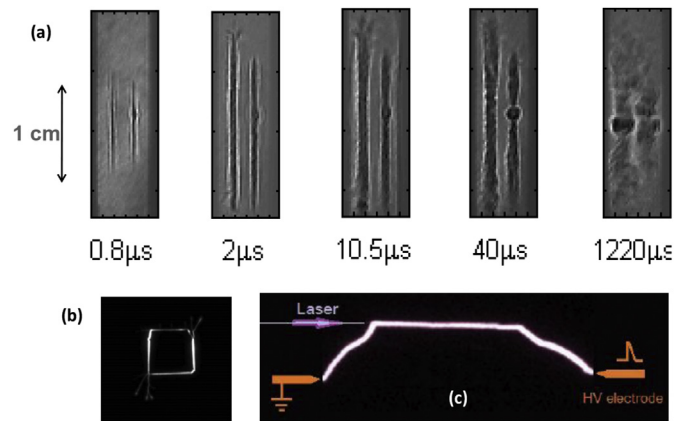


Fig. 3.14. (a) Schlieren images shows development of two parallel lines with the effect of a 2 s, 50 mJ microwave pulse for heating of 500 J, 200 fs laser pulse at 800 nm seed laser. (b) A square pattern created by microwave coupling with laser beams [234], (c) laser guided gliding arc control [235].

methane/air mixtures in much leaner conditions between 1 and 10 atm. At the same time, the results also showed that when both a spark plug (60 mJ) and pulsed microwave igniter are able to ignite the mixture, the flame propagated speeds are similar. The results confirmed the discussions in the previous sections that it is important for plasma to produce a large ignition kernel size greater than the critical radius to enhance ignition. Moreover, a large ignition kernel created by a pulsed microwave discharge can enhance ignition to flame transition, while not enhancing flame speed or lean burn limit.

To further increase the ignition volume, ignition pattern formation by multi-laser beam guided microwave discharge was investigated [233–235]. As shown in Fig. 3.14(a), by using two parallel laser beams generated by low energy 150–200 fs seed laser pulses and an overlapping subcritical microwave pulse, the extremely weak ionization in the parallel laser beams localizes the microwave energy deposition and creates a larger ignition volume. Fig. 3.14(b) shows that by using a similar technique, a well-designed square ignition pattern can be formed. In Fig. 3.14(c), by using the combination of laser ionization and a gliding arc, the gliding arc trajectory can be controlled. The controlled ignition pattern formation provides an innovative way to enhance ignition by creating an ignition kernel larger than the critical flame initiation radius.

Another way to create a large ignition volume is to use a gliding arc [38,82,89,111]. Recently, the dynamics of gliding has been studied by using high speed imaging and OH LIF imaging [111,236]. Fig. 3.15 (left) shows the time-resolved observation of gliding arc short cutting events and the dependence of emission intensity on time. It is seen that as a new pathway was formed at 50 μs at the



Fig. 3.13. Microwave assisted ignition in a cylindrical chamber. Left: electrode and resonator, Middle: direct picture of experimental device; and Right: microwave assisted ignition and flame propagation [71].

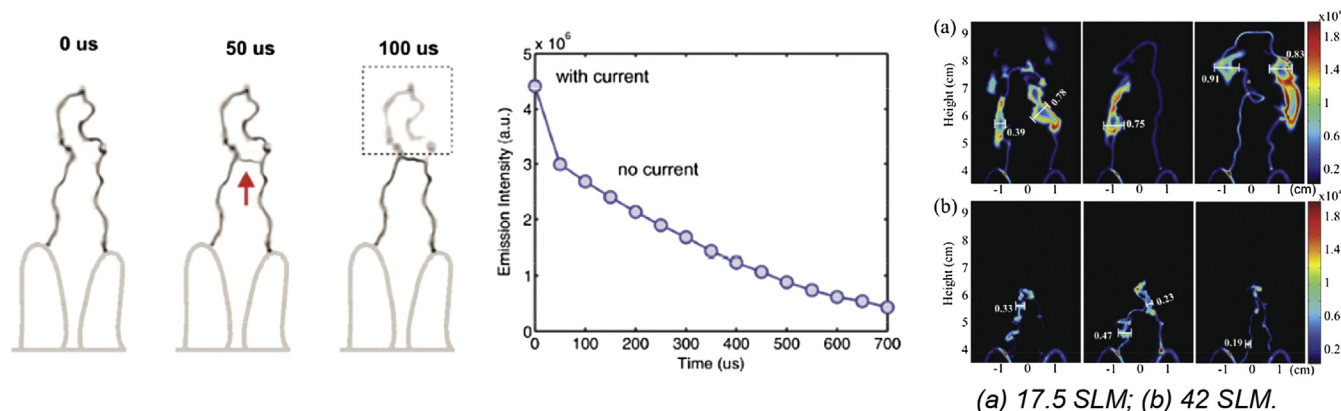


Fig. 3.15. Left: time resolved gliding arc imaging and emission intensity measurements; Right: three typical single-shot OH-PLIF images obtained using an exposure time of 2 μ s, showing the OH distributions and arc emission at two flow rates (a) 17.5 SLM, (b) 42 SLM [237]. The typical thickness of the OH distribution is labeled in the images with unit of centimeters [236].

upstream of the gliding arc, the luminescence intensity of downstream gliding arc decreased. The decay time was in the order of 500 μ s, comparable to the ignition delay time of n-heptane at 1100 K. The long decay time of a large short-cutting gliding arc can contribute to ignition enhancement of a large volume. Fig. 3.15 (right) shows the dependence of OH PLIF on the flow rate. It is seen that with the increase in flow rate, large scale (~ 0.5 –1 cm) distributed OH formation zones were observed. Although the mechanism of the formation is still under-investigation, the large scale OH distributions suggest that a gliding arc at turbulent flow can enhance ignition by creating large ignition kernels.

More recently, ignition and mixing enhancement using arc instability has also been studied [237,238]. As shown in Fig. 3.16, a short pulse high voltage discharge can produce flow turbulence via different mechanisms in a high speed flow, which include local superheating of the gas; discharge-induced shock wave, photo-dissociation and photo-ionization; and unsteady artificial separation inflow in disturbed zone [238]. The large unstable flow structures and the local heating, photoionization, and fuel oxidation will enhance ignition initiation and fuel/air mixing.

With the fundamental mechanisms of plasma enhanced combustion appropriately understood, one of the most important things is to understand how plasma can reduce activation energy of fuel oxidation, deposit energy to mixture, decompose fuel and reduce the mixture Lewis number, and model the discharge

dynamics. This requires fundamental studies of plasma combustion chemistry with advanced diagnostics in well-defined flame geometries to isolate the complicated couplings between different mechanisms.

4. Kinetic studies of plasma assisted combustion using idealized experiments

With the development of plasma technology and advanced laser diagnostics, significant progress has been made in developing new experimental platforms and diagnostic techniques for plasma assisted combustion and in understanding the underlying enhancement mechanisms of the plasma assisted combustion (Fig. 1.3). This section reviews the recent progress in the study of kinetic effects of non-equilibrium plasma on different combustion phenomena, including ignition, extinction, and flame propagation.

4.1. Kinetic process in plasma discharge

In 2001, the first work using nanosecond pulsed discharge to assist H_2 oxidation was published by Starikovskaia et al. [239]. The kinetic process of H_2 oxidation in a stoichiometric H_2 /air mixture activated by nanosecond pulsed discharge was studied at total pressures between 1 and 8 Torr and ambient temperature. The discharge device consisted of a quartz tube of length 200 mm and diameter 47 mm with a high voltage plate electrode and a ringed low voltage electrode with surfaces made of aluminum. Impulses of negative polarity voltage of amplitude 13 kV, 25 ns duration at FWHM with repetition frequency of $f = 40$ Hz. The transition radiation of H_2 ($3\sigma_g^+ \rightarrow b3\sigma_u^+$) was used to reconstruct the absolute concentration of excited H_2 in the mixture and compared with that with numerical modeling. Reasonable agreement was reported. Numerical modeling was further conducted employing a kinetic scheme consisting of about 750 species and 8700 reactions for H_2 /air mixtures.

Fig. 4.1 summarized the modeling results for every time interval for the rapidest channels of chemical conversions. In Fig. 4.1, the thickness of the arrow and the number near it correspond to the process rate, and exfoliation of the chemical component's frame reflects its variation for this period of time. The dynamics of this component number density at a specified time interval was shown as a layer-by-layer increase or decrease of the associated field. (1) The rapidest process for the first 10^{-7} s after the pulse was the dissociative quenching of the $N_2(B^3\Pi_g)$ by O_2 with the formation of atomic O. Next in the hierarchy was the reaction of H_2^+ conversion

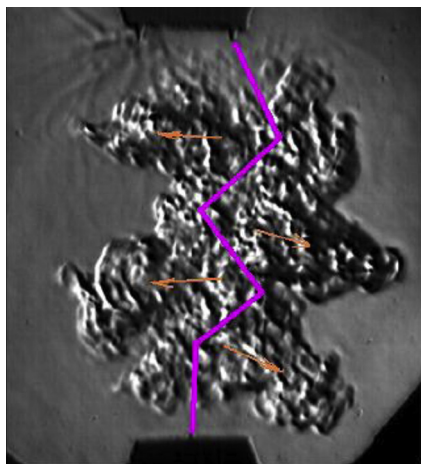


Fig. 3.16. Arc produced flow instability and jets [238].

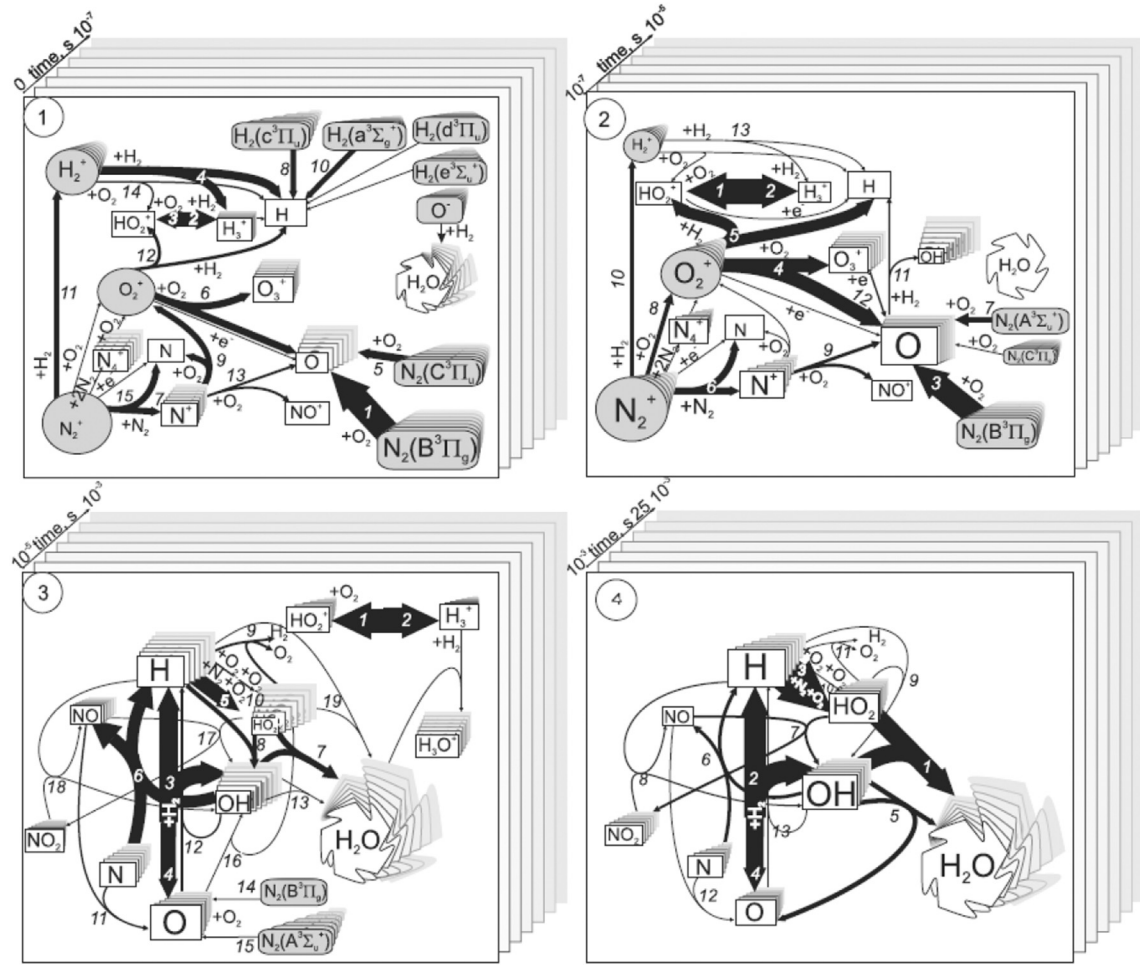


Fig. 4.1. Diagrams of active particle flows (1) time interval $\tau = 0-1 \times 10^{-7}$ s, (2) $\tau = 1 \times 10^{-7}-1 \times 10^{-5}$ s, (3) $\tau = 1 \times 10^{-5}-1 \times 10^{-3}$ s, (4) $\tau = 1 \times 10^{-3}-25 \times 10^{-3}$ s [239].

into H_3^+ and H. However, the contribution to atomic H production was limited due to the low concentration of H_2^+ . The main channel of H_2O formation was the H_2 reaction with O^- ion that was formed through the reaction $\text{O}_2 + e \rightarrow \text{O} + \text{O}^-$. (2) The number density of atomic O increased due to the dissociative quenching of $\text{N}_2(\text{B}^3\Pi_g)$ and $\text{N}_2(\text{A}^3\Sigma_u^+)$. Further production channels of atomic O included the destruction of O_2^+ . As the atomic O accumulation took place, it began to convert into H and OH in the reaction with H_2 . (3) The branching reaction $\text{O} + \text{H}_2(v=1) \rightarrow \text{H} + \text{OH}(\tau=1)$, along with the reverse process, was predominant up to the start of the next pulse, being the main step of the water formation chain. Nitrogen in metastable state $\text{N}_2(\text{A}^3\Sigma_u^+)$, in the reaction of dissociative quenching by O_2 , produced atomic O into the system. As a result of the tri-molecular reaction (R7) produced HO_2 and H_2O_2 via (R6). H_2O formation from HO_2 reacting with OH was observed. (4) At the final stage H and OH was formed via reaction (R3). Moreover, using the kinetic modeling, the kinetic involvement of atomic N and NO_x was identified. This study demonstrated that atomic O production is a very important kinetic process in plasma assisted combustion.

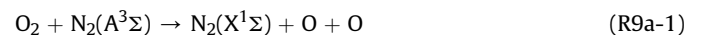
To understand the reaction pathways of atomic O production, Uddi et al. [160] conducted atomic O measurement in a rectangular shaped quartz reactor with nanosecond pulsed discharges using the Two Photon Laser Induced Fluorescence (TALIF) technique. The time histories of the absolute concentrations of atomic O were measured in CH_4/air and $\text{C}_2\text{H}_4/\text{air}$ mixtures after excitation of a single 25 ns discharge pulse with peak voltage 20 kV. Fig. 4.2 shows

the experimental results of time-dependent atomic O mole fractions generated by a single pulse discharge in air and CH_4/air mixture at $P = 60$ Torr. The peak mole fraction in air at 60 Torr is approximately 0.5×10^{-4} , with decay occurring on a time scale of about 2 ms. Peak mole fraction in a stoichiometric CH_4/air mixture was found to be nearly the same to that in pure air, but the rate of decay was faster by a factor two to three. In $\text{C}_2\text{H}_4/\text{air}$ mixture at $\Phi = 0.5$, the peak atomic O concentration was reduced by a factor of approximately four, compared to pure air, and the rate of decay increased by approximately two-orders of magnitude due to the greatly increased reaction rate of atomic O with C_2H_4 compared to with CH_4 at room temperature. The results in $\text{C}_2\text{H}_4/\text{air}$ mixture are shown in Fig. 4.3.

The experimental results were further compared with numerical modeling with GRI Mech 3.0 [240] for CH_4 and USC Mech II [241] for C_2H_4 , respectively, with combination of an air plasma model [160]. Excellent agreement was reported for both mechanisms. The numerical modeling also indicated that the primary formation pathways of atomic O were from electron impact reaction,



during the discharge and by collisions of electronically excited N_2 with O_2 for times up to $\sim 10 \mu\text{s}$ after the pulse,



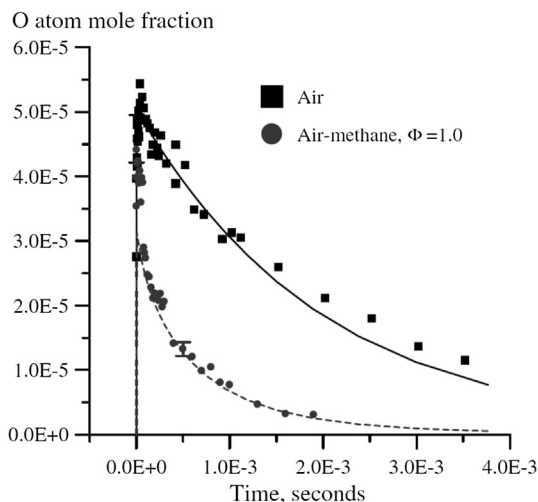


Fig. 4.2. Atomic O mole fraction vs. time after a single high voltage pulse in air and CH₄/air mixture at P = 60 Torr and Φ = 1.0, Dashed line, GRI Mech 3.0 [160].

The rapid reaction between fuel (e.g., C₂H₄) and atomic O reduced the atomic O concentration quickly in fuel/air mixtures (Fig. 4.3) and initiated the combustion process for ignition. This direct diagnostics significantly advanced our understanding of plasma assisted combustion at the elementary reaction level.

To understand the formation pathways of atomic O production by excited N₂ (N₂(A), N₂(B) and N₂(C)) at higher pressure, the absolute number density of N₂(A) was measured by Cavity Ring Down Spectroscopy (CRDS) and the densities of N₂(B) and N₂(C) were measured by Optical Emission Spectroscopy (OES) in a nanosecond pulsed discharge at atmospheric pressure in air [161]. The results in Fig. 4.4 show that in air plasma, the rise of atomic O concentration synchronizes with the decay of N₂(B) and N₂(C), that is, oxygen collisions with N₂(B) and N₂(C) are the major reaction pathways to produce atomic O in addition to direct electron impact oxygen dissociation.

Direct measurement of atomic O production was also done in CH₄/O₂/Ar diffusion flames with nanosecond discharge at 60 Torr [43]. Fig. 4.5 shows that comparison of atomic O and CH₂O formation with and without CH₄ in oxygen. It is seen that high O

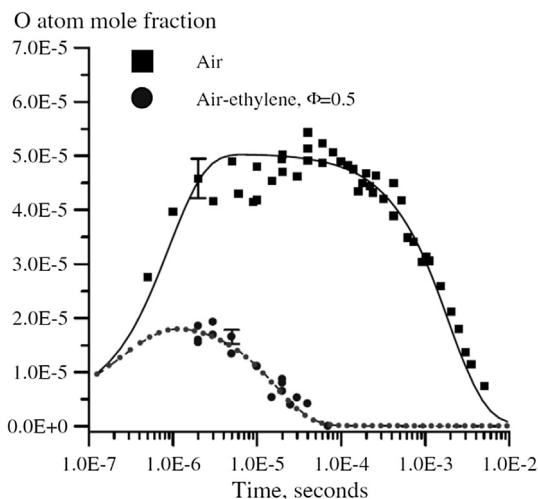


Fig. 4.3. Atomic O mole fraction vs. time after a single high voltage pulse in air and C₂H₄/air mixture at P = 60 Torr and Φ = 0.5. Dotted line, USC Mech II [160].

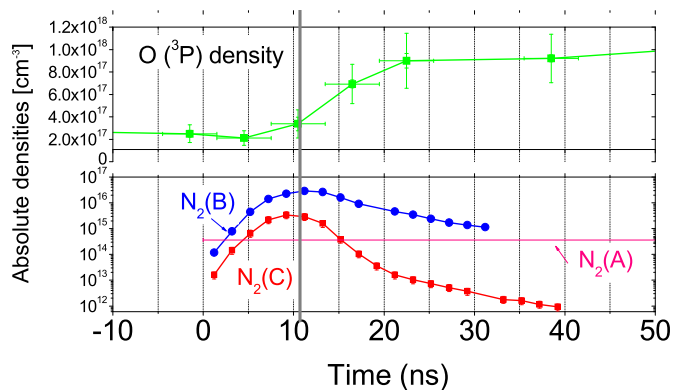


Fig. 4.4. Measurements of number density of excited nitrogen and atomic oxygen in air plasma [161].

concentration was produced by plasma discharge via reaction R8b in oxygen without fuel and collisions between O₂ and excited Ar, but the plasma produced atomic O radicals were consumed by reacting with CH₄ to form CH₂O in a fuel lean mixture. Recent experimental and numerical studies of *in situ* plasma discharge CH₄/O₂/He diffusion flames [106,144] showed that the following two reactions also contribute significantly in atomic O production, respectively, by approximately 2% and 26% via reactions,



In addition to the measurements of radical production by plasma discharge, *in situ* measurements of plasma generated intermediate species by mid-IR laser absorption spectroscopy of C₂H₄/Ar and C₂H₄/O₂/Ar mixtures activated by a nanosecond repetitively pulsed plasma were also conducted in a low temperature flow reactor (below 500 K) at a pressure of 60 Torr [168]. A recently developed kinetic mechanism (HP-Mech) for plasma activated C₂H₄ oxidation was assembled [168,242]. Fig. 4.6 shows that there exist three fuel consumption pathways for plasma activated low temperature C₂H₄ oxidation: (1) a plasma activated low temperature fuel oxidation pathway via O₂ addition reactions (left) to form RO₂ and O₂C₂H₄OH; (2) a direct fragmentation pathway via collisional dissociation by electrons, ions, and electronically excited

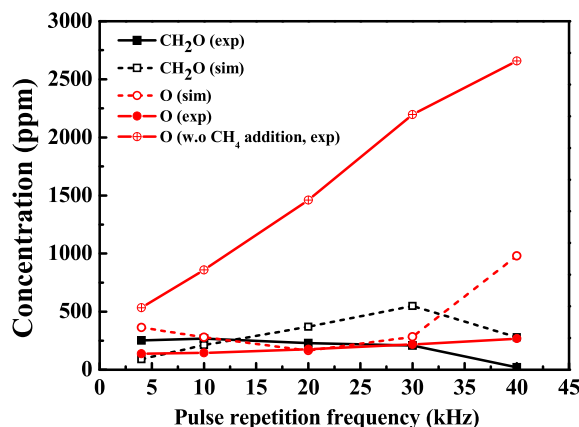


Fig. 4.5. Dependence of species concentrations at the burner exit on pulse repetition frequency (experiments: solid symbol and solid line; simulations: open symbol and dashed line) [106].

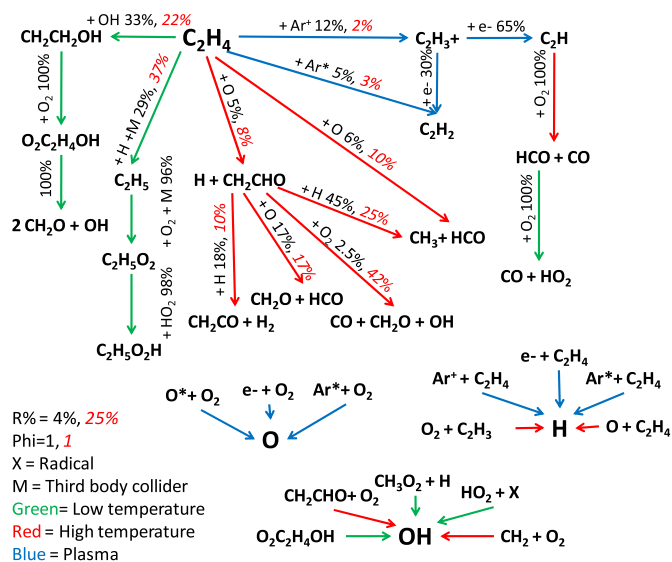


Fig. 4.6. Path flux analysis for fuel oxidation [168].

molecules (top right); and (3) a direct fuel oxidation pathway by plasma generated radicals such as atomic O (middle). It was found that the plasma activated low temperature oxidation pathway is dominant and leads to a larger amount of formaldehyde formation with lesser acetylene and negligible large hydrocarbon molecules compared to the decomposition experiment. The results also indicated that the latter two fuel consumption pathways were strongly dependent on O₂ and Ar concentrations due to their effect on the production of atomic oxygen and excited Ar. The comparison between model prediction and experiments in Fig. 4.7 shows that although the HP-Mech model [168,242] improved the overall prediction over USC-Mech II for plasma activated decomposition and oxidation, both models failed to predict quantitatively the H₂O and CH₄ formation. The results showed that the plasma combustion kinetics has a large uncertainty for low temperature fuel oxidation. Experimental data of intermediate species diagnostics are needed for future model development in plasma-assisted combustion.

Moreover, the effects of plasma produced O_3 , $O_2(a^1\Delta_g)$, and NO_x on ignition and flame propagation were also studied [156,157] and will be discussed in the following sections.

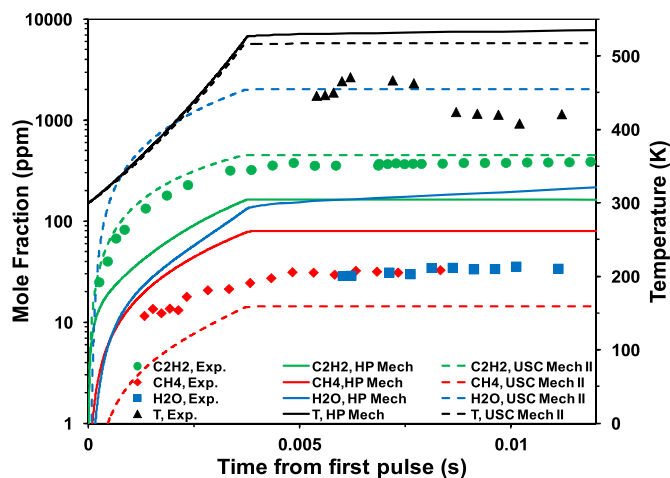


Fig. 4.7. Measurements and modeling of C_2H_2 , CH_4 , H_2O , and temperature after 150 pulses at 30 kHz repetition rate for a mixture of 6.25/18.75/75 $C_2H_4/O_2/Ar$ [168].

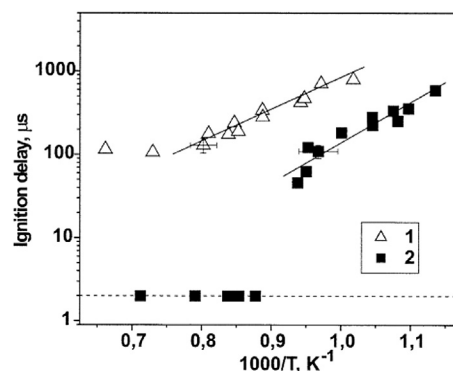


Fig. 4.8. Measured ignition delay time vs. gas temperature. Mixture $H_2:O_2:N_2:Ar = 6:3:11:80$. 1 – autoignition, 2 – with nanosecond discharge. $U = 160$ kV [213].

4.2. Effects of plasma on ignition

One of the pioneering studies of plasma effect on ignition delay time and plasma-combustion kinetics was conducted by Bozhentkov et al., in 2003 using nanosecond pulsed discharge in a shock tube to study the plasma-combustion kinetics [213]. A uniform nanosecond pulsed discharge in the form of the fast ionization wave was organized in the dielectric section. The end plate (EP) of the shock tube was a high voltage electrode of the discharge system. The discharge initiation was synchronized with the reflected shock wave. The peak voltage of the electric pulse varied from 100 to 160 kV with pulse duration of approximately 30–40 ns. The results showed that the nanosecond pulsed discharge was capable of activating the premixture behind the reflected shock wave nearly instantaneously while not elevating the temperature. As shown in Fig. 4.8, nanosecond discharge can significantly decrease the ignition delay of H_2 by nearly an order of magnitude. Similar observations were obtained for CH_4 mixtures at pressures from 0.3 to 2.3 atm. This study was one of the first carefully designed experiments to decouple the thermal effect of plasma on combustion and kinetic effect. Further experiments showed no noticeable difference of the voltage polarity effect on ignition delay measurements. The uniformity of the nanosecond pulsed discharge was also confirmed [112]. Along with the experiments, a kinetic model was also developed to simulate the effect of plasma on the combustible mixture. This work demonstrated the increased effectiveness or efficiency of non-equilibrium excitation over equilibrium excitation in a $H_2/O_2/N_2$ system as shown in Fig. 4.9.

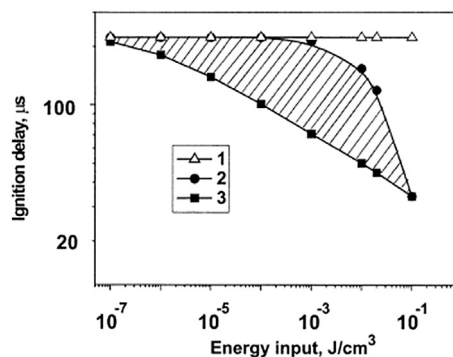


Fig. 4.9. Calculated ignition delay time of H_2 : O_2 : N_2 mixture (29.6:14.8:55.6) as a function of energy input at $P = 1$ atm; $T_0 = 1000$ K, $E/N = 300$ Td; 1 – auto-ignition; 2 – equilibrium excitation; 3 – non-equilibrium excitation [213].

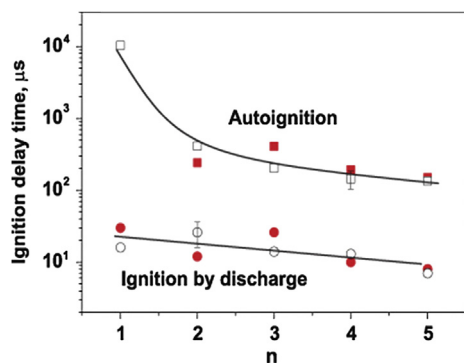


Fig. 4.10. The ignition delay time for the C_nH_{2n+2} containing mixtures versus the number of C atoms in C_nH_{2n+2} molecule. Closed points correspond to measurements and open points correspond to calculations. The initial temperature was between 1430 and 1450 K and the pressure was between 0.4 and 0.5 atm [247].

Since the earlier work in 2003, more experiments were conducted for a variety of fuels, pressures and temperatures [243–247]. Similar observations were obtained for C_1 to C_5 alkanes. Fig. 4.10 shows the ignition delays for different alkanes with and without plasma discharge. The initiation of the discharge with a

specific deposited energy of 10–30 mJ/cm³ lead to one order of magnitude of ignition delay reduction for C_1 to C_5 alkanes. In addition, the predicted results agreed well with the experimental data. Analysis showed that the effect of non-equilibrium plasma on ignition delay was primarily due to the production of atomic O and H whereas atomic O was shown to be the most effective in enhancing the ignition.

Despite the earnest efforts of Starikovskii et al., the experimental results measured through optical emission spectroscopy did not agree well with that of simulations, and still requires more detailed studies. As pointed out by the authors, time-resolved and *in situ* experimental measurements of the dominant radicals and intermediates are needed. Therefore, even though the experiments were fairly well-designed, the kinetics has remained a significant issue. In addition, the experiments were focused on high temperature ignition above the critical branching temperature of R2. Therefore, as discussed in Section 3.1, the major role of plasma was to add radicals to bypass chain initiation reaction (R1) to accelerate ignition.

Recently, Wu et al. [248] has investigated plasma assisted ignition below self-ignition threshold in CH_4 , C_2H_6 , C_3H_8 and C_4H_{10} /air mixtures at atmospheric pressures at temperatures from 300 to 800 K in a reaction chamber with 10 Hz, 10 ns repetitive pulse

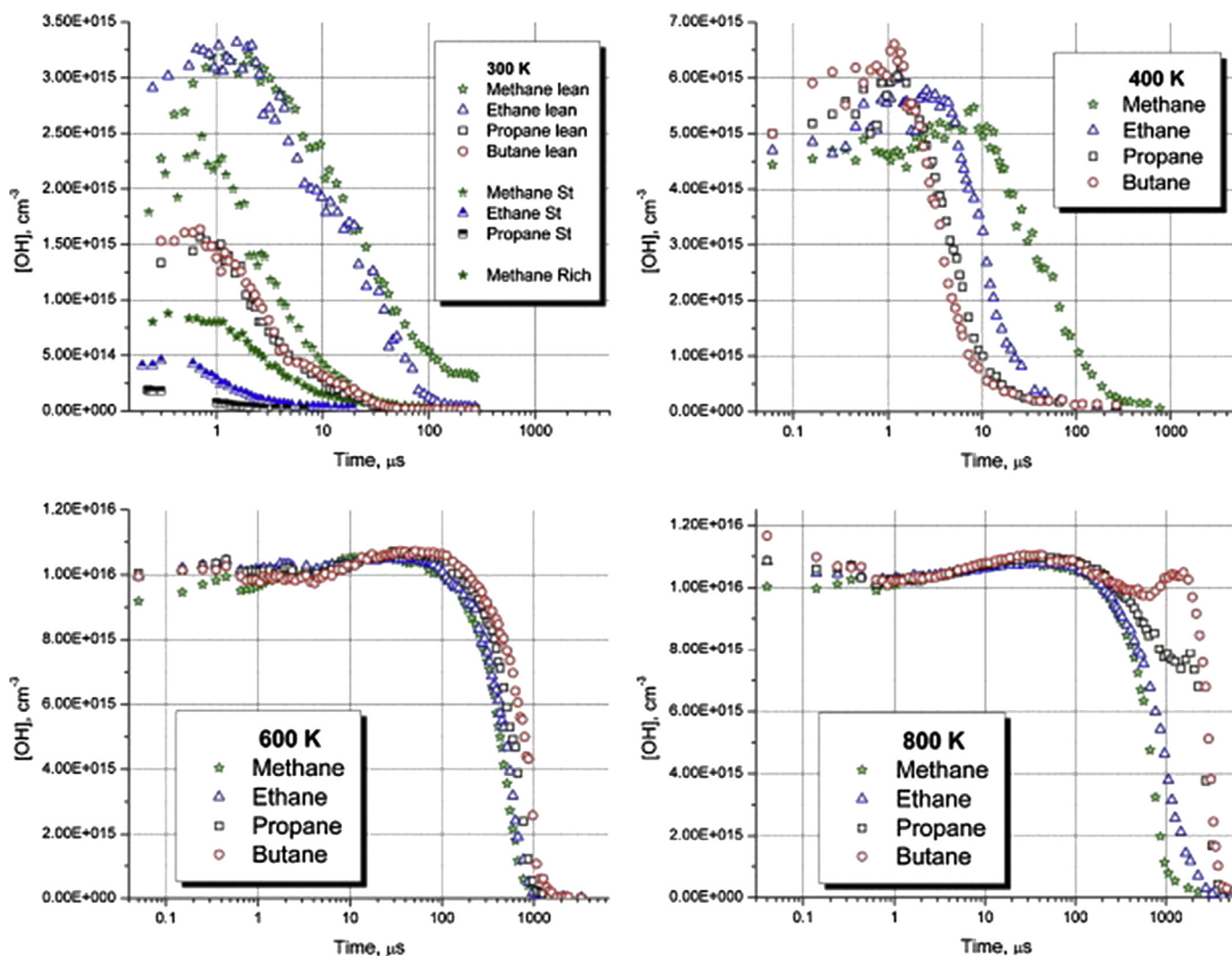
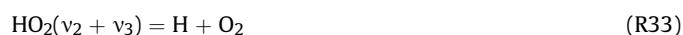


Fig. 4.11. OH evolution over time at four temperature points, from 300 to 800 K. $P = 1$ atm, $\Phi = 0.1$ (for $T = 400$ –800 K) [248].

discharge with 20 kV. The reactant flow rate was set at approximately 20 cm/s to allow each discharge pulse to occur in a fresh gas mixture. The time evolution of OH radicals in premixed fuel/air flows in the afterglow was studied using OH PLIF. The results are shown in Fig. 4.11. At 300 K, three different equivalence ratios were studied ($\Phi = 0.1, 1$ and 3.0). By comparing the OH evolution curves, the decay time of OH for the CH_4 mixture was found to be the longest, while those for butane appeared to be the shortest. This was due to the increased H abstraction rate by OH for larger hydrocarbons. Moreover, the OH evolution curves changed significantly when the temperature increased to 400 K. The CH_4 curve showed that the time for OH to reach its maximum increased to about 10 μs . This timescale significantly exceeded the time of plasma recombination under atmospheric pressure conditions. This indicates that some chain propagation/branching reactions may occur even at 400 K. A drastic change was observed when the temperature was raised to 500 K. The time of maximum OH remains in the range of 30–70 μs for all fuels. The increase in OH density clearly demonstrated the chain development processes and OH production continuation after the plasma channel recombination. Another noticeable change was the OH signal decay order, which was reversed compared to the case at 400 K. A third stage of OH was observed when the temperature reached 700 K and this stage became to be clear at 800 K as shown in Fig. 4.11. The maxima in OH concentration appeared in a single curve. The first peak may be related to the initial OH production in the discharge. The second peak is likely owing to chain reactions by the accumulation of intermediate species. The third peak may correspond to the low temperature chemistry because it was only observed for C_3H_8 and C_4H_{10} mixture. The authors also reported that all attempts with current available models failed to predict these results.

A later work by Starikovskiy [249] suggested a possible reason of the difficulty to reproduce the experimental results was the lack of vibrational–vibrational excitation of HO_2 . Vibrational excitation began to be very efficient at $E/N = 80$ –100 Td. The vibrational–vibrational energy exchange between excited N_2 and HO_2 is near-resonant process.



The vibrational quantum energy of N_2 is very close to the vibrational excitation of HO_2 where v_2 vibrational mode of HO_2 means O–H stretch and v_3 means O–O stretch. Thus, the vibrational–vibrational energy exchange can be extremely fast even at room temperature. The fast excitation and decomposition of vibrationally excited HO_2 leads to the canceling of the chain termination reactions and allows the oxidation process to develop even below the self-ignition threshold. By including the vibrational–vibrational excitation and decomposition of HO_2 , kinetic models can reasonably predict the experimental results of OH evolution curves reported in Ref. [248]. However, in this model, many of the low temperature oxidation pathways (in Fig. 4.6) were not considered. Given the large uncertainty and the pressure dependence in the rate constants related to reactions R32 and R33, quantitative diagnostic methods for HO_2 time evolution are needed. This diagnostic method will be discussed in Section 5.

Yin et al. [250] has developed a similar quartz reactor and measured ignition delays, time-resolved temperature, and OH concentrations in mildly preheated H_2/air mixtures ($T = 473$ –500 K). The reactor was made of a 280 mm long, 22×10 mm rectangular cross section quartz channel with wall thickness of 1.75 mm. The entire assembly was heated in a tube furnace to improve the plasma stability. The ignition delay times

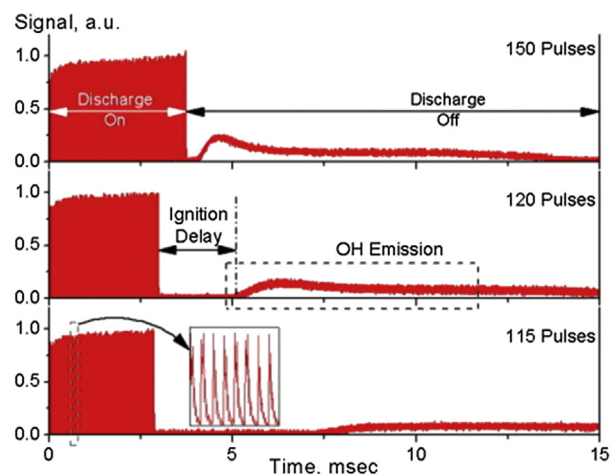


Fig. 4.12. UV emission traces in H_2/air excited by a nanosecond pulse discharge burst, $T_{\text{ini}} = 473$ K, $P = 80$ Torr, $\Phi = 1$ [250].

were measured by monitoring the intensity of excited OH (OH^*) emission at 310 nm through the side wall of the reactor, using a narrow bandpass filter (centered at 310 ± 2 nm, bandpass 10 ± 2 nm FWHM), a photomultiplier tube (PMT), and an oscilloscope. A typical emission trace in H_2/air mixture excited by the plasma with initial temperature, $T_{\text{ini}} = 473$ K is shown in Fig. 4.12. Emission during the discharge burst was primarily from N_2 second positive band system. N_2 emission decayed rapidly after each discharge pulse and disappeared after the burst. Self-sustained OH(A–X) emission appeared after the burst and lasted for several milliseconds which indicated ignition as shown in Fig. 4.12. It was found that ignition delay times increased steeply as the number of pulses was reduced. OH LIF and two-line OH LIF were used to measure the absolute OH concentrations and temperatures of the mixtures, respectively. For two-line OH LIF, the laser system was tuned to two absorption transitions in the OH A–X (1,0) band, $Q_1(5)$ at 282.667 nm and $Q_2(11)$ at 285.073 nm, chosen for optimum sensitivity in preheated mixtures during ignition, from 500 to 2000 K.

Absolute OH concentration and temperature in H_2/air mixtures excited by a discharge pulse burst at $T_{\text{ini}} = 500$ K, $P = 80$ Torr, $f = 10$ kHz, were plotted vs. time delay after the burst in Fig. 4.13. It

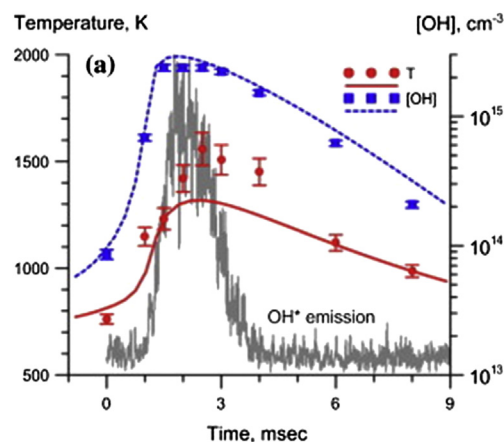


Fig. 4.13. Experimental and predicted temperature, OH concentration, and OH (A–X) emission traces after the discharge burst, H_2/air , $T_{\text{ini}} = 500$ K, $P = 80$ Torr, $f = 10$ kHz, $\Phi = 0.5$, 115 pulses [250].

can be seen the temperature immediately after the discharge burst was $T_f \approx 700\text{--}750\text{ K}$, which is approximately $200\text{--}250\text{ K}$ higher than the initial temperature of the mixture and significantly lower than the autoignition temperature at these conditions, $\sim 900\text{ K}$. Numerical modeling results were also shown in Fig. 4.13 as solid and dashed lines. The modeling well predicted the experiments and revealed that H atom accumulation (up to 0.1%) during the discharge primarily by R2 reaction together with temperature rise introduced ignition.

Besides the reactive radicals and intermediates, plasma can also produce stable species, such as NO_x . To study the effect of plasma generated NO_x on ignition, a gliding arc integrated counterflow system was developed to measure the decrease of ignition temperature on $\text{H}_2/\text{CH}_4/\text{air}$ diffusive ignition systems [38,138,139]. The counterflow system can be characterized by a flow velocity gradient (strain rate or inverse of residence time) on the centerline near the stagnation plane of the two opposite jets. The ignition temperature measurements were conducted at atmospheric pressure for CH_4 and H_2/air diffusion flame. NO_x was quantified by Fourier Transform Infrared Spectroscopy (FTIR). The experimental results together with computational results for H_2/air diffusion flame are shown in Fig. 4.14. It can be seen that with the plasma activation, ignition temperatures decreased significantly compared to the case of heated air (without plasma activation). To mimic the effect of plasma enhancement, 3600 ppm NO and 1200 ppm NO_2 were added into the heated air. The ignition temperature measurements showed good agreement between the case of NO_x addition and the results of gliding arc. Similar results were also obtained for CH_4/air diffusive ignition. Numerical simulations were conducted to understand the effect of ignition enhancement for methane with NO addition [138,139]. Fig. 4.15 shows the dependence of the maximum temperature on stretch rate at different oxidizer temperatures. It is seen that with NO addition at low oxidizer temperature (e.g., $900\text{--}1000\text{ K}$), a low temperature ignition limit appears. That means that plasma produced NO can accelerate ignition by causing low temperature ignition which does not occur without NO .

The authors further discussed the formation and catalytic cycle of NO_x for CH_4 and H_2 ignitions. The electron impact reactions (R8a) and

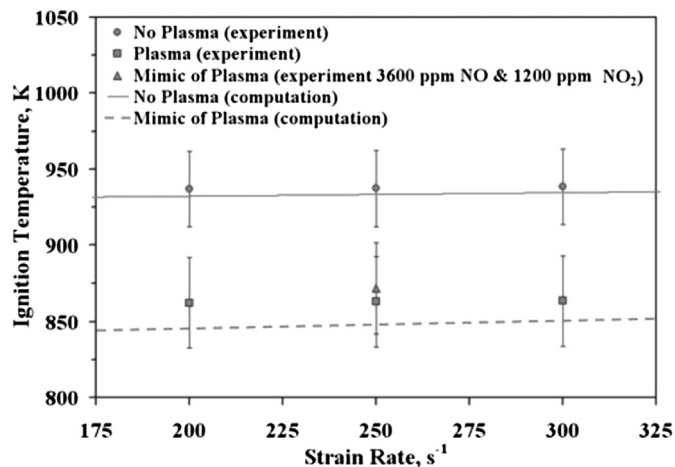


Fig. 4.14. Comparison of experimental and computational results of ignition temperatures with 20% H_2 in N_2 vs. air for preheated air and magnetic gliding arc [38].

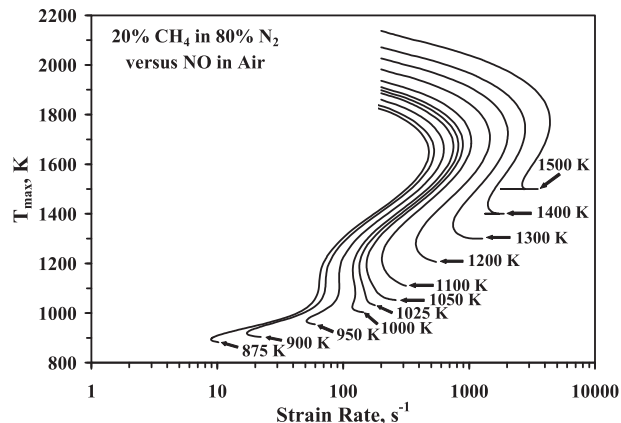


Fig. 4.15. S-curve response for 20% CH_4 in N_2 versus pre-heated air with 10,000 ppm NO as a function of maximum temperature and strain rate [38].

provide large concentrations of atomic O and atomic N therefore significantly contributing to the NO_x formation by reactions



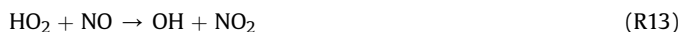
For CH_4/air diffusion flame, at low temperature, the reaction



converts CH_3 radicals inactive CH_3O_2 and thus the ignition process is slowed down. With the addition of NO , CH_3O_2 is catalytically oxidized by the NO_x reaction pathways,



to produce CH_3O and subsequently H radicals so that ignition will be enhanced at low temperature. For H_2/air ignition system, the formed inactive HO_2 radical via termination reaction (R7) is catalyzed by NO via the following pathways,



This process explained the catalytic effect of NO_x on ignition in plasma assisted combustion at low temperature.

4.3. The thermal and kinetic effects of plasma on flame extinction

With the same experimental setup, Ombrello and coworkers studied the effect of gliding arc discharge on CH_4/air diffusion flame extinction in a counterflow system at atmospheric pressure [38]. With plasma discharge of the airstream, up to a 220% increase in the extinction strain rate was observed. The authors further examined the impact of thermal and non-thermal mechanisms on the extension of extinction strain rates by direct comparison of measured temperature profiles via Rayleigh scattering thermometry and OH number density profiles via OH PLIF. It was found that the effect of the plasma on flame extinction was predominately thermal [38] due to the fast recombination of radicals which were generated by the discharge on the oxidizer side.

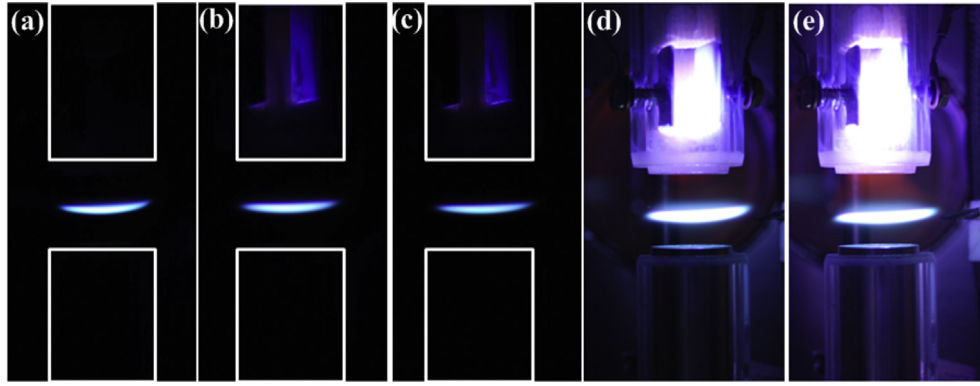


Fig. 4.16. Images of flames at $X_{\text{CH}_4} = 0.36$, $X_{\text{O}_2} = 0.28$ with balance of argon, $a = 178 \text{ s}^{-1}$, $d = 20 \text{ mm}$, $P = 60 \text{ Torr}$ (a) without discharge (b) $f = 5 \text{ kHz}$ (c) $f = 10 \text{ kHz}$ (d) $f = 20 \text{ kHz}$ (e) $f = 40 \text{ kHz}$ [43].

Recently Sun et al. [43,106] has conducted research about plasma on flame extinction at low pressures (60 Torr) by coupling nanosecond pulsed discharge with a counterflow system. The experimental setup consisted of a counterflow burner, which was located in a low pressure chamber. Two parallel bare copper electrodes were located inside the tubes of the upper (oxidizer side) burner to generate non-equilibrium discharge. Fig. 4.16(a)–(e) shows images of flames with and without the nanosecond non-equilibrium pulsed discharge at 60 Torr. The pulse repetition frequencies were increased from 5 to 40 kHz. The discharge was uniform in the transverse direction of the electrodes and no visible filamentary structure was observed for repetition frequency from 5 to 40 kHz. Fig. 4.16(d) and (e) shows a visible plasma jet issuing from the burner exit and reaching the reaction zone. The optical emission in the afterglow of an Ar/O₂ discharge is produced from the relaxation processes of excited species like Ar*, O(¹D), O(¹S), O₂(a¹Δ_g), and O₂(b¹Σ_g). During the relaxation processes, ground state atomic O can be produced. Therefore, the visible emission indicates that there exist significant concentrations of excited species, radicals, and atoms between the nozzle exit and the reaction zone that need to be quantitatively examined.

The absolute number density of atomic O was then quantified by Two Photon Laser Induced Fluorescence (TALIF) method [43,106,160,251] as shown in Fig. 4.17 and then used as a boundary conditions in the numerical modeling [43]. The results of extinction strain rate measurement together with numerical modeling shown

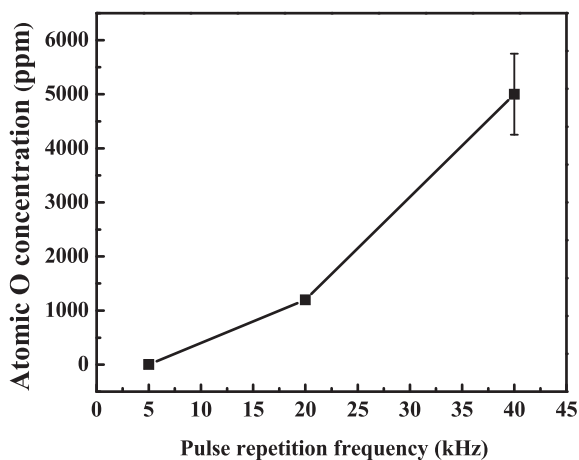


Fig. 4.17. Dependence of average atomic O concentration at the burner exit on the pulse repetition frequency [43].

in Fig. 4.18 indicate that for a CH₄/O₂/Ar diffusion flame, with the increase in discharge frequency on the oxidizer side, the extinction strain rates extended significantly. At the same time, the oxidizer side flow temperature also increased. In order to isolate the thermal effect, the extinction strain rates with plasma activation and that of just electrically heated flow were compared both experimentally and numerically using measured atomic O concentrations as boundary conditions. The results showed that even though the discharge can generate a significant amount of atomic O, most of the atomic O was quenched before being transported to the reaction zone at low temperature conditions. At high oxidizer side flow temperature conditions, the enhancement started to be more significant. More detailed analysis showed that if the oxidizer temperature was higher than a crossover temperature, which was about 900–1000 K at low pressure, approximately 80% of the atomic O can be transported to the reaction zone to enhance the flame. Therefore, in order to observe the kinetic enhancement from plasma on flame, the oxidizer temperature must be higher than the crossover temperature to avoid quenching.

One way to avoid quenching of the radicals is to add fuel into the oxidizer stream. Following this idea, Sun and coworkers [106] blended 2% CH₄ into the oxidizer side stream and activated by the plasma. In this way, the reactive species generated by the plasma reacted with the fuel rather than being recombined or quenched. After activation by the plasma, the CH₄ added into the

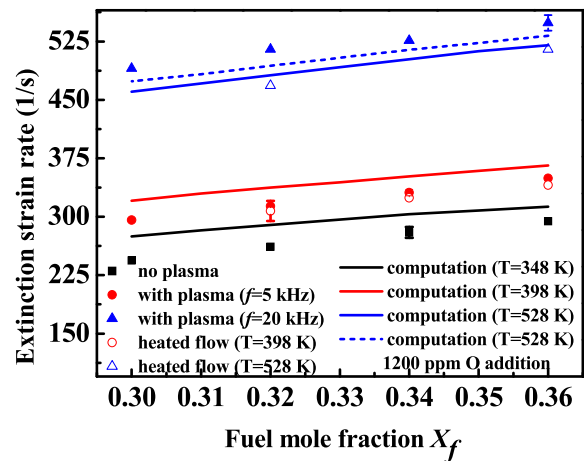


Fig. 4.18. Comparisons of extinction strain rates between experimental results with plasma activation and an electrically heated flow as well as numerical simulations at 60 Torr [43].

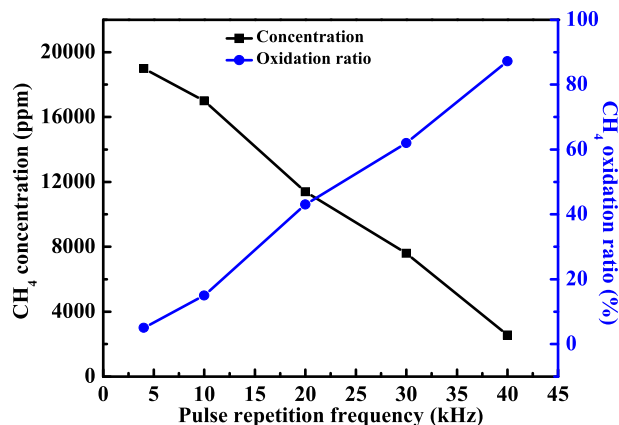


Fig. 4.19. Dependence of CH₄ concentrations and oxidization ratios on pulse repetition frequency [106].

oxidizer flow was oxidized. The concentrations of the products and atomic O were measured by FTIR, Gas Chromatography (GC) and TALIF. The results are summarized in Figs. 4.5, 4.19 and Fig. 4.20. The FTIR and GC measurements showed that with the increase in the discharge repetition frequency, the CH₄ oxidation ratio increased significantly and the production of CO, CO₂, H₂, and H₂O also increased together with the increase in the flow temperature at the nozzle exit. The experimental measurements were also compared with numerical modeling. It was concluded that the modeling results deviated significantly from the experiments mainly due to the uncertainty of the combustion kinetic mechanism at low temperature conditions (below 700 K) and unknown plasma reaction pathways. The path flux analysis revealed that O production by the plasma is the major source to initiate the low temperature CH₄ oxidation. Once O is generated by the discharge, it is consumed rapidly by CH₄ and its intermediate oxidized and dissociated products. Only a small amount of O recombines to O₂. The extinction strain rate measurements showed that with the increase in discharge frequency (CH₄ oxidation ratio), the extinction strain rates extended significantly. Numerical modeling can fairly predict the extinction strain rates with the FTIR and TALIF measured speciation as boundary conditions. FTIR measurements indicated significant amount of CO and H₂ formation as a result of CH₄ reforming. The authors further compared the effectiveness of CH₄

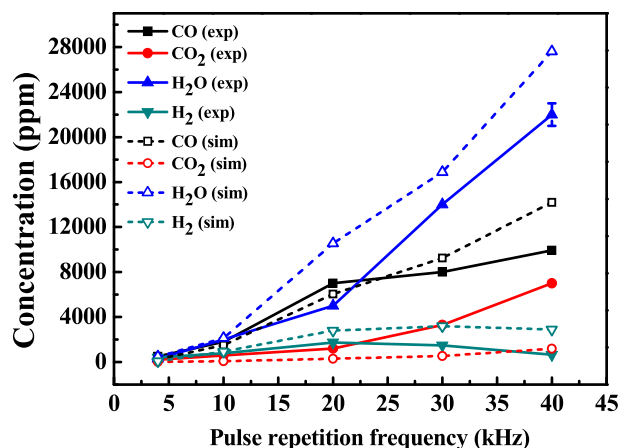


Fig. 4.20. Dependence of species concentrations at the burner exit on pulse repetition frequency (experiments: solid symbol and solid line; simulations: open symbol and dashed line) [106].

oxidation and fuel reforming on the extension of extinction strain rates. The comparison showed that the production of H₂ from fuel reforming can extend the extinction strain rate due to the increased fuel reactivity. However, the extension owing to CH₄ oxidation was much more effective. This is because when the flame approaches extinction, there is not enough residence time for the CH₄ to complete the oxidation reactions to release the chemical heat. However, plasma can dramatically accelerate the CH₄ oxidation to release the chemical energy at low temperature. The prompt chemical heat release extended the extinction limit.

The study in Refs. [43,106] demonstrated the effect of plasma-produced species on flame extinction. The experiments successfully isolated the interaction between plasma and flame. However, the lack of the coupling effect minimized the effect of the plasma on the flame due to the short lifetime of reactive species. Thus, the dominant effect of plasma on the reaction zone was not free from thermal enhancement effects. Therefore, it is very important to investigate the direct coupling effect between plasma and a flame, where plasma kinetics pathways modify the flame kinetic pathways. In order to focus on the kinetic performance of the plasma/flame interaction, Sun and coworkers [144] subsequently developed a novel well-defined counterflow flame system with an *in situ* discharge using porous electrodes as shown in Fig. 4.21. In this way, uniform discharge was generated between two burners as shown in the embedded picture in Fig. 4.21.

The ignition and extinction characteristics were studied by measuring the OH* emission intensity in the reaction zone since ignition or extinction happens with an abrupt change of the OH* emission. During the experiments, the strain rate (400 1/s), X_0 and the discharge frequency ($f = 24$ kHz) were held constant, while the CH₄ mole fraction on the fuel side, X_F , was varied. The relationship between OH* emission intensity as well as reaction zone peak temperature and X_F is shown in Fig. 4.22 with (a) $X_0 = 0.34$ and (b) 0.62. The temperatures of the reaction zone were measured by the Rayleigh scattering method. By starting from $X_F = 0$ and increasing X_F until it equaled 0.265, the OH* emission was negligible compared to the background noise, and no reaction zone was observed in Fig. 4.22(a). Further increase of X_F caused an abrupt increase in OH* emission intensity. This phenomenon was also identified by the appearance of a visible flame, indicating that ignition occurred. After ignition, further increase or decrease in X_F only caused very limited increase or decrease in the OH* emission intensity, respectively. But when the X_F was decreased to less than 0.20, an abrupt decrease in the OH* intensity was observed and the visible

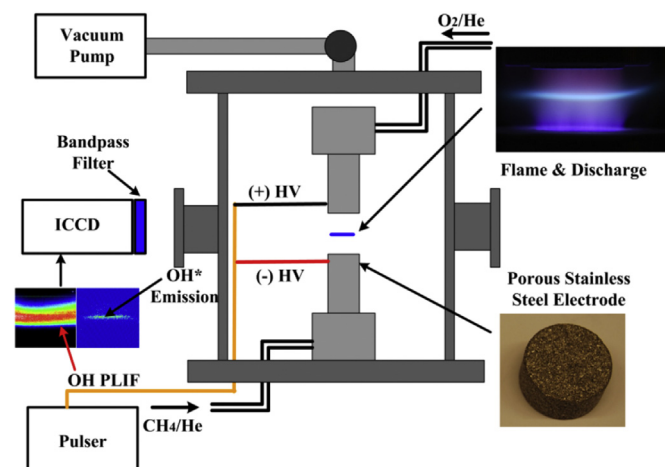


Fig. 4.21. Schematic of experimental setup integrating counterflow system with *in situ* discharge [144].

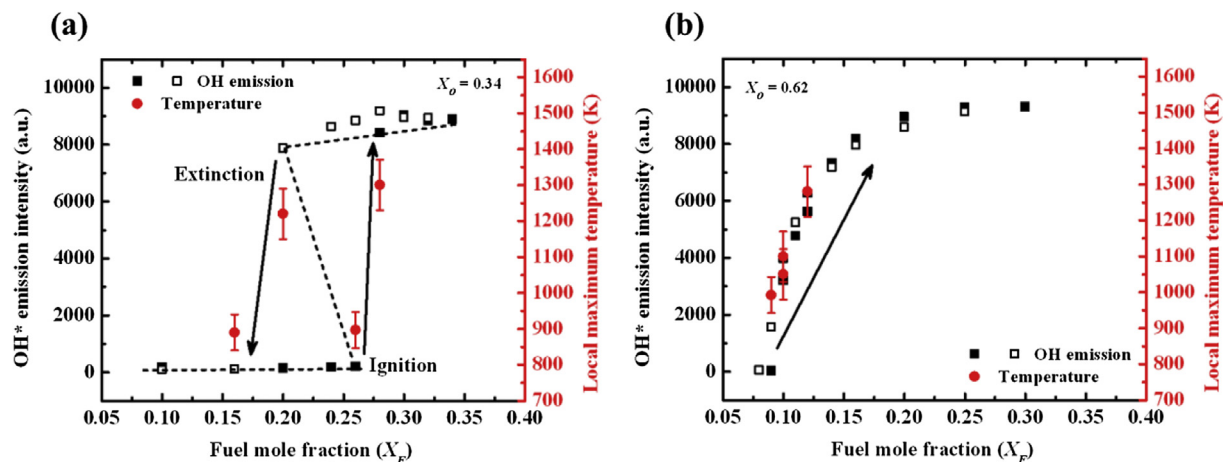


Fig. 4.22. Relationship between OH* emission intensity, local maximum temperature and fuel mole fraction, $f = 24$ kHz, $a = 400$ 1/s, (a) $X_0 = 0.34$, (b) $X_0 = 0.62$, (solid square symbols: increasing X_F , open square symbols: decreasing X_F) [144].

flame emission disappeared, indicating the extinction. This hysteresis of OH* emission intensity between ignition and extinction forms an S-curve of the flame which is the fundamental phenomena of ignition and extinction. The local maximum temperature measurement (reaction zone temperature) showed that the value just before ignition was only 897 ± 50 K. With further increasing X_F , ignition occurred and the local maximum temperature increased to approximately 1310 ± 80 K.

When X_0 was increased to 0.62, the ignition and extinction limits (Fig. 4.22(b)) merged at $X_F = 0.09$, resulting in a monotonic ignition and extinction S-curve Fig. 4.22(b). The temperature measurements also demonstrated a similar monotonic increase in the local maximum temperatures. The monotonic and fully stretched ignition and extinction S-curve could be explained by the fact that the plasma generated reactive species caused a transition of flame stabilization mode from the extinction-controlled to the ignition-controlled modes. This means that the extinction limit did not exist by the plasma/combustion chemistry interaction (Fig. 1.4),

thus the chemistry of flame stabilization was fully dictated by the ignition limit. These results were further confirmed by OH PLIF measurements which were identical to the OH* emission results.

In order to further understand the underlying mechanisms, numerical simulations were conducted at a condition prior to ignition with $X_F = 0.16$ and $X_0 = 0.34$ with constant electric field assumption. As indicated in Fig. 4.23, the results of path flux analysis showed that CH₄ was predominantly dissociated to CH₃ by H abstraction through collision with OH, electrons, O and H. The major reaction path of CH₃ was the oxidation to CH₂O and finally to HCO, CO and CO₂. OH and H (Fig. 4.23(b)) were predominantly generated through the reactions between O and fuel/fuel-fragments. Therefore, it can be concluded that O was the initiation source of fuel oxidation and determined the population of the radical pool as shown in Fig. 4.23(c).

The dominant formation pathway of O formation in this experiment was from direct electron impact of O₂, including reactions (R1)–(R3):

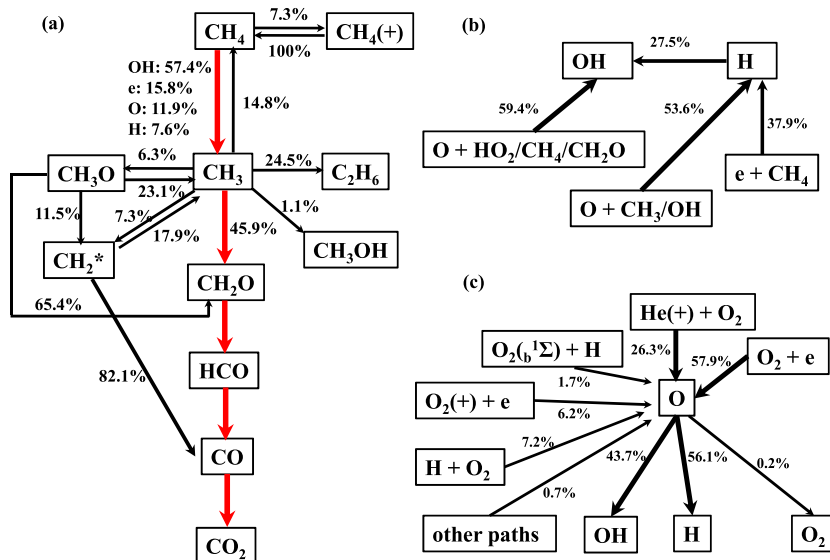


Fig. 4.23. Path flux analysis (a) CH₄ consumption pathways (red arrows: dominant reaction pathway) (a) OH and H formation pathways (b) reaction pathways of O, $X_F = 0.16$, $X_0 = 0.34$, $P = 72$ Torr, $f = 24$ kHz, $a = 400$ 1/s [144]. (For interpretation of the references to color in this figure legend, the reader is referred to the web version of this article.)

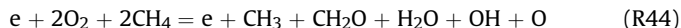


Once $O(^1D)$ and O^+ were produced, they were quickly quenched or recombined with electrons, respectively, to produce O . Another two important formation pathways of atomic O were from collisions between O_2 and He ions (He^+). Once atomic O was formed, it reacted with CH_4 and its fragments to generate OH and H to further oxidize CH_4 ; only a small fraction of atomic O recombined to form O_3 and O_2 .

Since plasma is the source of radicals, the radical generation from the plasma can change the chain branching effects in the reaction zone. Reaction R8 generated O which reacted with CH_4 to generate CH_3 and OH through reaction R41. Together with reaction R42, the generation of CH_3 promoted reaction R43 to generate H . The generation of H promoted the chain branching reaction R2 to generate OH and O and feedback to build up the radical pool.



A global reaction can be obtained by adding the above reactions together,



One can see clearly from the above global reaction that one high energy electron can lead to three radicals and other intermediate species at low temperature to decrease the global activation energy of fuel oxidation as indicated in Fig. 1.4.

Without plasma, the flame chemistry could not sustain the chain-branching reaction below the crossover temperature for the flames, exhibiting hysteresis between ignition and extinction (Fig. 1.4). However, the plasma enabled the chain branching reaction to be sustainable even at low temperatures by the positive loop between fuel oxidation and regeneration of the radical pool (R44). The dominant radical formation path was controlled by plasma, rather than the $H + O_2 = OH + O$ reaction. Thus, the strong radical pool significantly decreased the global activation energy for fuel oxidation at low temperatures. Finally, the excessive production of radicals from the plasma diminished the hysteresis between ignition and extinction.

As shown in Fig. 4.23, the oxidation path of CH_4 is relatively straight and does not contain any low temperature kinetics. In order to examine the effect of plasma on the low temperature chemical kinetics, dimethyl ether (DME) was employed as the fuel by Sun et al. [107]. By replacing CH_4 with DME and repeating the experiments, similar folded S-curves were observed by recording the OH PLIF. However, OH can only be used to characterize high temperature chemistry rather than low temperature chemistry. Therefore, CH_2O PLIF [252,253] was used to characterize the effect of plasma on low temperature chemistry. The relationship between CH_2O PLIF signal intensity (integration across burner gap) and fuel mole fraction at the fuel side nozzle exit, X_F , with a repetitive plasma discharge is shown in Fig. 4.24 at $f = 24$ kHz, and $X_O = 0.4$. As shown in Fig. 4.24, with the increase of the fuel mole fraction (X_F), the CH_2O PLIF signal intensity increases almost linearly. This

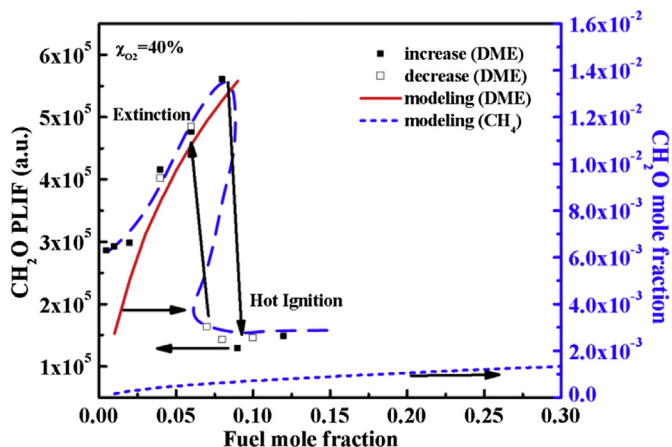


Fig. 4.24. Relationship between CH_2O PLIF and fuel mole fraction $X_O = 0.4$, $P = 72$ Torr, $f = 24$ kHz, $a = 250$ 1/s (symbols: experiments, lines: modeling, solid square symbols: increasing X_F , open square symbols: decreasing X_F for DME) [107].

linear increase of the CH_2O PLIF signal (proportional to CH_2O number density) with fuel mole fraction before ignition indicates the occurrence of low temperature DME oxidation. In addition, when the DME mole fraction at the fuel side nozzle exit is larger than 9% at $X_O = 0.4$, ignition occurs with a sharp decrease in the CH_2O PLIF signal intensity. After the ignition, the CH_2O PLIF signal intensity becomes insensitive to the change in DME mole fraction. On the other hand, when the DME mole fraction is decreased slowly to 7% at $X_O = 0.4$, extinction occurs along with a rapid increase in CH_2O PLIF signal intensity. Similar results can also be observed at $X_O = 0.6$ with ignition and extinction occurring at lower fuel mole fractions.

In order to confirm whether this pronounced formation of CH_2O before ignition is a unique response of DME oxidation relevant to the low temperature reactivity, numerical calculations for both DME and the CH_4 case [144] have been conducted. The modeling results before ignition for both DME and CH_4 as the fuels are also shown in Fig. 4.24. It shows that the CH_2O mole fraction is about 500 ppm for CH_4 cases at the identical conditions shown in Fig. 4.24, whereas the CH_2O mole fraction in DME studied here are about 10,000 ppm. The large difference in CH_2O formation between DME and CH_4 suggests that the low temperature reactivity in DME oxidation is activated by the *in situ* discharge.

In order to achieve the smooth transition between ignition and extinction, the radical concentrations generated from the plasma must be high enough. So the reaction fluxes for the low temperature pathway and the high temperature pathway can be comparable at low temperature conditions. In an attempt to increase the productivity of radicals, the discharge frequency is increased to 34 kHz and the results are shown in Fig. 4.25. A monotonic S-curve without hysteresis between ignition and extinction is successfully achieved by increasing the production of radicals. Therefore, a smooth transition between low temperature chemistry and high temperature chemistry is realized. This observation can be generalized to other larger hydrocarbon fuels (such as n-heptane, jet fuel) with two-stage ignition behaviors.

The authors conducted further numerical modeling and path flux analysis was performed at $X_F = 0.01$, $X_O = 0.4$, $f = 24$ kHz. As shown in Fig. 4.26(a), approximately 37% of DME reacts with atomic O to form OH and CH_3OCH_2 . The formed OH abstracts H from DME and continues to form DME radicals, CH_3OCH_2 . At the very first reaction step, about 54% of DME reacts with OH to form CH_3OCH_2 . There exist two reaction pathways for CH_3OCH_2 consumption. The first channel is the decomposition of CH_3OCH_2 directly to CH_2O and

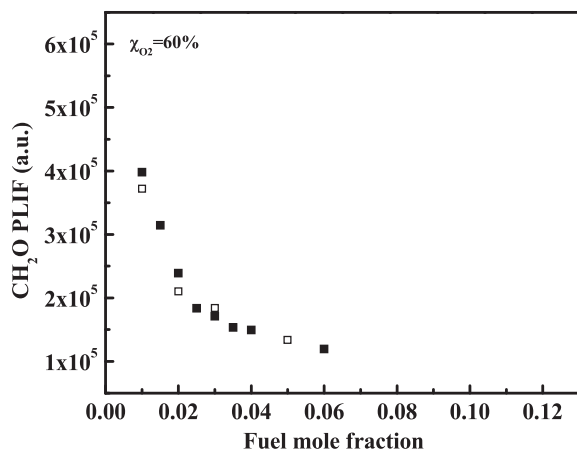


Fig. 4.25. Relationship between CH_2O PLIF and fuel mole fraction $X_{\text{O}} = 0.6$, $P = 72$ Torr, $f = 34$ kHz, $a = 250$ 1/s (solid square symbols: increasing X_F , open square symbols: decreasing X_F) [107].

CH_3 . This is a typical high temperature reaction pathway. The second channel is CH_3OCH_2 going through the low temperature chemistry reaction pathway via O_2 addition to form $\text{CH}_3\text{OCH}_2\text{O}_2$ (RO_2 radical). The subsequent isomerization of RO_2 to $\text{R}'\text{OOH}$ and decomposition to OH and CH_2O are the major (41%) formation pathways of CH_2O at low temperature. As shown in Fig. 4.26(b), the dominant formation pathways of OH and H are related with atomic O reactions. Therefore, atomic O produced by the plasma is the critical radical controlling the oxidation of DME at low temperature conditions. The major formation pathways (54%) of atomic O are from direct electron impact of O_2 (reactions R8a, R8b and R8c) and also the collision between He ions (He^+) and O_2 (R29) which counts 38% towards the formation of atomic O .

In order to further examine the effect of atomic O production on the PA-LTC, SENKIN [254] conducted homogeneous ignitions calculations employing a DME kinetic mechanism [255] with $\text{DME}/\text{O}_2/\text{He}$ (0.003/0.1/0.897 in mole fraction) mixture and investigated at 72 Torr, 650 K with and without 1000 ppm atomic O addition, respectively. The simulation is conducted at constant temperature condition to avoid further complicated kinetic temperature

dependence and very low DME concentration is chosen to prevent excessive heat release. Without atomic O addition, the low temperature chemistry is very slow at low pressure condition. The characteristic time is approximately 1 s for the formation of CH_2O . However, with 1000 ppm atomic O addition, the low temperature chemistry is significantly accelerated and the characteristic time for CH_2O formation is approximately 1 ms, three order of magnitude faster than the case without O addition. Further path flux analysis shows that atomic O addition significantly accelerates the reaction of H abstraction reaction of DME through $\text{CH}_3\text{OCH}_3 + \text{O} = \text{CH}_3\text{OCH}_2 + \text{OH}$ reaction. The subsequent formation and isomerization of $\text{CH}_3\text{OCH}_2\text{O}_2$, decomposition of $\text{CH}_2\text{OCH}_2\text{O}_2\text{H}$ to form CH_2O are considerably fast. In addition, approximately 90% of CH_2O formation is through the low temperature chemistry channel (formation of $\text{CH}_3\text{OCH}_2\text{O}_2$), as demonstrated in Fig. 4.26(a). Therefore, radical addition (atomic O production from the plasma in this study) activates the low temperature chemistry by initiating the H abstraction reaction of DME and modifies the global characteristic time scale of low temperature oxidation of DME. O addition increases the total enthalpy of the mixture and can cause approximately 9 K temperature rise if the same amount of enthalpy increase is used for thermal heating.

Through both the experiments and numerical modeling, Sun et al. [107] proved that CH_2O formation is dominated by PA-LTC of DME oxidation and atomic O production from plasma and subsequent radical productions initiate and control DME low temperature oxidation.

4.4. Effects of plasma on flames: the role of O_3 and $\text{O}_2(^1\Delta_g)$

Similar to flame extinction, the radical pool produced by the flame is rich and the kinetic effect of plasma on flame speed is difficult to be observed and quantified without a significant amount of energy input. Ombrello and his co-workers investigated the effect of O_3 [157] and excited oxygen (singlet delta oxygen, $\text{O}_2(^1\Delta_g)$) [156] on flame propagation using lifted flames in which the flame lift-off height is very sensitive to flame speed. Therefore, the plasma enhancement effect on flame speed can be identified without a significant amount of energy input. The lifted flame burner consisted of a central fuel jet with an inner diameter of 0.271 mm that was located in a 90 mm inner diameter quartz tube to contain the

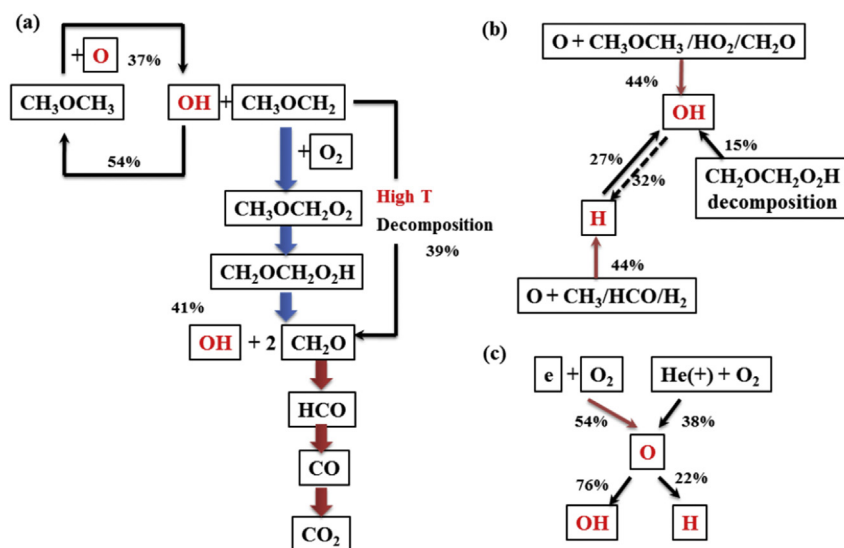


Fig. 4.26. Path flux analysis (a) DME consumption pathways (b) OH and H formation pathways (c) reaction pathways of O , $X_F = 0.01$, $X_{\text{O}} = 0.4$, $P = 72$ Torr, $f = 24$ kHz, $a = 250$ 1/s [107].

co-flow oxidizer. O_3 and $O_2(a^1\Delta_g)$ were produced by a DBD device and microwave discharge device, respectively.

The effect of O_3 was first studied on the $C_3H_8/O_2/N_2$ lifted flame. O_3 was generated by passing ultra-high purity O_2 through a dielectric barrier discharge device. The O_3 produced by the DBD device was quantified using a one-pass, line-of-sight absorption cell by employing Beer–Lambert's law in the flow downstream of where the O_2 and N_2 streams merged [157].

The lifted flame was established for fixed oxidizer co-flow velocity and O_2 loading (18% in 82% N_2). The lifted flame speeds were evaluated based upon the axial local flow velocity from the similarity solution of the cold flow at the measured liftoff heights with initial jet velocities as summarized in Fig. 4.27. It is clearly shown that there was an enhancement of the lifted flame speed with increasing O_3 concentration and the enhancement increased with the increase in the O_3 concentration. Approximately 3% of flame speed increase was observed by 1000 ppm O_3 addition, which was much less than the effect on ignition.

Numerical simulations were conducted for equivalence ratios of 0.8–1.2 with and without 5000 ppm of O_3 . The results showed that the laminar flame speed was enhanced more for lean and rich equivalence ratios than at stoichiometric because lean and rich premixed flames have relatively weaker reactivity and lower chemical heat release compared to the stoichiometric condition. The analysis showed the O_3 decomposition through



to produce atomic O in the preheating zone. The atomic O rapidly reacts with the fuel via reactions



OH can also be produced from the reaction of O_3 with H via



Then OH further reacts with fuel and fuel fragments to cause heat release in the pre-heat zone of the flame to enhance flame propagation speed.

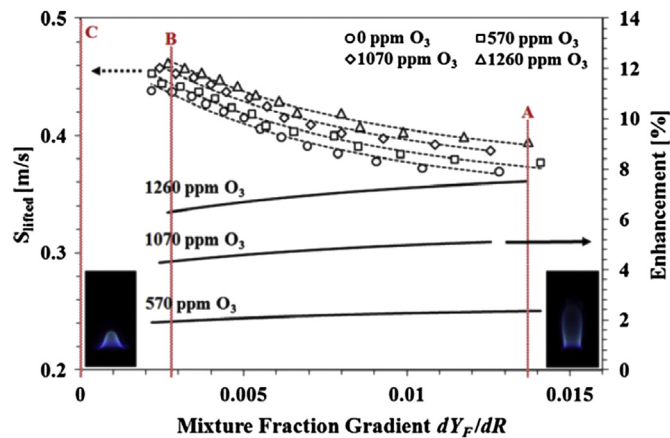


Fig. 4.27. Plot of the lifted flame speed, S_{lifted} , and percent enhancement of S_{lifted} as a function of mixture fraction gradient at 1 atm with and without O_3 addition. The inset pictures of the lifted flames show the differences in the flame front near the fuel nozzle (right) and far from the fuel nozzle (left) [157].

More challenging work was conducted by Ombrello et al. [156] on the same experimental platform to investigate the effect of excited O_2 ($O_2(a^1\Delta_g)$) which has an electronic excitation 0.98 eV. $O_2(a^1\Delta_g)$ has a mean radioactive lifetime of 2700 s [256] and therefore there is a possibility to isolate and transport $O_2(a^1\Delta_g)$ to the flame. In order to stabilize the lifted flame at reduced pressure conditions (3.61 kPa and 6.73 kPa), C_2H_4 was employed as the fuel. The most challenging part of that work was the isolation and the quantification of $O_2(a^1\Delta_g)$. In that study, $O_2(a^1\Delta_g)$ was produced in a microwave discharge and isolated from O_3 by NO addition to the plasma afterglow in a flow residence time on the order of 1 s. The NO addition in the concentration in the experiment has no interference with the effect of $O_2(a^1\Delta_g)$ and can catalytically remove O_3 from the system to isolate $O_2(a^1\Delta_g)$ via reaction (R47).



Reaction R49 is over three orders of magnitude faster than the reaction of NO with $O_2(a^1\Delta_g)$. NO_2 further reacts with O via reaction



Concentrations between 500 ppm and 2000 ppm of NO were added downstream of the plasma to give different concentrations of $O_2(a^1\Delta_g)$ at the flame front. The more NO that was added, the faster the O_3 and O were removed before they reacted with and quenched $O_2(a^1\Delta_g)$.

In this study, Argon (Ar) was used as the dilution gas to avoid the production of NO_x from the microwave discharge. The co-flow compositions were 15% O_2 in 85% Ar for 3.61 kPa and 11.9% O_2 in 88.1% Ar for 6.73 kPa. The concentration of $O_2(a^1\Delta_g)$ was measured quantitatively through off-axis integrated cavity output spectroscopy (ICOS) [257]. It was found that $O_2(a^1\Delta_g)$ increased the flame liftoff height of C_2H_4 flames, and hence the flame speed with the increase in $O_2(a^1\Delta_g)$ concentration as shown in Fig. 4.28. However, unlike the lifted flame at atmospheric pressure described in the work related to O_3 , a cold flow similarity solution does not correctly describe the low pressure experiments. Therefore, an indirect method was used to estimate the amount of flame speed enhancement. Fig. 4.28 indicates that approximately ten times the amount of $O_2(a^1\Delta_g)$ (~5500 ppm) was needed to achieve the same enhancement as O_3 (~500 ppm) which corresponded to approximately 1% flame speed enhancement.

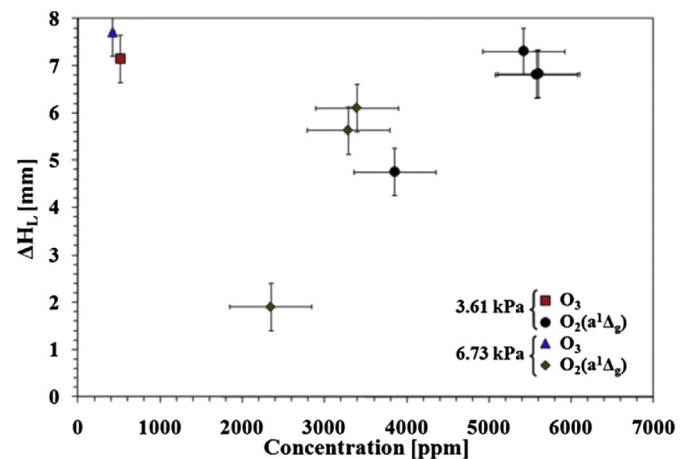
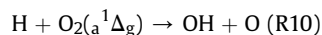


Fig. 4.28. Plot of experimental results of flame liftoff change with $O_2(a^1\Delta_g)$ and O_3 concentration for a plasma power of 80 W. The error bars denote the experimental uncertainties in the concentrations and change in flame liftoff height [156].

The authors also conducted numerical simulations to investigate the pathways of enhancement. They employed currently published collisional and reactive quenching reactions [258,259] and found that the results of enhancement of using the $O_2(a^1\Delta_g)$ concentrations in the experiments could be more than 5% which deviated with experiments significantly by a factor 5. Analysis showed $O_2(a^1\Delta_g)$ was dominantly consumed by chain branching reaction



in the preheating zone. Therefore, it is very possible that the quenching reactions of $O_2(a^1\Delta_g)$ with fuel and its fragments which are missing in current model decreased the concentration of $O_2(a^1\Delta_g)$ significantly and led to lesser enhancement. This work provided an important experimental platform to validate the kinetic mechanisms involving $O_2(a^1\Delta_g)$. More recent modeling work about $O_2(a^1\Delta_g)$ can be found in Refs. [260,261] and will be discussed later.

Wang et al. [158] investigated the effect of O_3 addition on the enhancement of flame speed directly for premixed CH_4 /air flames using the Heat Flux method. The O_3 was generated by a DBD ozone generator installed in the O_2 gas line. A heat flux burner was adopted for the adiabatic burning velocity measurement and all experiments were performed at atmospheric pressure. The burning velocity enhancement is shown in Fig. 4.29 with 2330 ppm and 3730 ppm O_3 addition as a function of equivalence ratio for CH_4 /air flame. Noticeable burning velocity enhancement was observed and the enhancement was more significant at off-stoichiometric conditions rather than at stoichiometric conditions. With 3730 ppm O_3 addition in the oxidizer, experimental results showed ~8% flame speed increase in fuel rich mixture and ~3.5% flame speed increase for the stoichiometric mixture. An O_3 kinetic mechanism involving 16 elementary reactions together with GRI-Mech 3.0 [240] was composed and validated through PREMIX [262] calculation, which gave good predictions of the burning velocities with and without O_3 addition as shown in Fig. 4.29. The simulation showed that the atomic O radicals contributed by O_3 in the preheating zone initiated and accelerated the chain-branching reactions and consequently increased the flame speed.

Similar experiments were conducted on the identical experimental platform for $H_2/CO/N_2$ /air premixed flames [159].

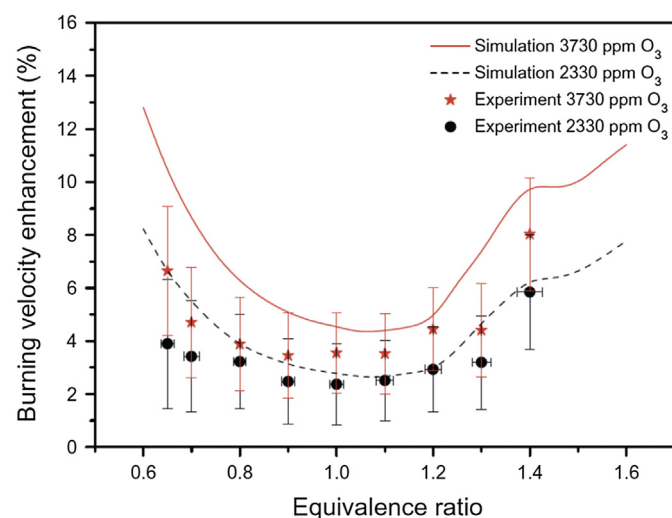


Fig. 4.29. Simulation and experimental results for burning velocity enhancement as a function of equivalence ratios [158].

Experimental data showed significant enhancement of the burning velocities due to O_3 addition. With 8500 ppm O_3 addition, maximum 18.74% of burning velocity enhancement was observed at an equivalence ratio of $\Phi = 0.7$.

By summarizing available data for CH_4 [158,263,264], and CO/H_2 [159], approximately 1% flame speed enhancement can be achieved by every 1000 ppm O_3 addition at 1 atm, which is far smaller than the kinetic effect of ozone on ignition and low temperature fuel oxidation.

Recently, a novel method to establish self-sustaining cool diffusion flames with well-defined boundary conditions has been experimentally demonstrated by adding ozone into the oxidizer stream in a counterflow configuration [108] (Fig. 4.30). It was found that the formation of atomic oxygen via the decomposition of ozone dramatically shortens the induction timescale of low temperature chemistry, extending the flammable region of cool flames, and enables the establishment of self-sustaining cool flames at pressure and time scales at which normal cool flames may not be observable. Cool flame chemistry [265–268] has been studied in the past for the interest of engine knock [267] and fuel reforming [265] in stirred reactor or flow reactor. However, this new method, for the first time, provided an opportunity to stabilize and study cool flame dynamics, structure, and chemistry simultaneously in well-known flame geometry at atmospheric pressure without oscillation nature. Extinction limits of n-heptane/oxygen cool diffusion flames were measured. A cool diffusion flame diagram for four different flame regimes was experimentally measured. Numerical simulations showed that the extinction limits of cool diffusion flames were strongly governed by species transport and low temperature chemistry activated by ozone decomposition. The structure of cool diffusion flame was further investigated by measuring the temperature and species distributions with a micro-probe sampling technique. It was found that the model over-predicts the rate of n-heptane oxidation, the heat release rate, and the flame temperature. Measurements of intermediate species, such as CH_2O , acetaldehyde, C_2H_4 , and CH_4 indicated that the model over-predicted the QOOH thermal decomposition reactions to form olefins, resulting in substantial over-estimation of C_2H_4 , and CH_4 concentrations. The new experimental method of cool flame provides an unprecedented platform to understand cool flame and low temperature chemistry.

The ozone assisted cool flames supported the discussions in Section 3, that is, plasma enhances ignition and low temperature fuel oxidation kinetically more than high temperature flame propagation. In future research, if a self-sustaining premixed cool flame is established by a similar method and appropriate diagnostic methods are developed, this method will bridge our knowledge gap of cool flames for more than one century. At high pressure, the cool flame chemistry will be enhanced. Quantitative study of cool

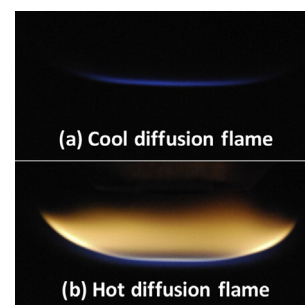


Fig. 4.30. Direct photos of n-heptane/oxygen cool diffusion flame (a) and hot diffusion flame (b) flames, observed at the identical flow condition, fuel mole fraction of 0.07 and strain rate of 100 s^{-1} [108].

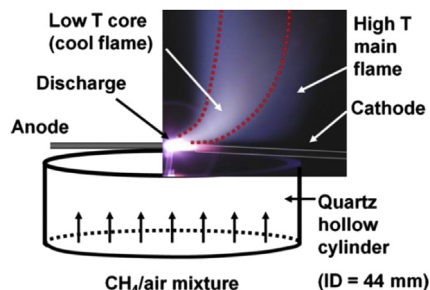


Fig. 4.31. Plasma assisted CH_4/air premixed flame. The red dotted lines represent the visible boundary of the low temperature CH_4 flame [269]. (For interpretation of the references to color in this figure legend, the reader is referred to the web version of this article.)

flames may provide a key solution to solve engine knocking and develop new engine technologies.

It is worth noting that the cool flame discussed above in Fig. 4.30 is controlled by low temperature chemistry of fuels (formation and decomposition of QOOH) which is different from fuel oxidation at low temperature condition. Another type of direct low temperature fuel oxidation by plasma discharge for small hydrocarbon fuels without low temperature chemistry had been also reported before by Kim et al. [269] in a plasma assisted premixed combustion system with ultra-lean CH_4/air mixture (Fig. 4.31). At low equivalence ratios, this low temperature flame was observed without the ignition by the surrounding high temperature flame. It was found that the temperature of the flame could be lower than 500 K. Because CH_4 has no low temperature chemistry, as reported low temperature flames by the authors is more like the flame regime shown in Figs. 1.4 and 4.22b (for CH_4 also). This low temperature flame is initiated by direct O production via reactions R8 and R9 and the subsequent partial fuel oxidation via reaction channels shown in Fig. 4.23. Therefore, it should be noted that different from the cool flames (radical production via plasma assisted QOOH formation and isomerization) of n-heptane, the low temperature CH_4 flame observed [269] is more likely the plasma assisted direct CH_4 partial oxidation/reforming via atomic O production [40]. These two flames, although both have low temperature, have different kinetic mechanisms and should not be confused.

5. Advanced diagnostics for plasma assisted combustion

5.1. Measurements of plasma properties

5.1.1. Thomson scattering for electron density and electron temperature measurement

The most beneficial advantage of non-equilibrium plasma on combustion enhancement is the radical production at low temperature conditions. Through the path flux analysis shown in Section 4.2, electron number density and electron temperature are two important parameters determining radical production through electron impact reactions. Therefore, the measurement of electron density and electron temperature is very important for the study of plasma assisted combustion and the validation of kinetic models.

Thomson scattering is an elastic scattering process involving photons scattering off of a free charged particle. This diagnostic technique is a non-intrusive, point measurement technique, and is therefore used to measure spatial and temporal electron number density, and electron temperature [270]. The major limitation of Thomson scattering is its weak scattering signal intensity owing to the low number density of free electrons in the plasma. Other

limitations include interference from Rayleigh scattering as well as plasma emission. Since the number densities of neutral species are much higher than the number density of free electrons in non-equilibrium plasmas, the Rayleigh signal is several orders of magnitude larger than the Thomson signal. However, since Doppler broadening is inversely proportional to the square root of the mass of the particle, and the mass of neutral species is about four orders of magnitude higher than that of free electrons, the Thomson scattering line width is significantly broader than that of the Rayleigh scattering. So several possible techniques for filtering the Rayleigh signal, including selective absorption and masking, can be applied to filter the Thomson scattering signal. The resulting Thomson scattering spectrum can be approximated by a Gaussian line shape if the electron energy distribution is Maxwellian, which can be used for inference of the average electron energy (electron temperature). The integrated Thomson scattering cross section is $6.65 \times 10^{-25} \text{ cm}^2$. Details on data processing for Thomson scattering can be found in Ref. [270].

In low electron density plasmas, where the incident light wavelength is much shorter than the effective distance between free electrons (proportional to Debye length), the Thomson scattering is considered incoherent, and thus the total intensity of the scattering is simply the sum of the intensities from each scattering electron. This is often described by the dimensionless parameter $\alpha = 1/(k\lambda_D)$, where k is the scattering wave vector magnitude (proportional to $1/\lambda$), and λ_D is the Debye length. If $\alpha \ll 1$, free electrons and ions do not significantly affect each other.

Fig. 5.1 shows a schematic of the Thomson Scattering experimental setup that was used by Roettgen et al. [270]. A frequency doubled (532 nm) Nd:YAG laser, with a pulse energy of ~600 mJ at 30 Hz repetition rate, serves as the pump source. This beam is focused into a glass test cell which can be filled with different gas mixtures at different pressures. The laser beam enters and exits the test cell through windows at Brewster's angle to reduce stray light. An achromatic doublet collection lens ($D = 31.5 \text{ mm}$, $f_{\text{lens}} = 200 \text{ mm}$) is placed at a scattering angle of 90° from the laser beam direction to optimally collect the scattered photons from the beam. The collimated scattering signal is then sent through an image rotator (three silver protected mirrors), which rotates both the image (to vertical orientation) and the polarization (to horizontal), since horizontal polarization maximizes the grating efficiency. The scattered light is then focused down onto a vertical slit with another achromatic doublet lens ($D = 31.5 \text{ mm}$, $f_{\text{lens}} = 200 \text{ mm}$), and enters the triple grating spectrometer [271]. Thomson scattering signal is collected from a 3 mm long, ~60 micron diameter volume of the discharge, spatially averaging the signals over this region.

The electron temperature is proportional to the half-width at half-maximum (HWHM) of the Thomson (Gaussian) profile, as follows:

$$\Delta\nu_D' = \frac{2\nu_0}{c} \sqrt{\frac{2 \ln(2) k_B T_e}{m_e}} \sin\left(\frac{\theta}{2}\right) \quad (5.1)$$

where $\Delta\nu_D'$ is HWHM, ν_0 is the incident radiation frequency, c is the speed of light in vacuum, k_B is the Boltzmann constant, m_e is the electron mass, θ is the scattering angle (90°), and T_e is the electron temperature. Thus, the electron temperature can be inferred directly from HWHM from the Gaussian fit. The electron number density is proportional to the integrated intensity of the Thomson profile. So calibration of the integrated intensity by pure rotational N_2 Raman spectrum was conducted to put the electron number density on an absolute scale.

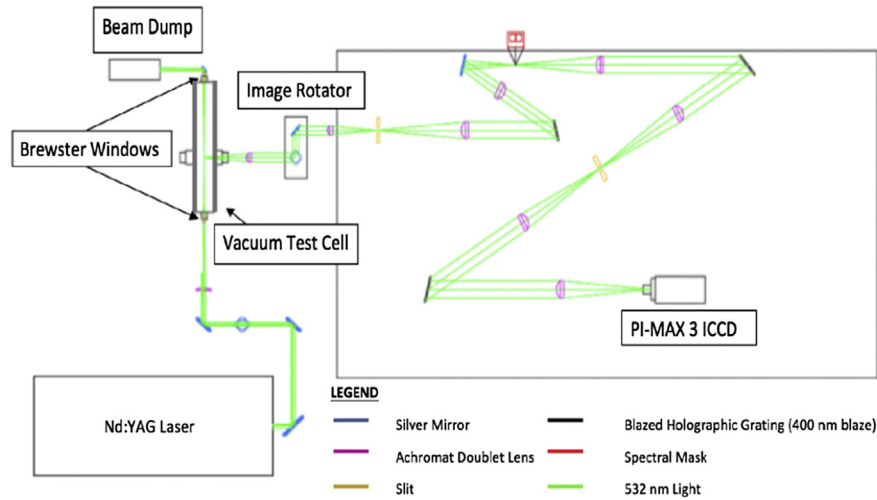


Fig. 5.1. Schematic diagram of the Thomson scattering experimental setup [270].

Electron number density was then calculated from the following equation:

$$n_e = \frac{A_e}{A_{N_2}} \frac{\left(\frac{d\sigma_{N_2}}{d\Omega}\right)_{532\text{nm}}}{\left(\frac{d\sigma_2}{d\Omega}\right)} n_{N_2} f_{J=6} \quad (5.2)$$

where n_e is electron number density, A_e is the integrated Thomson scattering signal intensity, A_{N_2} is the integrated $N_2 J = 6 \rightarrow 8$ Raman transition intensity, $(d\sigma_{N_2}/d\Omega)_{532\text{nm}}$ is the differential Raman cross-section area at 532 nm, $(d\sigma_2/d\Omega)$ is the differential Thomson scattering cross-section for vertically polarized light with 90° scattering angle, n_{N_2} is the number density of nitrogen (calculated from known temperature and pressure in the cell using ideal gas equation of state), and $f_{J=6}$ is the relative fraction of nitrogen molecules in the rotational level $J = 6$ (calculated from Boltzmann rotational distribution in rigid-rotor approximation).

Roettgen et al. [270] reported that the peak measured electron number density in a nanosecond pulsed pure He discharge at 200 Torr was $n_e \approx 3.5 \times 10^{15} \text{ cm}^{-3}$. After this, the electron density decayed exponentially over 3 μs . Peak electron temperature measured was approximately 4 eV. Thomson scattering technique is a diagnostic tool to investigate these two critical parameters for plasma assisted combustion and can provide valuable input parameters for numerical modeling.

Note that the Thomson scattering technique requires expensive equipment setup. Alternative electron number density measurements can also be made by using the Stark line broadening and the optical emission spectroscopy line-ratio method, respectively, in different ranges of electron number densities [272].

5.1.2. Electric field measurement

Another key parameter determining the electron energy is the reduced electrical field E/N where E is the electric field and N is the particle number density which is determined by temperature and pressure. Due to the effect of dielectrics and formation of sheath, the calculation of electric field in the bulk plasma region is not straightforward. Therefore, measurement of the electric field in the plasma discharge is very beneficial for both doing experiments and modeling. Several methods have been reported for the measurement of the electric field in the plasma discharge.

In 1992, Gavrilenko et al. [273] reported that coherent IR emission from H_2 molecule can be induced by laser light and a static electric field. The IR intensity depends quadratically on the intensity of the electric field. Therefore, this effect can be utilized to develop a nonlinear-optics method for the measurement of electric fields.

Based on this seminal work, Yatom et al. [274] measured the electrical field in a nanosecond H_2 plasma channel at $2 \times 10^5 \text{ Pa}$ by the Coherent Anti-Stokes Raman scattering method (CARS). CARS is based on the generation of coherent infrared radiation as a result of the biharmonic laser pumping of a symmetrical diatomic molecule in an external electric field. The dipole moment of the molecules is induced by the electric field therefore allowing the IR vibrational transitions in the dipole approximation. In the study of Ref. [274], A pump laser beam at $\lambda = 532 \text{ nm}$ was coaligned with the Stokes beam at $\lambda = 683 \text{ nm}$ to generate Anti-Stokes ($\lambda = 436 \text{ nm}$) and IR ($\lambda = 2.4 \mu\text{m}$) radiation. The electric field can be then calculated as

$$E = C \sqrt{\frac{I_{2.4}}{I_{436}} I_{532}} \quad (5.3)$$

where $I_{2.4}$ is the intensity of IR signal, I_{436} is the intensity of the anti-Stokes signal, I_{532} is the intensity of the pump laser, and C is the constant that depends on the experimental conditions. This technique still requires calibration of the constant C by performing the experiment in the given optical setup with a uniform and known electric field. By using this method, the electric field intensities of up to 30 kV/cm was reported for an experiment by applying $\sim 100 \text{ kV}$ high voltage pulse to a blade cathode placed at a distance of 20 mm from the anode.

Using H_2 as the active species, high signal-to-noise ratio and measurement sensitivity can be achieved owing to the large Raman cross section of H_2 [275]. It becomes challenging to measure the electric field in N_2 or air plasma. In 2009, Ito et al. [276] demonstrated the feasibility of electric field measurement based on the field-induced coherent Raman scattering in N_2 containing gas at atmospheric pressure for the first time. The minimum detectable field strength in air was as low as 100 V/mm. The detailed diagnostic study of the N_2 CARS based electric field measurement can be found in a recent work by Lempert et al. [275].

Starikovskaia et al. [277] measured the electric field in surface dielectric barrier discharge by measuring the relative intensity of the second positive ($N_2(C^3\Pi_u) - N_2(B^2\Pi_g)$, $v' - v'' = 0-0$,

$\lambda = 337.1$ nm) and the first negative ($N_2^+(B^2\Sigma_u^+) - N_2^+(X^2\Sigma_g^+)$, $v' - v'' = 0-0$, $\lambda = 391.1$ nm) systems of nitrogen. In order to link the intensity ratio of the two bands of N_2 to the electric field, two approaches can be applied. The first approach assumes quasi-steady-state. So the rate of population by direct electronic impact is equal to the rate of depopulation due to emission and quenching. The ratio of rate constants of excitation, k_C/k_B , depends upon the ratio of population of excited levels. The population of excited species and optical emission are then related to each other. On the other hand, the ratio of k_C/k_B can be calculated for a given EEDF using known cross sections. Therefore, electric field can be solved from the emission spectroscopy. The second approach requires calibration of the ratio of emissions of these two excited levels under fixed known E/N values in non-sustained discharge system. Employing this technique, 700–1000 Td reduced electric field values were calculated and reported in surface dielectric barrier discharge [277].

5.2. Measurements of plasma generated excited species

5.2.1. Measurement of ozone

Plasma can generate atomic O efficiently through electron impact reactions with O_2 . At low temperature conditions (below 500 K) without the presence of fuel, atomic O recombines with O_2 quickly to form ozone (O_3). O_3 has very long lifetime which is of approximately 3 days at room temperature, 1.5 h at 400 K and 1.5 s at 500 K. O_3 is one of the strongest oxidizers and can be efficiently produced at high pressure conditions. The concentration of O_3 can be accurately quantified by absorption method.

Under conditions of weak absorption, the radiation intensity of a light source (e.g., lasers, lamps) $I(\nu)$ transmitted through a homogeneous gas sample is given by the Beer–Lambert Law:

$$I(\nu) = I_0(\nu)\exp[-k(\nu)l_{abs}] \quad (5.4)$$

where $I_0(\nu)$ is the incident intensity, $k(\nu)$ is the absorption coefficient and l_{abs} is the absorption length. The absorption coefficient $k(\nu)$ is linked to the absorption cross section, σ and the number density N of the absorbers. With a known line strength, absorption cross section, and the absorption length, the absolute density of the absorber can be obtained [161].

In the work of Ref. [157] to quantify O_3 concentration, a mercury lamp with stable output of 253.7 nm UV light where O_3 has a peak absorption cross section of 1.137×10^{-17} cm² at 300 K, was used as the light source. Beer–Lambert Law was then employed to determine the O_3 concentration:

$$N_{ozone} = \frac{-\ln\left(\frac{I}{I_0}\right)}{\sigma_{ozone}l_{abs}} \quad (5.5)$$

where N_{ozone} is the absolute number density of O_3 , I is the intensity of the light with the presence of O_3 , I_0 is the intensity of light without the presence of O_3 , σ_{ozone} is the absorption cross-section of O_3 at the excitation wavelength of 253.7 nm, and l_{abs} is the path length. The authors [157] reported the concentration in parts per million of O_3 with an uncertainty of approximately 2% and a minimum detectable threshold of approximately 15 ppm in a microwave discharge cell at 1 atm.

5.2.2. Measurement of singlet delta oxygen, $O_2(a^1\Delta_g)$

Singlet delta oxygen ($O_2(a^1\Delta_g)$) is electronically excited O_2 to its first electronically excited low-energy level at 0.98 eV. Singlet delta oxygen has higher oxidation potential than O_2 and has a significantly long radiative lifetime which is longer than 4000 s, owing to

a spin forbidden transition to the ground state. Therefore, it has attracted much attention.

In the work conducted by Ombrello et al. [156], Integrated Cavity Output Spectroscopy (ICOS) [257] was adopted to obtain the absolute concentrations of $O_2(a^1\Delta_g)$ by measuring absorption feature of the (1,0) band of the $b^1\Sigma_g^+ - a^1\Delta_g$ Noxon system. A single-mode, fiber-pigtailed distributed-feedback diode laser (1505 nm, 0.0001 cm⁻¹ bandwidth) was coupled into the optical cavity in an off-axis alignment. The system measured the average number density of $O_2(a^1\Delta_g)$ across an 82.5 cm long absorption cell and provided accurate measurements down to 10^{14} molecules/cm³. The effective path length was greater than 78 km due to the multiple passes. In order to avoid quenching from atomic O and O_3 , NO was doped in the flow system to convert atomic O and O_3 to O_2 . $O_2(a^1\Delta_g)$ was produced in a microwave discharge cell at 3.61 kPa and then quantified by using Eq. (5.5). The sensitivity of this method is a few ppm at the experimental condition. Several thousand ppm of $O_2(a^1\Delta_g)$ produced by a microwave discharge was detected.

5.2.3. Measurement of electronically and vibrationally excited nitrogen

Stancu et al. [161] quantified electronically excited N_2 ($N_2(A)$, $N_2(B)$, and $N_2(C)$) in a pin-to-pin nanosecond pulsed discharge at 1 atm. $N_2(A)$ was studied by probing the ($2 \leftarrow 0$) vibrational band of the N_2 first positive system ($B^3\Pi_g \leftarrow A^3\Sigma_u^+$) in the vicinity of 770 nm using Cavity ring-down spectroscopy (CRDS). CRDS is a technique to improve the detection sensitivity from ppm to ppb level. Effective kilometer-absorption lengths in much smaller detection volumes can be achieved with the CRDS technique using high-finesse optical cavities.

In pulsed CRDS, a laser pulse is coupled into an optical cavity formed usually by two highly reflective mirrors. Each time the pulse reaches one of the mirrors a small fraction of the light leaks out. When the laser is tuned to an absorption transition of the species present inside the cavity, the decay of pulses is faster. The difference of the decay times, τ , for on-resonance and off-resonance measurements is proportional to the absorption coefficient:

$$k(\nu) = \frac{L}{cl_{abs}} \left(\frac{1}{\tau_{off-res}} - \frac{1}{\tau_{on-res}} \right) \quad (5.6)$$

where c is the speed of light, L is the cavity length, l_{abs} is the absorption length and $k(\nu)$ is the absorption coefficient as discussed in Section 5.2.1. $N_2(A)$ number density can be then calculated using the parameters on the right hand side of Eq. (5.5) measured in the experiments.

In order to quantify $N_2(B)$, and $N_2(C)$, optical emission spectroscopy is employed by Stancu et al. [161] in the range of 500–800 nm for $N_2(B)$, and 300–500 nm for $N_2(C)$, respectively. The local emissivity, e_λ , of a volumetric light source is

$$e_\lambda = \frac{1}{4\pi} h\nu A_{21} N_2 \phi(\lambda) \quad (5.7)$$

where $h\nu$ is the photon energy, A_{21} is the Einstein coefficient, N_2 is the population density of the upper state from where spontaneous emission occurs and $\phi(\lambda)$ is the normalized profile function. The emission intensity which is wavelength-dependent measured by a spectrometer corresponds to the line-of-sight integration of emissivity. In the pin–pin electrode configuration used by Stancu et al. [161], the discharge has cylindrical symmetry. An Abel transform is applied to obtain the local distribution of the emissivity $e_\lambda(r)$. However, the emission in absolute units is very difficult to obtain. Typically a calibrated light source is required to calibrate experimental parameters including the solid angle, length of collection

volume, response of the spectrometer and collection optics, and quantum efficiency of the detector. After calibration, the local particle densities of $N_2(B)$, and $N_2(C)$ can be obtained.

Measurement of vibrationally excited nitrogen $N_2(v)$ has also been conducted by Macko et al. [278] using CRDS. The absolute density of $N_2(v)$ at $v = 18$ level in a 2.3 Torr DC glow discharge was reported to be $(9 \pm 3.5) \times 10^{19} \text{ m}^{-3}$ [278]. Even though Montello et al. [165] did not quantify the absolute density of $N_2(v)$, he investigated N_2 vibrational loading and relaxation kinetics in non-equilibrium N_2 and air discharge using Picosecond coherent anti-Stokes Raman spectroscopy (CARS) to measure rotational/translational and vibrational temperature. Approximately 50% of coupled discharge power goes to the vibrational mode of nitrogen through electron impact excitation. More details on CARS will be discussed in Section 5.4.2.

5.3. Measurements of active radicals by laser induced fluorescence method

Active radicals such as O, H, and OH play an important role in plasma assisted combustion. Detection of active radicals in PAC has been conducted by using single and two photon laser induced fluorescence methods. The laser induced fluorescence method is an inelastic process in which photons are absorbed by the molecules or atoms and then re-emitted at the same or different wavelengths. The absorbed photons excite molecules or atoms to an energy level above the ground state, and then photons are released during the de-excitation process and can be detected. If only one photon is absorbed to generate excitation, it is generally called Laser Induced Fluorescence (LIF). If two photons are absorbed in order to excite the species to a higher energy level, it is called Two photon Absorption Laser Induced Fluorescence (TALIF).

5.3.1. OH measurement by OH PLIF method

The OH PLIF technique has been widely used to quantify the OH concentrations. If one photon is absorbed by the OH molecules, fluorescence occurs during the de-excitation process. The fluorescence signal, S_f , can be expressed as [279].

$$S_f = \eta V_c n_{OH} f_B B_{12} E \phi_j \quad (5.8)$$

where η represents the overall efficiency of the optical setup in collecting fluorescence photons, V_c is the collection volume, n_{OH} is the OH number density, f_B is the Boltzmann factor for OH molecules in the absorbing state, B_{12} is the Einstein absorption coefficient, E is the laser energy, and ϕ_j is the fluorescence quantum efficiency. Since η and V_c are not well-defined parameters, calibration by a known concentration of the species in the combustion system is required to quantify the OH measurement.

Choi et al. [280] studied the OH radical kinetics in repetitively pulsed H_2 /air nanosecond plasmas at $P = 54\text{--}94$ Torr and initial temperature of $T = 100\text{--}200\text{ }^\circ\text{C}$, equivalence $\Phi = 1.0$ at a flow velocity of 0.5 m/s employing a plasma activated quartz reactor [250]. A UV laser beam at 283 nm was used to excite the $A^2\Sigma^+ \leftarrow X^2\Pi(1,0)$ electronic transition, followed by fluorescence detection in the $A^2\Sigma^+ \rightarrow X^2\Pi(1,1)$ band centered at ~ 315 nm. OH LIF data obtained from the plasma experiment were put on an absolute scale after calibrating with an atmospheric-pressure near-adiabatic C_2H_4 /air flame–flame Hencken burner. It is noteworthy that the correction for differences in the collisional quenching and vibrational energy transfer (VET) rates, which accounts for the change of the fluorescence quantum efficiency (ϕ_j), was considered in detail in Ref. [280] for the calibration of absolute OH number density. It was pointed out that the ratio of the VET rate to the quenching rate

was greater in the low pressure plasma discharge cell than in the atmospheric pressure Hencken burner.

Through OH PLIF measurement, Choi et al. [280] found that the typical value of OH number density after a single discharge pulse was on the order of 10^{12} cm^{-3} . For a single discharge pulse, absolute OH number density increased rapidly during the initial ~ 0.1 ms after the discharge initiation and decayed relatively slowly, with a characteristic time scale of ~ 1 ms. In a repetitive burst mode, the absolute OH number density was observed to rise rapidly during the first approximately 10 pulses and then level off to a nearly steady-state plateau. After approximately 5–10 ms, ignition happened accompanying a sharp rise in OH number density.

OH measurements have also been conducted in plasma assisted ignition, stabilization, and flame extinction [56,144,147,249].

5.3.2. Atomic O and H measurement by TALIF method

The Two photon Absorption Laser Induced Fluorescence (TALIF) method, calibrated with Xenon, was used to measure the absolute atomic O concentration produced by the discharge. Ground state atomic O is excited by absorbing two photons at a wavelength of 225.7 nm. The transition between the excited $3p\ ^3P$ state and the $3s\ ^3S$ state releases a single photon at 844.6 nm. Xenon can be excited from $5p^6\ ^1S_0$ to $6p'[3/2]_2$ with two photons at 224.31 nm; de-excitation to $6s'\ [1/2]_1$ corresponds to fluorescence at 834.91 nm.

The number density of atomic O (N_O) was calculated using the following equation in terms of the known number density of Xenon (N_{Xe}) [281],

$$N_O = \frac{S_O}{S_{Xe}} g_{ND} \frac{a_{21}(Xe)}{a_{21}(O)} \left(\frac{\sigma^{(2)}(Xe)}{\sigma^{(2)}(O)} \right) \left(\frac{v_O}{v_{Xe}} \right)^2 \times \frac{1}{F_O(T)} N_{Xe} \quad (5.9)$$

where S_O and S_{Xe} are the observed fluorescence signals for O and Xenon, respectively, $a_{21} = A_{21}/A_{21} + Q$ is the fluorescence quantum yield (A_{21} and Q are the spontaneous emission and quenching rates, respectively), $\sigma^{(2)}$ is the two photon absorption cross sections of Xe and O, $F_O(T)$ is the atomic O Boltzmann factor for the lower level of the two photon absorption, v_i represents the photon energies, and g_{ND} is the neutral density filter factor (neutral density filter needs to be applied because the fluorescence from excited Xe is orders of magnitude higher than the fluorescence from excited atomic O). These values can be found or easily calculated based on the data in Refs. [251,281].

A typical schematic of the TALIF system employed in Ref. [43] is shown in Fig. 5.2. An Nd:YAG laser was used to generate 532 nm to pump a tunable dye laser operating at ~ 573 nm. This 573 nm beam was frequency doubled and mixed with the 1064 nm beam of the Nd:YAG laser to get a ~ 226 nm beam of $\sim 10\text{ }\mu\text{J/pulse}$ required for the TALIF diagnostics. The UV beam was focused 30 mm ahead of the probe volume to avoid saturation. The TALIF signal was focused by a lens with a 300 mm focal length and observed through an 850 nm bandpass filter of 40 nm FWHM using a photomultiplier. The atomic O TALIF signal was then quantified by Xenon TALIF signal [251,281]. The overall relative mole fraction uncertainty of the TALIF measurement was approximately $\pm 40\%$.

Yin et al. [282] measured the concentration of H in a $Ar/O_2/H_2$ nanosecond pulsed discharge in a point-to-point geometry at 40 Torr using TALIF. $H\ 3d^2D_{3/2,5/2} \leftarrow 1s^2S_{1/2}$ line was excited by two photons at 205.144 nm. Fluorescence at ~ 656 nm was measured and calibrated by Kr. The calibration process is very similar to the atomic O TALIF measurement discussed above but uses two photons excitation of $Kr\ 5p'[3/2]_2 \leftarrow 2p^6^1S_0$ line at 204.194 nm. Peak concentration of H during the discharge was reported to be approximately $6 \times 10^{15} \text{ cm}^{-3}$.

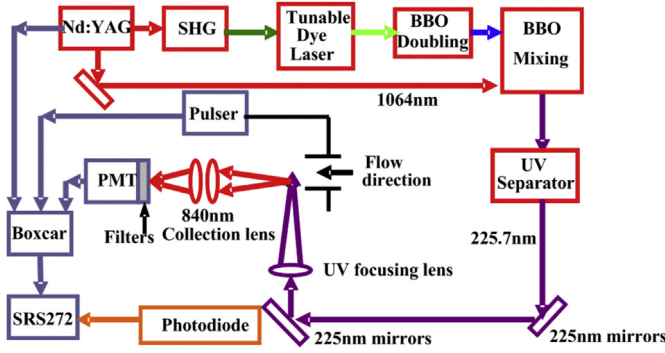


Fig. 5.2. Schematic of the TALIF setup for atomic O measurement [43].

5.4. Temperature measurements

As one of the most accurate and convenient methods, the thermocouple has been widely used for temperature measurements in combustion research. However, in plasma assisted combustion, due to the ionization of the working gas and unsteady nature of the problem, temperature measurement becomes very challenging. For example, the interaction between the strong electric field and thermocouple makes direct temperature measurement using a thermocouple fail. While special thermocouples [144] coated with ceramics may still apply for steady state problems in weakly ionized environments, advanced thermometry is needed for the diagnostic of plasma assisted combustion.

5.4.1. Planar Rayleigh scattering thermometry

Different from the LIF technique, the Rayleigh scattering technique relies upon the elastic scattering of light by particles much smaller than the wavelength of light used to perform the measurement. Since it is an elastic scattering process, there is no energy exchange between the incident light and the target particles. Thus, the scattered light is unshifted from its initial wavelength [279]. It is important to note that the scattered light signal peaks in the plane orthogonal to the incident light polarization orientation and different particles have different scattering cross-sections for the incident light. The differential scattering cross-section of a particular molecule or atom for Rayleigh scattering at 90° to the incident light is given by [283].

$$\left(\frac{d\sigma_i}{d\Omega}\right) = \frac{4\pi^2(\mu - 1)^2}{N_o^2\lambda^4} \quad (5.10)$$

where μ is the index of refraction of the gas at STP, N_o is the Loschmidt number ($2.69 \times 10^{19} \text{ cm}^{-3}$), and λ is the wavelength of the incident light. The intensity of the Rayleigh scattering, I_{Rayleigh} is described by the relation

$$I_{\text{Rayleigh}} = CIN\Omega l \left(\frac{d\sigma}{d\Omega}\right)_{\text{eff}} \quad (5.11)$$

where C is a calibration constant of the collection optics, I is the incident light intensity, N is the particle number densities, Ω is the solid angle of the collection optics, and l is the length of the laser beam segment imaged onto the detector, and $(d\sigma/d\Omega)_{\text{eff}}$ is the effective scattering cross-sections. In a reacting flow, the gas composition is very complex and the cross-sections can vary significantly. The effective scattering cross-sections need to be calculated using the following mole fraction weighted scattering cross-sections of different molecules or atoms in the flow.

$$\left(\frac{d\sigma}{d\Omega}\right)_{\text{eff}} = \sum X_i \left(\frac{d\sigma_i}{d\Omega}\right) \quad (5.12)$$

The interaction of light with particles is a function of species concentrations, scattering cross-sections, and particle density (temperature). Therefore, with known effective cross-sections, particle density (temperature) can be derived from Eq. (5.11). However, the values of C , I , Ω and l are not well-defined so calibration is still required to extract the quantitative results. The calibrations are conducted by comparing the signals with that from measurements with known composition, temperature and pressure to remove the uncertainty from C , I , Ω and l .

In the study of Sun et al. [144], Rayleigh scattering thermometry was employed to measure the temperatures of the flame with and without *in situ* plasma discharge in a counterflow burner. The flow composition was calculated using OPPDIF [284] to calculate the effective cross-sections. Only major species (He , O_2 , CH_4 , CO , CO_2 and H_2O) were considered during the calculation of effective cross-sections and these values can be found in Ref. [285]. The Rayleigh scattering measurement was conducted with an Nd:YAG laser at 532 nm and the signals were collected with an ICCD camera (Princeton Instrument, PI-MAX) with a narrow band filter near 532 nm. A total of 1500 images were accumulated and averaged to obtain a high signal to noise ratio. The maximum uncertainty of the Rayleigh scattering temperature measurements is found to be $\pm 80 \text{ K}$, depending on the measurement location. Fig. 5.3 shows the temperature profiles measured by Rayleigh scattering and compared with simulations with and without the *in situ* discharge in a counterflow flow system in the work of Ref. [144].

5.4.2. Coherent anti-Stokes Raman scattering (CARS) thermometry

CARS thermometry is a nonlinear optical technique involving a four-wave mixing process. The detailed mechanism of rotational CARS can be found in Ref. [286]. It can be used for high spatial and temporal resolution measurement of temperature distributions in flames and plasmas. Zuzek et al. [287] conducted rotational Coherent Anti-Stokes Raman scattering (CARS) thermometry measurement before ignition in the same plasma activated flow reactor used by Uddi et al. [160] in $\text{C}_2\text{H}_4/\text{air}$ at stoichiometric and fuel lean conditions at 40 Torr pressure. Air and fuel/air mixtures were excited by a burst of high-voltage nanosecond pulses (peak

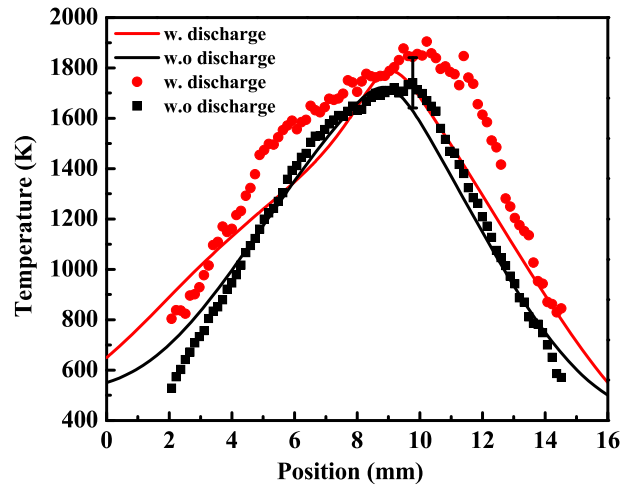


Fig. 5.3. Temperature profiles in a counterflow $\text{CH}_4/\text{O}_2/\text{He}$ diffusion flame with and without *in situ* discharge, $X_{\text{O}} = 53.5\%$, $X_{\text{f}} = 20\%$, $a = 400 \text{ 1/s}$, $P = 72 \text{ Torr}$ (symbols: experiments, lines: simulation) [145].

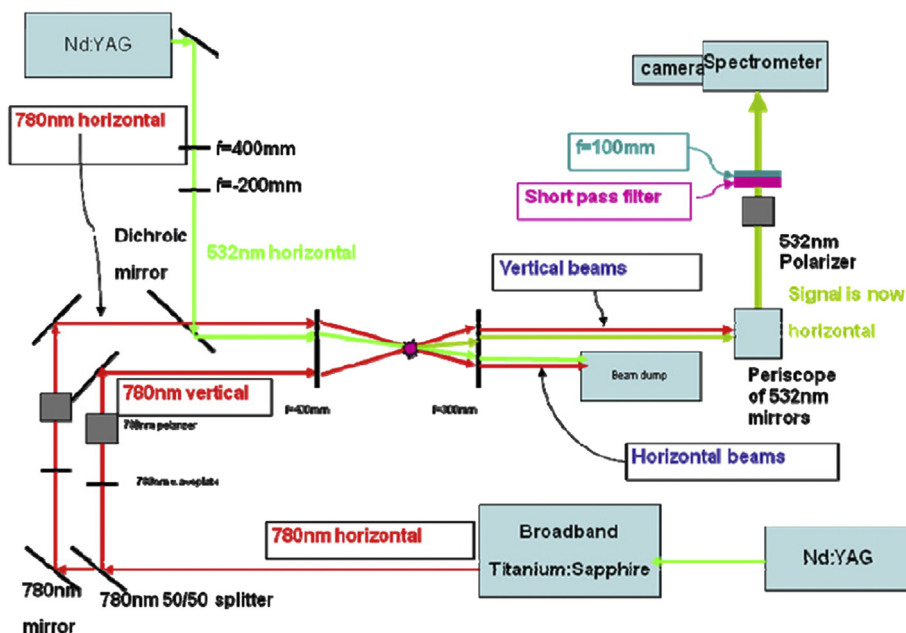


Fig. 5.4. Schematic diagram of pure rotational CARS apparatus [287].

voltage, 20 kV; pulse duration, ~25 ns) at a 40 kHz pulse repetition rate and a burst repetition rate of 10 Hz.

A schematic of the pure rotational CARS apparatus is shown in Fig. 5.4. An Nd:YAG pumped broadband Ti:sapphire laser with a center wavelength of approximately 780 nm and pulse duration of approximately 15 ns is split into two ‘pump’ beams, with approximately 20 mJ each, and orthogonal linear polarizations. The second harmonic output (532 nm) of a second Nd:YAG laser, with 10 ns pulse duration, is used to generate a horizontally polarized ‘probe’ beam. The pump and probe beams are overlapped in a focused planar phase matching geometry, using a 400 mm focal distance lens. The overlapped focused beams, which propagate parallel to the major axis of the electrodes, form an approximately cylindrically shaped measurement region ~0.1 mm in diameter and 1–2 mm long in the plasma. The pure rotational CARS signal beam is generated with vertical polarization, which allows for very significant (more than a factor of 1000) discrimination from stray, horizontally polarized, probe light using a right angle polarizer. The

CARS beam, after transmission through a short wavelength pass colored glass filter to eliminate residual pump scattering, is focused onto the entrance slit of a $\frac{1}{2}$ meter spectrometer, with an 1800 lines mm^{-1} grating and a gated ICCD camera.

Inference of rotational temperature is performed using the Sandia National Laboratories CARS code [288]. Fig. 5.5 shows the square root of the experimental ethylene–air CARS spectrum along with the best fit synthetic spectrum generated by the Sandia CARS code. While there are some statistical fluctuations that can be seen from the imperfect agreement between the experimental spectrum and best least squares fit, the overall rotational envelope is well reproduced, resulting in an inferred best fit rotational temperature of 860 K with uncertainty ± 80 –100 K. Compared to the spatially averaged rotational temperatures inferred from emission spectroscopy, especially under conditions where heat transfer clearly affects the temperature and may result in significant temperature gradient across the plasma, CARS measurement provides high spatial resolution measurement of temperature to clarify the effect of temperature gradient.

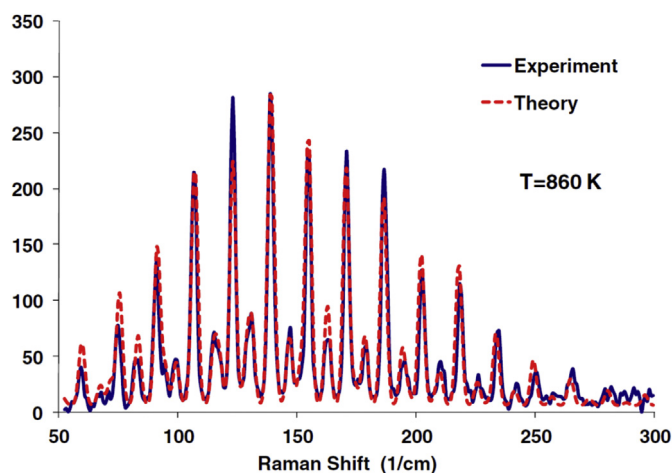


Fig. 5.5. Experimental and synthetic rotational CARS spectra in $\text{C}_2\text{H}_4/\text{air}$ ($\Phi = 1$) [287].

5.4.3. NO laser induced fluorescence (LIF) thermometry

Nitric oxide (NO) can be produced from the plasma discharge and as a trace gas naturally for temperature measurement using NO Laser Induced Fluorescence (LIF) thermometry. The NO LIF thermometry is based on a temperature dependent population of rotational and vibrational energy levels of NO molecules [289]. Sun et al. [43] implemented NO thermometry in a plasma assisted combustion system to measure the flow temperature at the downstream of plasma discharge and used NO thermometry to verify thermocouple temperature measurement. During the experiments, the laser beam was focused at the targeting position and scanned over a part of the NO absorption band from 226.25 nm to 226.29 nm which is most sensitive to the temperature range of interest. A PMT was used to collect the fluorescence and compared with modeling [290,291]. The measurements were conducted at the top burner exit as shown in Fig. 4.16 at 60 Torr without the presence of flame. NO was doped into the Ar/O_2 plasma and Fig. 5.6 shows a typical NO fluorescence spectrum from experiment normalized by laser intensity with discharge frequency 4 kHz and

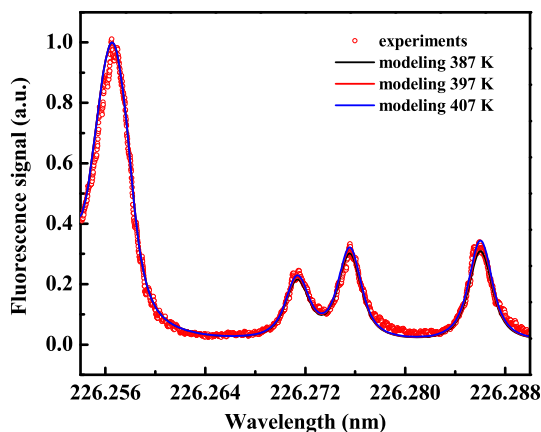


Fig. 5.6. NO thermometry fluorescence spectrum from experiment and modeling in the downstream of plasma discharge at 60 Torr.

modeling at different temperature. The thermocouple reading of the temperature was 387 K and the best fit of the spectrum was 397 K.

Recently, Watson et al. [292] measured one-dimensional flame temperature profile using NO thermometry with a different scan range from 225.13 to 225.19 nm in order to maximize the temperature sensitivity in a broad range from cold flow to burned gas. More details can be found in Ref. [292].

5.5. Measurement of intermediate species

5.5.1. CH₂O measurement by CH₂O PLIF method

A typical feature of plasma assisted combustion is low temperature combustion. As discussed in Ref. [107], low temperature combustion, including cool flame behavior, cannot be characterized by OH. CH₂O, however, is an excellent marker of low temperature combustion chemistry [107,293].

CH₂O molecule has several absorption bands suitable for laser excitation in the wavelength regime from 270 to 360 nm [252]. The third harmonic of a conventional Nd:YAG laser can be used for excitation of CH₂O. The main drawback of this alternative is that the laser line is overlapping with relatively weak rotational transitions of the molecules. However, the main advantage is that a standard Nd:YAG laser system can be used with high pulse energy available at 355 nm.

Sun et al. [107] employed CH₂O PLIF [252,253] excited by photons at 355 nm from the third harmonic from the Nd:YAG laser to study the plasma activated low temperature chemistry in a DME/He/O₂ diffusion flame. The fluorescence signal from the \tilde{A}^1A_2 to \tilde{X}^1A_1 transition band is collected by the ICCD camera with a bandpass filter from 400 to 450 nm. As discussed in Section 4.3, the CH₂O PLIF signal was successfully obtained and used as DME low temperature chemistry marker. However, the quantification of the CH₂O PLIF signal is very challenging because the unknown quenching rates from different species. In addition, temperature and pressure were also found to have a quenching effect on the fluorescence [253]. For quantitative measurements, mid-IR laser absorption and molecular beam mass spectrometry are the alternative methods [294].

5.5.2. Measurement of H₂O, CH₄, CH₂O and C₂H₂ by mid-IR absorption method

The advantage of mid-IR laser absorption spectroscopy is its ability to make quantitative, sensitive (sub-ppm level), time-dependent measurements of multiple species and temperatures

for small hydrocarbons to address fuel oxidation kinetics at low temperature [294]. Lefkowitz et al. [294] conducted *in situ* mid-IR laser absorption spectroscopy of C₂H₄/Ar pyrolysis and C₂H₄/O₂/Ar oxidation activated by a nanosecond repetitively pulsed plasma in a low temperature flow reactor at a pressure 60 Torr (see Fig. 4.7). The implementation of mid-IR laser absorption spectroscopy in non-equilibrium, low temperature plasma is challenging owing to the small dimensional restraints required to sustain uniform plasma. To overcome this challenge, Lefkowitz et al. [294] developed a miniature Herriott cell integrated with the flow reactor to lengthen the path length in the plasma region. The Herriott cell is comprised of two opposed 12.7 mm OD, 50 mm focal length concave mirrors, which are centered 30 mm downstream of the leading edge of the electrodes. The laser beam enters a 2 mm hole in one of the mirrors and exits through the same hole after 24 passes through the plasma test section, resulting in a total absorption path length in the plasma of 1.08 m. An external cavity quantum cascade laser operating in the 7–7.8 μ m (mid-IR) range was used to measure temperature, H₂O, CH₄, and C₂H₂ during and after the activation of plasma discharge using the direct laser absorption spectroscopy technique.

In Ref. [294], all speciation measurements were quantified using direct absorption. This experiment provided *in situ* diagnostic data of intermediate hydrocarbon species in low temperature plasma activated fuel pyrolysis and oxidation for the first time. By changing the laser wavelength to 2831 cm⁻¹, CH₂O formation in PAC can also be measured. This is an on-going experiment at PU by the authors.

5.5.3. Faraday rotation spectroscopy for HO₂ measurement

As discussed in Section 4.2, HO₂ is an important species for low temperature fuel oxidation. HO₂ can be formed through reaction R7 at low temperature conditions owing to the H production from plasma. Brumfield et al. [167,293] demonstrated a mid-infrared Faraday rotation spectroscopy (FRS) to *in situ* quantify HO₂ formation directly at atmospheric pressure in a flow reactor with He/O₂/DME as a working gas. In contrast to the optical absorption methods, FRS is a dispersion based magneto-optical technique that is selective only to paramagnetic radical species. Therefore, signals from diamagnetic molecules, such as H₂O, are suppressed, which significantly mitigates the spectral interference.

In the work of Brumfield et al. [167,293], a longitudinal magnetic field is applied to the exit of the flow reactor. This induces magnetic circular birefringence for spectral transitions belonging to the paramagnetic species, resulting in the Faraday effect. The amount of polarization rotation depends on the strength of the applied magnetic field, the intensity of the optical transitions, and the number density of the paramagnetic species. Linearly-polarized laser light from an external cavity quantum cascade laser with a well-defined polarization axis is passed through the sample located within a longitudinal magnetic field. Tunable light for probing the HO₂ Q-branch transitions in the ν_2 bending fundamental around 1400 cm⁻¹ (7.1 μ m) is used. The polarization rotation of the transmitted light is transformed into intensity variations using a polarizer (polarization analyzer). The FRS signal encoded in the light intensity can then be measured with a photodetector. The signal can then be modeled by taking into account system parameters to calculate the laser frequency dependent RMS signal voltage (V_{RMS}) at the output of the detector:

$$V_{RMS}(\bar{\nu}) = GP_0 \sin 2\theta \Theta_{RMS}(\bar{\nu}) \quad (5.13)$$

where G is an experimental factor that combines the transmission through the wire grid polarizers, the detector gain, and the optical collection efficiency at the detector. The optical power incident on the wire grid polarizer is given by P_0 , and the polarization analyzer

offset angle is given by θ . $\Theta_{RMS}(\bar{\nu})$ is the root mean square value for the Faraday rotation angle as a function of optical frequency. The Θ_{RMS} spectrum is calculated for individual HO_2 transitions at discrete frequency points over the spectral window by numerically calculating the first Fourier component at the magnetic field modulation frequency. The model used for spectral fitting requires the following input parameters: the RMS value of the magnetic field, the temperature of the gas sample in the reactor exit, and the optical path length. Four parameters in the model were used as variables: the HO_2 number density (n_{HO_2}), the collision broadened line width ($\Delta\bar{\nu}_{HWHM}$), a signal offset, and a frequency offset. The signal and frequency offsets have been implemented to account for systematic errors due to electromagnetic interference (EMI) from the Helmholtz coils and an offset of the wavemeter frequency reading respectively. $\Delta\bar{\nu}_{HWHM}$ is a fitted parameter because the collisional broadening for HO_2 is unknown for gas mixtures composed of 90% He and 10% O_2 at 1 atm pressure. A non-linear least squares fitting algorithm has been implemented to find the best fit and determine the HO_2 number density (n_{HO_2}) in the sample. With FRS technique, Brumfield et al. [166] demonstrated HO_2 quantification at atmospheric pressure in a combustion environment for the first time. The results from both experiments and modeling are shown in Fig. 5.7.

It is worth noting that quantification of absorption spectroscopy and LIF requires the distribution in quantum state of species which is typically Boltzmann. However, the non-equilibrium nature of plasma poses significant challenges on the diagnostics with non-Boltzmann distribution in quantum state of species. This effect is associated with the collisional energy transfer process which depends on time, states, energy of particles, and pressure. Another issue is the unknown cross-sections for plasma produced species present in the flow. For example, the quantification of temperature through Rayleigh scattering thermometry can be compromised. Moreover, the measurement of electron number density and electric field over all electron energy range is also difficult. To the authors' knowledge, these issues have not been well addressed in detail.

6. Development of kinetic mechanisms and methods for plasma combustion modeling

Modeling of plasma discharge in air and conventional combustion has been widely addressed in other reviews and thus will

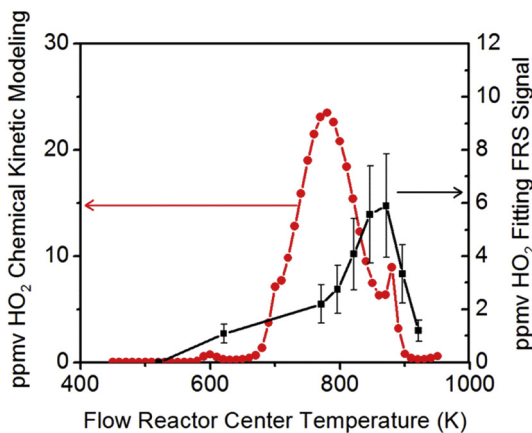


Fig. 5.7. The HO_2 concentration versus flow reactor temperature for: data obtained from a chemical kinetic modeling (red) and concentration data retrieved by fitting the experimental FRS spectra (black) [293]. (For interpretation of the references to color in this figure legend, the reader is referred to the web version of this article.)

not be discussed here. The purpose of this section is to discuss the recent efforts to model plasma assisted combustion. Because fuel oxidation mechanism has not been emphasized in the plasma modeling community and the fact that plasma kinetics is often ignored in the combustion community, the major challenge of modeling plasma assisted combustion is the lack of predictive detailed kinetic mechanisms. The first step in an attempt to model plasma assisted combustion is to combine the plasma kinetic mechanisms (e.g. air plasma) with existing combustion kinetic mechanisms by adding a few well-known interactions between plasma generated species and the combustion kinetic mechanism. Therefore, there may exist many missing reaction pathways and intermediate species. Moreover, due to the limited data available in well-defined experimental conditions, the developed mechanisms for plasma assisted combustion often lack comprehensive validations with different experimental methods under broad pressure and temperature conditions. In this section, we will discuss a few recent efforts to develop validated plasma assisted combustion mechanisms.

6.1. Coupling plasma mechanisms with combustion mechanisms

Adamovich et al. [194] developed a kinetic model by combining an air plasma model [295] with a high temperature hydrocarbon oxidation mechanism (GRI Mech 3.0 [240] or USC Mech II [241]) to model CH_4/air and $\text{C}_2\text{H}_4/\text{air}$ plasmas. This combined kinetic model is supplemented by CH_4 , C_2H_4 , and C_2H_2 dissociation reactions by the direct electron impact and the collisions with electronically excited N_2 . The model was further extended by Sun et al. [106] to include other dilution gases such as He and Ar. For example, in order to consider species dissociation by reactions with excited Ar and He, and dissociation of CH_4 by electron impact reactions, additional elementary reactions involving the dilution gases (He/Ar), fuel, oxygen are required in the kinetic model. Table 4 [106] presents the reactions describing the interactions between

Table 4

List of Ar/He/ CH_4 related reactions involved in Ar/He/ O_2 / CH_4 mixture discharge [106].

Reaction	Rate ($\text{cm}^3 \text{s}^{-1}$)	Reference
$\text{e} + \text{CH}_4 = \text{e} + \text{CH}_3 + \text{H}$	σ^a	[281]
$\text{e} + \text{CH}_4 = \text{e} + \text{CH}_4(+)$	σ	[296]
$\text{e} + \text{CH}_4(+) = \text{CH}_2 + 2\text{H}$	$1.7 \times 10^{-7} (300/T)^{0.5}$	[296]
$\text{e} + \text{CH}_4(+) = \text{CH}_3 + \text{H}$	$1.7 \times 10^{-7} (300/T)^{0.5}$	[296]
$\text{CH}_4(+) + \text{O}_2 = \text{CH}_4 + \text{O}_2(+)$	5×10^{-10}	[296]
$\text{Ar} + \text{e} = \text{Ar}^* + \text{e}$	Σ	[296]
$\text{Ar} + \text{e} = \text{Ar}(+) + 2\text{e}$	Σ	[296]
$\text{Ar}^* + \text{O}_2 = \text{Ar} + 2\text{O}$	2×10^{-10}	[296]
$\text{Ar}(+) + \text{O}_2 = \text{Ar} + \text{O}_2(+)$	1×10^{-10}	[296]
$\text{Ar}^* + \text{CH}_4 = \text{Ar} + \text{CH}_2 + 2\text{H}$	3.3×10^{-10}	[296]
$\text{Ar}^* + \text{CH}_4 = \text{Ar} + \text{CH} + \text{H}_2 + \text{H}$	5.8×10^{-10}	[296]
$\text{Ar}^* + \text{CH}_4 = \text{Ar} + \text{CH}_3 + \text{H}$	5.8×10^{-10}	[296]
$\text{Ar}^* + \text{CH}_4 = \text{Ar} + \text{CH}_2 + \text{H}_2$	5.8×10^{-10}	[296]
$\text{Ar}(+) + \text{CH}_4 = \text{Ar} + \text{CH}_3(+) + \text{H}$	6.5×10^{-10}	[296]
$\text{Ar}(+) + \text{CH}_4 = \text{Ar} + \text{CH}_2(+) + \text{H}_2$	1.4×10^{-10}	[296]
$\text{He} + \text{e} = \text{He}^* + \text{e}$	Σ	[297]
$\text{He} + \text{e} = \text{He}(+) + 2\text{e}$	Σ	[297]
$\text{He}^* + \text{O}_2 = \text{He} + \text{O}_2(+) + \text{e}$	$1.5 \times 10^{-11} T^{0.5}$	[297]
$\text{He}^* + \text{O} = \text{He} + \text{O}(+) + \text{e}$	$1.5 \times 10^{-11} T^{0.5}$	[297]
$\text{He}(+) + \text{O}_2 = \text{He} + \text{O}(+) + \text{O}$	$0.6 \times 10^{-11} T^{0.5}$	[297]
$\text{He}(+) + \text{O}_3 = \text{He} + \text{O}_2 + \text{O}(+)$	$0.6 \times 10^{-11} T^{0.5}$	[297]
$\text{He}(+) + \text{O}_2(^1\Delta_g) = \text{He} + \text{O}(+) + \text{O}$	$0.6 \times 10^{-11} T^{0.5}$	[297]
$\text{He}(+) + \text{O}(^1D) = \text{He} + \text{O}(+)$	$2.9 \times 10^{-12} T^{0.5}$	[297]
$\text{He} + 2\text{O} = \text{He}^* + \text{O}_2$	1×10^{-33}	[297]
$\text{He} + \text{O}(^1D) = \text{He} + \text{O}$	1×10^{-10}	[109]
$\text{He}^* + \text{CH}_4 = \text{He} + \text{CH} + \text{H}_2 + \text{H}$	5.6×10^{-13}	[298]

^a The rate is calculated by the Boltzmann solver using experimentally measured cross-sections, σ .

plasma kinetics and fuel oxidation kinetics. The kinetic models also incorporated chemical reactions of electronically excited species, electron-ion recombination reactions, ion–ion neutralization processes, ion–molecule collisional energy transfer reactions, and electron attachment and detachment processes.

The rate coefficients of electron impact ionization, dissociation, and electronic excitation as well as the electron energy distribution function (EEDF) are normally calculated by using a Boltzmann equation solver (such as BOLSIG [299]) with the input of electron impact cross-sections. Similar plasma assisted combustion kinetic models containing H_2 , CH_4 to C_5H_{12} were developed by Aleksandrov et al. [246] and Starikovskaia et al. [239]. Since no reliable cross-section data are available for large hydrocarbons such as C_3H_8 , C_4H_{10} and C_5H_{12} , the authors assumed that these cross-sections are similar to those for C_2H_6 . Among these kinetic models, the H_2 /air plasma model [239] is a detailed state-to-state kinetic model including 750 chemical and 8700 vibrational energy exchange processes with 254 species. To the authors' knowledge, the most updated electron impact cross section data have been documented, respectively, in references for O_2 [300], N_2 [301], H_2 [302], CO [303], CO_2 [304], H_2O [305], and simple hydrocarbon molecules (CH_4 , C_2H_6 , C_2H_4 , C_2H_2 , C_3H_8 , C_3H_6 [306], and $n-C_4H_{10}$ [307] (only for ionization).

Uddi et al. [160] showed that the kinetic model predictions using the model developed by Adamovich et al. [194] were in good overall agreement with the experimental data for TALIF O measurements. However, the overall agreement might be partly due to the “lucky or magic choice” of the E/N ratio. In addition, for the fuel oxidation products, different combustion kinetic models had very different predictions and the results differ by almost one order of magnitude as shown in Fig. 6.1. Since the same set of plasma reactions and rates were used in both cases, the difference between the two kinetic models was from the difference between the reactions and rates used by GRI Mech 3.0 [240] and USC Mech II [241].

Note that both GRI Mech and USC Mech were developed for the purpose of high temperature combustion. As pointed out by Sun et al. [106], fuel oxidation kinetic mechanisms have rarely been validated at low temperature conditions. Figs. 4.6 and 4.7 show clearly that there exist many low temperature fuel oxidation pathways which are missing in GRI and USC Mech. In addition, the predicted low temperature species concentrations (H_2O and CH_4)

differ by even one order. Therefore, there are large uncertainties in existing plasma combustion mechanisms at low temperature and high pressure conditions, especially for large molecule liquid fuels.

6.2. Recent developments of plasma mechanisms

To extend the validity of combustion modeling to high pressure and lower temperature conditions, a collaborative effort to develop a comprehensive high pressure plasma combustion mechanism (HP-Mech/plasma) for small hydrocarbon including ($H_2/H_2O_2/O_3/CO/CH_2O/CH_3OH$) has been carried out by the team members of the AFOSR multi-university research initiative on plasma assisted combustion (MURI-plasma) at Penn State, Princeton, and Ohio State. The approach is to take the advantage of the recent development of a high pressure hydrogen mechanism [308], formaldehyde and methanol mechanism [309], formaldehyde and acetylene mechanism [242], O_3 decomposition rate [310], and NO_x mechanism [311]. Reactions of $O(^1D)$ with fuels/ $N_2/O_2/CO/CO_2/H_2O/CH_2O$ and O_2 singlet with fuels/ $H/OH/CH_3/H_2/CH_4$ are updated using the best estimates of the energy barriers and rate constants. Low temperature fuel oxidation pathways including RO_2 and aldehyde formation are also added using similarity rules [312,313]. Fig. 6.2 and Fig. 6.3 show the preliminary validation of the HP-Mech/plasma for H_2 and CO mixtures with NO_x addition from low to high pressures [314]. The results show that the new mechanism can well reproduce the experimental data in the variable pressure flow reactor [209]. Fig. 6.3 also shows the comparison of predicted flame speeds of O_3 addition in methane/air mixture. It is seen that the new model has better agreement with the experimental data than the previous model. The current HP-Mech/plasma is still in a preliminary version. Comprehensive validations and improvement in the future are needed.

In recent years, another great effort has been made on the development of the kinetic mechanisms of excited molecules for plasma assisted combustion. Among different electronically excited molecules, singlet $O_2(^1\Delta_g)$ has drawn significant attention. The $O_2(^1\Delta_g)$ molecule is metastable. Its radiation lifetime (without collisional quenching) is about 65 min, and the collisional lifetime in a CH_4 /air mixture at 1 atm is 4.2×10^{-2} s [315]. The long lifetime and the chemical potential of $O_2(^1\Delta_g)$ to intensify the chain branching reactions such as $H + O_2(^1\Delta_g) \rightarrow OH + O$ make it an important target for the study of plasma assisted combustion. $O_2(^1\Delta_g)$ related chemistry has been studied for a long time, but is limited to room temperature and with small molecules. Here, only the recent progress of $O_2(^1\Delta_g)$ related to plasma assisted combustion will be reviewed.

Starik et al. [315] developed a kinetic mechanism containing a $O_2(^1\Delta_g)$ sub-mechanism and investigated the effect of the presence of $O_2(^1\Delta_g)$ in a CH_4 /air mixture on the laminar flame speeds. The mechanism includes three major reaction channels: (1) the quenching of $O_2(^1\Delta_g)$: $O_2(^1\Delta_g) + M = O_2(X^3\Sigma_g^-) + M$, in which M is any molecule or atom in the mixture and $O_2(X^3\Sigma_g^-)$ denotes the ground state of oxygen; (2) the dissociation of $O_2(^1\Delta_g)$: $O_2(^1\Delta_g) + M = 2O + M$; (3) formation of $O_2(b^1\Sigma_g^+)$ molecules: $O_2(^1\Delta_g) + O_2 = O_2(b^1\Sigma_g^+) + O_2$ as well as chemical reactions involving $O_2(b^1\Sigma_g^+)$ molecules. The reaction rate constants involving excited O_2 were either taken from experimental measurements or calculated by the bond-energy-bond-order method. The model was then used to calculate flame speeds for CH_4 /air mixtures at different equivalence ratios and $O_2(^1\Delta_g)$ concentrations. Fig. 6.4 shows the results of the calculated flame speeds (U_n in the figure) with $O_2(^1\Delta_g)$ mole fraction at 0, 0.05 and 0.1 of total O_2 concentration at incoming flow temperature $T_0 = 300$ K and 450 K.

It can be seen that an increase in the temperature and in the concentration of $O_2(^1\Delta_g)$ molecules leads to an increase in the

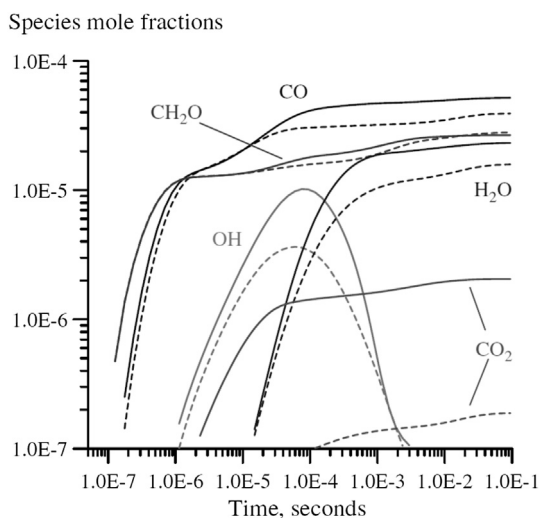


Fig. 6.1. Fuel oxidation product mole fractions after a single high-voltage pulse in C_2H_4 /air at $P = 60$ Torr and $\Phi = 0.5$. solid lines, GRI Mech 3.0; dotted lines, USC Mech II [160].

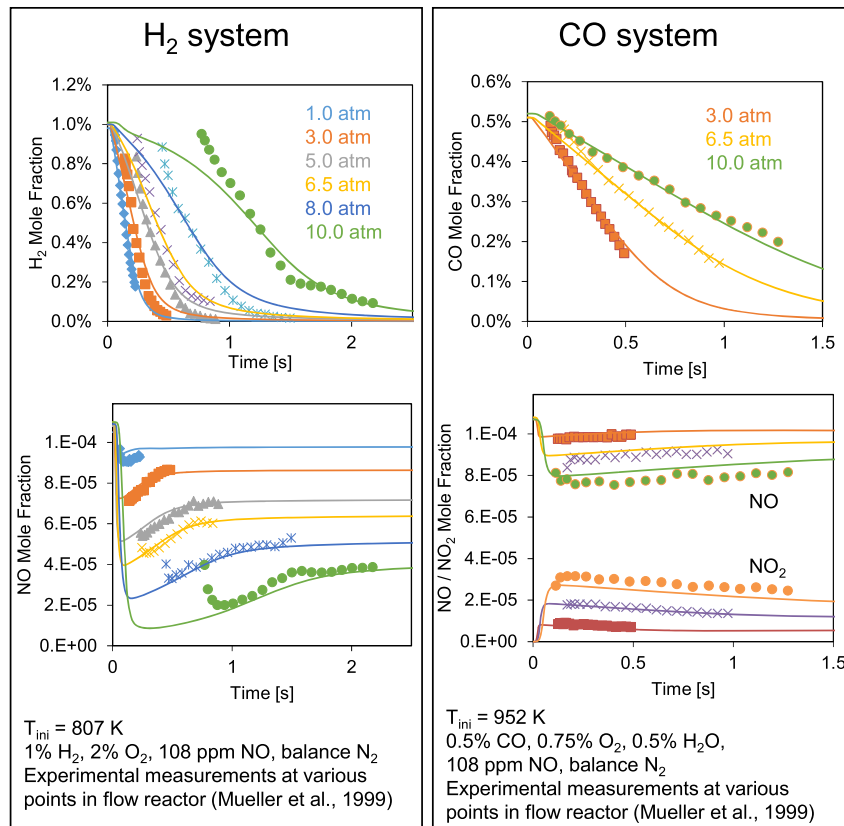


Fig. 6.2. Preliminary validation of HP-Mech/plasma mechanism for $H_2/CO/NO$ mixture.

flame speed. A major increase in the flame speed was observed at fuel lean conditions but only a minor effect was identified with the stoichiometric mixture. At $T_0 = 450$ K, converting 10% of O_2 into $O_2(a^1\Delta_g)$ can increase flame speed by approximately 70% for the mixture with $\Phi = 0.45$ and only ~20% for the stoichiometric mixture. For the fuel rich mixture ($\Phi = 1.9$), the flame speed increased by ~40%. At $T_0 = 300$ K, the increase in the flame speed was even smaller: for stoichiometric and fuel rich ($\Phi = 1.6$) mixtures, the increase was about 17%. The authors explained that the main reason of the flame speed increase is the acceleration of chain branching due to the abundance of $O_2(a^1\Delta_g)$ molecules in the mixtures. The abundance of $O_2(a^1\Delta_g)$ molecules in the mixture causes an increase in the rates of all reactions resulting in the

formation of highly reactive atoms and radicals responsible for the chain branching development.

Regarding the effect of $O_2(a^1\Delta_g)$ on combustion, the work conducted by Ombrello et al. [156] suggested that the missing quenching reactions of $O_2(a^1\Delta_g)$ caused the over-prediction of the flame speed enhancement by $O_2(a^1\Delta_g)$. Recently, Popov [260] developed a kinetic model including several quenching mechanisms of $O_2(a^1\Delta_g)$ to describe the impact of single delta oxygen $O_2(a^1\Delta_g)$ on the evolution of H_2/O_2 mixture. The impact of $O_2(a^1\Delta_g)$ admixture on the ignition of H_2/O_2 mixtures was studied.

Fig. 6.5 presents the calculation results of ignition delay times of H_2/air mixture at $\Phi = 1$, $P = 1$ atm and at different initial concentrations of $O_2(a^1\Delta_g)$ and atomic O. As can be seen, the addition of 1% $O_2(a^1\Delta_g)$ does not lead to a significant decrease in ignition delay owing to the quenching of $O_2(a^1\Delta_g)$ by H and HO_2 . It was reported that most of the collisions between $O_2(a^1\Delta_g)$ and H atom, $O_2(a^1\Delta_g) + H$, lead to the quenching of $O_2(a^1\Delta_g)$. The efficiency of this quenching reaction is more than 80% and the fraction of the reaction $O_2(a^1\Delta_g) + H \rightarrow OH + O$ is only 10–20%. The dominant process determining the degree of $O_2(a^1\Delta_g)$ impact was its deactivation by HO_2 molecules. As a result, in a H_2/O_2 system of high pressure, where the number density of HO_2 can be sufficiently high, the impact of $O_2(a^1\Delta_g)$ on the ignition delay time of these mixtures is relatively small, compared to the effect of atomic O.

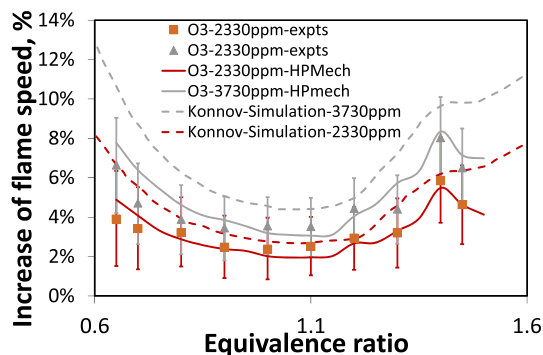


Fig. 6.3. Comparison of simulated results (HP-Mech/plasma and GRI Mech 3 with an updated O_3 mechanism by Konnov and coworkers [240]) with experimental results for burning velocity enhancement by ozone as a function of equivalence ratios.

6.3. Plasma assisted combustion modeling

Numerical modeling can provide valuable insights in the understanding of plasma assisted combustion. However, one difficulty in the modeling of plasma assisted combustion is the scarcity of experimental data to validate numerical modeling. Another

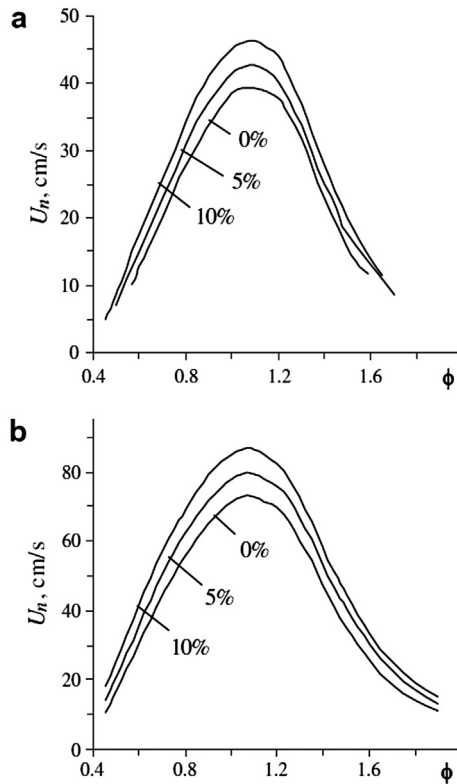


Fig. 6.4. Predicted dependence of laminar flame speeds on Φ for the CH_4 /air mixture with $O_2(a^1\Delta_g)$ mole fraction at 0, 0.05 and 0.1 of total O_2 concentration for (a) $T_0 = 300$ K and (b) $T_0 = 450$ K at $P = 1$ atm [315].

difficulty is that plasma assisted combustion modeling often experiences large gradients of temperature and species concentrations, which significantly affect the EEDF and therefore the rate constants of electron impact reactions. Since there are large amounts of missing reaction pathways such as electron impact reactions of different fuels, the reactions between excited species,

and fuel fragments, experimental data play a critical role in improving the validity of numerical modeling.

Typical detailed modeling methods for nanosecond pulsed plasma assisted combustion are the zero-dimensional model [160] and the one-dimensional model [316]. Details about the physical model can be found in Refs. [316,317]. Only the technical challenges will be discussed here. The zero-dimensional model does not solve the Poisson equation and charge motion and therefore does not resolve the sheath formation and charge drifting and diffusion which determine the intensity of electric field (E) in the bulk plasma region. In the work of Uddi et al. [160], E was adjusted as a parameter in the zero-dimensional model until the peak atomic O concentration matched with the experimental value. Then, the decay of atomic O from experiments and modeling results were studied. Nagaraja et al. [316] conducted time accurate one-dimensional modeling of the nanosecond pulsed discharge in H_2 /air mixture. The modeling results showed good agreement with experimentally measured OH concentrations before ignitions and the ignition delay time. Compared to the zero-dimensional modeling, one-dimensional modeling is still computationally very expensive due to the multi-time scale nature of plasma assisted combustion and special/temporal resolution. It is worth noting that in the one-dimensional and high dimensional models, to improve the computation efficiency, EEDF is often solved beforehand and tabulated for the rest of calculation. Therefore, the effect of flow composition change on EEDF will not be appropriately considered.

7. Technical challenges and future research

Plasma assisted combustion provides numerous opportunities in both engineering applications and in scientific research. At the same time, plasma assisted combustion is a very complicated system coupling plasma kinetics, combustion kinetics, and flame and fluid dynamics. As such, there are still many knowledge gaps from discharge development to fundamental understanding and numerical modeling capabilities.

For plasma assisted combustion in internal combustion engines, the development of a large volume discharge of a size greater than the critical flame radius at high pressure is very important. Unfortunately, although many studies have shown that microwave, gliding arc, and short pulsed repetitive discharge enhanced engine performance, the observed enhancement was often limited to low engine pressures. In addition, the discharge device is expensive and produces serious electrical noise. To improve the ignition control in advanced HCCI, PPCI, and RCCI engines, one of the major challenges for plasma assisted combustion is to develop a plasma discharge which can produce large volume discharge at high pressure.

Moreover, the increasingly stringent low NO_x emission standards as well as the requirement of fuel flexibility and higher efficiency in power generation also create a great opportunity for plasma assisted combustion to enhance flame stabilization in ultra-lean and low temperature combustion. For example, the combination of a microtube gas turbine combustor with non-equilibrium plasma may have a great potential to solve the problems both in flame flashback and lean blow-off. In addition, the combination of microwave with gliding arc and/or short pulse repetitive discharge has the potential to stabilize ultra-lean gas turbine combustion of fuels with large variation in heating values. It is worth noting that plasma assisted low temperature combustion can reduce NO_x formation. However, at the same time, plasma also produces NO_x (this effect may be significant at high pressure condition) depending on the mixture and combustion environment. The key challenge here is to develop methods to design efficient high pressure micro-discharge with minimized NO_x emissions. Furthermore, plasma is a promising technique to extend the flight envelope of gas turbine

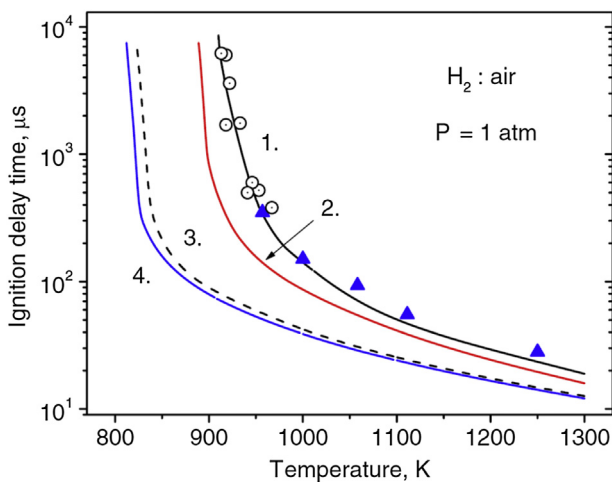


Fig. 6.5. Dependences of the ignition delay time of stoichiometric H_2 /air mixture on the initial temperature at $P = 1$ atm and at the various admixtures of $O_2(a^1\Delta_g)$ and O. Signs correspond to the experimental data, curves correspond to the calculation results without $O_2(a^1\Delta_g)$ and O (curve 1) and with 1% $[O_2(a^1\Delta_g)]/[O_2]$ (curve 2), 0.1% $[O]/[O_2]$ (curve 3), and 1% $[O_2(a^1\Delta_g)]/[O_2] + 0.1\%$ $[O]/[O_2]$ (curve 4) [260].

afterburner relight. A large volume ignition by non-equilibrium plasma is able to avoid the failure of afterburner relight at very low pressure. As shown in Section 2, for unmanned aerial vehicles, plasma assisted combustion can effectively extend the engine limit burn limit. In scramjet combustion, non-equilibrium plasma also provides good opportunities from selective fuel reforming of endothermic fuels to ignition and combustion enhancement. However, the key issue is the large energy consumption of plasma in a high speed flow and the main challenge is how to produce a discharge at the interface of fuel air mixing away from the engine walls. Many filament discharges only occur near the electrodes. In addition, the introduction of plasma may complicate the system and the optimized location for plasma generator may not be realized owing to the challenge of engineering design.

The observation of plasma activated low temperature combustion and cool flames suggests that non-equilibrium plasma is an effective technique for fuel processing and emission control. With today's slow progress in cellulosic biofuel production, heavy fuel residue processing, and fuel production from waste materials, non-equilibrium plasma is certainly an attractive approach to improve the fuel conversion efficiency. For example, the plasma generated cool flames and low temperature oxidation can be used for *in situ* fuel processing, reforming, and producing valuable chemicals from heavy fuels, waste plastic materials, and cokes. However, the major challenge is that we still do not know what the best plasma discharge is for each of these applications.

In research, despite the significant advancement in the last few years, many of the underlying plasma/combustion interaction mechanisms remain unknown. For example, the energy coupling between different electronic, vibrational, and rotation excitations has not been well understood. There are many missing reaction pathways in plasma assisted combustion. The existing plasma mechanisms have not been extensively validated in practical application conditions. Experimental data and cross-sectional areas for large hydrocarbon fuels are scarce. There are large uncertainties in *ab initio* quantum chemistry computation for reaction rate constants involving excited species and electrons. Accurate modeling of plasma assisted combustion even in one dimension is still challenging. In order to address these challenges, future efforts on experimental methods, kinetic mechanism development, numerical modeling, and diagnostics are needed.

In experimental study, the challenge is how to design fundamental experiments which have well understood flow and boundary conditions and are easier to model from both combustion and plasma point of views. Most of the studies of plasma assisted combustion in the past have described plasma as a “magic black box” which enhanced combustion significantly but with complicated coupling between flow, combustion, and plasma. In order to advance the understanding and the validation for modeling of plasma assisted combustion, quantitative results such as electric field, electron temperature, and species distribution need to be measured directly or extracted from the experiments. Therefore, it is extremely important to design well-defined experimental platforms to produce high quality quantitative data, especially at high pressure.

Flow reactors, shock tube, rapid combustion, jet stirred reactors, and counterflow flame systems are good examples of well-defined combustion systems. However, the development of well-defined (e.g., uniform) plasma discharge in these experimental systems is challenging, especially at high pressure. Moreover, *in situ* optical diagnostics is also critical to understand the kinetic processes of plasma discharge and fuel oxidation. Many of the previous studies have focused on the measurements of small radicals (e.g., H, O, and OH). However, measurements of intermediate species such as CH_2O , H_2 , CH_4 , C_2H_2 , C_2H_4 , HO_2 , and H_2O_2 are equally important to

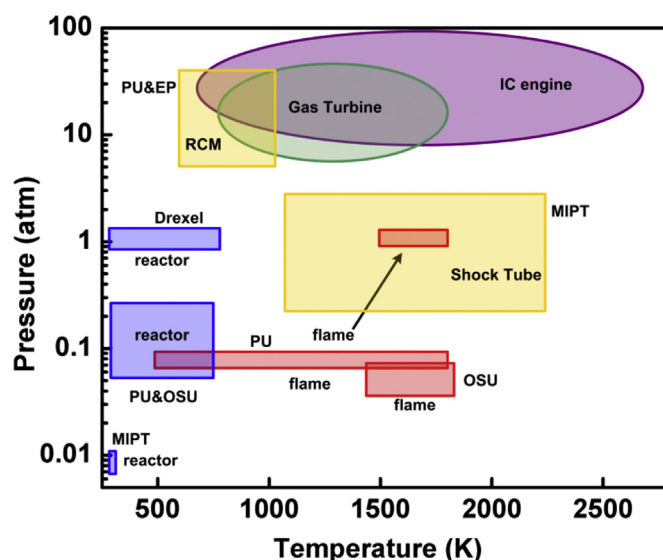


Fig. 7.1. experimental conditions of fundamental plasma assisted combustion research and operating conditions of gas turbines and IC engines (PU: Princeton University, Drexel: Drexel University, OSU: The Ohio State University, MIPT: Moscow Institute of Physics and Technology, EP: Ecole Polytechnique).

understand the chemistry and reaction pathways. Mid-infrared laser diagnostics has provided unprecedented opportunities for detecting these intermediate species.

As discussed in this paper, the kinetic enhancement of non-equilibrium plasma on combustion is more significant at low temperature conditions. However, few experimental data sets are available at low temperatures. As such, the validity of current plasma assisted combustion kinetic models at low temperature conditions is still in question. New combustion kinetic models validated at low temperature conditions are needed for further numerical investigation. Furthermore, due to the multi-time scale nature of plasma assisted combustion systems, time history measurement of intermediate species is also very important.

Most practical engine applications are at high pressures. Fig. 7.1 summarizes the experimental conditions of fundamental research conducted in plasma assisted combustion. It is seen that current research has only been carried at lower pressures rather than at high pressure gas turbine and IC engine conditions. Although some

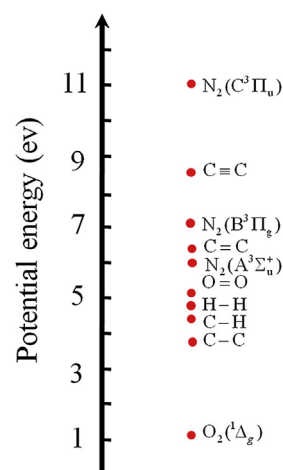


Fig. 7.2. Potential energy diagram.

rapid compression machine studies have extended the experiment to higher pressure, the discharge is not uniform and it is difficult to understand the fundamental kinetics. Unfortunately, high pressure causes thermal instability and local collisional thermalization of plasma. Therefore, developing experimental methods to generate stable, uniform non-equilibrium plasma under practical combustor pressure conditions is a challenging question for fundamental research. This challenge is not only open to the combustion society but also to the plasma research society.

Understanding the energy transfer between different excited energy modes is difficult. Due to the high excitation energy, plasma can introduce many new reaction pathways between excited species and through the collisions of excited species with neutral molecules. In N_2 , He, and Ar plasma systems, the electronic excitation energies are very high (above 5 eV for N_2 , and 10 eV for Ar and He). As shown in Fig. 7.2, the excitation energy is much higher than the chemical bond energy of most hydrocarbon fuels. Hence, the excited species contain a significant amount of energy, and are capable of dissociating a fuel molecule in a single collision. This phenomenon can lead to drastic changes in the transport and chemical properties of the combustible mixture. Energy transfer involving vibrationally excited species such as $N_2(v)$, $O_2(v)$ and $HO_2(v)$ is even more complicated. Unfortunately, few diagnostics of electronically and vibrationally excited molecules have been made. The studies of new reaction pathways involving energy transfer of excited species in plasma assisted combustion require advanced diagnostic techniques to quantitatively detect these species *in situ*.

Modeling of plasma assisted combustion is also difficult. Plasma discharge is a multi-physical, multi-scale, and non-equilibrium process. The characteristic time of plasma kinetics ranges from sub-nanoseconds to milliseconds, which is vastly different from the characteristic time of combustion kinetics. The non-equilibrium and multi-time scale nature make the numerical modeling of plasma assisted combustion extremely challenging. For example, appropriate modeling of unsteady, multidimensional short pulse discharge including the sheath effect is still difficult. Most of the existing methods are based on the estimated E/N distribution and the non-equilibrium Boltzmann solver without considering the sheath effect and the coupling between electric field and charge motion. An efficient and validated plasma modeling approach is needed.

8. Conclusion

Significant advancements in plasma assisted combustion have been made in both practical applications and fundamental understanding. New observations of plasma assisted ignition enhancement, flame speed enhancement, ultra-lean combustion, cool flames, flameless combustion, emission reduction, and low temperature fuel reforming are reported in internal combustion engines, gas turbines, turbulent flames, high speed propulsion systems, and fuel processing. Several significant advances in understanding of non-thermal and thermal effects, kinetic pathways of atomic oxygen production, diagnostics of electronically and vibrationally excited species, plasma combustion kinetics of sub-explosion limit ignition, plasma assisted low temperature combustion, transitions of the classical ignition S-curve, dynamics of the minimum ignition energy, and the transport effect by non-equilibrium plasma discharge, have been made. These findings and advances create many new opportunities in the development of efficient plasma discharges for practical applications and in future research. However, there are still large knowledge gaps in both discharge development and fundamental understanding and modeling capabilities. In engineering applications, development of efficient plasma discharge for large volume ignition at high

pressure is the key to extend plasma assisted combustion in engines. In research, understanding of the energy coupling between different electronic, vibrational, and rotation excitations remain challenging. The existing plasma mechanisms have not been extensively validated in practical application conditions. There are many missing reaction pathways in plasma assisted combustion. Experimental data and cross-section areas for large hydrocarbon fuels are scarce. Accurate modeling of plasma assisted combustion even in one-dimensional is still difficult due to the multi-timescale and non-equilibrium nature of plasma. In order to address these challenges, future efforts on experiments, kinetic mechanism, numerical modeling, and diagnostics are needed.

Acknowledgment

This work was supported by AFOSR MURI research grant FA9550-07-1-0136 and AFOSR grant FA9550-13-1-0119 from the Air Force Office of Scientific Research, with Drs. Julian Tishkoff and Chipping Li as the technical monitors. This work is also prepared in memory of Prof. Kenichi Takita, a pioneer of plasma torch application in supersonic combustors.

References

- [1] Chu S, Majumdar A. Opportunities and challenges for a sustainable energy future. *Nature* 2012;488:294–303.
- [2] Christensen M, Hultqvist A, Johansson B. Demonstrating the multi-fuel capability of a homogeneous charge compression ignition engine with variable compression ratio. *SAE Trans* 1999;108:2099–113.
- [3] Dec J. Advanced compression-ignition engines – understanding the in-cylinder processes. *Proc Combust Inst* 2010;32:2727–42.
- [4] Lu X, Han D, Huang Z. Fuel design and management for the control of advanced compression-ignition combustion modes. *Prog Energy Combust Sci* 2011;37:741–83.
- [5] Manente V, Johansson B, Cannella W. Gasoline partially premixed combustion, the future of internal combustion engines? *Int J Engine Res* 2011;12:194–208.
- [6] Reitz RD. Directions in internal combustion engine research. *Combust Flame* 2013;160:1–8.
- [7] Curran HJ, Gaffuri P, Pitz WJ, Westbrook CK. A comprehensive modeling study of iso-octane oxidation. *Combust Flame* 2002;129:253–80.
- [8] Mongia HC, Lafayette W. On continuous NOx reduction of aero-propulsion engines. In: 48th AIAA aerospace sciences meeting including the new Horizons forum and aerospace exposition, Orlando, Florida: AIAA-2010-1329.
- [9] McManus K. Low-emissions gas turbine combustion: design trends and challenges. In: Fall meeting of the eastern states section of the combustion institute; 2013. Clemson, SC.
- [10] Mao C. Experimental investigation of a multiplex fuel injector module. In: 42nd aerospace sciences meeting including the new horizons forum and aerospace exposition, 5–8 January 2004, Reno, Nevada; 2004. AIAA-2004-135.
- [11] Hsu K, Goss LP. Characteristics of a trapped-vortex combustor introduction. *J Propuls Power* 1998;14:57–69.
- [12] Schwer D, Kailasanath K. Numerical investigation of the physics of rotating-detonation-engines. *Proc Combust Inst* 2011;33:2195–202.
- [13] Moorthy JVS, Rajinikanth B, Charyulu BVN, Amba Prasad Rao G. Scramjet combustor development: a review. *J Aerosp Eng Technol* 2012;2:28–41.
- [14] Yu G, Fan XJ. Supersonic combustion and hypersonic propulsion. *Adv Mech* 2013;43:449–71.
- [15] Jiang Z, Yu H. Experiments and development of long-test-duration hypervelocity detonation-driven shock tunnel (LHDst). In: 52nd AIAA aerospace sciences meeting including the new horizons forum and aerospace exposition, National Harbor, Maryland; 2014. AIAA-2014-1012.
- [16] <http://www.netl.doe.gov/research/coal/energy-systems/gasification/gasification/hydrogen-turbines>.
- [17] Santner J, Dryer FL, Ju Y. The effects of water dilution on hydrogen, syngas, and ethylene flames at elevated pressure. *Proc Combust Inst* 2013;34:719–26.
- [18] Katsuki M, Hasegawa T. The science and technology of combustion in highly preheated air. *Symp Int Combust* 1998;27:3135–46.
- [19] Cavaliere A, de Joannon M. Mild combustion. *Prog Energy Combust Sci* 2004;30:329–66.
- [20] Buhre BJP, Elliott LK, Sheng CD, Gupta RP, Wall TF. Oxy-fuel combustion technology for coal-fired power generation. *Proc Combust Inst* 2005;31:283–307.

- [21] Larfeldt J. An industrial perspective on plasma assisted combustion. Lund, Sweden: Lecture at Lund University; 2014.
- [22] Hu Q, Sommerfeld M, Jarvis E, Ghirardi M, Posewitz M, Seibert M, et al. Microalgal triacylglycerols as feedstocks for biofuel production: perspectives and advances. *Plant J* 2008;54:621–39.
- [23] Kohse-Höinghaus K, Osswald P, Cool T, Kasper T, Hansen N, Qi F, et al. Biofuel combustion chemistry: from ethanol to biodiesel. *Angew Chem Int Ed* 2010;49:3572–97.
- [24] Dooley S, Won SH, Chaos M, Heyne J, Ju Y, Dryer FL, et al. A jet fuel surrogate formulated by real fuel properties. *Combust Flame* 2010;157:2333–9.
- [25] Bessee GB, Hutzler SA, Wilson GR. Propulsion and power rapid response research and development (R&D) support: analysis of synthetic aviation fuels. San Antonio TX: Southwest Research Inst.; 2011.
- [26] Blakey S, Rye L, Wilson CW. Aviation gas turbine alternative fuels: a review. *Proc Combust Inst* 2011;33:2863–85.
- [27] Dale BE, Kim S. Biomass refining global Impact—the biobased economy of the 21st century. Biorefineries-industrial processes and products: status quo and future directions. 2006. p. 41–66.
- [28] Ju Y. Recent progress and challenges in fundamental combustion research. *Adv Mech* 2014;44:201402.
- [29] Westbrook CK. Biofuels combustion. *Annu. Rev Phys Chem* 2013;64:201–19.
- [30] Won SH, Dooley S, Veloo PS, Wang H, Oehlschlaeger MA, Dryer FL, et al. The combustion properties of 2,6,10-trimethyl dodecane and a chemical functional group analysis. *Combust Flame* 2014;161:826–34.
- [31] Diévert P, Won SH, Gong J, Dooley S, Ju Y. A comparative study of the chemical kinetic characteristics of small methyl esters in diffusion flame extinction. *Proc Combust Inst* 2012;34:821–9.
- [32] Harper MR, Van Geem KM, Pyl SP, Marin GB, Green WH. Comprehensive reaction mechanism for n-butanol pyrolysis and combustion. *Combust Flame* 2011;158:16–41.
- [33] Rasi S, Veijanen A, Rintala J. Trace compounds of biogas from different biogas production plants. *Energy* 2007;32:1375–80.
- [34] Besenbacher F, Chorkendorff I, Clausen BS, Hammer B, Molenbroek AM, Nørskov JK, et al. Design of a surface alloy catalyst for steam reforming. *Science* 1998;279:1913–5.
- [35] DoE. Report of the basic energy sciences workshop on basic research needs for clean and efficient combustion of 21st century transportation fuels. 2006.
- [36] Starikovskiy A, Aleksandrov N. Plasma assisted ignition and combustion. *Prog Energy Combust Sci* 2013;39:61–110.
- [37] Starikovskaia SM. Plasma assisted ignition and combustion. *J Phys D Appl Phys* 2006;39:R265–99.
- [38] Ombrello T, Qin X, Ju Y, Gutsol A, Fridman A, Carter C. Combustion enhancement via stabilized piecewise. *AIAA J* 2006;44:142–50.
- [39] Lou G, Bao A, Nishihara M, Keshav S, Utkin YG, Rich JW, et al. Ignition of premixed hydrocarbon–air flows by repetitively pulsed, nanosecond pulse duration plasma. *Proc Combust Inst* 2007;31:3327–34.
- [40] Kim W, Godfrey M, Cappelli M. The role of in situ reforming in plasma enhanced ultra lean premixed methane/air flames. *Combust Flame* 2010;157:374–83.
- [41] Takita K, Uemoto T, Sato T, Ju Y, Masuya G, Ohwaki K. Ignition characteristics of plasma torch for hydrogen jet in an airstream. *J Propuls Power* 2000;16:227–33.
- [42] Leonov SB, Yarrantsev DA, Napartovich AP, Kochetov IV. Plasma-assisted combustion of gaseous fuel in supersonic duct. *IEEE Trans Plasma Sci* 2006;34:2514–25.
- [43] Sun W, Uddi M, Ombrello T, Won SH, Carter C, Ju Y. Effects of non-equilibrium plasma discharge on counterflow diffusion flame extinction. *Proc Combust Inst* 2011;33:3211–8.
- [44] Kimura I, Aoki H, Kato M. The use of a plasma jet for flame stabilization and promotion of combustion in supersonic air flows. *Combust Flame* 1981;42:297–305.
- [45] Barbi E, Mahan JR, O'Brien WF, Wagner TC. Operating characteristics of a hydrogen-argon plasma torch for supersonic combustion applications. *J Propuls Power* 1989;5:129–33.
- [46] Takita K. Ignition and flame-holding by oxygen, nitrogen and argon plasma torches in supersonic airflow. *Combust Flame* 2002;128:301–13.
- [47] Takita K, Abe N, Masuya G, Ju Y. Ignition enhancement by addition of NO and NO₂ from a N₂/O₂ plasma torch in a supersonic flow. *Proc Combust Inst* 2007;31:2489–96.
- [48] Kobayashi K, Tomioka S, Mitani T. Supersonic flow ignition by plasma torch and H₂/O₂ torch. *Journal of propulsion and power. J Propuls Power* 2004;20:294–301.
- [49] Wagner TC, O'Brien WF, Northam GB, Eggers JM. Plasma torch igniter for scramjets. *J Propuls Power* 1989;5:548–54.
- [50] Jacobsen LS, Carter CD, Baurle RA, Jackson TA, Williams S, Bivolaru D, et al. Plasma-assisted ignition in scramjets. *J Propuls Power* 2008;24:641–54.
- [51] Leonov SB, Yarrantsev DA. Plasma-induced ignition and plasma-assisted combustion in high-speed flow. *Plasma Sources Sci Technol* 2007;16:132–8.
- [52] Esakov I, Grachev L, Khodataev K, Van Wie D. Experiments on propane ignition in high-speed airflow using a deeply under critical microwave discharge. In: 42nd AIAA aerospace sciences meeting including the new horizons forum and aerospace exposition, Reno, Nevada; 2004. AIAA-2004-0840.
- [53] Williams S, Popovic S, Vuskovic L, Carter C, Jacobson L, Kuo S, et al. Model and igniter development for plasma assisted combustion. No. AFRL-VS-HA-TR-2004-1132. Air Force Research Lab Hanscom AFB MA Space Vehicles Directorate; 2004.
- [54] Klimov A, Bityurin V, Kuznetsov A, Tolkunov B, Vystavkin N, Vasiliev M. External and internal plasma-assisted combustion. In: 42nd AIAA aerospace sciences meeting including the new horizons forum and aerospace exposition, Reno, Nevada; 2004. AIAA-2004-1014.
- [55] Shikhov VM, Chernikov AV, Ershov AP, Konstantinovskii RS, Shikhova LV, Zlobin VV. propane–butane–air mixture ignition and combustion in the aerodynamic channel with the stagnant zone. In: 42nd AIAA aerospace sciences meeting including the new horizons forum and aerospace exposition, Reno, Nevada; 2004. AIAA-2004-0838.
- [56] Do H, Im S, Cappelli M, Mungal MG. Plasma assisted flame ignition of supersonic flows over a flat wall. *Combust Flame* 2010;157:2298–305.
- [57] Kailasanath K. Recent developments in the research on pulse detonation engines. *AIAA J* 2003;41:145–59.
- [58] Dean AJ. A review of PDE development for propulsion applications. In: 45th AIAA aerospace sciences meeting including the new horizons forum and aerospace exposition, Reno, Nevada; 2007. AIAA-2007-0985.
- [59] Starikovskiy A, Aleksandrov N, Rakitin A. Plasma-assisted ignition and deflagration-to-detonation transition. *PhilosTrans R Soc A Math Phys Eng Sci* 2012;370:740–73.
- [60] Rakitin AE, Starikovskii AY. Mechanisms of deflagration-to-detonation transition under initiation by high-voltage nanosecond discharges. *Combust Flame* 2008;155:343–55.
- [61] Busby K, Corrigan J, Yu ST, Hoke J, Cathey M, Gundersen M. Effects of corona, spark and surface discharges on ignition delay and deflagration-to-detonation times in pulsed detonation engines. In: 45th AIAA aerospace sciences meeting including the new horizons forum and aerospace exposition, Reno, Nevada; 2007. AIAA-2007-1028.
- [62] Lefkowitz J, Ju Y, Stevens C, Ombrello T, Schauer F, Hoke J. The effects of repetitively pulsed nanosecond discharges on ignition time in a pulsed detonation engine. In: 49th AIAA/ASME/SAE/ASEE joint propulsion conference, San Jose, CA; 2013. AIAA-2013-3719.
- [63] Warris AM, Weinberg F. Ignition and flame stabilization by plasma jets in fast gas streams. *Symp Int Combust* 1985;20:1825–31.
- [64] Matveev I, Matveeva S, Gutsol A, Fridman A. Non-equilibrium plasma igniters and pilots for aerospace application. In: 43rd AIAA aerospace sciences meeting including the new horizons forum and aerospace exposition, Reno, Nevada; 2005. AIAA-2005-1191.
- [65] Ganguly BN. Hydrocarbon combustion enhancement by applied electric field and plasma kinetics. *Plasma Phys Control Fusion* 2007;49:B239.
- [66] Choi WS, Neumeier Y, Jagoda J. Stabilization of a combustion process near lean blow off by an electric discharge. In: 42nd AIAA aerospace sciences meeting including the new horizons forum and aerospace exposition, Reno, Nevada; 2004. AIAA-2004-982.
- [67] Pilla G, Galley D, Lacoste DA, Lacas F, Veynante D, Laux CO. Stabilization of a turbulent premixed flame using a nanosecond repetitively pulsed plasma. *IEEE Trans Plasma Sci* 2006;34:2471–7.
- [68] Ikeda Y, Moon A, Kaneko M. Development of microwave-enhanced spark-induced breakdown spectroscopy. *Appl Opt* 2010;49:2471–7.
- [69] Lefkowitz J, Ju Y, Tsuruoka R, Ikeda Y. A study of plasma-assisted ignition in a small internal combustion engine. In: 50th AIAA aerospace sciences meeting including the new horizons forum and aerospace exposition, Nashville, Tennessee; 2012. AIAA-2012-1133.
- [70] Wolk B, DeFilippo A, Chen JY, Dibble R, Nishiyama A, Ikeda Y. Enhancement of flame development by microwave-assisted spark ignition in constant volume combustion chamber. *Combust Flame* 2013;160:1225–34.
- [71] Wang Q, Zhang G, Liu Y, Hou L, Liu C, Wang Z, et al. Visual features of microwave ignition of methane–air mixture in a constant volume cylinder. *Appl Phys Lett* 2013;103:204104.
- [72] Maly R. Spark ignition: its physics and effect on the internal combustion engine. *Fuel economy*. Springer US; 1984. p. 91–148.
- [73] Mariani A, Foucher F. Radio frequency spark plug: an ignition system for modern internal combustion engines. *Appl Energy* 2014;122:151–61.
- [74] Dale JD, Smy PR, Clements RM. Laser ignited internal combustion engine—an experimental study. *SAE Tech Paper*. 1978. p. 780329.
- [75] Ma JX, Alexander DR, Poulain DE. Laser spark ignition and combustion characteristics of methane–air mixtures. *Combust Flame* 1998;112:492–506.
- [76] Herdin G, Klausner J, Wintner E, Weinrotter M, Graf J, Iskra K. Laser ignition: a new concept to use and increase the potentials of gas engines. In: ASME 2005 intern. combust. engine div. fall tech. conf; 2005. p. 673–81.
- [77] Morsy MH. Review and recent developments of laser ignition for internal combustion engines applications. *Renew Sustain Energy Rev* 2012;16:4849–75.
- [78] Kofler H, Tauer J, Tartar G, Iskra K, Klausner J, Herdin G, et al. An innovative solid-state laser for engine ignition. *Laser Phys Lett* 2007;4:322–7.
- [79] Cathey CD, Tang T, Shiraishi T, Urushihara T, Kuthi A, Gundersen MA. Nanosecond plasma ignition for improved performance of an internal combustion engine. *IEEE Trans Plasma Sci* 2007;35:1664–8.
- [80] Liu JB, Sinibaldi J, Brophy C, Kuthi A, Jiang C, Ronney P, et al. Transient plasma ignition of quiescent and flowing air/fuel mixtures. *IEEE Trans Plasma Sci* 2005;33:844–9.
- [81] Shiraishi T, Urushihara T, Gundersen MA. A trial of ignition innovation of gasoline engine by nanosecond pulsed low temperature plasma ignition. *J Phys D Appl Phys* 2009;42:135208.

- [82] Czernichowski A. Gliding arc: applications to engineering and environment control. *Pure Appl Chem* 1994;66:1301–10.
- [83] Behbahani HF, Warris AM, Weinberg FJ. The destruction of nitric oxide by nitrogen atoms from plasma jets: designing for thermal stratification. *Combust Sci Technol* 1983;30:289–302.
- [84] Penetrante BM, Brusasco RM, Merritt BT, Pitz WJ, Vogtlin GE. Plasma-assisted catalytic reduction of NOx. *SAE Tech Paper*. 1998. p. 982508.
- [85] Kim HH, Takashima K, Katsura S, Mizuno A. Low-temperature NOx reduction processes using combined systems of pulsed corona discharge and catalysts. *J Phys D Appl Phys* 2001;34:604–13.
- [86] Puchkarev V, Gundersen M. Energy efficient plasma processing of gaseous emission using a short pulse discharge. *Appl Phys Lett* 1997;71:3364–6.
- [87] Urashima K, Chang JS, Ito T. Reduction of NOx from combustion flue gases by superimposed barrier discharge plasma reactors. *IEEE Trans Ind Appl* 1997;33:879–86.
- [88] Khacef A, Cormier JM, Pouvesle JM. NOx remediation in oxygen-rich exhaust gas using atmospheric pressure non-thermal plasma generated by a pulsed nanosecond dielectric barrier discharge. *J Phys D Appl Phys* 2002;35:1491–8.
- [89] Fridman A. Plasma chemistry. Cambridge University Press; 2008.
- [90] Brethes-Dupouey S, Peyrou R, Held B. Removal of H₂S in air by using gliding discharges. *Eur Phys J Appl Phys* 2000;11:43–58.
- [91] Du CM, Yan JH, Cheron B. Decomposition of toluene in a gliding arc discharge plasma reactor. *Plasma Sources Sci Technol* 2007;16:791–7.
- [92] Yu L, Tu X, Li X, Wang Y, Chi Y, Yan J. Destruction of acenaphthene, fluorene, anthracene and pyrene by a dc gliding arc plasma reactor. *J Hazard Mater* 2010;180:449–55.
- [93] Higashi M, Uchida S, Suzuki N, Fuji KI. Soot elimination and NOx and SOx reduction in diesel-engine exhaust by a combination of discharge plasma and oil dynamics. *IEEE Trans Plasma Sci* 1992;20:1–12.
- [94] Okubo M, Kuroki T, Miyairi Y, Yamamoto T. Low-temperature soot incineration of diesel particulate filter using remote nonthermal plasma induced by a pulsed barrier discharge. *IEEE Trans Plasma Sci* 2004;40:1504–12.
- [95] Martin AR, Shawcross JT, Whitehead CJ. The oxidation of carbon soot in a non-thermal, atmospheric pressure plasma: experiment and modelling. *J Adv Oxid Technol* 2005;8:126–32.
- [96] Cha M, Lee S, Kim K, Chung S. Soot suppression by nonthermal plasma in coflow jet diffusion flames using a dielectric barrier discharge. *Combust Flame* 2005;141:438–47.
- [97] Bromberg L, Cohn DR, Rabinovich A, Alexeev N, Samokhin A, Ramprasad R, et al. System optimization and cost analysis of plasma catalytic reforming of natural gas. *Int J Hydrogen Energy* 2000;25:1157–61.
- [98] Bromberg L, Cohn DR, Rabinovich A, Alexeev N. Plasma catalytic reforming of methane. *Int J Hydrogen Energy* 1999;24:1131–7.
- [99] Fridman A, Nester S, Kennedy LA, Saveliev A, Mutaf-Yardimci O. Gliding arc gas discharge. *Prog Energy Combust Sci* 1998;25:211–31.
- [100] Kaske G, Kerke L, Muller R. Hydrogen production in the Huls plasma-reforming process. *Hydrogen energy progress VI*. 1986. p. 1.
- [101] Paulmier T, Fulcheri L. Use of non-thermal plasma for hydrocarbon reforming. *Chem Eng J* 2005;106:59–71.
- [102] Petipas G, Rollier JD, Darnon A, Gonzalez-Aguilar J, Metkemeijer R, Fulcheri L. A comparative study of non-thermal plasma assisted reforming technologies. *Int J Hydrogen Energy* 2007;32:2848–67.
- [103] Zhou LM, Xue B, Kogelschatz U, Eliasson B. Nonequilibrium plasma reforming of greenhouse gases to synthesis gas. *Energy Fuels* 1998;12:1191–9.
- [104] Hammer T, Kappes T, Baldauf M. Plasma catalytic hybrid processes: gas discharge initiation and plasma activation of catalytic processes. *Catal Today* 2004;89:5–14.
- [105] Tao X, Bai M, Li X, Long H, Shang S, Yin Y, et al. CH₄/CO₂ reforming by plasma—challenges and opportunities. *Prog Energy Combust Sci* 2011;37:113–24.
- [106] Sun W, Uddi M, Won SH, Ombrello T, Carter C, Ju Y. Kinetic effects of non-equilibrium plasma-assisted methane oxidation on diffusion flame extinction limits. *Combust Flame* 2012;159:221–9.
- [107] Sun W, Won SH, Ju Y. In situ plasma activated low temperature chemistry and the S-curve transition in DME/oxygen/helium mixture. *Combust Flam* 2014;1–10. e.
- [108] Won SH, Jiang B, Diévar P, Sohn CH, Ju Y. Self-sustaining n-heptane cool diffusion flames activated by ozone. *Proc Combust Inst* 2015. <http://dx.doi.org/10.1016/j.proci.2014.05.021>.
- [109] Hicks A, Norberg S, Shawcross P, Lempert WR, Rich JW, Adamovich IV. Singlet oxygen generation in a high pressure non-self-sustained electric discharge. *J Phys D Appl Phys* 2005;38:3812–24.
- [110] Raizer YP. Gas discharge physics. Barcelona: Springer; 1991.
- [111] Sun ZW, Zhu JJ, Li ZS, Aldén M, Leipold F, Salewski M, et al. Optical diagnostics of a gliding arc. *Opt Express* 2013;21:6028–44.
- [112] Starikovskaya SM, Kukavets AY, Nudnova MM, Starikovskii AY. Analysis of the spatial uniformity of the combustion of a gaseous mixture initiated by a nanosecond discharge. *Combust Flame* 2004;139:177–87.
- [113] Raizer YP, Shneider MN, Yatsenko NA. Radio-frequency capacitive discharge. CRC Press; 1995.
- [114] Lukes P, Clupek M, Babicky V, Janda V, Sunka P. Generation of ozone by pulsed corona discharge over water surface in hybrid gas–liquid electrical discharge reactor. *J Phys D Appl Phys* 2005;38:409–16.
- [115] Chen J. Direct current Corona-Enhanced chemical reactions [Ph.D dissertation]. Department of Mechanical Engineering, The University Of Minnesota; 2002.
- [116] Chen Z, Ju Y. Theoretical analysis of the evolution from ignition kernel to flame ball and planar flame. *Combust Theory Model* 2007;11:427–53.
- [117] Brande WT. The Bakerian lecture: on some new electro-chemical phenomena. *Philos Trans R Soc Lond* 1814;104:51–61.
- [118] Haseloff CE, Kirkby PJ. XLV. The electrical effects produced by the explosion of hydrogen and oxygen. *London, Edinburgh Dublin Philos J Sci* 1904;8(46):471–81.
- [119] Kirkby PJ. A theory of the chemical action of the electric discharge in electrolytic gas. *Proc R Soc Lond Ser A* 1911:151–74.
- [120] Lawton J, Payne KG, Weinberg FJ. Flame-arc combination. *Nature* 1962;193:736–8.
- [121] Chen DCC, Lawton J, Weinberg FJ. Augmenting flames with electric discharges. *Symp Int Combust* 1965:743–54.
- [122] Lewis B. The effect of an electric field on flames and their propagation. *J Am Chem Soc* 1931;53:1304–13.
- [123] Calcote HF. Electrical properties of flames: burner flames in transverse electric fields. *Symp Combust Flame Explos Phenom* 1949;3:245–53.
- [124] Wortberg G. Ion-concentration measurements in a flat flame at atmospheric pressure. *Symp Int Combust* 1965;10:651–5.
- [125] Jagers HC, Von Engel A. The effect of electric fields on the burning velocity of various flames. *Combust Flame* 1971;16:275–85.
- [126] Heinsohn RJ, Wolfhorst DE, Becker PM. The effects of an electric field on an opposed-jet diffusion flame. *Combust Flame* 1967;11:288–96.
- [127] Won SH, Ryu SK, Kim MK, Cha MS, Chung SH. Effect of electric fields on the propagation speed of tribrachial flames in coflow jets. *Combust Flame* 2008;152:496–506.
- [128] Bradley D, Ibrahim S. Electron temperatures in flame gases: experiment and theory. *Combust Flame* 1975;24:169–71.
- [129] Tewari GP, Wilson JR. An experimental study of the effects of high frequency electric fields on laser-induced flame propagation. *Combust Flame* 1975;24:159–67.
- [130] Clements RM, Smith RD, Smy PR. Enhancement of flame speed by intense microwave radiation. *Combust Sci Technol* 1981;26:77–81.
- [131] Groff EG, Krage MK. Microwave effects on premixed flames. *Combust Flame* 1984;56:293–306.
- [132] MacLachy CS, Clements RM, Smy PR. An experimental investigation of the effect of microwave radiation on a propane-air flame. *Combust Flame* 1982;45:161–9.
- [133] Ogawa S, Sakai Y, Sato K, Seka S. Influence of microwave on methane–air laminar flames. *Jpn J Appl Phys* 1998;37:179–85.
- [134] Stockman ES, Zaidi SH, Miles RB, Carter CD, Ryan MD. Measurements of combustion properties in a microwave enhanced flame. *Combust Flame* 2009;156:1453–61.
- [135] Ju Y, Macheret SO, Shneider MN, Miles RB, Sullivan DJ. Numerical study of the effect of microwave discharge on the premixed methane–air flame. In: 42nd AIAA aerospace sciences meeting including the new horizons forum and aerospace exposition, 5–8 January, Reno, Nevada; 2004. AIAA–2004–3707.
- [136] Zaidi SH, Stockman E, Qin X, Zhao Z, Macheret S, Ju Y, et al. Measurements of hydrocarbon flame speed enhancement in high-Q microwave cavity. In: 44th AIAA aerospace sciences meeting including the new horizons forum and aerospace exposition, Reno, Nevada; 2006. AIAA–2006–1217.
- [137] Michael JB, Miles RB. Ultra-lean combustion sustained by pulsed subcritical microwaves. In: 42nd AIAA plasmadynamics lasers conf., Honolulu, Hawaii; 2011. AIAA–2011–3446.
- [138] Ombrello T, Ju Y, Fridman A. Kinetic ignition enhancement of diffusion flames by nonequilibrium magnetic gliding arc plasma. *AIAA J* 2008;46:2424–33.
- [139] Ombrello T, Ju Y. Kinetic ignition enhancement of H₂ versus fuel-blended air diffusion flames using nonequilibrium plasma. *IEEE Trans Plasma Sci* 2008;36:2924–32.
- [140] Fridman A, Gutsol A, Gangoli S, Ju Y, Ombrello T. Characteristics of gliding arc and its application in combustion enhancement. *J Propuls Power* 2008;24:1216–28.
- [141] Williams FA. Combustion theory. Benjamin-Cummings Publishing Co; 1985.
- [142] Glassman I. Combustion. 2nd ed. Academic Press; 1987.
- [143] Law CK. Combustion physics. Cambridge University Press; 2010.
- [144] Sun W, Ombrello T, Won SH, Carter C, Ju Y. Direct ignition and S-curve transition by in situ nanosecond pulsed discharge in methane/oxygen/helium counterflow flame. *Proc Combust Inst* 2013;34:847–55.
- [145] Sun W. Non-equilibrium plasma assisted combustion [Ph.D dissertation]. Department of Mechanical and Aerospace Engineering, Princeton University; 2013. http://dataspace.princeton.edu/jspui/bitstream/88435/dsp01pn89d663g/1/Sun_princeton_0181D_10496.pdf.
- [146] Samukawa S, Hori M, Rauf S, Tachibana K, Bruggeman P, Kroesen G, et al. The 2012 plasma roadmap. *J Phys D Appl Phys* 2012;253001.
- [147] Yin Z, Adamovich I, Lempert W. OH radical and temperature measurements during ignition of H₂–air mixtures excited by a repetitively pulsed nanosecond discharge. *Proc Combust Inst* 2013;34:3249–58.
- [148] Zuzek Y, Bowman S, Choi I. Pure rotational CARS studies of thermal energy release and ignition in nanosecond repetitively pulsed hydrogen–air plasmas. *Proc Combust Inst* 2011;33:3225–32.

- [149] Mintusov E, Serdyuchenko A, Choi I, Lempert WR, Adamovich IV. Mechanism of plasma assisted oxidation and ignition of ethylene–air flows by a repetitively pulsed nanosecond discharge. *Proc Combust Inst* 2009;32:3181–8.
- [150] Starikovskiy A, Rakitin A, Correale G, Nikipelov A, Urushihara T, Shiraishi T. Ignition of hydrocarbon–air mixtures with non-equilibrium plasma at elevated pressures. In: 50th AIAA aerospace sciences meeting including the new horizons forum and aerospace exposition, Nashville, Tennessee; 2012. AIAA-2012–0828.
- [151] Stepanyan SA, Boumehdi MA, Vanhove G, Starikovskaia SM. Time-resolved electric field measurements in nanosecond surface dielectric discharge, comparison of different polarities, ignition of combustible mixtures by surface discharge in a rapid compression machine. In: 51st AIAA aerospace sciences meeting including the new horizons forum and aerospace exposition, Grapevine (Dallas/Ft. Worth region), Texas; 2013. AIAA-2013–1053.
- [152] Cathey C, Cain J, Wang H, Gundersen MA, Carter C, Ryan M. OH production by transient plasma and mechanism of flame ignition and propagation in quiescent methane–air mixtures. *Combust Flame* 2008;154:715–27.
- [153] Starik AM, Kuleshov PS, Titova NS. Initiation of combustion of a hydrogen–air mixture with ozone impurity by UV laser radiation. *Tech Phys* 2008;53: 235–43.
- [154] Kozlov V, Starik AM, Titova NS. Enhancement of combustion of a hydrogen–air mixture by excitation of O₂ molecules to the $\frac{1}{2}\Delta_g$ state. *Combust Explos Shock Waves* 2008;44:371–9.
- [155] Smirnov VV, Stelmakh OM, Fabelinsky VI, Kozlov DN, Starik AM, Titova NS. On the influence of electronically excited oxygen molecules on combustion of hydrogen–oxygen mixture. *J Phys D Appl Phys* 2008;41:192001.
- [156] Ombrello T, Won SH, Ju Y, Williams S. Flame propagation enhancement by plasma excitation of oxygen. Part II: effects of O₂($\frac{1}{2}\Delta_g$). *Combust Flame* 2010;157:1916–28.
- [157] Ombrello T, Won SH, Ju Y, Williams S. Flame propagation enhancement by plasma excitation of oxygen. Part I: effects of O₃. *Combust Flame* 2010;157: 1906–15.
- [158] Wang ZH, Yang L, Li B, Li ZS, Sun ZW, Aldén M, et al. Investigation of combustion enhancement by ozone additive in CH₄/air flames using direct laminar burning velocity measurements and kinetic simulations. *Combust Flame* 2012;159:120–9.
- [159] Liang X, Wang Z, Weng W, Zhou Z, Huang Z, Zhou J. Study of ozone-enhanced combustion in H₂/CO/N₂/air premixed flames by laminar burning velocity measurements and kinetic modeling. *Int J Hydrogen Energy* 2012;1–12.
- [160] Uddi M, Jiang N, Mintusov E, Adamovich IV, Lempert WR. Atomic oxygen measurements in air and air/fuel nanosecond pulse discharges by two photon laser induced fluorescence. *Proc Combust Inst* 2009;32:929–36.
- [161] Stancu GD, Kaddouri F, Lacoste DA, Laux CO. Atmospheric pressure plasma diagnostics by OES, CRDS and TALIF. *J Phys D Appl Phys* 2010;43:124002.
- [162] Mintusov EI, Pancheshnyi SV, Starikovskiy AY. Propane–air flame control by non-equilibrium low temperature pulsed nanosecond barrier discharge. In: 42nd AIAA aerospace sciences meeting including the new horizons forum and aerospace exposition, Reno, Nevada; 2004. AIAA-2004-1013.
- [163] Moeck JP, Lacoste DA, Laux CO, Paschereit CO. Control of combustion dynamics in a swirl-stabilized combustor with nanosecond repetitively pulsed discharges. In: 51st AIAA aerospace sciences meeting including the new horizons forum and aerospace exposition, Grapevine (Dallas/Ft. Worth region), Texas; 07–10 January, 2013. AIAA-2013–0565.
- [164] Semtsovd JB, Kulatilaka WD, Roy S, Frederickson KA, Lempert WR, Gord JR. Femtosecond TALIF imaging of atomic hydrogen in pulsed, non-equilibrium plasmas. In: 52nd AIAA aerospace sciences meeting including the new horizons forum and aerospace exposition, national harbor, Maryland; 2014. AIAA-2014–1359.
- [165] Montello A, Yin Z, Burnette D, Adamovich IV, Lempert WR. Picosecond CARS measurements of nitrogen vibrational loading and rotational/translational temperature in non-equilibrium discharges. *J Phys D Appl Phys* 2013;46: 464002.
- [166] Brumfield B, Sun W, Ju Y, Wysocki G. Direct in situ quantification of HO₂ from a flow reactor. *J Phys Chem Lett* 2013;4:872–6.
- [167] Brumfield B, Sun W, Wang Y, Ju Y, Wysocki G. Dual modulation Faraday rotation spectroscopy of HO₂ in a flow reactor. *Opt Lett* 2014;39:1783–6.
- [168] Lefkowitz JK, Uddi M, Windom B, Lou GF, Ju Y. In situ species diagnostics and kinetic study of plasma activated ethylene pyrolysis and oxidation in a low temperature flow reactor. *Proc Combust Inst* 2015. <http://dx.doi.org/10.1016/j.proci.2014.08.001>.
- [169] Pai D, Lacoste D, Laux C. Nanosecond repetitively pulsed discharges in air at atmospheric pressure—the spark regime. *Plasma Sources Sci Technol* 2010;19:065015.
- [170] Bak MS, Do H, Mungal MG, Cappelli MA, Soo M, Godfrey M. Plasma-assisted stabilization of laminar premixed methane/air flames around the lean flammability limit. *Combust Flame* 2012;159:3128–37.
- [171] Starikovskaia SM. Plasma-assisted ignition and combustion: nanosecond discharges and development of kinetic mechanisms. *J Phys D Appl Phys* 2014;47:353001.
- [172] Ikeda Y, Nishiyama A, Kaneko M. Microwave enhanced ignition process for fuel mixture at elevated pressure of 1MPa. In: 47th AIAA aerospace sciences meeting including the new horizons forum and aerospace exposition, Orlando, Florida; 2009. AIAA-2009-223.
- [173] Thelen BC, Chun D, Toulson E, Lee T. A study of an energetically enhanced plasma ignition system for internal combustion engines. *IEEE Trans Plasma Sci* 2013;41:3223–32.
- [174] Shukla B, Gururajan V, Eisazadeh-Far K, Windom B, Singleton D, Gundersen MA, et al. Effects of electrode geometry on transient plasma induced ignition. *J Phys D Appl Phys* 2013;46:205201.
- [175] Singleton D, Pendleton SJ, Gundersen MA. The role of non-thermal transient plasma for enhanced flame ignition in C₂H₄–air. *J Phys D Appl Phys* 2011;44: 022001.
- [176] Lacoste DA, Moeck JP, Durox D, Laux CO, Schuller T. Effect of nanosecond repetitively pulsed discharges on the dynamics of a swirl-stabilized lean premixed flame. *J Eng Gas Turbines Power* 2013;135:101501.
- [177] Barbosa S, Pilla G, Lacoste D, Scouffaire P, Ducruix S, Laux CO, et al. Influence of a repetitively pulsed plasma on the flame stability domain of a lab-scale gas turbine combustor. In: *Proc Eur Combust Meet*; 2009.
- [178] Cathey C, Wang F, Tang T, Kuthi A, Gundersen MA, Sinibaldi JO, et al. Transient plasma ignition for delay reduction in pulse detonation engines. In: 45th AIAA aerospace sciences meeting including the new horizons forum and aerospace exposition, Reno, Nevada; 2007. AIAA-2007–443.
- [179] Foucher F, Higelin P, Mounaïn-Rousselle C, Dagaut P. Influence of ozone on the combustion of n-heptane in a HCCI engine. *Proc Combust Inst* 2013;34: 3005–12.
- [180] Takita K, Murakami K, Nakane H, Masuya G. A novel design of a plasma jet torch igniter in a scramjet combustor. *Proc Combust Inst* 2005;30:2843–9.
- [181] Matsubara Y, Takita K, Masuya G. Combustion enhancement in a supersonic flow by simultaneous operation of DBD and plasma jet. *Proc Combust Inst* 2013;34:3287–94.
- [182] Do H, Cappelli MA, Mungal MG. Plasma assisted cavity flame ignition in supersonic flows. *Combust Flame* 2010;157:1783–94.
- [183] Leonov SB, Kochetov IV, Napartovich AP, Sabel VA, Yarrantsev DA. Plasma-induced ethylene ignition and flameholding in confined supersonic air flow at low temperatures. *IEEE Trans Plasma Sci* 2011;39:781–7.
- [184] Leonov SB, Yarrantsev DA, Napartovich AP, Kochetov IV. Ignition I. Researcher L. Plasma-assisted ignition and flameholding in high-speed flow. In: 44th AIAA aerospace sciences meeting including the new horizons forum and aerospace exposition, Reno, Nevada; 2006. AIAA-2006-563.
- [185] Leonov S, Yarrantsev D, Carter C. Experiments on electrically controlled flameholding on a plane wall in a supersonic airflow. *J Propuls Power* 2009;25:289–94.
- [186] Esakov II, Grachev LP, Khodataev KV, Vinogradov VA, Van Wie DM. Efficiency of propane–air mixture combustion assisted by deeply undercritical MW discharge in cold high-speed airflow. In: 44th AIAA aerospace sciences meeting including the new horizons forum and aerospace exposition, Reno, Nevada; 2006. AIAA-2006-1212.
- [187] Brieschenk S, O'Byrne S, Kleine H. Laser-induced plasma ignition studies in a model scramjet engine. *Combust Flame* 2013;160:145–8.
- [188] Song CL, Bin F, Tao ZM, Li FC, Huang QF. Simultaneous removals of NO_x, HC and PM from diesel exhaust emissions by dielectric barrier discharges. *J Hazard Mater* 2009;166:523–30.
- [189] Lee DH, Kim KT, Kang HS, Song YH, Park JE. Plasma-assisted combustion technology for NO_x reduction in industrial burners. *Environ Sci Technol* 2013;47:10964–70.
- [190] Billig FS. Research on supersonic combustion. *J Propuls Power* 1993;9: 499–514.
- [191] Dooley S, Won SH, Heyne J, Farouk TI, Ju Y, Dryer FL, et al. The experimental evaluation of a methodology for surrogate fuel formulation to emulate gas phase combustion kinetic phenomena. *Combust Flame* 2012;159:1444–66.
- [192] Masuya G, Takita K, Takahashi K, Takatori F, Ohzeki H. Effects of airstream mach number on H/N plasma igniter. *J Propuls Power* 2002;18:679–85.
- [193] Takita K, Moriaki A, Kitagawa T, Masuya G. Ignition and flame-holding of H₂ and CH₄ in high temperature airflow by a plasma torch. *Combust Flame* 2003;132:679–89.
- [194] Adamovich IV, Choi I, Jiang N, Kim JH, Keshav S, Lempert WR, et al. Plasma assisted ignition and high-speed flow control: non-thermal and thermal effects. *Plasma Sources Sci Technol* 2009;18:034018.
- [195] Kim W, Do H, Mungal MG, Cappelli MA. A study of plasma-stabilized diffusion flames at elevated ambient temperatures. *IEEE Trans Plasma Sci* 2008;36:2898–904.
- [196] Chen Z, Burke MP, Ju Y. Effects of Lewis number and ignition energy on the determination of laminar flame speed using propagating spherical flames. *Proc Combust Inst* 2009;32:1253–60.
- [197] Suckewever A. Knite Inc. 2010. personal communication.
- [198] ElSabbagh M, Kado S, Ikeda Y, Sasaki K. Measurements of rotational temperature and density of molecular nitrogen in spark-plug assisted atmospheric-pressure microwave discharges by rotational raman scattering. *Jpn J Appl Phys* 2011;50:076101.
- [199] Ju Y, Maruta K. Microscale combustion: technology development and fundamental research. *Prog Energy Combust Sci* 2011;37:669–715.
- [200] Pavel N, Tsunekane M, Taira T. Nd:YAG/Cr⁴⁺:YAG monolithic micro-laser with multiple-beam output for engine ignition. *Opt Express* 2011;19:9378–84.
- [201] Seurin JF, Xu G, Wang Q, Guo B, Van Leeuwen R, Miglo A, et al. High-brightness pump sources using 2D VCSEL arrays. *Proc SPIE* 2010;7615: 76150F.
- [202] Ehn A, Zhu J, Petersson P, Li ZS, Aldén M, Fureby C, et al. Plasma assisted combustion: effects of O₃ on large scale turbulent combustion studied with

- laser diagnostics and large eddy simulations. *Proc Combust Inst* 2015;35. <http://dx.doi.org/10.1016/j.proci.2014.05.092>.
- [203] Schauer F, Stutrud J, Bradley R. Detonation initiation studies and performance results for pulsed detonation engine applications. In: 39th AIAA aerospace sciences meeting & exhibit, Reno Nevada; 2001. AIAA-2001-1129.
- [204] Serbin S, Mostipanenko A, Matveev I, Tropina A. Improvement of the gas turbine plasma assisted combustor characteristics. In: 49th AIAA aerospace sciences meeting including the new horizons forum and aerospace exposition, Orlando, Florida; 2011. AIAA-2011-61.
- [205] Versailles P, Chishty WA, Vo HD. Application of dielectric barrier discharge to improve the flashback limit of a lean premixed dump combustor. *J Eng Gas Turbines Power* 2012;134:031501.
- [206] Grundmann J, Müller S, Zahn RJ. Treatment of soot by dielectric barrier discharges and ozone. *Plasma Chem Plasma Process* 2005;25:455–66.
- [207] Hammer T. Non-thermal plasma application to the abatement of noxious emissions in automotive exhaust gases. *Plasma Sources Sci Technol* 2002;11: A196–201.
- [208] Mintoussov E, Anokhin E, Starikovskii AY, Tsyganov D. Plasma-assisted combustion and fuel reforming. In: 45th AIAA aerospace sciences meeting including the new horizons forum and aerospace exposition, Reno, Nevada; 2007. AIAA-2007-1382.
- [209] Mueller MA, Kim TJ, Yetter RA, Dryer FL. Flow reactor studies and kinetic modeling of the H_2/O_2 reaction. *Int J Chem Kinet* 1999;31:113–25.
- [210] Zheng XL, Law CK. Ignition of premixed hydrogen/air by heated counterflow under reduced and elevated pressures. *Combust Flame* 2004;136:168–79.
- [211] Burke MP, Chaos M, Dryer FL, Ju Y. Negative pressure dependence of mass burning rates of $H_2/CO/O_2$ diluent flames at low flame temperatures. *Combust Flame* 2010;157:618–31.
- [212] Maas U, Warnatz J. Ignition processes in hydrogen/oxygen mixtures. *Combust Flame* 1988;74:53–69.
- [213] Bozhakov SA, Starikovskaia SM, Starikovskii AY. Nanosecond gas discharge ignition of H_2 - and CH_4 -containing mixtures. *Combust Flame* 2003;133: 133–46.
- [214] Ju Y, Sun W, Burke MP, Gou X, Chen Z. Multi-timescale modeling of ignition and flame regimes of n-heptane–air mixtures near spark assisted homogeneous charge compression ignition conditions. *Proc Combust Inst* 2011;33: 1245–51.
- [215] Diévert P, Won SH, Dooley S, Dryer FL, Ju Y. A kinetic model for methyl decanoate combustion. *Combust Flame* 2012;159:1793–805.
- [216] Won SH, Windom B, Jiang B, Ju Y. The role of low temperature fuel chemistry on turbulent flame propagation. *Combust Flame* 2014;161:475–83.
- [217] Arnold ST, Dotan I, Williams S, Viggiano AA, Morris RA. Selected ion flow tube studies of air plasma cations reacting with alkylbenzenes. *J Phys Chem A* 2000;104:928–34.
- [218] Sun W, Chen Z, Gou X, Ju Y. A path flux analysis method for the reduction of detailed chemical kinetic mechanisms. *Combust Flame* 2010;157:1298–307.
- [219] Lewis B, Von Elbe G. Combustion, flames and explosions of gases. 3rd ed. Academic Press; 1987.
- [220] Ju Y, Maruta K, Niioka T. Combustion limits. *Appl Mech Rev* 2001;54:257–77.
- [221] Lakshminsha KN, Paul PJ, Mukunda HS. On the flammability limit and heat loss in flames with detailed chemistry. *Symp Int Combust* 1990;23:433–40.
- [222] Platt J, Tien J. Flammability of a weakly stretched premixed flame: the effect of radiation loss. In: Fall meeting of the eastern states section of the combustion institute; 1990.
- [223] Ju Y, Guo H, Maruta K, Liu F. On the extinction limit and flammability limit of non-adiabatic stretched methane–air premixed flames. *J Fluid Mech* 1997;342:315–34.
- [224] Ju Y, Choi CW. An analysis of sub-limit flame dynamics using opposite propagating flames in mesoscale channels. *Combust Flame* 2003;133: 483–93.
- [225] Maruta K, Yoshida M, Guo H, Ju Y, Niioka T. Extinction of low-stretched diffusion flame in microgravity. *Combust Flame* 1998;112:181–7.
- [226] Clavin P. Dynamic behavior of premixed flame fronts in laminar and turbulent flows. *Prog Energy Combust Sci* 1985;11:1–59.
- [227] Guo H, Smallwood G, Liu F, Ju Y, Gulder O. The effect of hydrogen addition on flammability limit and NO_x emission in ultra-lean counterflow CH_4 /air premixed flames. *Proc Combust Inst* 2005;30:303–11.
- [228] Weinberg FJ, Wilson JR. A preliminary investigation of the use of focused laser beams for minimum ignition energy studies. *Proc R Soc Lond A Math Phys Sci* 1971;321:41–52.
- [229] Ballal DR, Lefebvre AH. The influence of spark discharge characteristics on minimum ignition energy in flowing gases. *Combust Flame* 1975;24: 99–108.
- [230] Chen Z, Burke MP, Ju Y. On the critical flame radius and minimum ignition energy for spherical flame initiation. *Proc Combust Inst* 2011;33:1219–26.
- [231] Kim HH, Won SH, Santner J, Chen Z, Ju Y. Measurements of the critical initiation radius and unsteady propagation of n-decane/air premixed flames. *Proc Combust Inst* 2013;34:929–36.
- [232] Zhang H, Chen Z. Spherical flame initiation and propagation with thermally sensitive intermediate kinetics. *Combust Flame* 2011;158:1520–31.
- [233] Michael JB, Dogariu A, Schneider MN, Miles RB. Subcritical microwave coupling to femtosecond and picosecond laser ionization for localized, multipoint ignition of methane/air mixtures. *J Appl Phys* 2010;108:093308.
- [234] Miles RB. In: AFOSR plasma assisted combustion multi-university research initiative review meeting; 2013.
- [235] Leonov SB. Studies of ignition and flame holding by non-equilibrium transient plasmas. In: AFOSR-ARO basic combustion research review meeting; 2013.
- [236] Zhu J, Sun Z, Li Z, Ehn A, Aldén M, Salewski M, et al. Dynamics, OH distributions and UV emission of a gliding arc at various flow-rates investigated by optical measurements. *J Phys D Appl Phys* 2014;47:295203.
- [237] Leonov S, Isaenkov YI, Yarrantsev D, Schneider MN. Fast mixing by pulse discharge in high-speed flow. In: 14th AIAA/AHI space planes and hypersonic systems and technologies conference, Canberra, Australia; 2006. AIAA-2006-8129.
- [238] Leonov S, Isaenkov YI, Firsov AA, Nothnagel SL, Gimelshein SF, Shneider MN. Jet regime of the after spark channel decay. *Phys Plasmas* 2010;17:053505.
- [239] Starikovskaia SM, Starikovskii AY, Zatspein DV. Hydrogen oxidation in a stoichiometric hydrogen–air mixture in the fast ionization wave. *Combust Theory Model* 2001;5:97–129.
- [240] Smith GP, Golden DM, Frenklach M, Moriarty NW, Eiteneer B, Goldenberg M, et al. GRI-3.0 Mechanism. http://www.me.berkeley.edu/gri_mech/.
- [241] Wang H, You X, Joshi AV, Davis SG, Laskin A, Egolfopoulos F, et al. USC mech version II. High-temperature combustion reaction model of $H_2/CO/C_1$ – C_4 compounds. May 2007. http://ignis.usc.edu/USC_Mech_II.htm.
- [242] Shen X, Yang X, Santner J, Sun J, Ju Y. Experimental and kinetic studies of acetylene flames at elevated pressures. *Proc Combust Inst* 2015. <http://dx.doi.org/10.1016/j.proci.2014.05.106>.
- [243] Anikin NB, Starikovskaia SM, Starikovskii AY. Study of the oxidation of alkanes in their mixtures with oxygen and air under the action of a pulsed volume nanosecond discharge. *Plasma Phys Rep* 2004;30:1028–42.
- [244] Kosarev IN, Aleksandrov NL, Kindysheva SV, Starikovskaia SM, Starikovskii AY. Kinetics of ignition of saturated hydrocarbons by nonequilibrium plasma: C_2H_6 - to C_5H_{12} -containing mixtures. *Combust Flame* 2009;156:221–33.
- [245] Anikin NB, Starikovskaia SM, Starikovskii AY. Oxidation of saturated hydrocarbons under the effect of nanosecond pulsed space discharge. *J Phys D Appl Phys* 2006;39:3244–52.
- [246] Aleksandrov NL, Kindysheva SV, Kosarev IN, Starikovskaia SM, Starikovskii AY. Mechanism of ignition by non-equilibrium plasma. *Proc Combust Inst* 2009;32:205–12.
- [247] Kosarev IN, Aleksandrov NL, Kindysheva SV, Starikovskaia SM, Starikovskii AY. Kinetic mechanism of plasma-assisted ignition of hydrocarbons. *J Phys D Appl Phys* 2008;41:032002.
- [248] Wu L, Lane J, Cernansky NP, Miller DL, Fridman AA, Starikovskii AY. Plasma-assisted ignition below self-ignition threshold in methane, ethane, propane and butane–air mixtures. *Proc Combust Inst* 2011;33:3219–24.
- [249] Starikovskii AY. Kinetics of plasma-assisted oxidation and ignition below self-ignition threshold. In: 50th AIAA aerospace sciences meeting including the new horizons forum and aerospace exposition, Nashville, Tennessee; 2012. AIAA-2012-0244.
- [250] Yin Z, Adamovich IV. Ignition delay and time-resolved temperature measurements in nanosecond pulse hydrogen–air and ethylene–air plasmas at elevated initial temperatures. In: 49th AIAA aerospace sciences meeting including the new horizons forum and aerospace exposition, Orlando, Florida; 2011. AIAA-2011-1212.
- [251] Niemi K, Schulz-von der Gathen V, Döbele HF. Absolute atomic oxygen density measurements by two-photon absorption laser-induced fluorescence spectroscopy in an RF-excited atmospheric pressure plasma jet. *Plasma Sources Sci Technol* 2005;14:375–86.
- [252] Brackmann C, Nygren J, Bai X, Li Z, Bladh H, Axelsson B, et al. Laser-induced fluorescence of formaldehyde in combustion using third harmonic Nd:YAG laser excitation. *Spectrochim Acta Part A Mol Biomol Spectrosc* 2003;59: 3347–56.
- [253] Metz T, Bai X, Ossler F, Aldén M. Fluorescence lifetimes of formaldehyde (H_2CO) in the A band system at elevated temperatures and pressures. *Spectrochim Acta Part A Mol Biomol Spectrosc* 2004;60:1043–53.
- [254] Lutz AE, Kee RJ, Miller JA. SENKIN: a FORTRAN program for predicting homogeneous gas phase chemical kinetics with sensitivity analysis. 1997.
- [255] Zhao Z, Chaos M, Kazakov A, Dryer FL. Thermal decomposition reaction and a comprehensive kinetic model of dimethyl ether. *Int J Chem Kinet* 2008;40: 1–18.
- [256] Kasha M. Singlet oxygen electronic structure and energy transfer. CRC Press, Inc.; 2000.
- [257] Williams S, Gupta M, Owano T, Baer DS, O’Keefe A, Yarkony DR, et al. Quantitative detection of singlet O_2 by cavity-enhanced absorption. *Opt Lett* 2004;29:1066–8.
- [258] Starik AM, Titova NS. Possibility of initiation of combustion of CH_4 – O_2 (air) mixtures with laser-induced excitation of O_2 molecules. *Combust Explos Shock Waves* 2004;40:499–510.
- [259] Popov NA. The effect of nonequilibrium excitation on the ignition of hydrogen–oxygen mixtures. *High Temp* 2007;45:261–79.
- [260] Popov NA. Effect of singlet oxygen $O_2(a^1\Delta_g)$ molecules produced in a gas discharge plasma on the ignition of hydrogen–oxygen mixtures. *Plasma Sources Sci Technol* 2011;20:045002.
- [261] Sharipov A, Starik A. Kinetic mechanism of CO – H_2 system oxidation promoted by excited singlet oxygen molecules. *Combust Flame* 2012;159: 16–29.
- [262] Kee RJ, Grcar JF, Smooke MD, Miller JA. A FORTRAN program for modeling steady laminar one-dimensional premixed flames. 1985. Sandia National Laboratory Report SAND85–8240.

- [263] Nomaguchi T, Koda S. Spark ignition of methane and methanol in ozonized air. *Symp Int Combust* 1988;1677–82.
- [264] Halter F, Higelin P, Dagaut P. Experimental and detailed kinetic modeling study of the effect of ozone on the combustion of methane. *Energy Fuels* 2011;25:2909–16.
- [265] Naidja A, Krishna CR, Butcher T, Mahajan D. Cool flame partial oxidation and its role in combustion and reforming of fuels for fuel cell systems. *Prog Energy Combust Sci* 2003;29:155–91.
- [266] Mantashyan AA. Cool flames and oscillations in hydrocarbon oxidation. *Twenty-Fifth Symp Int Combust* 1994;25:927–32.
- [267] Lignola PG, Reverchon E. Cool flames. *Prog Energy Combust Sci* 1987;13:75–96.
- [268] Griffiths JF, Scott SK. Thermokinetic interactions: fundamentals of spontaneous ignition and cool flames. *Prog Energy Combust Sci* 1987;13:161–97.
- [269] Kim W, Mungal MG, Cappelli MA. Formation and role of cool flames in plasma-assisted premixed combustion. *Appl Phys Lett* 2008;92:051503.
- [270] Roettgen A, Shkurenkov I, Adamovich IV, Lempert WR. Thomson scattering studies in He and He/H₂ nanosecond pulsed nonequilibrium plasmas. In: 52nd AIAA aerospace sciences meeting including the new horizons forum and aerospace exposition, National Harbor, Maryland; 2014. AIAA-2014-1358.
- [271] Noguchi Y, Matsuoka A, Bowden MD, Uchino K, Muraoka K. Measurements of electron temperature and density of a micro-discharge plasma using laser Thomson scattering measurements of electron temperature and density of a micro-discharge plasma using laser Thomson scattering. *Jpn J Appl Phys* 2001;40:326–9.
- [272] Zhu XM, Walsh JL, Chen WC, Pu YK. Measurement of the temporal evolution of electron density in a nanosecond pulsed argon microplasma: using both Stark broadening and an OES line-ratio method. *J Phys D Appl Phys* 2012;45:295201.
- [273] Gavrilenko VP, Kupriyanova EB, Okolokulak DP, Ochkin V, Savinov SY, Tskhai SN, et al. Generation of coherent IR light on a dipole-forbidden molecular transition with biharmonic pumping in a static electric field. *JETP Lett* 1992;56:1–5.
- [274] Yatomi S, Tskhai S, Krasik YE. Electric field in a plasma channel in a high-pressure nanosecond discharge in hydrogen: a coherent anti-stokes raman scattering study. *Phys Rev Lett* 2013;111:255001.
- [275] Lempert WR, Kearney SP, Barnat EV. Diagnostic study of four-wave-mixing-based electric-field measurements in high-pressure nitrogen plasmas. *Appl Opt* 2011;50:5688–94.
- [276] Ito T, Kobayashi K, Mueller S, Luggenhölscher D, Czarnetzki U, Hamaguchi S. Electric field measurement in an atmospheric or higher pressure gas by coherent Raman scattering of nitrogen. *J Phys D Appl Phys* 2009;42:092003.
- [277] Starikovskaia SM, Allegraud K, Guaitella O, Rousseau A. On electric field measurements in surface dielectric barrier discharge. *J Phys D Appl Phys* 2010;43:124007.
- [278] Macko P, Cunge G, Sadeghi N. Density of N₂(X¹Σ⁺_g;v = 18) molecules in a dc glow discharge measured by cavity ringdown spectroscopy at 227 nm: validity domain of the technique. *J Phys D Appl Phys* 2001;34:1807–11.
- [279] Eckbreth AC. Laser diagnostics for combustion temperature and species. Taylor and Francis; 1996.
- [280] Choi I, Yin Z, Adamovich IV, Lempert WR. Hydroxyl radical kinetics in repetitively pulsed hydrogen–air nanosecond plasmas. *IEEE Trans Plasma Sci* 2011;39:3288–99.
- [281] Uddi M. Non-equilibrium kinetic studies of repetitively pulsed nanosecond discharge plasma assisted combustion [Ph.D dissertation]. Department of Mechanical Engineering, Ohio State University; 2008., https://etd.ohiolink.edu/rws_etd/document/get/osu1220625444/inline.
- [282] Yin Z, Eckert Z, Adamovich IV, Lempert WR. Time-resolved radical species and temperature distributions in an Ar–O₂–H₂ mixture excited by a nanosecond pulse discharge. *Proc Combust Inst* 2015. <http://dx.doi.org/10.1016/j.proci.2014.05.073>.
- [283] Miles RB, Lempert WR, Forkey JN. Laser rayleigh scattering. *Meas Sci Technol* 2001;12:R33.
- [284] Kee RJ, Rupley FM, Miller JA, Coltrin ME, Grcar JF, Meeks E, et al. Chemkin collection, release 3.7.1. San Diego, CA: Reaction Design, Inc.; 2003.
- [285] Gardiner WC, Hidaka Y, Tanzawa T. Refractivity of combustion gases. *Combust Flame* 1981;40:213–9.
- [286] Aldén M, Bengtsson PE, Edner H. Rotational CARS generation through a multiple four-color interaction. *Appl Opt* 1986;25:4493–500.
- [287] Zuzek Y, Choi I, Uddi M, Adamovich IV, Lempert WR. Pure rotational CARS thermometry studies of low-temperature oxidation kinetics in air and ethene–air nanosecond pulse discharge plasmas. *J Phys D Appl Phys* 2010;43:124001.
- [288] Palmer R. The CARSFT computer code for calculating coherent anti-Stokes Raman spectra: user and programmer information. SAND89-8206. Livermore, CA: Sandia National Labs; 1989.
- [289] Kronmayer H, Ifecho P, Hecht C, Dreier T, Wiggers H, Schulz C. Gas-temperature imaging in a low-pressure flame reactor for nano-particle synthesis with multi-line NO–LIF thermometry. *Appl Phys B* 2007;88:373–7.
- [290] Bessler WG, Schulz C, Sick V, Daily JW. A versatile modeling tool for nitric oxide LIF spectra. In: 3rd joint meeting of the US sections of the combustion institute, Chicago; 2003.
- [291] Settersten TB, Patterson BD, Humphries IVWH. Radiative lifetimes of NO A²Σ⁺(v' = 0, 1, 2) and the electronic transition moment of the A²Σ⁺–X²Π system. *J Chem Phys* 2009;131:104309.
- [292] Watson GMG, Munzar JD, Berghthorson JM. Diagnostics and modeling of stagnation flames for the validation of thermochemical combustion models for NO_x predictions. *Energy Fuels* 2013;27:7031–43.
- [293] Guo H, Sun W, Haas FM, Farouk T, Dryer FL, Ju Y. Measurements of H₂O₂ in low temperature dimethyl ether oxidation. *Proc Combust Inst* 2013;34:573–81.
- [294] Lefkowitz JK, MacDonald W, Adams S, Ju Y, Windom B, Uddi M. Time dependent measurements of species formation in nanosecond-pulsed plasma discharges in C₂H₄/O₂/Ar mixtures. In: 52nd AIAA aerospace sciences meeting, National Harbor, Maryland; 2014. AIAA-2014-1179.
- [295] Kossyi I, Kostinsky A. Kinetic scheme of the non-equilibrium discharge in nitrogen–oxygen mixtures. *Plasma Sources Sci Technol* 1992;1:207–20.
- [296] Kosarev IN, Aleksandrov NL, Kindysheva SV, Starikovskaia SM, Starikovskii AY. Kinetics of ignition of saturated hydrocarbons by nonequilibrium plasma: CH₄-containing mixtures. *Combust Flame* 2008;154:569–86.
- [297] Shane Stafford D, Kushner MJ. O₂(a¹Δ_g) production in He/O₂ mixtures in flowing low pressure plasmas. *J Appl Phys* 2004;96:2415–65.
- [298] Tsuji M, Kobara K, Obase H, Kouno H, Nishimura Y. Dissociative excitation of CH₄ by collisions with helium active species. *J Chem Phys* 1991;94:277–82.
- [299] Hagelaar GJM, Pitchford LC. “Bolsig+”. Available at: <http://www.bolsig.laplace.univ-tlse.fr/>.
- [300] Itikawa Y. Cross sections for electron collisions with oxygen molecules. *J Phys Chem Ref Data* 2009;38:1–20.
- [301] Itikawa Y. Cross sections for electron collisions with nitrogen molecules. *J Phys Chem Ref Data* 2006;35:31–53.
- [302] Yoon JS, Song MY, Han JM, Hwang SH, Chang WS, Lee B, et al. Cross sections for electron collisions with hydrogen molecules. *J Phys Chem Ref Data* 2008;37:913.
- [303] Brunger MJ, Buckman SJ. Electron–molecule scattering cross-sections. I. Experimental techniques and data for diatomic molecules. *Phys Rep* 2002;357:215–458.
- [304] Itikawa Y. Cross sections for electron collisions with carbon dioxide. *J Phys Chem Ref Data* 2002;31:749–67.
- [305] Mason N, Itikawa Y, Mason N. Cross sections for electron collisions with water molecules. *J Phys Chem Ref Data* 2005;34:1–22.
- [306] Shirai T, Tabata T, Tawara H, Itikawa Y. Analytic cross sections for electron collisions with hydrocarbons: CH₄, C₂H₆, C₂H₄, C₂H₂, C₃H₈, and C₃H₆. *Atomic Data Nucl Data Tables* 2002;80:147–204.
- [307] Jiao CQ, DeJoseph CA, Garscadden A. Electron impact ionization and ion reactions in n-butane. *J Phys D Appl Phys* 2007;40:A09–14.
- [308] Burke MP, Chaos M, Ju Y, Dryer FL, Klippenstein SJ. Comprehensive H₂/O₂ kinetic model for high – pressure combustion. *Int J Chem Kinet* 2011;44:444–74.
- [309] Labbe NJ, Sivaramakrishnan R, Klippenstein SJ, Diévar P, Yang X, Santner J, et al. A detailed analysis of the kinetics of methanol combustion. *Combust Flame* 2015 [submitted for publication].
- [310] Peukert SL, Sivaramakrishnan R, Michael JV. High temperature shock tube studies on the thermal decomposition of O₃ and the reaction of dimethyl carbonate with O-atoms. *J Phys Chem A* 2013;117:3729–38.
- [311] Klippenstein SJ, Harding LB, Glarborg P, Miller JA. The role of NNH in NO formation and control. *Combust Flame* 2011;158:774–89.
- [312] Yang XL, Felsmann D, Kurimoto N, Krüger J, Wada T, Tan T, et al. Kinetic studies of methyl acetate pyrolysis and oxidation in a flow reactor and a low-pressure flat flame using molecular-beam mass spectrometry. *Proc Combust Inst* 2015. <http://dx.doi.org/10.1016/j.proci.2014.05.058>.
- [313] Liu D, Santner J, Togbé C, Felsmann D, Koppmann J, Lackner A, et al. Flame structure and kinetic studies of carbon dioxide-diluted dimethyl ether flames at reduced and elevated pressures. *Combust Flame* 2013;160:2654–68.
- [314] Yang XL, Togai K, Yetter R, Ju Y. Preliminary validation of HP-Mech/plasma for H₂/O₂/NO and methane/O₃ reaction systems. 2015 [submitted for publication].
- [315] Starik AM, Kozlov VE, Titova NS. On the influence of singlet oxygen molecules on the speed of flame propagation in methane–air mixture. *Combust Flame* 2010;157:313–27.
- [316] Nagaraja S, Yang V, Yin Z, Adamovich I. Ignition of hydrogen–air mixtures using pulsed nanosecond dielectric barrier plasma discharges in plane-to-plane geometry. *Combust Flame* 2014;161:1026–37.
- [317] Bao A. Ignition of hydrocarbon fuels by a repetitively pulsed nanosecond pulse duration plasma [Ph.D dissertation]. Department of Mechanical Engineering, Ohio State University; 2008.